



**HAL**  
open science

# Selective Growth and Characterization of InAs and InSb Nanostructures

Wijden Khelifi

► **To cite this version:**

Wijden Khelifi. Selective Growth and Characterization of InAs and InSb Nanostructures. Micro and nanotechnologies/Microelectronics. Université de Lille, 2024. English. NNT : 2024ULILN001 . tel-04581674

**HAL Id: tel-04581674**

**<https://theses.hal.science/tel-04581674>**

Submitted on 21 May 2024

**HAL** is a multi-disciplinary open access archive for the deposit and dissemination of scientific research documents, whether they are published or not. The documents may come from teaching and research institutions in France or abroad, or from public or private research centers.

L'archive ouverte pluridisciplinaire **HAL**, est destinée au dépôt et à la diffusion de documents scientifiques de niveau recherche, publiés ou non, émanant des établissements d'enseignement et de recherche français ou étrangers, des laboratoires publics ou privés.

UNIVERSITÉ DE LILLE

ÉCOLE DOCTORALE SCIENCE DE L'INGÉNIERIE ET DES SYSTÈMES ENGSYS

IEMN - INSTITUT D'ÉLECTRONIQUE DE MICROÉLECTRONIQUE ET DE NANOTECHNOLOGIE

Thesis defended by **Wijden Khelifi**

Defended on 15<sup>th</sup> February, 2024

In order to become Doctor from Université de Lille

Academic Field : Electronics, Microelectronics, Nanoelectronics and  
Micro-waves

# Selective Growth and Characterization of InAs and InSb Nanostructures

## Thesis supervised by

Ludovic Desplanque      Thesis Director

Bruno Grandidier      Co-Supervisor

## Committee members

### Referees

Dr. Yamina André      Associate professor at Clermont Auvergne University

Dr. Bertrand Kierren      Professor at Lorraine University

### Examiners

Dr. Hermann Sellier      Associate professor at Grenoble Alpes University

Dr. Xavier Wallart      Research Director at IEMN      **committee President**

### Supervisors

Dr. Bruno Grandidier      Research Director at IEMN

Dr. Ludovic Desplanque      Associate professor at Lille University



UNIVERSITÉ DE LILLE

ÉCOLE DOCTORALE SCIENCE DE L'INGÉNIERIE ET DES SYSTÈMES ENGSYS

IEMN - INSTITUT D'ÉLECTRONIQUE DE MICROÉLECTRONIQUE ET DE NANOTECHNOLOGIE

Thèse soutenue par **Wijden Khelifi**

Soutenue le 15 février 2024

Pour obtenir le grade de Docteur de l'Université de Lille

Domaine académique : Électronique, Microélectronique,  
Nanoelectronique et Micro-ondes

## **Croissance sélective et caractérisation des nanostructures d'InAs et d'InSb**

### **Thèse encadrée par**

Ludovic Desplanque      Directeur de thèse

Bruno Grandidier      Co-encadrant

### **Membres du comité**

#### **Rapporteurs**

Dr. Yamina André

Maître de conférences (HDR) à l'Université Clermont Auvergne

Dr. Bertrand Kierren

Professeur à l'Université de Lorraine

#### **Examineurs**

Dr. Hermann Sellier

Maître de conférences à l'Université Grenoble Alpes

Dr. Xavier Wallart

Directeur de recherche à l'IEMN

**Président du jury**

#### **Encadrants**

Dr. Bruno Grandidier

Directeur de recherche à l'IEMN

Dr. Ludovic Desplanque

Maître de conférences (HDR) à l'Université de Lille



# Acknowledgements

I extend my heartfelt acknowledgments to those who have played pivotal roles in shaping my academic journey. This thesis is not just the culmination of research; it is a testament to the unwavering support and guidance I've received throughout this endeavor.

Foremost among those deserving my deepest gratitude are my thesis director, Dr. Ludovic Desplanque, and my co-supervisor, Dr. Bruno Grandidier. Their mentorship, unwavering commitment, patience and profound reservoirs of knowledge have been the bedrock of this research.

Dr. Ludovic Desplanque exceptional mentorship shaped the essence of this thesis. I am profoundly thankful for his flexibility, accessibility, his extensive knowledge, that have significantly contributed to reinforcing and deepening my understanding throughout this thesis. Dr. Bruno Grandidier challenged me to transcend my limitations, fostering profound academic transformation. I have always during this thesis benefited from his precious advices, suggestions as well as his positive outlook.

I would like to express my sincere gratitude to the members of my thesis defense committee: Dr. Yamina André, Dr. Bertrand Kierren, Dr. Hermann Sellier, and Dr. Xavier Wallart for their evaluation of my work, as well as for their insightful comments and suggestions.

I'm deeply thankful to the members of the Epiphy group, whose contributions were instrumental in the success of this research. Special thanks go to Dr. Xavier Wallart and Dr. Christophe Coinon for their substantial contributions in the realm of MBE growth processes.

This thesis has also benefited from the resources and facilities provided by the Central of Micro Nano Fabrication as well as the Near Field Platforms. I would like to express my gratitude to all the engineers of these platforms.

Many thanks go to the Physics group members. Dr. Maxime Berthe played an indispensable role in my development, offering invaluable insights and guidance in the intricate Nanoprobe technique. Special thanks go also, to Dr. Pierre Capiod who contributed significantly to my understanding of Low-Temperature Scanning Tunneling Microscopy. Dr. Dominique Deremes expertise in Atomic Force Microscopy proved indispensable in my training in this SPM technique.

I acknowledge with profound gratitude Dr. Gilles Patriarche at C2N and Dr. Pierre-Henry Jouneau and Nicolas Chaize at CEA Leti for their crucial transmission electron microscopy measurements. My sincere thanks to Dr. Hermann Sellier for the cryogenic magneto-transport measurements at Néel Institute.

I am deeply appreciative of the unwavering availability and assistance provided by Nora Benbahlouli, Andy Ledent and Cintia Ayres Pereira in administrative matters. Thank you Emmanuelle Gillmann for your great tips and the positive and invigorating energy you bring during conversations.

To my colleagues and friends Houda, Yevheniia, the inspiring Nemanja, Thomas, Jawad, Ilyas, Niels, Clément, Cristiane, Rita, Thoai, and Jacqueline.. Thank you for being an indispensable part of this adventure! Your unwavering support, shared experiences and funny jokes have made this journey more special and enjoyable.

Lastly, my heartfelt thanks to my family for their unwavering faith, love, and support, which initiated this journey. Their constant companionship is immeasurable.

أحبكم كثيرا!!

This academic odyssey has enriched my knowledge, honed my skills, and ignited a passionate fervor for my field. Challenges were embraced as opportunities for growth. My profound appreciation goes to all who contributed to my academic and personal development.

---

# Abstract

In the landscape of electronic device fabrication, the semiconductor compounds indium arsenide (InAs) and indium antimonide (InSb) have emerged as materials of significant interest for high speed telecommunications and infrared optoelectronics. More recently, their excellent electron transport characteristics, characterized by high mobility and a strong spin orbit coupling, render them highly conducive for applications that exploit quantum transport phenomena. However, their deployment is often hampered by the lattice mismatch they possess with conventional III-V substrates, making them defective. This thesis proposes a solution for fabricating good-quality in-plane InAs and InSb nanostructures, using selective area growth by molecular beam epitaxy in SiO<sub>2</sub> apertures.

A structural and morphological study of InAs and InSb two-dimensional layers and nanowires on GaAs and InP substrates oriented along the [001] and [111] directions has been carried out. The optimization of the growth parameters led to the fabrication of continuous and faceted planar nanostructures with minimized threading defects. These systems were then studied by four-tip scanning tunnelling microscopy in ultra-high vacuum, a technique that eliminates the need for electrode fabrication to characterize the transport properties. The comparison of transport in surface-reconstructed InAs nanowires and core-shell InAs/GaSb nanowires revealed the benefits of embedding the InAs nanowires to significantly increase the electron mobility in the nanowires.

Unlike the InAs nanowires, which can be protected by a thin layer of arsenic to prevent their surface oxidation during their transfer to air, there is no effective protection for InSb. The final part of the thesis therefore focuses on characterizing the deoxidation of InSb (001) and (111) surfaces using a combination of Raman spectroscopy and scanning tunnelling microscopy. This latter study paves the way for subsequent measurements of the transport in InSb nanowires by four-tip scanning tunnelling microscopy.

In conclusion, the structural and electronic quality of the InAs and InSb nanowires produced in this work is compatible with the ballistic transport regime. These results lay down the foundations for the fabrication of the more complex III-V structures, highly prized for the design of quantum devices.

**Key words : InAs, InSb, III-V heterostructures, nanowires, quantum transport, selective area epitaxial growth, multiple-tip scanning tunneling microscopy, transport measurements**

# Résumé

Les composés d'arséniure et d'antimoniure d'indium figurent parmi les candidats les plus prometteurs pour la conception de dispositifs quantiques, grâce à leurs propriétés électroniques supérieures telles que la haute mobilité des électrons et le fort couplage spin-orbite. Cependant, leur déploiement est souvent entravé par le désaccord de maille qu'ils possèdent avec les substrats III-V conventionnels et qui les rend défectueux. Cette thèse propose une solution pour fabriquer des nanostructures d'InAs et d'InSb de bonne qualité, grâce à une croissance sélective par épitaxie par jets moléculaires dans des ouvertures de SiO<sub>2</sub>.

Une étude structurale et morphologique de couches bi-dimensionnelles et de nanofils d'InAs et InSb sur des substrats de GaAs ou d'InP orientés suivant les directions [001] et [111] a été réalisée. L'optimisation des paramètres de croissance a conduit à la fabrication de nanostructures planaires continues et facettées avec une minimisation des défauts émergents. Ces systèmes ont ensuite été étudiés par microscopie à effet tunnel à quatre pointes en ultraviolet, technique qui permet de s'astreindre de la fabrication d'électrodes pour caractériser les propriétés de transport. La comparaison du transport dans des nanofils InAs reconstruits en surface et des nanofils cœur-coquille InAs/GaSb a révélé l'intérêt d'une encapsulation des nanofils d'InAs pour augmenter sensiblement la mobilité électronique dans les nanofils.

Contrairement aux nanofils d'InAs, qui peuvent être protégés par une fine couche d'arsenic pour éviter l'oxydation de leur surface pendant leurs transferts à l'air, il n'existe pas de protection efficace pour l'InSb. Aussi, la dernière partie de la thèse porte sur la caractérisation de la désoxydation des surfaces d'InSb (001) et (111) en combinant la spectroscopie Raman et la microscopie à effet tunnel. Cette dernière étude ouvre la voie à des mesures ultérieures de transport de nanofils InSb par microscopie à effet tunnel à quatre pointes.

En conclusion, la qualité structurale et électronique des nanofils d'InAs et InSb réalisée dans ce travail est compatible avec le régime de transport balistique. Ces résultats jettent les bases pour la fabrication de structures III-V plus complexes actuellement recherchées pour la conception de dispositifs quantiques.

**Mots clés : InAs et InSb, hétérostructures III-V, nanofils, épitaxie par jets moléculaires par croissance sélective, microscopie à effet tunnel à pointes multiples, transport électronique.**

# Contents

<b>Introduction</b>	<b>1</b>
<b>1 In-plane III-V nanostructures for advanced quantum devices</b>	<b>6</b>
1 Introduction . . . . .	6
2 Epitaxial growth of nanostructures . . . . .	7
2.1 Epitaxial growth . . . . .	7
2.1.1 Principle . . . . .	7
2.1.2 Epitaxial techniques . . . . .	8
2.2 Methods for growing nanowires . . . . .	8
2.2.1 The Vapour-Liquid-Solid technique . . . . .	9
2.2.2 Selective area growth . . . . .	9
3 Electron transport . . . . .	10
3.1 Experimental methods for the exploration of ballistic resistance . . . . .	10
3.2 Other methods for the exploration of ballistic effects . . . . .	13
4 Low electron effective mass InAs and InSb nanostructures . . . . .	15
4.1 Transport and crystal quality . . . . .	15
4.2 Lattice mismatch accommodation . . . . .	16
4.3 InAs nanostructures . . . . .	18
4.3.1 InAs thin films and 2DEG . . . . .	18
4.3.2 Bottom-up InAs NW and networks . . . . .	20
4.4 InSb nanostructures . . . . .	26
4.4.1 InSb thin films and 2DEG . . . . .	26
4.4.2 Bottom-up InSb NWs and networks . . . . .	27
5 Thesis objectives . . . . .	30
<b>2 Experimental techniques</b>	<b>39</b>
1 Introduction . . . . .	39
2 Molecular Beam Epitaxy (MBE) . . . . .	40
2.1 The IEMN MBE System . . . . .	41
2.1.1 Epitaxial growth . . . . .	42
2.1.2 Growth control with Reflexion High Energy Electron Diffraction (RHEED) . . . . .	43
2.2 Definition of the mask . . . . .	44
2.3 Control of the mask openings . . . . .	46
2.4 Selective Epitaxial growth . . . . .	48
2.5 Contact deposition for cryogenic measurements . . . . .	49
3 Scanning Tunnelling Microscopy . . . . .	50
3.1 Tunnelling current . . . . .	50
3.2 Tip preparation . . . . .	53
3.3 Omicron LT-STM . . . . .	54
3.4 Four-Probe-STM (4P-STM) . . . . .	56
3.4.1 Technical description . . . . .	56

3.4.2	Measurements of the resistance . . . . .	57
4	Atomic Force Microscopy AFM . . . . .	60
5	Hall effect measurements . . . . .	61
6	Complementary characterization techniques . . . . .	63
7	Conclusion . . . . .	64
<b>3</b>	<b>Transport properties of oxidized and reconstructed InAs (111) nanostructures</b>	<b>67</b>
1	Introduction . . . . .	67
2	Optimizing growth conditions . . . . .	67
2.1	Thin films . . . . .	68
2.1.1	Growth conditions . . . . .	68
2.1.2	Morphology of the InAs surface . . . . .	69
2.1.3	InAs film relaxation . . . . .	71
2.2	InAs 111 nanowires . . . . .	73
3	Transport properties of InAs films with oxidized surfaces . . . . .	76
4	Transport properties of InAs (111) nanowires with cleaned facets . . . . .	78
4.1	Sample transfer protocol . . . . .	78
4.2	4P-STM measurements . . . . .	79
4.2.1	Resistivity of the reference 2D Electron Gas . . . . .	80
4.2.2	Sheet resistance of InAs nanowires . . . . .	84
5	Conclusion . . . . .	87
<b>4</b>	<b>In-plane InAs/GaSb nanostructures grown on III-V (001) substrates</b>	<b>91</b>
1	Introduction . . . . .	91
2	InAs/AlGaSb 2-Dimensional-Electron-Gas (2DEG) . . . . .	92
2.1	Presentation . . . . .	92
2.2	Growth conditions . . . . .	93
2.3	Hall effect measurements . . . . .	94
2.4	In-situ 4P STM Transport measurements . . . . .	96
2.5	Comparison between both techniques . . . . .	100
3	InAs/GaSb in-plane nanowires . . . . .	101
3.1	Growth conditions . . . . .	101
3.2	Morphological study . . . . .	105
3.3	Transport measurements . . . . .	107
3.4	Device fabrication for magneto-transport measurements . . . . .	112
4	Conclusion . . . . .	115
<b>5</b>	<b>MBE growth and characterization of InSb nanostructures</b>	<b>119</b>
1	Introduction . . . . .	119
2	InSb growth optimization on InP wafers . . . . .	120
2.1	Nucleation of InSb on un-masked InP(100) . . . . .	120
2.2	Growth of InSb on un-masked InP(111) <sub>B</sub> . . . . .	123
2.3	Selective area growth of InSb on InP(111) <sub>B</sub> . . . . .	127
2.3.1	Nucleation of InSb inside nanoscale openings . . . . .	127
2.3.2	Selective growth of in-plane InSb nanowires . . . . .	129
3	Atomic structures of the InSb (100) and (111) <sub>B</sub> surfaces resulting from deoxidation	133
3.1	The InSb (100) surface reconstruction after deoxidation . . . . .	134
3.1.1	Growth of the InSb heterostructure . . . . .	134
3.1.2	Monitoring the oxide desorption . . . . .	135
3.1.3	STM study of the surface structure . . . . .	136



3.2	Reconstruction of the InSb (111) <sub>B</sub> surface . . . . .	138
3.2.1	Monitoring the oxygen desorption . . . . .	138
3.2.2	STM study of the surface structure . . . . .	140
4	Conclusion . . . . .	141
	<b>Conclusion</b>	<b>146</b>
	<b>Appendix 1 : Fundamentals of ballistic versus diffusive transport</b>	<b>149</b>
	<b>Appendix 2: Masks layouts</b>	<b>157</b>
	<b>List of Publications and Communications</b>	<b>161</b>

# List of Figures

1.1	Simplified schematic representation of adsorption, incorporation, diffusion and nucleation processes during epitaxy. . . . .	7
1.2	(a) Schematic representation of the two-tip resistance measurement configuration in which the contact resistance influences the measured total resistance. (b) Illustration of contacting a single multiwall nanotube in a SEM setup equipped with a moveable probe [25]. (c) Schematic diagram of a 2-probe transport measurement performed on an InAs nanowire with an atomic force microscope. The current is measured for fixed bias voltage $V_{sd}$ as a function of tip-electrode distance $L$ . [7] (d) Resistance measured by cAFM as a function of tip-contact distance $L$ (symbols), with linear fits for the ballistic transport regime ( $L$ below 200 nm), for which the resistance is independent of $L$ , and the drift transport regime ( $L$ above 200 nm) for which the resistance increases linearly with $L$ . [7].	12
1.3	Schematic representation of the four-probe resistance measurement configuration in which the contact resistances are excluded from the measured total resistance. . . . .	13
1.4	(a) Nomarski optical micrograph of a Hall bar device. (b) SEM image of a 0.5 $\mu\text{m}$ -wide four terminal device with lead numbers indicated. (c) The bend resistance for four-terminal devices of various widths (0.2, 0.35, 0.5, 0.65 $\mu\text{m}$ ) as a function of magnetic field applied perpendicular to the plane of the 2DEG. The measurements were performed at 1.5 K [28]. . . . .	14
1.5	InAs/InSb unit cell. Adapted from [37]. . . . .	16
1.6	Plot of semiconductors bandgap versus lattice constant [38]. . . . .	17
1.7	Schematics of different types of interfaces between dissimilar film and substrate. (a) Unstrained coherent interface, (b) strained coherent interface, (c) semi-coherent interface with dislocations, (d) incoherent interface, Adapted from [41].	17
1.8	InAs/barrier Quantum well structure and its relative conduction band structure scheme . . . . .	19
1.9	SEM image viewed at 85° from normal of a pair of connected nanowires grown on InP ridges pitched at 3.5 $\mu\text{m}$ . The inset is a close-up to the intersection. The scale bar is 100 nm (adapted from [55]). . . . .	22
1.10	(a) Schematic illustration of TASE of InAs nanowire inside a lateral ( $\text{SiO}_2$ ) template [57] (b) Colorized 3D-SEM image of a template structure containing Si pads and InAs NWs covered by a $\text{SiO}_2$ film (c) SEM image of a complex pattern filled by InAs NWs and Si pads inside the $\text{SiO}_2$ template (d) Schematic of the measurement device. Metallic probes (yellow) are connected to an InAs NW cross junction (red), covered by a protective oxide template (green). The current $I_{out}$ at one terminal in response to a bias voltage $V_{bias}$ is measured as a function of gate voltage $V_{gate}$ . (e) False-colored SEM image of a single NW (left) and two cross sections (right). (f) Electrical conductance $G = V_{bias}/I$ of a single NW (blue) and a NW cross-junction (red) as a function of gate voltage at 4 K [58]. . . . .	23

1.11	(a) Example of complex NW networks composed of the $\langle 11\bar{2} \rangle$ NW family [16]. (b) Scanning electron micrograph of an InAs SAG Aharonov–Bohm ring (yellow) contacted by Ti/Au leads (purple) and covered with SiNx dielectric and a top-gate electrode (red). The loop area (A) corresponds to $0.9 \mu\text{m}^2$ . . . . .	24
1.12	HAADF STEM image recorded after 150 nm GaSb growth followed by 10 nm InAs in apertures directed along (a) [110] and (b) [1–10] [60]. . . . .	25
1.13	InSb quantum well. (a) Layer stack of the InSb/GaAs heterostructure, where the layer constituents and thicknesses are indicated. (b) Scanning transmission electron micrograph of the structure of (a) obtained in High Angle Annular Dark Field Mode along the [110] zone axis [65]. . . . .	27
1.14	(a) Vertical stemless InSb nanowires [72] (b) Measured Quantum Point Contact (QPC) conductance versus the top-gate voltage at 6K presenting quantized conductance behaviour [72] (c) , InSb nanocrosses resulting from the merging process between two InSb nanowires. The inset shows InAs and InSb segments in orange and red, respectively, and the Au–In droplet is in yellow [71]. . . . .	28
1.15	(a) SEM image of an InSb NW array defined with $100 \text{ nm} \times 2.6 \mu\text{m}$ apertures [73]. (b) . STEM image of the cross-section of an InSb in-plane nanowire grown inside a 50 nm wide aperture. White scale bar is 20nm [73] (c) HAADF image in the red rectangle of image (b) showing the absence of threading defects in the nanostructure. Black scale bar is 10nm. . . . .	29
1.16	(a) SEM images showing the growth steps starting by the In sowing at $465^\circ\text{C}$ to the InSb nanowires growth in the mask apertures, every SEM images is represented by a scheme on the top of it.[22] (b) False colored SEM image of the InSb Quantum Point Contact (QPC) device. Contacts are blue, the gate is purple, and the NW is yellow away from the electrodes. The scale bar is 500 nm. A magnetic field is applied along the in-plane direction perpendicular to the NW [22]. (c) Zero-DC-bias pinch-off traces of the device shown in panel a, taken at field values between 0 and 5.5 T with intervals of 0.3 T [22]. . . . .	30
2.1	Photographs of (a) III-V MBE Riber compact 21 reactor composed of : a transfer rod of samples from the intermediate chamber to the growth chamber (orange box) III-V growth chamber (black box), ion pump (blue box), RHEED screen with the camera (yellow box) and the valved cracker sources and shutters (green box), (b) Chamber for Electron Spectroscopy for Chemical Analysis (ESCA). . . . .	41
2.2	The RHEED oscillations principle [12]. . . . .	44
2.3	Sketch of the different steps for the mask preparation that is used for selective area growth. . . . .	44
2.4	Layout of the selectively grown nanostructures designed for the 4P measurements. More details about the layout are given in Figure A.6 in the Appendix 2 . . . . .	45
2.5	Influence of a wet etching time on the mask aperture for (a) an InSb(100) wafer after 30s of etching, (b) an InSb(100) wafer after 20s of etching. . . . .	47
2.6	Influence of a wet etching time of 30 s on the SiO <sub>2</sub> mask aperture for two different wafer orientations: (a) an InP (111) wafer and (b) an InP (100) wafer. The nominal width of the mask aperture is 100 nm. . . . .	48
2.7	SEM images of selectively grown InSb nanostructures on an InSb (100) substrate: (a) NWs (500nm, 200nm, 100nm and 50nm nominal widths (left to right)) with [110] and [100] orientations; (b) Aharonov-Bohm ring InSb nanostructures; (c) grid with 50nm, 100nm, 200nm and 500nm-wide NWs (left to right and top to bottom view); (d) honeycomb lattice. . . . .	49

2.8	Principle of the tunneling effect through a potential barrier (vacuum). . . . .	51
2.9	Illustration of the tip etching method. (a) Formation of the meniscus. (b) Wire etching mostly in the meniscus region and the necking phenomenon. (c) The tip sharp apex starts to appear by continuous etching of the lower part. (f) The lower part breaks off producing a sharp tip. . . . .	53
2.10	SEM image of the tip apex, the inset shows a zoom of the apex. The scale in the inset image is 2 $\mu$ m. . . . .	54
2.11	Photograph of the LT-STM system. . . . .	55
2.12	Photograph of the 4P-STM system. . . . .	57
2.13	(a) Representative scheme of the four-probe STM measurements inside the analysis chamber. (b) SEM image of the four probes closely approached to an InAs surface inside the analysis chamber of the four-probe STM. . . . .	58
2.14	(a) SEM image of four tips positioned in an arbitrary geometry on a sample. (b) 3D scheme illustrating four aligned non equidistant probes in contact with a sample. . . . .	59
2.15	(a) SEM image illustrating the 4P-STM measurements of an InAs nanowire. The current is injected by the source (blue) and the voltage is measured between the two inner probes (red tips). In this image the measured nanowire is coloured in yellow. d is considered as the varying distance between the two inner probes. . . . .	60
2.16	Schematic representations of the (a) AFM scanning principle and (b) the convolution effect due to the finite size of the tip. . . . .	61
2.17	(a) Etched sample with hall bars and van der Pauw microstructures. Indium balls (droplets) are deposited on the InAs mesa. (b) 3D scheme of samples B and C with InAs etched Hall bars. . . . .	62
3.1	SEM and AFM images of samples A (a,d). B (b,e) (the scale bar in the inset of (b) is 1 $\mu$ m-long) and C (c,f) respectively. The inset in (f) is a magnified view of the surface inside the blue rectangle in (f) where the scale bar is 250 nm-long. . . . .	69
3.2	AFM images and height profiles taken along the blue line plotted in the AFM images of samples A (a,d), B (b,e,) and C (c,f) respectively. Red dashed lines in (d), (e) and (f) correspond to the multiples of the theoretical InAs(111) monolayer step height (3.5 $\text{\AA}$ ). . . . .	71
3.3	(a) XRD data compared to the simulated spectrum assuming a 50% strain relaxation of the film for the 10 nm-thick epitaxial InAs layer on InP (111) <sub>B</sub> , (b) XRD data compared to the simulated spectrum assuming a 70% strain relaxation of the film for the 30 nm-thick epitaxial InAs layer on InP (111) <sub>B</sub> . . . . .	72
3.4	SEM images of (a,b) InAs nanowires grown on InP(111) <sub>B</sub> wafers with a nominal width of 100nm for different crystallographic orientations on sample A <sub>SEL</sub> and B <sub>SEL</sub> respectively. The blue-aqua arrows underline numerous defects on the nanowires. (c,d) $[\bar{2}11]$ -oriented nanowires with 1000 nm, 500 nm, 200 nm, 100 nm and 50 nm nominal widths for the sample A <sub>SEL</sub> and B <sub>SEL</sub> respectively. The blue-aqua arrows underline defects on the nanowires. . . . .	74
3.5	(a) SEM images of 200 nm-wide InAs NWs with different in-plane orientations (rotation every 10° from $[0\bar{1}1]$ to $[\bar{2}11]$ ) grown by SAE on InP(111) <sub>B</sub> (sample C <sub>SEL</sub> ). The different facets that are formed at the end of the NWs are highlighted in the different insets. (b) SEM images of 200 $\mu$ m-long and $[\bar{2}11]$ oriented InAs NWs with different nominal widths (1000 nm down to 50nm from left to right) (sample C <sub>SEL</sub> ). (c) Schematic representation of the nanowire geometry along the $\langle\bar{2}11\rangle$ orientation.[5] (d) Schematic representation of the nanowire geometry along the $\langle 1\bar{1}0 \rangle$ orientations [9]. . . . .	75

3.6	(a) AFM image of a series of 200 nm-wide-nanowires along the $[\bar{1}01]$ direction of the sample $C_{SEL}$ . (b) Height profile of the NW series along the blue line plotted in (a). . . . .	76
3.7	Scheme illustrating the transfer process of sample $C_{SEL}$ from the MBE system to the 4P-STM system. . . . .	79
3.8	False coloured SEM image illustrating the 4P-STM measurement with four aligned and equidistant probes. The blue outer probes are used to inject (source) and collect (sink) the current, whereas the red inner probes measured the potential drop V1-V2. . . . .	80
3.9	(a) Curves of the 4P-STM measurements for the sample C at room temperature for different distances d between the two inner probes. Inset: 2P measurements performed at d = 9.6 $\mu\text{m}$ . (b) Curves of the 115K 4P-STM measurements for sample C prepared on an InP(111) <sub>B</sub> wafer for different distances d between the two inner probes. Inset: the 2P measurements performed at d=10 $\mu\text{m}$ . . . . .	81
3.10	Four-probe resistances of the InAs film grown on InP(111) <sub>B</sub> SI wafers (sample C) at RT and at 115K as a function of equidistant probe separations (square and rhombus) and Hall bars resistances measured at RT and at 77K (cross). The dashed horizontal lines correspond to the mean values of the 4P resistances. . . . .	83
3.11	Schematic of the distance d measured including the uncertainty induced by the radius of the STM tip based on the SEM images. . . . .	84
3.12	(a) 4P averaged V(I) curves measured on a 100 nm-wide and $[0\bar{1}1]$ -oriented nanowire (grown on an InP(111) <sub>B</sub> SI wafer (sample $C_{SEL}$ )) for different inter-probe distances d. (b) 2P averaged I(V) curves measured on the same nanowire for different inter-probe distances d. . . . .	85
3.13	4-Probe resistance versus d. (Left) Measurement carried out on 100 nm-wide NWs grown on an InP(111) <sub>B</sub> SI wafer (sample $C_{SEL}$ ). (Right) Measurements carried out on 200 nm-wide NWs. Lines correspond to best fits. . . . .	86
3.14	Summary of the sheet resistances measured in InAs NWs of sample $C_{SEL}$ and from literature benchmarked with the sheet resistance of the sample C (oxidized and non-oxidized). . . . .	88
4.1	(a) Band diagram and charge carrier distribution simulated with Nextnano simulation for the InAs/Al <sub>0.8</sub> Ga <sub>0.2</sub> Sb quantum well. (b) Band diagram and charge carrier distribution simulated with Nextnano simulation of the InAs/GaSb quantum well. . . . .	93
4.2	Structures the InAs/Al <sub>0.8</sub> Ga <sub>0.2</sub> Sb (a) and InAs/GaSb. (b) epilayers grown on semi-insulating GaAs (100) SI. . . . .	94
4.3	XRD spectrum of the InAs/Al <sub>0.8</sub> Ga <sub>0.2</sub> Sb sample compared to the simulated spectrum assuming a full relaxation of the GaSb layer and fully strained InAs and AlGaSb layers with respect to GaSb. . . . .	95
4.4	SEM image of the four probes contacting the heterostructure surface inside the UHV analysis chamber of the four probe-STM. . . . .	97
4.5	Multiple and reproducible 4P measurement at d=15 $\mu\text{m}$ , (inset) 2P measurement for the same distance d=15 $\mu\text{m}$ . . . . .	98
4.6	Curves of the 4P-STM measurements for the InAs/Al <sub>0.8</sub> Ga <sub>0.2</sub> Sb quantum well at 115K for different distances d between the two inner probes. . . . .	99
4.7	Variation of the four-point probe resistance as a function of equidistant probe separation and equivalent four-probe resistances deduced from Hall measurements (crosses). Horizontal dash lines are projections of the Hall values over the full range of distances to guide the eye. . . . .	101

4.8	Layout for the selectively grown nanostructures designed for the 4P-measurements. More details about the layout are given in Figure A.7 of the Appendix 2 . . . . .	102
4.9	Layout of the selectively grown nanostructures for cryogenic measurements. More details about the layout are given in Figure A.8 of the Appendix 2 . . . . .	103
4.10	Cross-section scheme representing the InAs/GaSb core-shell nanostructures grown on InP (001). . . . .	104
4.11	SEM images of the InAs/GaSb selectively grown nanostructures on InP (100) SI wafers: (a) Overview of a nanostructure field. (b,c) Images of complex networks and hall bar nanoribbons. (d,e,f) Images of simple nanowires with 100 nm and 200 nm nominal widths along different crystallographic orientations, with zooms of the side facets in the insets. (g) Ring nanostructures. . . . .	105
4.12	HAADF and associated EDX micrographs of nanowires grown by SAG inside [110]-oriented openings with a nominal width of 100 nm (a-e) and 200 nm (f-j) and [100]-oriented openings with a nominal width of 100 nm (k-o) and 200 nm (p-t). The scale bar represents 50 nm. . . . .	106
4.13	TEM bright field micrographs of in-plane [110] or [100]-oriented InAs/GaSb NWs grown inside (a and e) a 200 nm-wide mask aperture or (b and f) a 100 nm-wide mask aperture, (c and g) a 100 nm-wide mask aperture, (d and h) a 200 nm-wide mask aperture. (e), (f), (g) and (h) are magnified views of the InP-GaSb interface inside the blue rectangles indicated in images (a), (b), (c) and (d) respectively. . . . .	107
4.14	Colorized SEM image presenting a 4P measurement performed on one branch of a cross-bar NW (in green). The current is injected and collected by external probes (blue) and the voltage is measured by the internal probes (red) separated by the distance d. . . . .	108
4.15	(a) Multiple 4P measurement at d= 2580 nm for a 100 nm wide nanowire with the [110] orientation grown on an InP (100) SI wafer. (b) 4P averaged V(I) curves measured with different inner probe separations on the same nanostructure. . . . .	108
4.16	(Left) SEM image showing the tip deterioration during the probe approach on one nanowire and (Right) SEM image presenting the nanowire after measurements. . . . .	109
4.17	4P-resistance versus distance d for 100 nm wide NWs (left) or 200 nm-wide NWs (Right). Lines correspond to the best linear fit. NWs grown on an InP(100) SI wafer . . . . .	110
4.18	Sheet resistance estimated from four-probe resistance measurements on all the measured NWs benchmarked with the sheet resistance of InAs/GaSb 2DEG. InAs NWs are grown on InP (111) <sub>B</sub> SI wafer, InAs/GaSb NWs are grown on an InP (100) SI wafer and InAs/GaSb QW grown on a GaAs (100) SI wafer. . . . .	111
4.19	False coloured tilted SEM images of InAs/GaSb based devices. The blue coloured patterns are the InAs/GaSb NWs, the orange coloured layers correspond to the (Ti/Pt) layers and the yellow coloured structures refer to the (Ti/Au) thick contacts. (a) NWs junctions-based devices, (b) Aharonov-Bohm (rings) nanostructure-based devices. The inset in (b) is a zoomed SEM image on the part of the nanostructure where the (Ti/Pt) contacts are deposited. . . . .	113
4.20	Magneto-resistance variations depending to the applied magnetic field of InAs/GaSb junction of two perpendicular 100 nm-wide and 4.25 μm long NWs grown along the [100] and [010] orientations. . . . .	114



4.21	Magneto-transport measurements performed at 0.3K on single NW with 12 $\mu\text{m}$ 2P (a) or 2 $\mu\text{m}$ 4P (b) configuration. . . . .	115
5.1	SEM images of the samples (a) V <sub>100</sub> , (b) V <sub>200</sub> , and (c) V <sub>300</sub> . InSb islands grown on InP(100) wafers . . . . .	121
5.2	AFM image of the InSb nanostructures after the deposition of a nominal thickness of 10 nm on the InP (100) substrate at (a) 390°C (sample T <sub>100</sub> ) and (b) 405°C (sample T <sub>200</sub> ). Scale bar is 1 $\mu\text{m}$ . (c) Height profile of an InSb island of sample T <sub>100</sub> along the [1 $\bar{1}$ 0] (green line) and the [110] (blue line) directions. (d) Height profile of an InSb island of sample T <sub>200</sub> along the [1 $\bar{1}$ 0] (green line) and the [110] (blue line) directions. (e) The Table summarizes the mean width along both crystal directions for the islands observed on samples T <sub>1[100]}</sub> and T <sub>200</sub> . . . . .	122
5.3	(a) variation of the InP (111) <sub>B</sub> surface covered by InSb at different growth rates for the deposition of a nominal thickness of 10 nm at 390°C and corresponding AFM images of the surface for growth rates of (b) 0.05 ML/s, (c) 0.1 ML/s and (d) 0.2 ML/s. . . . .	124
5.4	SEM (a, d and g) micrographs, AFM images (b, e and h) and XRD spectra (c, f and i) of InSb layers on InP(111) <sub>B</sub> with a nominal deposited thickness of 10 nm (sample A), 30 nm (sample B) and 100 nm (sample C) respectively. Inset of (a) and (g) display a magnified view of a hillock observed on the surface. Scale bars are 200 nm long. . . . .	125
5.5	(a) AFM image of the sample B. (b) Depth profile of the hole along the purple line in (a), (c) Higher resolution AFM image than in (a) showing InSb terraces. (d) Height profile along the black line in (c). . . . .	126
5.6	SEM images of the InSb deposition with a nominal thickness of 10 nm by atomic H-assisted MBE into SiO <sub>2</sub> openings forming an array of 20 $\mu\text{m}$ -long parallel nanowires oriented along $[\bar{2}11]$ with different widths from 1 $\mu\text{m}$ (first opening from left), 500 nm (openings 2 to 5), 200 nm (openings 6 to 9), 100 nm (openings 10 to 13) and 50 nm (last four openings to the right). (a) sample SAG1, (b) sample SAG2, (c) sample SAG3 and (d) sample SAG4. InSb NWs grown on InP (111) <sub>B</sub> wafers . . . . .	128
5.7	SEM images of different patterns of the sample SAG5 (30 nm-thick InSb NWs grown on an InP (111) <sub>B</sub> wafer at 390°C with a growth rate of 0.05ML/s and a flux ratio of 120). (a) 200 nm-wide InSb NWs in different in-plane orientations (rotation every 10° from $[0\bar{1}1]$ to $[\bar{2}11]$ ) of SAG5. (b) SEM images of 20 $\mu\text{m}$ -long and $[\bar{2}11]$ oriented InSb NWs with different nominal widths (1000 nm down to 50 nm from left to right). (c) Rings with 1 $\mu\text{m}$ inner diameters. Pattern opening is 100 nm. . . . .	129
5.8	AFM images of 30 nm-thick InSb nanowires grown by SAG on InP(111) <sub>B</sub> with a growth rate of 0.05 ML/s and a Sb/In flux ratio of 120 (sample SAG5). Nominal aperture widths are 50 nm (a and c) and 100 nm (b and d) for in-plane orientation along the $[\bar{2}11]$ direction (a and b) or the $[0\bar{1}1]$ direction (c and d). (e) Height profiles along the green, red, blue and black lines in (a), (b), (c) and (d) respectively. The inset shows a height profile along the two (black and orange) lines in (d). . . . .	131

5.9	(a) HAADF-STEM cross section of a $[01\bar{1}]$ -oriented InSb NW belonging to sample SAG5 (30 nm-thick InSb NWs grown on an InP (111) <sub>B</sub> wafer at 390°C with a growth rate of 0.05ML/s and a flux ratio of 120). Scale bar is 50 nm. Elemental mapping of the cross-section highlighting (b) Si (pink) and O (light blue), (c) Sb (red), (d) In (green) and (e) P (blue). Scale bar is 40 nm. (f) Magnified view of the area delimited by a blue dashed square in (a). Scale bar is 10 nm. (g) High-resolution image of the InSb/InP interface. Scale bar is 5 nm. (h) Numerical filtered image of the red dashed square area in (g) highlighting the interface misfit dislocations (green circles), scale bar is 3 nm. . . . .	132
5.10	(a) Scheme illustrating the transfer process of the InSb/Al <sub>0.3</sub> In <sub>0.7</sub> Sb QW from the MBE system to the LT-STM system. (b) UHV-Raman spectra of the heterostructure before and upon simultaneous annealing and hydrogen sputtering of the sample. The transverse acoustic, transverse and longitudinal optical, the Fuchs-Kliewer surface phonon modes are labelled TA, TO, LO, FK respectively. The spectra are vertically shifted for convenience. The inset illustrates the Raman spectrum of the heterostructure compared to an InSb (100) substrate spectrum. . . . .	135
5.11	(a) STM image of the InSb (100) surface obtained at 77K. Feedback parameters $V_s = -0.75V$ and $I_t = 110$ pA. (b) Magnified view corresponding to the green square shown in (a). (c) Height profile along the blue segment in (a), black dashed lines correspond to mean value of the fluctuations of the blue profile at each terrace level (d) FFT image of an enlarged part of (b), green circles correspond to bright points. (f) Inverted FFT image of (d). . . . .	137
5.12	(a) STM image of the InSb/In <sub>0.7</sub> Al <sub>0.3</sub> Sb quantum well (sample bias = -0.7V, tunnelling current 110pA). (b) enlarged flower-like pattern of the InSb/In <sub>0.7</sub> Al <sub>0.3</sub> Sb quantum well (sample bias = -0.7V, tunnelling current 110pA). (c) STM image of the $c(8 \times 2)$ InSb(100) surface acquired at 77 K ( $25 \times 25$ nm <sup>2</sup> , sample bias: 0.5 V, tunnelling current: 50 pA). White rectangles indicate $c(8 \times 2)$ unit cells for two differently tilted domains. The frame is drift corrected and rotated to align the $[110]$ direction horizontally in order to show the structure angles clearly. (d) Enlarged “protruding defect”. (e) “Elongated long” form. (f) “Elongated short” form [22]. All STM images are measured at 77K. . . . .	138
5.13	UHV-Raman spectra of the InSb/InP(111) <sub>B</sub> heterostructure before and after 1h of simultaneous annealing and hydrogen sputtering. . . . .	139
5.14	(a) STM image of the InSb (111) <sub>B</sub> surface measured at 77K. Feedback parameters: $V_s = -1.8V$ and $I_t = 150$ pA. (b) Atomically-resolved STM image showing two different types of defects surrounded by a blue diamond. (c) FFT image of an enlarged part of (a), green circles correspond to bright points. (d) and (e) Height profiles along the blue segments in (a) and (b) respectively. (f) Comparison with the literature [25] for an occupied-state STM image measured at room temperature, where the atomic structure corresponds to a $(3 \times 3)$ reconstruction. . . . .	140
A.1	Diffusive and ballistic transport in a channel. . . . .	150
A.2	Simplified scheme of a ballistic conductor with a length $L$ connected to two electrodes 1 and 2 with Fermi energies $E_{F1}$ and $E_{F2}$ respectively. $M$ is the number of channels in which electrons propagate between the electrodes. . . . .	151



A.3	(a) Schematic diagram of the experimental setup. The nanotube contact is lowered under SPM control to a liquid metal surface. After contact is established, the current $I$ is measured as the fiber is moved into the liquid metal, so that the conductance can be determined as a function of the position of the nanotube contact. (b) Conductance as a function of the dipping length into the liquid mercury contact. The quantized conductance of $G_0$ corresponds to a single nanotube making contact to mercury. The other quantized conductance values correspond to two and three nanotubes making contact to the metal. [Adapted from [4]]. . . . .	153
A.4	The 1D quantum transport across multiple NW junctions. (a) False-colored SEM image of a device with 0 cross-junctions. (b) Conductance versus $V_{\text{gate}}$ curves for various numbers of cross-junctions in the transport channel ( $l= 300$ nm, blue; $l= 800$ nm, red; $l= 900$ nm, green; $l= 1200$ nm, brown; $l= 1500$ nm, orange; $l= 1700$ nm, black). On all curves, the same average contact resistance of $6.7 \text{ k}\Omega$ has been subtracted. (c) Experimental plateau resistance (symbols) as a function of channel length $l$ . The values are obtained by averaging the data in (b) over the full width at half-maximum of the minima of the transconductance. The error reflects the standard deviation. The red dotted lines in the SEM inset mark the position of the right contact relative to the position of the left contact that corresponds $L= 0$ at the bottom axis. [8]. . . . .	154
A.5	(a) Geometry of the cleaved-edge overgrowth (CEO) device. The fabrication starts with a high-quality 2DEG created by epitaxial growth of a unilaterally doped GaAs quantum well onto a [001] GaAs substrate [10]. (b) A representative result of a two-terminal conductance measurement of a CEO wire at 300 mK. . . . .	155
A.6	(a) Layout of the selective epitaxy designed to grow nanostructures on (111)-oriented substrates for the 4P measurements (Same as Figure 2.4) (b) Sun-like pattern with 100 nm-wide and 10 $\mu\text{m}$ -long rectangles tilted by $10^\circ$ . (c) 20 $\mu\text{m}$ -long rectangles with different widths . . . . .	158
A.7	Layout of the selective epitaxy designed to grow nanostructures on (100)-oriented substrates for 4P measurements . . . . .	159
A.8	Layout of the selectively grown nanostructures designed for the cryogenic measurements . . . . .	160

# List of Tables

3.1	Samples growth conditions . . . . .	68
3.2	Growth conditions and structural properties of the InAs layer relaxation for the different InAs thin films studied in this chapter. . . . .	72
3.3	Hall measurements of samples B and C at RT and at 77K. . . . .	77
3.4	Four-probe-resistance against the distance $d$ at 300K. . . . .	81
3.5	Four-probe resistance against the distance $d$ at 115K. . . . .	82
3.6	Mobilities, charges densities and sheet resistances of samples B and C at different temperatures. . . . .	84
4.1	Hall data measured on $\text{Al}_{0.8}\text{Ga}_{0.2}\text{Sb}/\text{InAs}$ and $\text{GaSb}/\text{InAs}$ heterostructures at RT and 77K. . . . .	95
4.2	Four-probe-resistance with respect to the inter-probe distance $d$ measured at 300K on the $\text{InAs}/\text{Al}_{0.8}\text{Ga}_{0.2}\text{Sb}$ heterostructure. . . . .	98
4.3	Four-probe-resistance against the distance $d$ at 115K of the $\text{InAs}/\text{Al}_{0.8}\text{Ga}_{0.2}\text{Sb}$ sample. . . . .	100
4.4	4P resistance against the distance $d$ at 300K of the $\text{InAs}/\text{GaSb}$ sample . . . . .	100
4.5	Summary of the sheet resistances of all the measured nanowires. . . . .	110
5.1	Growth conditions of $V_{1_{100}}$ , $V_{2_{100}}$ , $V_{3_{100}}$ , $T_{1_{100}}$ and $T_{2_{100}}$ samples. . . . .	120
5.2	Growth conditions of samples $V_{1_{111}}$ , $V_{2_{111}}$ , $V_{3_{111}}$ , sample A, sample B and sample C. . . . .	123
5.3	Growth conditions for 10 nm-thick selective area grown InSb on $\text{InP}(111)_B$ samples. . . . .	127
5.4	Growth conditions of the $\text{InSb}/\text{Al}_{0.3}\text{In}_{0.7}\text{Sb}$ quantum well . . . . .	134

# Nomenclature

<b>AFM</b>	Atomic Force Microscopy
<b>CMOS</b>	Complementary Metal-Oxide-Semiconductor
<b>DC</b>	Direct Current
<b>EDX</b>	Energy-Dispersive X-ray Spectroscopy
<b>FETs</b>	Field-Effect Transistors
<b>HAADF-STEM</b>	High-Angle Annular Dark-Field Scanning Transmission Electron Microscopy
<b>HF</b>	Hydrofluoric Acid
<b>HVPE</b>	Hydride Vapor Phase Epitaxy
<b>IPA</b>	Isopropyl Alcohol
<b>JJ</b>	Josephson Junction
<b>LHe</b>	Liquid Helium
<b>LN2</b>	Liquid Nitrogen
<b>LT-STM</b>	Low Temperature Scanning Tunneling Microscopy
<b>MBE</b>	Molecular Beam Epitaxy
<b>ML</b>	Monolayer
<b>MOCVD</b>	Metal-Organic Chemical Vapor Deposition
<b>MOSFET</b>	Metal-Oxide-Semiconductor Field-Effect Transistor
<b>MWCNT</b>	Multi-Walled Carbon Nanotube
<b>NBR</b>	Negative-Bend Resistance
<b>NPLC</b>	Number of Power Line Cycle
<b>NWs</b>	Nanowires
<b>QW</b>	Quantum Well
<b>R<sub>2P</sub></b>	Two-Point Resistance
<b>R<sub>4P</sub></b>	Four-Point Resistance
<b>RF</b>	Radio-Frequency
<b>RHEED</b>	Reflection High-Energy Electron Diffraction
<b>RT</b>	Room Temperature
<b>SAG</b>	Selective Area Growth
<b>SEM</b>	Scanning Electron Microscopy
<b>SiO<sub>2</sub></b>	Silicon Dioxide
<b>SOC</b>	Spin-Orbit Coupling

<b>TASE</b>	Template Assisted Selective Epitaxy
<b>TEM</b>	Transmission Electron Microscopy
<b>UCF</b>	Universal Conductance Fluctuations
<b>UHV</b>	Ultra-High Vacuum
<b>VLS</b>	Vapor-Liquid-Solid
<b>XRD</b>	X-Ray Diffraction
<b>1D</b>	One-Dimensional
<b>2D</b>	Two-Dimensional
<b>2DEG</b>	Two-Dimensional Electron Gas
<b>4P-STM</b>	Four-Probe Scanning Tunneling Microscopy

# Introduction

**N**ANOWIRES (NWs) are one-dimensional systems with length up to several tens of micrometres and diameters generally below a hundred of nanometres. When the size of the diameter becomes small enough, they confine the carriers in two dimensions and allow them to propagate freely along the third dimension. This property was quite appealing for electronic applications and, combined with a high surface to volume ratio, made the NWs very sensitive to the environment [1]. These semiconducting nanostructures have been developed during the last two decades in the frame of ‘the More than Moore’ strategy for electronic devices [2] to pursue the very famous Moore’s law, which supposes the doubling of the number of transistors on a chip every 18 months. Nowadays, this law has become a real challenge for two main reasons: the first one concerns the size of the transistors as it has reached the ultimate limit (few nanometers) [3]; the second issue is the power consumption as we count about 20 billion of transistors per computer chip [4]. Based on their amazing transport properties and particularly their high electron mobility related to their reduced electron effective mass, some of the compound - semiconductor NWs were considered as particularly appealing for the new generation of Complementary Metal-Oxide-Semiconductor (CMOS) technology addressing a low energy consumption while keeping large ON current capabilities [5], [6]. Nowadays, even though III-V NWs, such as InAs NWs, continue to be seen as candidates of choice for Radio-Frequency RF applications [5], [7] or Tunnel FETs, their ability to replace silicon in CMOS technology is still uncertain. Instead, they have become more and more interesting for the fabrication of quantum devices exploiting coherent electron transport [8], as InAs and InSb exhibit a low electron effective mass, a high carrier mobility and a strong spin-orbit coupling [9]–[11]. Such nanowires are either vertically grown on substrates using the vapor phase growth techniques such as Metal-Organic Chemical Vapor Deposition (MOCVD) and Molecular Beam Epitaxy (MBE) techniques [8], [12], or grown directly in the plane of the substrate by combining these techniques with a

selective area growth thanks to the design of a nanoscale dielectric mask at the surface of the substrate. While the growth of nanowires in a vertical model allows overcoming the lattice mismatch issue, in-plane growth eases the process of nano-devices. Indeed, the vertical growth of NWs often involves their transfer to another wafer with a more or less precise position [13]. Furthermore, the fabrication of complex circuits including vertical or tilted NW arrays is very complicated [13]. Therefore, the selective area growth (SAG) of in-plane nanowires using a dielectric mask with openings perfectly defined on the wafer is very attractive [14]. MOCVD based epitaxy has been naturally first used for in-plane SAG benefiting from the preferential decomposition of metal-organic precursors in the mask openings [10], [15]. One of the first groups that was interested by the epitaxial selective growth of planar nanowires with MBE is the EPIPHY group at IEMN. They studied the effect of growth parameters on the morphology of InP and InAs NWs and demonstrated the importance of the use of an atomic hydrogen flux during the growth to enhance the selectivity for GaSb SAG [14]. Then, InGaAs NW based MOSFET and tunnel diodes were fabricated with this process during the thesis of Alexandre Bucamp to study their electrical properties [16]. These measurements revealed the difficulty to evaluate the NW properties independently from the device imperfections (gate oxide, ohmic contacts etc).

In this context, my thesis project aims at the elaboration of high quality in-plane InAs and InSb NWs using SAG-MBE and the characterization of their intrinsic electronic properties, benchmarked with their quantum well counterparts. To do so, multiple-probe scanning tunnelling microscopy (4P-STM) will be used as a powerful tool for the characterization of the electron transport properties of InAs at the nanoscale in UHV [17], [18]. The ultimate goal is to demonstrate ballistic electron transport in the nanostructures. As the chemistry of the semiconductor surfaces has a strong impact on the transport properties in nanostructures with high surface to volume ratio, low temperature STM will be further used to study the reconstruction of the InSb (100) and InSb (111) surfaces. This thesis is divided in 5 chapters. The first one summarizes the ongoing developments for the fabrication of one-dimensional structure with III-V compounds. Among the different methods used for the growth of semiconductor nanowires, I will focus on the (selective) epitaxial growth, which is central to this thesis. I will particularly address results obtained with low electron effective mass materials such as InAs and InSb. Indeed, these materials have received much attention for the fabrication of advanced quantum devices and, despite lattice mismatch issues, can be grown with a high structural quality on different substrates. As a result, I will summarize the best electrical

performances reported in these systems, encompassing the typical techniques used for the transport characterization, in particular based on four-point probes.

Chapter II is dedicated to the description of the tools and methods used in this thesis both for the nanostructure fabrication and for their morphological, structural and electrical characterization.

The third chapter deals with the study of InAs two-dimensional (2D) and one-dimensional (1D) nanostructures grown on InP(111) substrates. In both cases, an optimization of the growth conditions has been performed. A morphological study of the InAs in-plane nanowires followed by a 4P-STM study leads to a comparative analysis of the conductance of in-plane NWs along two different crystallographic orientations as well as their benchmark with InAs 2D films and with other results from the literature. The impact of the surface chemistry on the electron transport properties is highlighted by comparing oxidized and reconstructed semiconductor surfaces initially protected with an As cap.

Chapter IV is dedicated to InAs nanostructures grown on (100) III-V substrates. In addition to the 4P-STM characterization, transport measurements with conventional electrodes are performed. We show the interest of embedding the InAs NWs in GaSb to improve the electron mobility in InAs for both the 2D-Electron-Gas (2DEG) and in-plane NWs.

The last chapter deals with InSb grown on InP in the form of thin films and in-plane nanowires. We show how high quality in-plane nanostructures can be achieved on InP(111)<sub>B</sub> substrates by optimizing the MBE growth conditions and propose a method to recover a high surface quality in an ultra-high vacuum system after air exposure of the sample. Finally, a conclusion and some perspectives for the design of ballistic transport-based device are proposed.

## Bibliography

- [1] Y. Li, F. Qian, J. Xiang, and C. M. Lieber, ‘Nanowire electronic and optoelectronic devices’, *Mater. Today*, vol. 9, no. 10, pp. 18–27, Oct. 2006, doi: 10.1016/S1369-7021(06)71650-9.
- [2] C. Thelander et al., ‘Nanowire-based one-dimensional electronics’, *Mater. Today*, vol. 9, no. 10, pp. 28–35, Oct. 2006, doi: 10.1016/S1369-7021(06)71651-0.
- [3] R. Quhe et al., ‘Sub-10 nm two-dimensional transistors: Theory and experiment’, *Phys. Rep.*, vol. 938, pp. 1–72, Nov. 2021, doi: 10.1016/j.physrep.2021.07.006.
- [4] H. El-Aawar, ‘Increasing the Transistor Count by Constructing A Two-Layer Crystal Square on A Single Chip’, *Int. J. Comput. Sci. Inf. Technol.*, vol. 7, no. 3, pp. 97–105, Jun. 2015, doi: 10.5121/ijcsit.2015.7308.
- [5] B. Mirkhaydarov et al., ‘Solution-Processed InAs Nanowire Transistors as Microwave Switches’, *Adv. Electron. Mater.*, vol. 5, no. 1, p. 1800323, 2019, doi: 10.1002/aelm.201800323.
- [6] M. S. Ram, K.-M. Persson, M. Borg, and L.-E. Wernersson, ‘Low-Power Resistive Memory Integrated on III–V Vertical Nanowire MOSFETs on Silicon’, *IEEE Electron Device Lett.*, vol. 41, no. 9, pp. 1432–1435, Sep. 2020, doi: 10.1109/LED.2020.3013674.
- [7] L.-E. Wernersson, ‘Narrow gap nanowires: From nanotechnology to RF-circuits on Si’, *J. Appl. Phys.*, vol. 117, no. 11, p. 112810, Mar. 2015, doi: 10.1063/1.4913836.
- [8] P. Aseev et al., ‘Selectivity Map for Molecular Beam Epitaxy of Advanced III–V Quantum Nanowire Networks’, *Nano Lett.*, vol. 19, no. 1, pp. 218–227, Jan. 2019, doi: 10.1021/acs.nanolett.8b03733.
- [9] S. Li et al., ‘Coherent Charge Transport in Ballistic InSb Nanowire Josephson Junctions’, *Sci. Rep.*, vol. 6, no. 1, Art. no. 1, Apr. 2016, doi: 10.1038/srep24822.
- [10] J. Gooth et al., ‘Ballistic One-Dimensional InAs Nanowire Cross-Junction Interconnects’, *Nano Lett.*, vol. 17, no. 4, pp. 2596–2602, Apr. 2017, doi: 10.1021/acs.nanolett.7b00400.
- [11] X. Zhou, S. A. Dayeh, D. Aplin, D. Wang, and E. T. Yu, ‘Scanned electrical probe characterization of carrier transport behavior in InAs nanowires’, *J. Vac. Sci. Technol. B Microelectron. Nanometer Struct. Process. Meas. Phenom.*, vol. 24, no. 4, pp. 2036–2040, Jul. 2006, doi: 10.1116/1.2213267.



- [12] G. Zhang, S. Sasaki, K. Tateno, H. Gotoh, and T. Sogawa, ‘Au-free InAs nanowires grown in In-particle-assisted vapor-liquid-solid mode: growth, structure, and electrical property’, *AIP Adv.*, vol. 3, no. 5, p. 052107, May 2013, doi: 10.1063/1.4804542.
- [13] D. Dalacu, A. Kam, D. G. Austing, and P. J. Poole, ‘Droplet Dynamics in Controlled InAs Nanowire Interconnections’, *Nano Lett.*, vol. 13, no. 6, pp. 2676–2681, Jun. 2013, doi: 10.1021/nl400820w.
- [14] M. Fahed, L. Desplanque, D. Troadec, G. Patriarche, and X. Wallart, ‘Selective area heteroepitaxy of GaSb on GaAs (001) for in-plane InAs nanowire achievement’, *Nanotechnology*, vol. 27, no. 50, p. 505301, Nov. 2016, doi: 10.1088/0957-4484/27/50/505301.
- [15] H. Schmid et al., ‘Template-assisted selective epitaxy of III–V nanoscale devices for coplanar heterogeneous integration with Si’, *Appl. Phys. Lett.*, vol. 106, no. 23, p. 233101, Jun. 2015, doi: 10.1063/1.4921962.
- [16] A. Bucamp, ‘Croissance sélective et caractérisation de nanostructures de matériaux III-V élaborées par épitaxie par jets moléculaires’, *These de doctorat, Université de Lille (2018-2021)*, 2019. [Online]. Available: <https://www.theses.fr/2019LILUI067>
- [17] I. Miccoli, F. Edler, H. Pfnür, and C. Tegenkamp, ‘The 100th anniversary of the four-point probe technique: the role of probe geometries in isotropic and anisotropic systems’, *J. Phys. Condens. Matter*, vol. 27, no. 22, p. 223201, May 2015, doi: 10.1088/0953-8984/27/22/223201.
- [18] X. Zhou, S. A. Dayeh, D. Aplin, D. Wang, and E. T. Yu, ‘Direct observation of ballistic and drift carrier transport regimes in InAs nanowires’, *Appl. Phys. Lett.*, vol. 89, no. 5, p. 053113, Aug. 2006, doi: 10.1063/1.2236589.

# 1

## In-plane III-V nanostructures for advanced quantum devices

### **1 Introduction**

This chapter starts by introducing the existing methods to grow 1D semiconducting nanostructures focusing on selective area epitaxy to achieve in-plane nanowires. It is followed by a description of the techniques developed to measure the electronic transport in 1D nanostructures. Then, the crystallographic and exceptional transport properties of InAs and InSb semiconductors are highlighted. Their usefulness as nanowires for advanced quantum device fabrication is explained through examples taken from the literature.

## 2 Epitaxial growth of nanostructures

### 2.1 Epitaxial growth

#### 2.1.1 Principle

The word epitaxy comes from Greek roots and means growing “above in an ordered manner”. The epitaxy is a technique that allows growing crystalline thin layers (layer by layer) at the nanometric scale on crystalline substrates. This latter is a bulk-grown material where low-indexed planes as (100) or (111) orientations are parallel to its surface. It is generally fabricated using Czochralski (known as Cz) to obtain high-crystalline-quality materials [1]. In epitaxy, the substrate acts as a seed crystal during growth as the incoming atoms follow its structure. When the epitaxially grown layer is with the same material as the wafer, the process is called homoepitaxy. When the structure or the chemical composition of the deposited layers are different from the wafer, it is called a heteroepitaxy; growing an InAs film on a GaAs wafer for example.

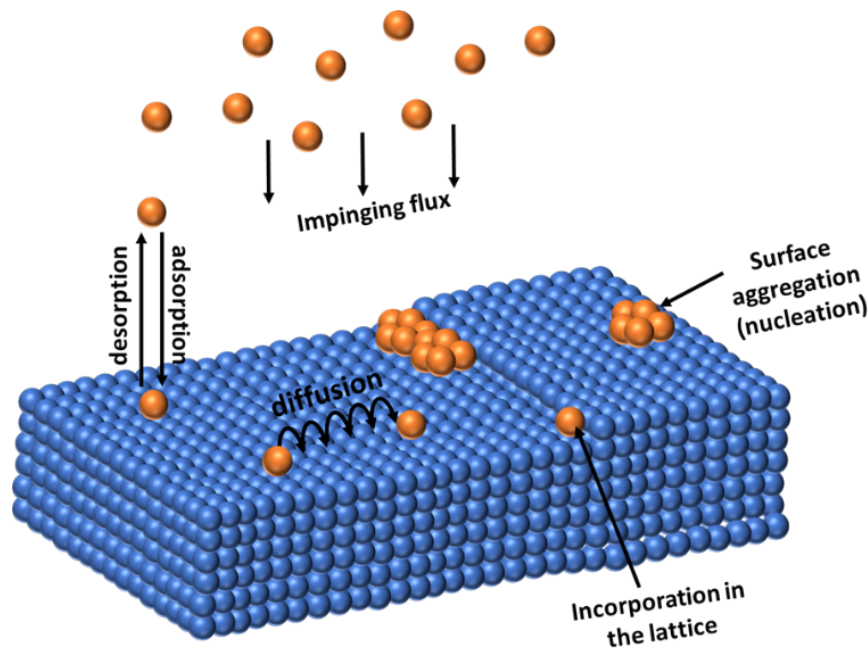


Figure 1.1 – Simplified schematic representation of adsorption, incorporation, diffusion and nucleation processes during epitaxy.

Different mechanisms happen during epitaxy (Figure 1.1). The first step is adsorption: an atom is adsorbed when it condensates on the surface. Then it can diffuse along the surface and incorporate in energetically favourable sites. The driving force for such mechanisms is the free

energy reduction of the system. Adatoms are formed and act as nucleation sites that can be seeded for further atom agglomeration. The growth of multiple nucleation sites leads to their coalescence yielding, in most cases, a uniform film on the surface [2], [3]. For III-V compound semiconductors, group-III elements are first adsorbed on the surface and then create bonding with group-V elements.

### **2.1.2 Epitaxial techniques**

In the context of epitaxial growth, diverse methodologies have been refined to fabricate high-quality crystalline layers. Metalorganic Chemical Vapor Deposition (MOCVD) emerges as a versatile method, capitalizing on the decomposition of metalorganic precursors upon contact with a heated substrate, yielding a uniform epitaxial layer. This approach is esteemed for its broad applicability across various materials and its scalability for industrial production. In contrast, Molecular Beam Epitaxy (MBE) adopts a more refined trajectory by facilitating the deposition of atoms in a high-vacuum environment. This precision-driven technique allows for the meticulous assembly of atomic layers, making it indispensable for semiconductor devices where the integrity of layer composition and thickness is critical. MBE ability to manipulate growth rates with exceptional precision, down to 0.01 Mono-Layer per second (ML/s), allows for exact control over the thickness and composition of the nanostructures, making it essential for producing semiconductors, metals, and other materials for advanced electronic and photonic devices [4], [5]. Moreover, growing nanostructures in UHV conditions has a great impact on the purity and crystalline quality of the grown layers. Other growth techniques, such as Hydride Vapor Phase Epitaxy (HVPE), which is based on the reaction of hydrogen chloride with metal elements, enable the deposition of substantially thicker layers at comparatively higher rates, thereby serving as a pivotal technique for the fabrication of optoelectronic devices.

## **2.2 Methods for growing nanowires**

Low dimension nanostructures are the key point of advanced applications as quantum devices. Therefore, semiconductor nanowires, for example, were extensively studied in the last decade [6], [7]. Added to their high surface to volume ratio advantage [8], these nanostructures can exhibit quantum confinement effects. This phenomenon takes place when carriers are confined into dimensions that are smaller than the de Broglie wavelength, generating discrete

energy levels [8]. In the case of quantum computing systems for example, this property allows a precise control of energy states, enabling the manipulation of quantum bits (qubits) [6]. Different methods have been proposed for the bottom-up fabrication of such nanostructures. The main ones use the Vapour-Liquid-Solid (VLS) technique or the Selective Area Growth (SAG), which are detailed below.

### 2.2.1 The Vapour-Liquid-Solid technique

The VLS technique has been extensively used since the fabrication of the first silicon whiskers synthesized by Au-catalysed VLS growth four decades ago [9]. This method consists in the exposure of the substrate to vapor-phase precursors, which react with a catalyst. The catalyst acts as a nucleation seed for crystal growth, and the nanostructure grows from the liquid-solid interface. Growing vertical nanowires by Vapour Liquid Solid based on Chemical Vapor Deposition (VLS-CVD) was reported since the early 2000s [10]. This approach can be done with a gold nanoparticle or using an indium droplet as catalyst [4]. The use of the catalyst helps to promote local and unidirectional growth of the nanowire. In fact, the Au nanoparticles react with the substrate or reactant species and create an eutectic alloy. The crystal grows in a way that it is elongated beneath the particle in contact with the top of the nanowire. The growth on (111) oriented wafers usually gives vertical non tilted nanowires [10]. The nanowire growth direction depends on the total free energy of the system and the free energy of the particle/substrate interface and its dimensions depend on the diameter of the Au particle.

### 2.2.2 Selective area growth

The Selective Area Growth (SAG) is a crucial method for nanowire growth taking advantage of the high degree of control over the shape and position of the growing nanostructures. Engineering the morphology and the structural properties of the growing nanowires can be done by changing the geometry of the pattern, the wafer orientation, and the growth parameters. SAG started to attract attention in the seventies with the development of integrated circuit technologies [11]. This approach satisfies the need to grow different semiconductor layers with different properties (crystallographic orientation, shape, width, length, etc...) on the same substrate [12]. It benefited from the advances in the lithography and etching techniques at that period. In this method, a dielectric mask (mostly SiO<sub>2</sub>) is used and patterns can be designed on the mask by means of a resist exposure. Then, the mask is etched leaving windows

with different possible shapes and orientations. The growth occurs in openings while the mask surface is free from deposition.

In the nineties, the Chemical Vapor Deposition (CVD) was adopted for the selective epitaxy of nanostructures [13]. This technological step, improved significantly the selectivity of the growth as it took advantage of the CVD technique ability to control the growth rate and composition of epitaxial layers using gas precursors [12]. Since then, the impact of growth conditions as the growth rate, temperature, growth pressures or fluxes on selectivity and shape of the grown structures has been extensively studied. The progress in nanolithography has then paved the way for the fabrication of high aspect ratio in-plane nanowires with sub-micrometric widths and tens of  $\mu\text{m}$  length. The morphology of SAG structures is driven by the surface diffusion (SD) length of adatoms. Several works were devoted to the study and simulation of the SD length of several III-V semiconductors depending of the wafer orientation, pattern dimensions and crystallographic orientations [14], [15].

In 2019, Aseev et al. proposed a selectivity map indicating the range of growth temperatures and growth rates for which optimized selectivity can be achieved in MBE for different semiconductors [16]. The works initiated at IEMN several years ago demonstrated the extension of the selectivity map by using an atomic hydrogen flux during the MBE growth by preventing the nucleation of crystallites on the mask for different III-V compound semiconductors [17]–[19].

Nowadays, the SAG is a crucial technique for high crystal quality nanowires used for quantum device conception [20], [21]. This technique gives also the advantage of conceiving complex device geometries that might be challenging to achieve using other growth methods. This offers a vast landscape for semiconductor nanowire applications [20], [22], [23].

During this work, we focus on InAs and InSb in-plane NWs grown by selective area MBE. As one-dimensional III-V heterostructures are known to give rise to ballistic transport [24], the Appendix presents the ballistic transport fundamentals and the next section is dedicated to the methods suitable for the measurements of transport in NWs.

## 3 Electron transport

### 3.1 Experimental methods for the exploration of ballistic resistance

#### (a) With two probes

The two probes (2P) measurements are the most straightforward approach to measure a resistance. Figure 1.2(a) displays a schematic representation of 2P measurements. In this setup, a pair of electrodes facilitates both current injection and voltage probing. As presented in the scheme, the measured resistance  $R_{2P} = \frac{V}{I}$  is a sum of serial resistances: the sample resistance and the contacts resistances ( $R_C$  and  $R'_C$ ) resulting from the electrodes interactions with the sample surface.

$$R_{2P} = R_C + R'_C + R_{\text{sample}} \quad (1.1)$$

In order to study the transport properties of nanostructures, it is very convenient to work with ultra sharp metallic tips with diameters around some tens of nanometers which can be arbitrarily positioned along a nanostructure thanks to piezoelectric transducer. For example, H.J. Li et al. contacted a vertical multiwall carbon nanotube with a single tip, while the other extremity of the nanotube was connected to the substrate used for their growth [25]. Measurements took place in a scanning electron microscope (SEM) equipped with a movable tip as shown in Figure 1.2(b). In this case the contact resistance was negligible in comparison with the nanotube. The measured conductance was found to be 460 times the quantum conductance  $G_0$  based on the extracted I-V data, accounting for a ballistic transport through the different multiple walls of the nanotube.

2P measurements were also carried out on InAs nanowires using a single scanning probe [7]. These measurements are carried out by means of a diamond coated conductive tip of an atomic force microscope, the other electrodes being deposited on the InAs nanowires by lift-off process (see Figure 1.2(c)). One of the macroscopic Ohmic contact, shown to the right in the schematic, was kept floating and did not contribute to the current flow acquired during the measurements. A DC bias voltage was applied between the two probes and the current was measured as a function of the distance (L) between the deposited contact and the movable tip. The evolution of the measured resistance versus L is shown in Figure 1.2(d). For short tip-electrode distances, the resistance remained constant and the electron transport is considered ballistic. For distances above 200 nm, that is considered as the nanowires mean free path, the resistance varies linearly depending to L, signature of a diffusive transport. The observation of such a transition implies small contact resistances, which, based on the scarcity of similar results in the literature, might be difficult to achieve.

### (b) With four probes in a linear geometry

For 2P measurements, the contact resistance is usually much higher than the sample resistance,

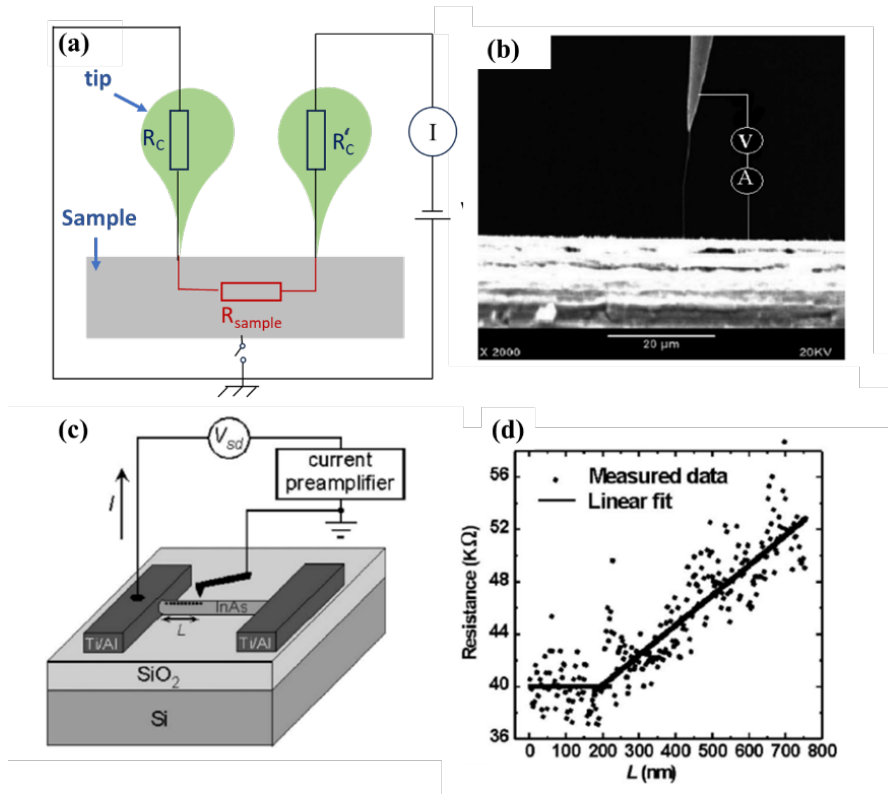


Figure 1.2 – (a) Schematic representation of the two-tip resistance measurement configuration in which the contact resistance influences the measured total resistance. (b) Illustration of contacting a single multiwall nanotube in a SEM setup equipped with a moveable probe [25]. (c) Schematic diagram of a 2-probe transport measurement performed on an InAs nanowire with an atomic force microscope. The current is measured for fixed bias voltage  $V_{sd}$  as a function of tip-electrode distance  $L$ . [7] (d) Resistance measured by cAFM as a function of tip-contact distance  $L$  (symbols), with linear fits for the ballistic transport regime ( $L$  below 200 nm), for which the resistance is independent of  $L$ , and the drift transport regime ( $L$  above 200 nm) for which the resistance increases linearly with  $L$ . [7].

hiding the small resistance variations in the sample. In order to overcome this issue, the 4P method gives access to the sample resistance and suppresses the contribution of the contact resistances in the measurements. A four-point measurement circuit is illustrated in Figure 1.3. Here, the two external electrodes are used to inject and collect the current into the sample while the two inner electrodes measure the voltage induced by the injection of the current. The current injected inside the sample is independent of the contact resistance at the source and drain contacts. If the voltage measurement is performed with a large internal resistance such as  $R_V \gg R_{\text{sample}} + R_{C2} + R_{C3}$  then the contribution of the contact resistance to the measured resistance can be neglected and  $R_{4P}$  equals the sample resistance.

4P measurements with W tips were performed on graphene nanoribbon grown on a SiC substrate in a multiple-probe scanning tunnelling microscope (STM). The STM tips, which can be arbitrarily positioned on the surface under the supervision of a scanning electron microscope,



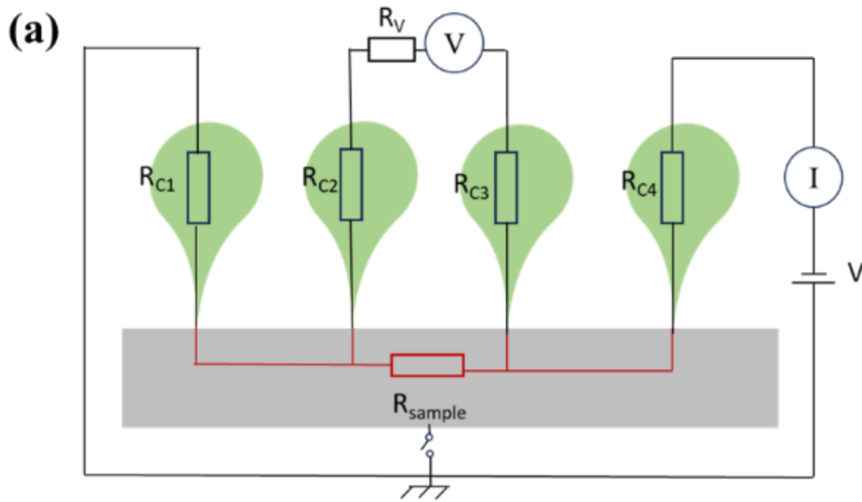


Figure 1.3 – Schematic representation of the four-probe resistance measurement configuration in which the contact resistances are excluded from the measured total resistance.

were pressed in contact with the nanoribbon. Barinhaus et al. measured a 4P resistance almost equal to the 2P resistance, corresponding to  $1/G_0$ . This result is characteristic of a single-channel ballistic transport involving invasive contacts [26]. In those measurements, the mean free path exceeded  $10\mu\text{m}$  at RT. Interestingly, when the contacts were more gentle, as the feedback loop of the STM allows a good control of the vertical height position of the tips, the 4P resistance dropped to 100 Ohms [27]. In contrast, the 2P  $I(V)$  curve shows a non-linear behaviour with a slope around zero volt, yielding a resistance in the  $\text{M}\Omega$  range. Therefore, the non-invasiveness of the probes led to a resistance almost null, consistent with a ballistic regime.

### 3.2 Other methods for the exploration of ballistic effects

The Negative Bend Resistance (NBR) is another method of evidencing the ballistic transport using 4-terminal devices. Figure 1.4(a) and Figure 1.4(b) are respectively a Nomarski optical micrograph of a Hall bar device and a SEM image showing four metallic electrodes deposited on an InSb based  $50\mu\text{m}$ -wide-Hall bar [28]. The InSb hall bars in this work exhibit electron density, electron mobility and a mean free path of  $4.1 \times 10^{11} \text{ cm}^{-2}$ ,  $8000 \text{ cm}^2/\text{V}\cdot\text{s}$  and  $840 \text{ nm}$  respectively at 1.5K. The bend resistance is given by the ratio between the current measured between lead 2 and lead 3 and the voltage measured between the adjacent leads 1 and 4 (Figure 1.4(a)). When the transport is ballistic, the electrons injected at the lead 2 can go ballistic to the lead 4 without scattering. Conversely, in the case of diffusive transport, the electrons spend a longer time in the junction due to scattering events and the applied electric

field will push them to the lead 3. Consequently, the bend resistance is negative when the number of ballistic electrons exceeds the number of diffusive electrons. A clever way to change the magnitude of the negative resistance consists in applying a perpendicular magnetic field. As a result, the magnetic field modifies the in-plane trajectory of the electrons and allows to tune the bend resistance as shown in Figure 1.4(c).

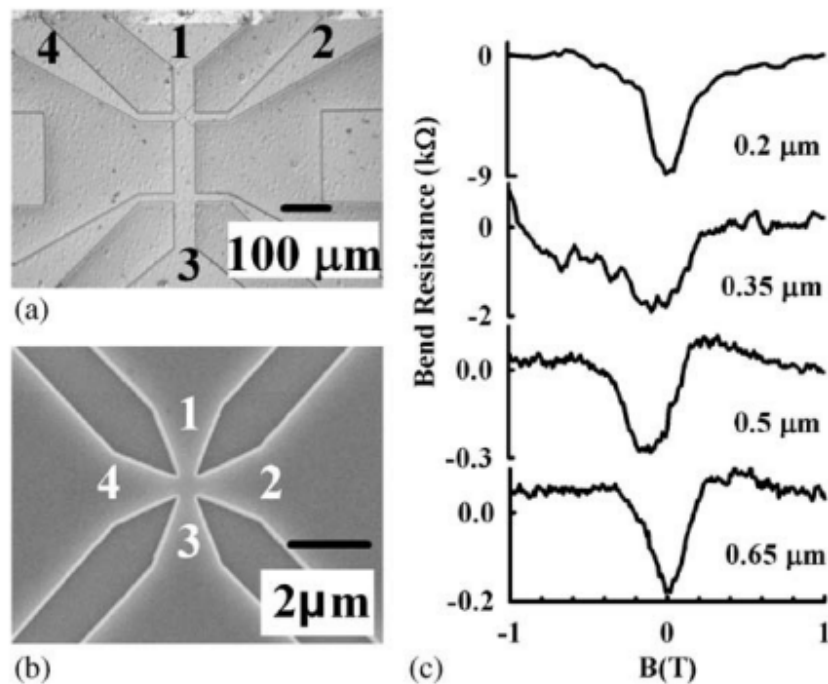


Figure 1.4 – (a) Nomarski optical micrograph of a Hall bar device. (b) SEM image of a  $0.5 \mu\text{m}$ -wide four terminal device with lead numbers indicated. (c) The bend resistance for four-terminal devices of various widths ( $0.2$ ,  $0.35$ ,  $0.5$ ,  $0.65 \mu\text{m}$ ) as a function of magnetic field applied perpendicular to the plane of the 2DEG. The measurements were performed at  $1.5 \text{ K}$  [28].

The measurements of a NBR provides a useful signature of ballistic transport inside the InSb nanojunctions. Other works have highlighted ballistic transport in InSb/AlInSb quantum wells by observing NBR even at room temperature [29], [30].

Aharonov-Bohm nanostructures are interesting systems for the ballistic transport studies as they allow the investigation of the quantum interference phenomena arising from the Aharonov-Bohm effect. This effect emerges when charged particles interact with an electromagnetic potential within a region where there is no magnetic field. Interferences are observed in the case of a coherent electron transport [16]. The Aharonov-Bohm effect becomes observable by processing ring-like geometries on which at least two metallic contacts are deposited for electrons to circumnavigate the ring.

Josephson junction (JJ) are also useful devices for the investigation of the ballistic transport

in nanowires junctions. A JJ is formed by a thin insulating layer that is sandwiched between two layers of superconducting material. These components bear the name of Brian Josephson, who, in 1962, predicted the phenomenon: the Cooper pairs of superconducting electrons could successfully tunnel across the non-superconducting barrier, connecting one superconductor to the other with no applied voltage. By growing InSb nanowires, S. Li et al. built JJ that showed periodic modulations of the critical current in the transport measurements of their junctions. The modulation is the signature of ballistic effects in the nanowire. Therefore, the quality of the transparent interfaces enhanced the proximity-induced superconductivity in the nanowire junction, while the high structural quality of the InSb nanowires enabled a long mean free path [31].

## 4 Low electron effective mass InAs and InSb nanostructures

This section concentrates on the III-V compounds of interest for this work: InAs and InSb. We will describe the transport properties and crystalline structures of the InAs and InSb bulk and will later discuss studies performed with 2D heterostructures and 1D nanostructures used as the active part of advanced quantum devices.

### 4.1 Transport and crystal quality

With electron effective masses of  $0.023m_0$  and  $0.014m_0$  in InAs and InSb respectively (against  $1.08m_0$  in Si), these semiconducting materials offer excellent transport properties. In bulk materials, the theoretical electron mobility is  $40000 \text{ cm}^2/\text{V.s}$  in InAs and  $77000 \text{ cm}^2/\text{V.s}$  in InSb at room temperature, this latter being the highest value among all III-V semiconductors [32]. Also both materials exhibit strong spin-orbit interaction (SOC) and large Landé g-factor (around -15 and -51 for InAs and InSb respectively) [33], [34]. These properties are particularly appealing for spintronic devices used in quantum computing applications [21], [35]. However, charge carrier scattering from crystal defects, impurities or surface states can significantly alter the transport properties and growing high quality material is essential.

Both materials crystallize in a zinc-blende structure composed of two face-centred cubic (fcc) sub-lattices as shown in Figure 1.5. One sub-lattice is occupied by In as a group III-element

and the other sub-lattice is occupied by either As or Sb as group-V elements. In the zinc-blende structure, each atom is tetrahedrally coordinated to four nearest atoms. There are three main crystallographic orientations, also known as crystallographic planes or directions for InAs and InSb [36]. The (100) plane is the most commonly used wafer orientation and it forms square like crystal lattices. The (110) plane is also used for InAs and InSb nanostructures growth. It forms a diamond-like lattice of atoms. Finally, the (111) crystallographic orientation forms a hexagonal lattice of atoms.

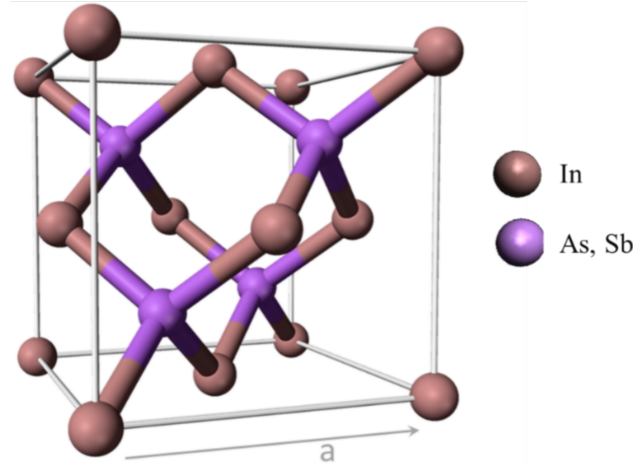


Figure 1.5 – InAs/InSb unit cell. Adapted from [37].

InAs and InSb lattice constants as shown in Figure 1.6 are respectively around 6.06 Å and 6.48 Å. This figure displays the band gap versus the lattice constant of several semiconductor materials. Due to their low energy direct band gaps, InAs and InSb are particularly appealing for mid infrared sources and detectors. As InAs and InSb substrates are expensive and their high conductivity impedes the device insulation, there is a need to find alternatives, in particular by growing them on GaAs and InP substrates, which can be purchased as semi-insulating. However, Figure 1.6 shows that the lattice constants of InAs and InSb (marked by red circles) do not match with the lattice constants of commonly used GaAs and InP wafers (pointed by green arrows). Their integration on highly mismatched GaAs or InP substrates usually degrades their crystal quality and thus their optical and electronic properties.

## 4.2 Lattice mismatch accommodation

In general, for 2D layer growth, the lattice mismatch  $f$  is given by [39]:

$$f = \frac{a_{\text{sub}} - a_{\text{layer}}}{a_{\text{sub}}} \quad (1.2)$$

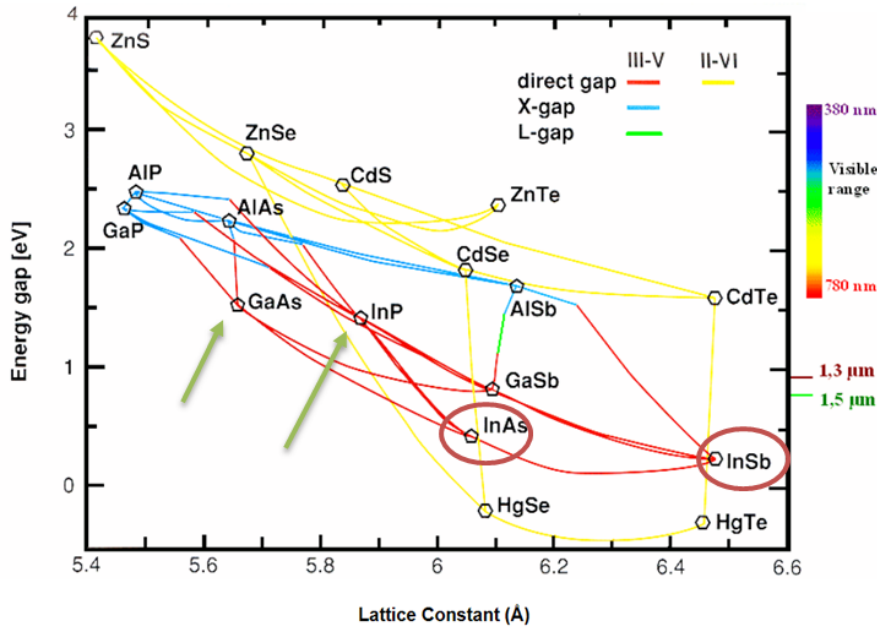


Figure 1.6 – Plot of semiconductors bandgap versus lattice constant [38].

Where  $a_{\text{sub}}$  is the lattice constant of the wafer and  $a_{\text{layer}}$  is the lattice constant of the grown 2D film on the wafer. Figure 1.7 illustrates the different layer-substrate interfaces that can appear depending on the lattice mismatch. At  $f = 0$ , a fully coherent interface with no defects can be achieved (Figure 1.7(a)), an evident example of such a case is the homoepitaxy. When  $f < 2\%$ , the interface is strained but still coherent (Figure 1.7(b)) as the strain relaxation is still elastic [40]. Generally, the growth in this case takes place according to the Frank-van der Merwe (2D layer by layer growth).

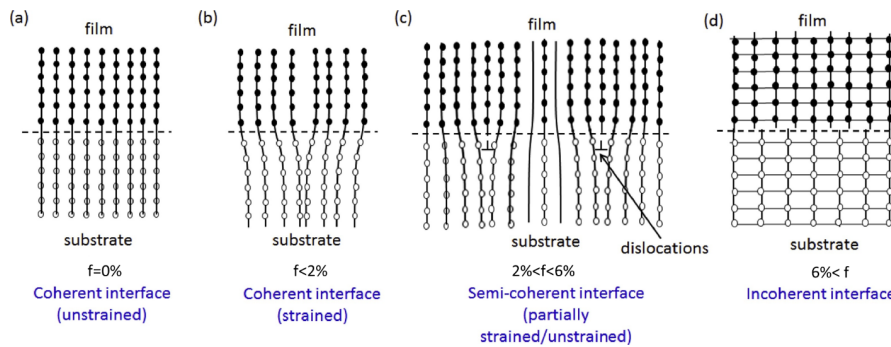


Figure 1.7 – Schematics of different types of interfaces between dissimilar film and substrate. (a) Unstrained coherent interface, (b) strained coherent interface, (c) semi-coherent interface with dislocations, (d) incoherent interface, Adapted from [41].

Figure 1.7(c) illustrates the case where  $2\% < f < 6\%$ . The elastic deformation of the lattice is not sufficient to accommodate the whole mismatch and after a critical thickness, additional relaxation occurs first by the deformation of the surface and then by the introduction of misfit dislocations (plastic deformation). In this case, the growth generally follows a Stranski-

Krastanov mode with a 2D layer initially formed that turns to the formation of 3D strained islands on the top surface before dislocation loops are introduced. If  $f$  exceeds 6%, this results in the formation of an incoherent interface with a misfit dislocation network at the interface (Figure 1.7(d)). Therefore 6% is considered as a practical limit of the lattice misfit  $f$  contributing to the strain at the interface. Generally, these conditions promote a Volmer-Weber 3D growth mode where isolated and plastically relaxed islands grow directly on the surface.

Based on Equation 1.2, the lattice mismatches are the following: 3.3% for InAs-InP and 7.2% for InAs-GaAs, 10.4% for InSb-InP and 14% for InSb-GaAs. With a 3.3% lattice mismatch, the critical thickness for the growth of InAs on InP substrate is about 3 to 5 nm. Above this threshold, 3D islands are formed.

In this thesis, we target the growth of InAs and InSb nanostructures on InP or GaAs, with a thickness of a few tens of nanometers. Unavoidably, we will have to manage strain relaxation in order to limit its impact on the electron transport properties inside the material.

### 4.3 InAs nanostructures

In this section, a short overview of the methods investigated for the achievement of InAs 2D films and nanowires on mismatched substrate is proposed. We will also discuss their use in advanced quantum device.

#### 4.3.1 InAs thin films and 2DEG

As already discussed, InAs exhibits a low electron effective mass that can provide a large electron mobility at room temperature. However, it is highly mismatched with commonly used III-V semiconductor wafers. In order to protect electron transport inside the InAs channel from defect scattering, a good crystalline quality of the layer is recommended. One method consists of growing a metamorphic buffer layer to accommodate the lattice mismatch between GaAs or InP wafer and InAs and reduce the density of dislocations that thread into the channel [42]. To push away surface states due to oxidation or simply dangling bonds and prevent electron scattering, a top barrier layer is, also, highly desirable. The electrons thus confined inside the InAs channel with limited scattering phenomena form a two-dimensional-electron gas (2-DEG). Figure 1.8 illustrates the InAs/barrier quantum well and its relative

conduction band structure.

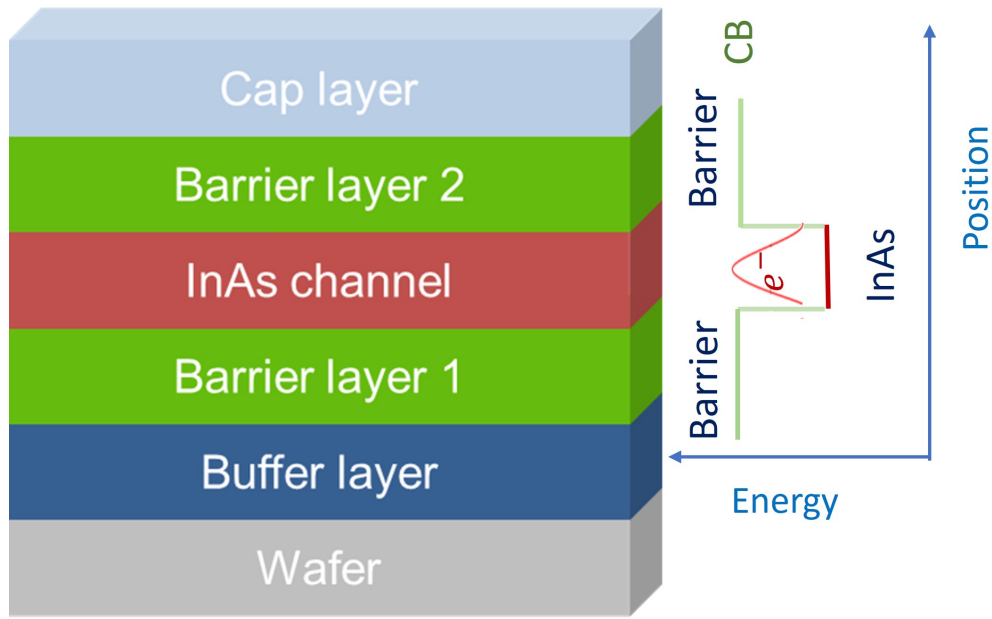


Figure 1.8 – InAs/barrier Quantum well structure and its relative conduction band structure scheme .

#### (a) InAs/InGaAs/InAlAs 2DEG

Several works were carried out for the fabrication of high quality InAs quantum wells using ternary alloys of III-V semiconductors for barrier and buffer layers. This gives more flexibility in the lattice mismatch and the band gaps adjustment. InAs/InGaAs/InAlAs heterostructures emerged as attractive quantum wells for High-Electron-Mobility-transistors (HEMTs) [43]. T. Akazaki et al. demonstrated the enhancement of the HEMT characteristics by inserting a thin pseudomorphic 4 nm-thick-InAs channel into an  $\text{In}_{0.52}\text{Al}_{0.48}\text{As}/\text{In}_{0.53}\text{Ga}_{0.47}\text{As}$  quantum well on InP [44]. The best electron mobility recorded for this system is  $111000 \text{ cm}^2/\text{V}\cdot\text{s}$  for a charge density of  $2.3 \times 10^{12} \text{ cm}^{-2}$  at 10K [44].

#### (b) InAs/Al(Ga)Sb 2DEG on GaAs, InP and GaSb substrates

GaSb and AlSb are best candidates to be used as buffer and barrier layers since they exhibit only 0.6% and 1.2% of lattice mismatch respectively with InAs. They also provide a large conduction band offset with InAs (1.35 eV or 0.93 eV for AlSb or GaSb respectively) allowing deep electron confinement into the InAs channel which is particularly interesting for low power consumption, high speed or spintronic device fabrication [17], [45]-[47].

H.R. Blank et al. from Herbert Kroemer group at UCSB reported electron mobility larger than  $25000 \text{ cm}^2/\text{V}\cdot\text{s}$  at room temperature and exceeding  $900000 \text{ cm}^2/\text{V}\cdot\text{s}$  at 12K in InAs/Al(Ga)Sb



quantum wells grown on GaAs(100) wafers by MBE [42]. In their work, they reported a strong influence of the buffer layer material on the morphology and the transport properties of the quantum well. A clear enhancement of the mobility (up to  $944000 \text{ cm}^2/\text{V.s}$ ) was obtained by changing the AlSb buffer layer by a GaSb one. Ballistic transport inside InAs/AlSb quantum wells was evidenced by the measurements of plateaus in the conductance of constrictions formed by surface gates [48].

With pure GaSb barrier (without Al), the electron mobility in the InAs channel is generally lower as the smaller conduction band offset results in a lower confinement of electrons in the channel. In such a system grown on a GaAs substrate, a thickness of 200 nm only for the GaSb buffer layer is enough to obtain a peak electron mobility of  $25200 \text{ cm}^2/\text{V.s}$  at 60 K with a carrier concentration of about  $7.35 \times 10^{11} \text{ cm}^{-2}$ , despite the presence of a large density of threading dislocations [49].

Due to its broken gap band line-up, the InAs/GaSb system can also exhibit interesting properties for quantum transport. Indeed, the hybridization gap that can be engineered in a composite InAs/GaSb channel may result in topologically protected edge states that could significantly improve the robustness of charge transport against disorder [50], [51].

These different works demonstrated the versatile application fields of the InAs quantum wells. One challenge remains however the fabrication of 1D nanostructures from these 2D layers. AlGaSb is indeed very sensitive to oxidization and top-down etching to achieve sub-micron wide nanostructures without degrading the electron transport properties is particularly challenging. For this reason, bottom-up solution have been developed. The following part gives an overview on this topic.

### 4.3.2 Bottom-up InAs NW and networks

#### (a) Growth of out-of-plane nanowires

Growing vertical InAs nanowires by Vapour Liquid Solid based on Chemical Vapor Deposition (VLS-CVD) was reported since the early 2000s[10]. The evolution of InAs nanowire (NW) fabrication has been marked by significant research efforts, focusing on optimizing the VLS growth mechanism to create vertically aligned, high-quality NWs suitable for quantum device applications. Tomioka et al. utilized Selective-area Metal-Organic Vapor-Phase Epitaxy (SA-MOVPE) to integrate InAs/InAlAs core-multishell NWs on silicon, demonstrating the potential of vertical surrounding-gate transistors directly on Si substrates. This approach bypassed



the obstacle of lattice mismatch with the substrate and removed the need for metal catalysts, thus avoiding potential impurities. The resulting vertical surrounding-gate transistors (VSGTs) exhibited an excellent switching behaviour [52]. Koblmüller et al. adopted a similar catalyst-free approach, utilizing solid-source Molecular Beam Epitaxy (MBE) with an amorphous SiO<sub>x</sub> mask [53]. This method produced vertically aligned InAs nanowires, with growth rates and uniformity in diameter and length modifiable via precise temperature control. Their approach yielded nanowires with diameters of approximately 50 nm, demonstrating minimal variation along their lengths, which is crucial for consistent electronic properties. Moreover, Grégoire et al. broke new ground with the Hydride Vapor Phase Epitaxy (HVPE) growth of InAs nanowires, achieving vertical alignment and uniform diameter without the use of metal catalysts due to the strategic use of a SiO<sub>x</sub> dielectric mask. The growth rate control was fine-tuned through the adjustment of the III/V ratio and growth temperature, resulting in nanowires up to 26 μm in length. These HVPE-grown nanowires displayed phase-pure zinc blende crystal structures with occasional wurtzite segments due to high As<sub>4</sub> partial pressures, contributing to their unique optical emission properties evidenced by a photoluminescence peak at 0.445 eV, blue-shifted from bulk InAs due to quantum confinement [54]. Together, these investigations not only exhibit the practicality and adaptability of the VLS technique without the necessity for a metal catalyst but also demonstrate how such precise control over the growth process can yield nanowires which are highly conductive, of good structural integrity and optical properties.

Complex InAs inclined nanowire networks can also be achieved using VLS. For that, Dalacu et al. performed the growth of 35° inclined InAs nanowires grown from gold catalysts deposited on the (111) sidewall of an InP ridge defined on an InP(100) substrate [55]. Interconnected wires can be obtained when the tilted InAs NWs growing in different (111) directions meet each other (Figure 1.9). This method is however very challenging due the precision required for the positioning of the catalysts. Moreover, integrating such nanostructures into devices implies their cut from the substrate and transfer to a host substrate for processing. This is generally done by ultrasonic dispersion in an IPA solution before nanostructures can be picked up and dispersed on the host wafer. The random positioning and the high probability of degradation of the nanostructures during the transfer prevent this solution from being sufficiently scalable and reliable for an industrial process. Finally, in order to fabricate complex nanostructures with a scalable process, in-plane nanowires can also be directly grown on the substrate. The next part presents the main works dedicated to this method for InAs NW integration.

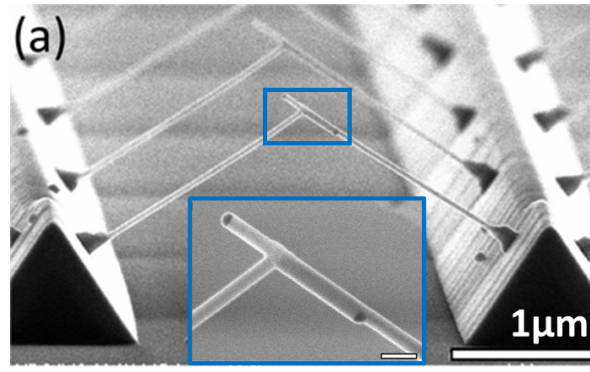


Figure 1.9 – SEM image viewed at  $85^\circ$  from normal of a pair of connected nanowires grown on InP ridges pitched at  $3.5 \mu\text{m}$ . The inset is a close-up to the intersection. The scale bar is 100 nm (adapted from [55]).

### (b) Selective area growth of in-plane InAs nanowires and networks

Selective area growth has the advantage of easily tailoring the shape and dimensions of in-plane nanostructures thanks to nanoscale lithography. However, compared to the vertical nanowires, which are freestanding, one has to deal now with the resistivity of the underlying substrate as well as its lattice mismatch with InAs.

Several works were carried out for improving the quality of in-plane InAs nanowires on highly mismatched substrates (Si, GaAs and InP). One interesting approach is the so-called template assisted selective growth (TASE) demonstrated, by H. Schmid et al. at IBM [56]. In this technique, InAs is grown from a Si nano-seed by MOCVD inside a  $\text{SiO}_2$  mold (Figure 1.10(a)) [57]. Arrays of nanowires and complex shapes were achieved as illustrated in Figure 1.10(b) and Figure 1.10(c) [58]. By this method, high quality InAs complex networks, junctions and hall bars were also demonstrated. The sheet carrier density and the sheet resistance measured on  $28 \text{ nm} \times 40 \text{ nm}$  cross-sectional-InAs nano-Hall-bars reached respectively  $9.1 \times 10^{11} \text{ cm}^{-2}$  and  $1260 \Omega/\square$  at room temperature revealing an electron mobility of about  $6200 \text{ cm}^2/\text{V.s}$  at 4K.

Later on, using this technique, the same group demonstrated ballistic electron transport inside InAs cross junctions (Figure 1.10(d) and 1.10(e)) [58]. TASE offers the possibility to control the Fermi level in the InAs NW with a back gate control thanks to the insulating  $\text{SiO}_2$  layer in-between InAs NW and the Si substrate. With this method, conductance plateaus at 4K were measured in the transfer characteristic of the device (Figure 1.10(f)). Ballistic transport with an electron mean free path of about 930 nm was deduced from these measurements.

On GaAs or InP substrates, the method for growing in-plane NW is slightly different: the lateral dimensions are defined by the mask aperture but the thickness and cross-section shape

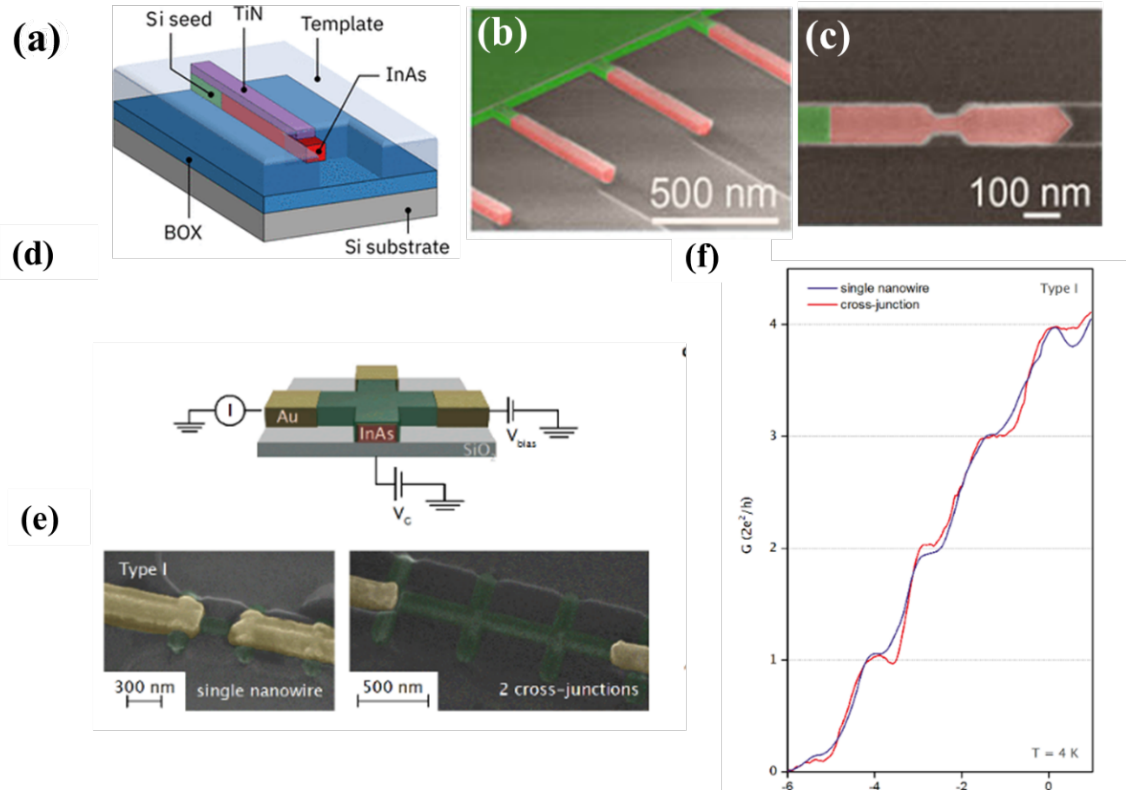


Figure 1.10 – (a) Schematic illustration of TASE of InAs nanowire inside a lateral ( $\text{SiO}_2$ ) template [57] (b) Colorized 3D-SEM image of a template structure containing Si pads and InAs NWs covered by a  $\text{SiO}_2$  film (c) SEM image of a complex pattern filled by InAs NWs and Si pads inside the  $\text{SiO}_2$  template (d) Schematic of the measurement device. Metallic probes (yellow) are connected to an InAs NW cross junction (red), covered by a protective oxide template (green). The current  $I_{out}$  at one terminal in response to a bias voltage  $V_{bias}$  is measured as a function of gate voltage  $V_{gate}$ . (e) False-colored SEM image of a single NW (left) and two cross sections (right). (f) Electrical conductance  $G = V_{bias}/I$  of a single NW (blue) and a NW cross-junction (red) as a function of gate voltage at 4 K [58].

are determined by the growth conditions. Two methods can be used: growing directly InAs on the mismatched substrate or using an intermediate Ga(As)Sb nano-template to accommodate the mismatch.

#### Direct growth with mismatched interface:

Using Chemical Beam Epitaxy (CBE) (where the growth selectivity is achieved thanks to the selective decomposition of the organometallic precursors), Lee et al. have studied the effect of the InP wafer orientation on the InAs NW growth. They found that InAs grown on a  $\text{SiO}_2$  patterned InP(110) substrate exhibits the best crystal quality with As rich conditions. However, for other oriented wafers, an As/In flux ratio close to unity ensures the best InAs spreading inside the mask openings. Misfit dislocations at the interface between InAs nanowires and InP substrates, arising from a 3.3% lattice mismatch, were observed by high angle annular dark field scanning transmission electron microscopy (HAADF-STEM) imaging. Particularly on

InP(110) substrates, the dislocation density reaches  $3 \times 10^5 \text{ cm}^{-1}$ , suggesting a mostly relaxed InAs layer. These dislocations are critical as they may influence the electronic properties of the nanowires. From Hall effect measurements performed at 2K, the authors determined electron density and mobility of  $0.9$  to  $2.1 \times 10^{17} \text{ cm}^{-3}$  and  $5000 \text{ cm}^2/\text{V.s}$ , respectively, for a  $[\bar{1}\bar{1}0]$  oriented 140 nm to 180 nm wide-nanowire grown on an InP(111)<sub>B</sub> wafer [59]. They estimated a mean free path for the electrons between 20 nm and 100 nm.

Selective area growth of in-plane InAs NW can also be achieved by MBE but one has to finely tune the growth conditions and promote In re-evaporation from the mask to succeed. It can be achieved with a low growth rate and a sufficiently high substrate temperature. Aseev et al. proposed a selectivity map summarizing the range of selectivity for InAs [24]. Complex in-plane InAs NW networks were successfully grown on InP(111) wafer (Figure 1.11(a)) and they demonstrated phase-coherent electron transport on  $\mu$ -scale distances with Aharonov-Bohm oscillations measured at 20 mK on ring nanostructures with a top-gate (Figure 1.11(b)) [16].

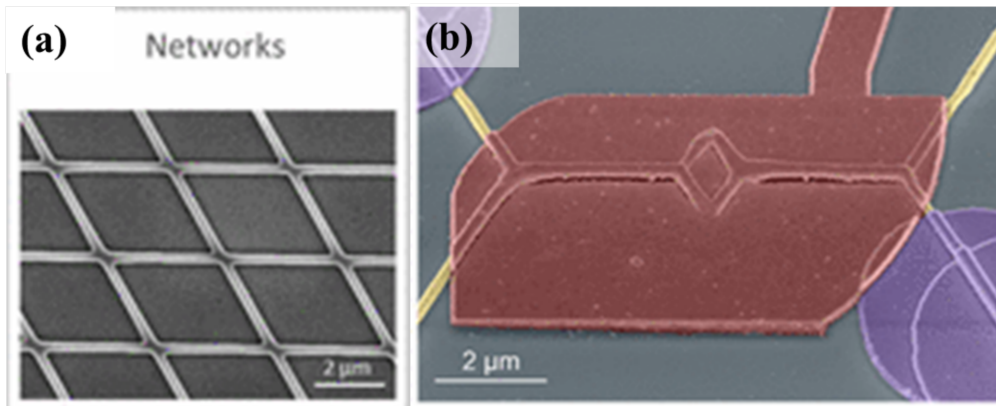


Figure 1.11 – (a) Example of complex NW networks composed of the  $\langle 11\bar{2} \rangle$  NW family [16]. (b) Scanning electron micrograph of an InAs SAG Aharonov–Bohm ring (yellow) contacted by Ti/Au leads (purple) and covered with SiN<sub>x</sub> dielectric and a top-gate electrode (red). The loop area (A) corresponds to  $0.9 \mu\text{m}^2$ .

Growth with a nano-template for mismatch accommodation:

Using semiconductor buffer layers as templates for the InAs nanowire growth is also shown to be a successful technique for growing high quality in-plane InAs nanostructures on GaAs substrate [65]. The works led during the PhD thesis of Maria Fahed at IEMN demonstrated how the use of an atomic hydrogen flux during the growth could enlarge the window of selectivity and achieve continuous and relaxed GaSb islands on  $\mu\text{m}$ -long and 100nm-wide patterns designed on GaAs (100) substrate. Thanks to this method, the interface misfit dislocations are far from the InAs channel and clean interface between InAs and GaSb can be obtained. Figures 1.12(a) and 1.12(b) are HAADF STEM cross section micrographs of in-plane InAs

nanowires grown by MBE on top of a GaSb nano-template on GaAs (100) substrate. Up to date, electrical characterizations on such in-plane InAs NW have not been reported.

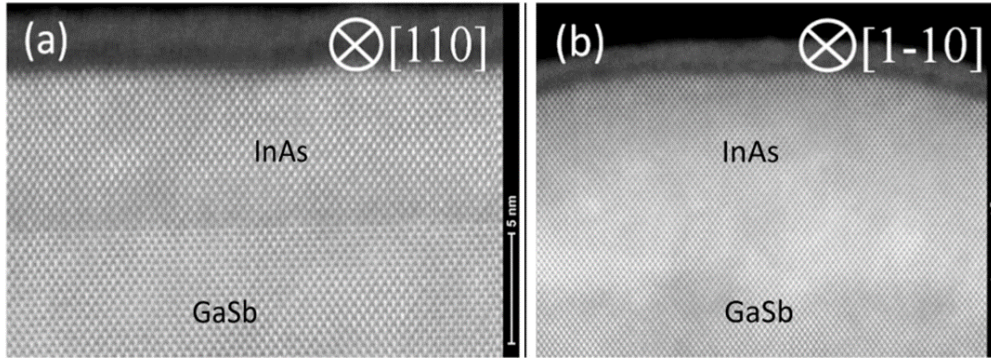


Figure 1.12 – HAADF STEM image recorded after 150 nm GaSb growth followed by 10 nm InAs in apertures directed along (a) [110] and (b) [1-10] [60].

Furthermore, Filip Krizek et al. explored the fabrication of InAs nanowires using molecular beam epitaxy (MBE) on semi-insulating substrates using a GaAsSb buffer layer [61]. In their method, they meticulously controlled the growth environment, including substrate temperature and material flux rates, to optimize the single and complex nanowire structure in different crystallographic orientations. They employed top-gate geometries to precisely control the carrier density, a key factor in effective gating for both classical and quantum devices. Their observations revealed that conductance in these nanowires does not fully pinch off even at very negative gate voltages, with the down and up gate traces showing significant hysteresis. The team achieved an average mobility in buffered nanowires of around  $5600 \pm 1300 \text{ cm}^2/\text{V}\cdot\text{s}$ , with peaks reaching approximately  $7600 \text{ cm}^2/\text{V}\cdot\text{s}$  at 20 mK. This high mobility, along with the observed structural uniformity and consistency in the nanowires, underscored the importance of buffer layers in improving interface quality and enhancing electron mobility. Moreover, Martin Friedl et al. study presented a scalable method for creating branched In(Ga)As nanowire arrays using GaAs nanomembranes as templates, [62]. By controlling the width of nanomembranes and the duration of growth, they successfully fabricated nanowires with cross-sections less than 50 nm, and scaling down to 20 nm led to the formation of homogeneous InGaAs nanowires. These nanowires demonstrated phase-coherent, quasi-1D quantum transport properties. Magnetoconductance measurements revealed coherence lengths of approximately 130 nm and spin-orbit lengths estimated to be at least 280 nm, indicative of their potential for hosting Majorana fermions in quantum computing applications.



## 4.4 InSb nanostructures

InSb exhibits lower electron effective mass and stronger spin-orbit coupling than InAs. It is thus particularly appealing for magneto-transport experiments. One disadvantage of this material is its large mismatch with other III-V semiconductors, making the fabrication of high quality heterostructures challenging. In the following, an overview of the different methods for the growth of InSb nanostructures either in the form of thin film or in the form of nanowire is proposed.

### 4.4.1 InSb thin films and 2DEG

One way to confine electrons into InSb with larger bandgap barriers is to grow a thick metamorphic buffer from a GaAs substrate to reach a lattice parameter authorizing the growth of a strained  $\text{Al}_x\text{In}_{1-x}\text{Sb}/\text{InSb}$  heterostructure with  $x$  sufficiently low to avoid the relaxation of the InSb channel. An example of such a structure is depicted in Figure 1.13. With this method, Orr et al reported room temperature mobility as high as  $51000 \text{ cm}^2/\text{V} \cdot \text{s}$  with a carrier concentration of  $5.8 \times 10^{11} \text{ cm}^{-2}$ , while low-temperature mobility below 40 K reached  $248000 \text{ cm}^2/\text{V} \cdot \text{s}$  for a carrier concentration of  $3.9 \times 10^{11} \text{ cm}^{-2}$  [63]. More recently, electron mobility exceeding  $350000 \text{ cm}^2/\text{V} \cdot \text{s}$  at low temperature were achieved on top gated InSb/InAlSb quantum well grown also on a GaAs (100) wafer [64].

InSb/InAlSb quantum wells exhibit fascinating transport characteristics for advanced quantum devices. Despite the difficulty to grow high quality InSb 2DEG, this heterostructure is very attractive for advanced quantum devices [8]. One example is the study of the Josephson effects. By taking advantage of the large spin-orbit coupling of this material as well as its large Landé  $g$ -factor and its high electron mobility, C.T. Ke et al achieved  $\pi$ -Josephson junctions (JJ) [65]. The JJ exhibits a carrier density and an electron mobility that are respectively around  $2.7 \times 10^{11} \text{ cm}^{-2}$  and  $150000 \text{ cm}^2/\text{V} \cdot \text{s}$ . They proved the ballistic superconductivity effect inside these devices with a mean free path around  $1.3 \mu\text{m}$ . In the work of Lei et al, spin-splitting of Landau levels at a magnetic field of 2T was demonstrated.

A recent work reported electron density and mobility inside an InSb/InAlSb quantum well of  $2.4 \times 10^{11} \text{ cm}^{-2}$  and  $260000 \text{ cm}^2/\text{V} \cdot \text{s}$  respectively, signatures of Ising quantum Hall ferromagnetism at filling factor  $\nu = 2$  when the Landau level energy is equal to the Zeeman energy [66]. The InSb/InAlSb quantum well is therefore a promising candidate for advanced

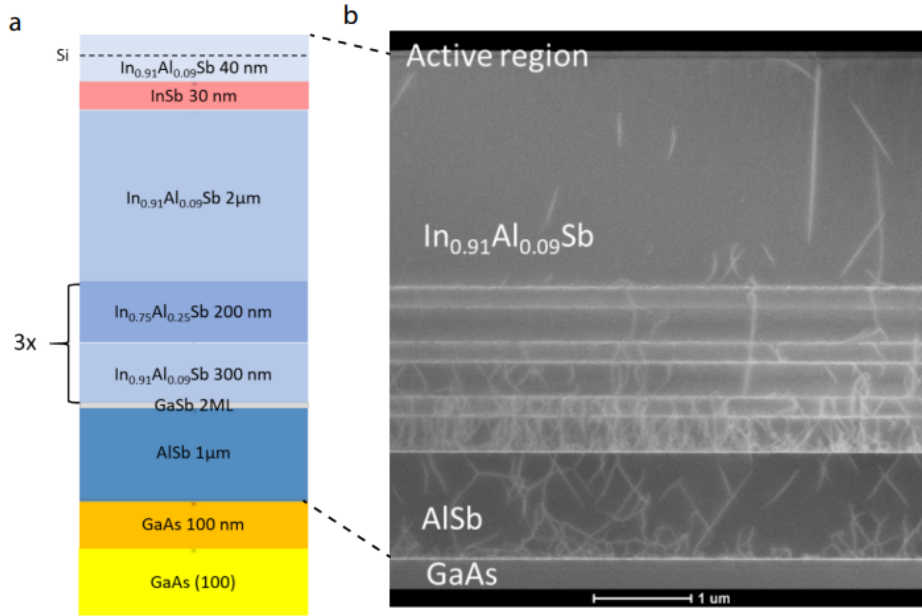


Figure 1.13 – InSb quantum well. (a) Layer stack of the InSb/GaAs heterostructure, where the layer constituents and thicknesses are indicated. (b) Scanning transmission electron micrograph of the structure of (a) obtained in High Angle Annular Dark Field Mode along the  $[110]$  zone axis [65].

quantum devices and Majorana fermion investigations. But, once again, the fabrication of 1D structures from a 2DEG is impacted by etching process.

#### 4.4.2 Bottom-up InSb NWs and networks

##### (a) VLS vertical nanowires

The growth of 1D InSb nanostructures started with the growth of vertical nanowires by means of the VLS approach. Since the lattice mismatch between InSb and other III-V compound semiconductors is significantly high, growing vertical InSb nanowires sparked the interest of several research works that aimed at benefiting from the unique transport properties inside this crystal. The earliest studies into InSb nanowires, spearheaded by Zotov et al., revealed their remarkable suitability for high-tech applications due to their unique electronic characteristics [67]. Yet, the challenge of integrating these nanowires with Si or other III-V materials persisted because of InSb large lattice mismatch. To overcome this obstacle, researchers developed innovative methods to fabricate InSb nanowires, ranging from electrodeposition within porous templates to self-nucleation processes and advanced molecular beam epitaxy (MBE), often employing the vapor-liquid-solid (VLS) principle and using gold as a catalyst [68]–[71]. However, the use of gold has been a double-edged sword, aiding growth but also poten-

tially introducing defect sites. The pursuit of precise nanowire placement has led to progress, though transferring the delicate structures to suitable substrates for device construction has been a complex task. While recent breakthroughs have enabled the formation of intersecting nanowire networks through gold-assisted VLS growth, the industry still faces the challenge of fabricating complex circuits directly on substrates without the need for nanowire transfer [20], [22].

In terms of transport properties, field effect electron mobility as large as  $57000 \text{ cm}^2/\text{V} \cdot \text{s}$  at cryogenic temperature was reported by Badawi et al for stemless VLS grown nanowires with a diameter of about  $190 \text{ nm}$  (Figure 1.14(a)) [72]. In this work, the observation of conductance plateaus aligned with multiples of  $e^2/h$  (Figure 1.14(b)) in the transfer characteristic of the NW evidenced the ballistic behaviour of electron transport inside the NW at  $6\text{K}$  for source-drain separation of  $2 \mu\text{m}$ .

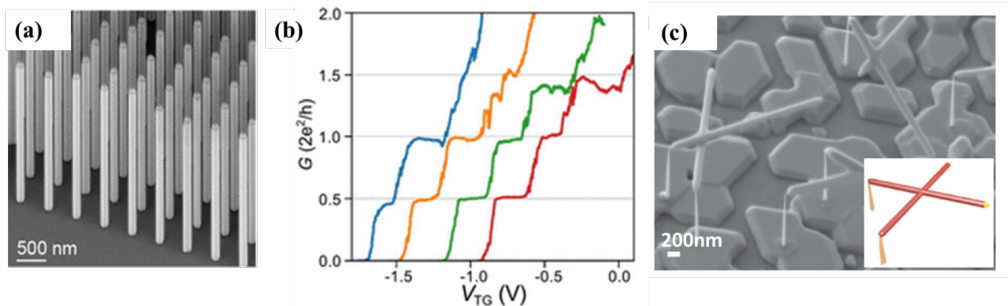


Figure 1.14 – (a) Vertical stemless InSb nanowires [72] (b) Measured Quantum Point Contact (QPC) conductance versus the top-gate voltage at  $6\text{K}$  presenting quantized conductance behaviour [72] (c) , InSb nanocrosses resulting from the merging process between two InSb nanowires. The inset shows InAs and InSb segments in orange and red, respectively, and the Au–In droplet is in yellow [71].

With the VLS technique, InSb nanowire crosses were achieved [71]. Figure 1.14(c) displays horizontal InSb nano-crosses standing on InP–InAs stems. The maximum Hall mobility measured inside these cross-junctions reaches  $10000 \text{ cm}^2/\text{V}\cdot\text{s}$ .

### (b) Selective area growth

InSb is the compound III-V semiconductor with the lowest band gap but also with a high mismatch relatively to larger band gap semiconductors. Hence, mismatch accommodation is required to achieve in-plane NW on semi-insulating substrates. In previous work, the MBE growth of in-plane InSb NWs on GaAs (100) wafers has been demonstrated by the Epiphy group at IEMN thanks to the use of an AlGaSb buffer layer prior to the  $\text{SiO}_2$  mask fabrication [73], [74]. Figure 1.15(a) is a SEM image of  $50 \text{ nm}$ -wide nanowires grown in the  $[110]$  direction. Continuous InSb nanowires have been achieved despite the lattice mismatch thanks to the use



of an atomic hydrogen flux during the MBE growth, enabling selective area growth for a quite low temperature. Figures 1.15(b) and Figure 1.15(c) display STEM micrographs of the cross section of a 50 nm-wide NW grown with this technique, revealing a threading defect free material [73].

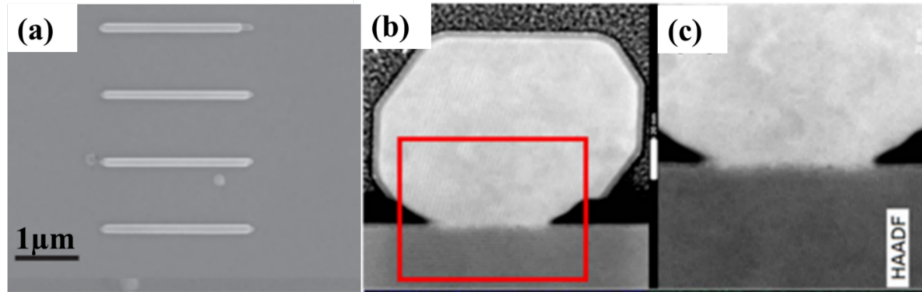


Figure 1.15 – (a) SEM image of an InSb NW array defined with  $100 \text{ nm} \times 2.6 \text{ m}$  apertures [73]. (b) . STEM image of the cross-section of an InSb in-plane nanowire grown inside a 50 nm wide aperture. White scale bar is 20nm [73] (c) HAADF image in the red rectangle of image (b) showing the absence of threading defects in the nanostructure. Black scale bar is 10nm.

Another technique developed in the group of L.P. Kouwenhoven demonstrated high crystalline quality in-plane InSb NW and complex networks by means of the metal sown selective area approach. This technique is based on the selective deposition of a metal seed inside the mask aperture before the NW growth as illustrated in Figure 1.16(a) for a ring-like pattern [22]. A low temperature electron mobility larger than  $20000 \text{ cm}^2/\text{V}\cdot\text{s}$  was reported in this work and quantum interference devices revealed a  $8 \text{ } \mu\text{m}$  phase-coherent length at 50 mK. Figure 1.16(b) and Figure 1.16(c) display respectively a coloured SEM image of the InSb nano-device used for transport measurements and the conductance plateaus revealed under magnetic field.

More recently, Op het Veld et al. reported the fabrication of high quality InSb nanowire networks on InP(111) wafers via MOCVD in-plane selective area growth [20]. A key parameter for this achievement was the modulation of the V/III precursor ratio to a very large value, yielding extensive and interconnected networks of nanowires with consistent diameters near 60 nm and lengths of several microns. By controlling the nucleation to a singular point, the growth process promotes the development of a single crystalline structure throughout the entire network. This uniformity is essential for preserving the integrity of quantum states and ensuring coherent electron transport over longer distances, both of which are crucial for the reliable operation of quantum devices. With this technique, they evidenced ballistic transport regime in the nanowire network and traced phase-coherent electron transport over distances of approximately  $9 \text{ } \mu\text{m}$ . The capability to sustain electron coherence over such lengths, without disruption from defects, marks a significant stride toward realizing topological

quantum computing architectures based on hybrid semiconductor-superconductor association.

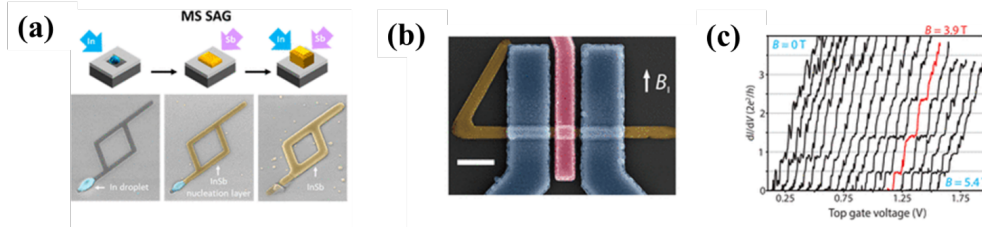


Figure 1.16 – (a) SEM images showing the growth steps starting by the In sowing at  $465^{\circ}\text{C}$  to the InSb nanowires growth in the mask apertures, every SEM images is represented by a scheme on the top of it. [22] (b) False colored SEM image of the InSb Quantum Point Contact (QPC) device. Contacts are blue, the gate is purple, and the NW is yellow away from the electrodes. The scale bar is 500 nm. A magnetic field is applied along the in-plane direction perpendicular to the NW [22]. (c) Zero-DC-bias pinch-off traces of the device shown in panel a, taken at field values between 0 and 5.5 T with intervals of 0.3 T [22].

All of these results have been achieved after device processing including a chemical treatment of the InSb surface, this latter being very sensitive to oxidization. During this thesis, we aim at measuring the intrinsic properties of InAs and InSb in-plane NW by developing either an efficient passivation shell protecting channel from oxidization or an efficient capping process to transfer the sample from MBE reactor to a 4-probe STM set-up without oxidizing the surface. We hope that this method could further enhance the transport properties inside the materials.

## 5 Thesis objectives

In this chapter, we summarized the different process for the epitaxial growth of InAs and InSb nanostructures, highlighting their pivotal role in ongoing progresses to build ballistic devices. The SAG technique was described as an original and effective approach for the controlled growth of one-dimensional structures. The different studies show the crucial impact of the growth conditions on the crystalline quality and consequently on the transport properties of the nanostructures. Comparing the electron mobility measured by Hall measurement on 2D systems and the one deduced from the transfer characteristics of gated nanowire devices, a systematic degradation of the transport properties can be noticed, suggesting an impact of the 1D shaping of the material and extrinsic limitations coming from device processing (contacts, gate oxide...).

The objective of this thesis is to estimate the intrinsic transport properties of InAs and InSb 1D nanostructures, benefiting from the precision of four-probe Scanning Tunnelling Microscopy (4P-STM) and taking advantage of the ability that this technique gives to carry out mea-

surements in UHV conditions. The intrinsic conductance of both 2D layers and 1D in-plane selectively grown InAs NWs will be investigated to determine the charge carrier mobilities and the sheet resistance. The effect of the channel oxidation and the buffer layers will be studied as well as the influence of highly mismatched substrates on the crystal quality and the transport properties. As the surface to volume ratio is important for nanowires, we will also study the surface reconstructions of InSb surfaces by means of the LT-STM systems paving the way for a better understanding of the transport properties in 1D InSb nanostructures with reduced thicknesses.

## Bibliography

- [1] J. Friedrich, ‘Methods for Bulk Growth of Inorganic Crystals: Crystal Growth’, in Reference Module in Materials Science and Materials Engineering, Elsevier, 2016. doi: 10.1016/B978-0-12-803581-8.01010-9.
- [2] K. W. Böer and U. W. Pohl, ‘Properties and Growth of Semiconductors’, in Semiconductor Physics, K. W. Böer and U. Pohl, Eds., Cham: Springer International Publishing, 2017, pp. 1–26. doi: 10.1007/978-3-319-06540-3<sub>1</sub> – 1.
- [3] U. W. Pohl, ‘Thermodynamics of Epitaxial Layer-Growth’, in Epitaxy of Semiconductors: Physics and Fabrication of Heterostructures, U. W. Pohl, Ed., in Graduate Texts in Physics. , Cham: Springer International Publishing, 2020, pp. 207–250. doi: 10.1007/978-3-030-43869-2<sub>6</sub>.
- [4] M. Yamaguchi, I. Horiuchi, J. H. Paek, and N. Sawaki, ‘In-assisted Catalyst-free MBE-VLS Growth of InAs Nanowires on Si Substrate’, AIP Conf. Proc., vol. 1399, no. 1, pp. 229–230, Dec. 2011, doi: 10.1063/1.3666338.
- [5] J. R. Arthur, ‘Molecular beam epitaxy’, Surf. Sci., vol. 500, no. 1, pp. 189–217, Mar. 2002, doi: 10.1016/S0039-6028(01)01525-4.
- [6] E. Zhuo et al., ‘Hole-type superconducting gatemon qubit based on Ge/Si core/shell nanowires’, Npj Quantum Inf., vol. 9, no. 1, Art. no. 1, May 2023, doi: 10.1038/s41534-023-00721-9.
- [7] X. Zhou, S. A. Dayeh, D. Aplin, D. Wang, and E. T. Yu, ‘Direct observation of ballistic and drift carrier transport regimes in InAs nanowires’, Appl. Phys. Lett., vol. 89, no. 5, p. 053113, Aug. 2006, doi: 10.1063/1.2236589.
- [8] P. Harrison and A. Valavanis, Quantum Wells, Wires and Dots: Theoretical and Computational Physics of Semiconductor Nanostructures. John Wiley Sons, 2016.
- [9] R. S. Wagner and W. C. Ellis, ‘Vapor-Liquid-Solid Mechanism of Single Crystal Growth’, Appl. Phys. Lett., vol. 4, no. 5, pp. 89–90, Dec. 2004, doi: 10.1063/1.1753975.
- [10] W. Lu, J. Xian et al.’Semiconductor Nanowires: From Next-Generation Electronics to Sustainable Energy (Smart Materials Series, Volume 11): 9781849738156 - AbeBooks’, 2023. [Online]. Available: <https://www.abebooks.com/9781849738156/Semiconductor-Nanowires->

Next-Generation-Electronics-Sustainable-1849738157/plp

- [11] U. W. Pohl, ‘Methods of Epitaxy’, in *Epitaxy of Semiconductors: Physics and Fabrication of Heterostructures*, U. W. Pohl, Ed., in *Graduate Texts in Physics*. , Cham: Springer International Publishing, 2020, pp. 427–467. doi: 10.1007/978-3-030-43869-2\_11.
- [12] T. Kuech, *Handbook of Crystal Growth: Thin Films and Epitaxy*. Elsevier Science, 2015.
- [13] J. Holleman, A. Hasper, and J. Middelhoek, ‘In Situ Growth Rate Measurement of Selective LPCVD of Tungsten’, *J. Electrochem. Soc.*, vol. 138, no. 4, p. 989, Apr. 1991, doi: 10.1149/1.2085758.
- [14] T. Ujihara, Y. Yoshida, W. Sik Lee, and Y. Takeda, ‘Pattern size effect on source supply process for sub-micrometer scale selective area growth by organometallic vapor phase epitaxy’, *J. Cryst. Growth*, vol. 289, no. 1, pp. 89–95, Mar. 2006, doi: 10.1016/j.jcrysgro.2005.11.088.
- [15] X.-Q. Shen, D. K. Daisuke Kishimoto, and T. N. Tatau Nishinaga, ‘Arsenic Pressure Dependence of Surface Diffusion of Ga on Nonplanar GaAs Substrates’, *Jpn. J. Appl. Phys.*, vol. 33, no. 1R, p. 11, Jan. 1994, doi: 10.1143/JJAP.33.11.
- [16] P. Aseev et al., ‘Selectivity Map for Molecular Beam Epitaxy of Advanced III–V Quantum Nanowire Networks’, *Nano Lett.*, vol. 19, no. 1, pp. 218–227, Jan. 2019, doi: 10.1021/acs.nanolett.8b03733.
- [17] M. Fahed, L. Desplanque, D. Troadec, G. Patriarche, and X. Wallart, ‘Selective area heteroepitaxy of GaSb on GaAs (001) for in-plane InAs nanowire achievement’, *Nanotechnology*, vol. 27, no. 50, p. 505301, Nov. 2016, doi: 10.1088/0957-4484/27/50/505301.
- [18] M. Fahed, ‘Selective area growth of in-plane III-V nanostructures using molecular beam epitaxy’, *These de doctorat, Lille 1*, 2016. [Online]. Available: <https://www.theses.fr/2016LIL10114>
- [19] A. Bucamp, ‘Croissance sélective et caractérisation de nanostructures de matériaux III-V élaborées par épitaxie par jets moléculaires’, *These de doctorat, Université de Lille (2018-2021)*, 2019. [Online]. Available: <https://www.theses.fr/2019LILUI067>
- [20] R. L. M. Op Het Veld et al., ‘In-plane selective area InSb–Al nanowire quantum networks’, *Commun. Phys.*, vol. 3, no. 1, p. 59, Mar. 2020, doi: 10.1038/s42005-020-0324-4.
- [21] N. P. de Leon et al., ‘Materials challenges and opportunities for quantum computing hardware’, *Science*, vol. 372, no. 6539, p. eabb2823, Apr. 2021, doi: 10.1126/science.abb2823.

- [22] P. Aseev et al., ‘Ballistic InSb Nanowires and Networks via Metal-Sown Selective Area Growth’, *Nano Lett.*, vol. 19, no. 12, pp. 9102–9111, Dec. 2019, doi: 10.1021/acs.nanolett.9b04265.
- [23] J. Arbiol and Q. Xiong, *Semiconductor Nanowires: Materials, Synthesis, Characterization and Applications*. Elsevier Science, 2015.
- [24] M. Heiblum, M. I. Nathan, D. C. Thomas, and C. M. Knoedler, ‘Direct Observation of Ballistic Transport in GaAs’, *Phys. Rev. Lett.*, vol. 55, no. 20, pp. 2200–2203, Nov. 1985, doi: 10.1103/PhysRevLett.55.2200.
- [25] H. J. Li, W. G. Lu, J. J. Li, X. D. Bai, and C. Z. Gu, ‘Multichannel Ballistic Transport in Multiwall Carbon Nanotubes’, *Phys. Rev. Lett.*, vol. 95, no. 8, p. 086601, Aug. 2005, doi: 10.1103/PhysRevLett.95.086601.
- [26] J. Baringhaus et al., ‘Exceptional ballistic transport in epitaxial graphene nanoribbons’, *Nature*, vol. 506, no. 7488, Art. no. 7488, Feb. 2014, doi: 10.1038/nature12952.
- [27] J. Aprojanz, I. Miccoli, J. Baringhaus, and C. Tegenkamp, ‘1D ballistic transport channel probed by invasive and non-invasive contacts’, *Appl. Phys. Lett.*, vol. 113, no. 19, p. 191602, Nov. 2018, doi: 10.1063/1.5054393.
- [28] N. Goel et al., ‘Ballistic transport in InSb mesoscopic structures’, *Phys. E Low-Dimens. Syst. Nanostructures*, vol. 26, no. 1, pp. 455–459, Feb. 2005, doi: 10.1016/j.physe.2004.08.080.
- [29] N. Goel, S. J. Chung, M. B. Santos, K. Suzuki, S. Miyashita, and Y. Hirayama, ‘Ballistic transport in InSb quantum wells at high temperature’, *Phys. E Low-Dimens. Syst. Nanostructures*, vol. 20, no. 3, pp. 251–254, Jan. 2004, doi: 10.1016/j.physe.2003.08.012.
- [30] A. M. Gilbertson et al., ‘Room temperature ballistic transport in InSb quantum well nanodevices’, *Appl. Phys. Lett.*, vol. 99, no. 24, p. 242101, Dec. 2011, doi: 10.1063/1.3668107.
- [31] S. Li et al., ‘Coherent Charge Transport in Ballistic InSb Nanowire Josephson Junctions’, *Sci. Rep.*, vol. 6, no. 1, Art. no. 1, Apr. 2016, doi: 10.1038/srep24822.
- [32] S. S. Li, *Semiconductor Physical Electronics*. Springer Science Business Media, 2012.
- [33] J. A. Zúñiga, S. T. P. Merchancano, and L. E. B. Marínez, ‘Spin polarization in non-magnetic nanostructures’, *J. Phys. Conf. Ser.*, vol. 614, no. 1, p. 012006, Apr. 2015, doi: 10.1088/1742-6596/614/1/012006.

- [34] K.-Y. Lu, Z.-Y. He, M.-M. Zu, and S.-Y. Guo, ‘Rashba Spin-Orbit-Coupling Based Electron-Spin Filter in Double-Layered Semiconductor Nanostructure’, *IEEE Electron Device Lett.*, vol. 43, no. 10, pp. 1645–1648, Oct. 2022, doi: 10.1109/LED.2022.3196374.
- [35] A. Das, Y. Ronen, Y. Most, Y. Oreg, M. Heiblum, and H. Shtrikman, ‘Zero-bias peaks and splitting in an Al–InAs nanowire topological superconductor as a signature of Majorana fermions’, *Nat. Phys.*, vol. 8, no. 12, pp. 887–895, Dec. 2012, doi: 10.1038/nphys2479.
- [36] O. Madelung, *Semiconductors: Data Handbook*. Berlin, Heidelberg: Springer, 2004. doi: 10.1007/978-3-642-18865-7.
- [37] J. Si, ‘Novel InSb-based infrared detector materials (Invited)’, *Infrared Laser Eng.*, vol. 51, no. 1, p. 20210811, 2022, doi: 10.3788/IRLA20210811.
- [38] S. Nakamura, ‘Background story of the invention of efficient blue InGaN light emitting diodes (Nobel Lecture): Invention of the efficient blue InGaN LEDs’, *Ann. Phys.*, vol. 527, no. 5–6, pp. 335–349, Jun. 2015, doi: 10.1002/andp.201500801.
- [39] A. Trampert, ‘Heteroepitaxy of Large-Misfit Systems: Role of Coincidence Lattice’, *Cryst. Res. Technol.*, Jan. 2000. [Online]. Available: [https://www.academia.edu/34483453/Heteroepitaxy\\_of\\_Large\\_Misfit\\_Systems\\_Role\\_of\\_Coincidence\\_Lattice](https://www.academia.edu/34483453/Heteroepitaxy_of_Large_Misfit_Systems_Role_of_Coincidence_Lattice).
- [40] J. W. Matthews and A. E. Blakeslee, ‘Defects in epitaxial multilayers: I. Misfit dislocations’, *J. Cryst. Growth*, vol. 27, pp. 118–125, Dec. 1974, doi: 10.1016/S0022-0248(74)80055-2.
- [41] A. Bhattacharyya and D. Maurice, ‘On the evolution of stresses due to lattice misfit at a Ni-superalloy and YSZ interface’, *Surf. Interfaces*, vol. 12, pp. 86–94, Sep. 2018, doi: 10.1016/j.surfin.2018.05.007.
- [42] H.-R. Blank, M. Thomas, K. C. Wong, and H. Kroemer, ‘Influence of the buffer layers on the morphology and the transport properties in InAs/(Al,Ga)Sb quantum wells grown by molecular beam epitaxy’, *Appl. Phys. Lett.*, vol. 69, no. 14, pp. 2080–2082, Sep. 1996, doi: 10.1063/1.116886.
- [43] M. Borg, *Scaling of InGaAs/InAlAs and InAs/AlSb HEMTs for Microwave/mm-wave Applications*. Chalmers University of Technology, 2007.
- [44] T. Akazaki, H. Takayanagi, J. Nitta, and T. Enoki, ‘InAs-inserted-channel InAlAs/InGaAs inverted HEMTs with direct ohmic contacts’, *Phys. E Low-Dimens. Syst. Nanostructures*,

vol. 2, no. 1, pp. 458–462, Jul. 1998, doi: 10.1016/S1386-9477(98)00094-0.

[45] I. Knez and R.-R. Du, ‘Quantum spin Hall effect in inverted InAs/GaSb quantum wells’, *Front. Phys.*, vol. 7, no. 2, pp. 200–207, Apr. 2012, doi: 10.1007/s11467-011-0204-1.

[46] S. Mueller et al., ‘Edge transport in InAs and InAs/GaSb quantum wells’, *Phys. Rev. B*, vol. 96, no. 7, p. 075406, Aug. 2017, doi: 10.1103/PhysRevB.96.075406.

[47] H. Kroemer, ‘The 6.1Å family (InAs, GaSb, AlSb) and its heterostructures: a selective review’, *Phys. E Low-Dimens. Syst. Nanostructures*, vol. 20, no. 3, pp. 196–203, Jan. 2004, doi: 10.1016/j.physe.2003.08.003.

[48] S. J. Koester, C. R. Bolognesi, M. J. Rooks, E. L. Hu, and H. Kroemer, ‘Quantized conductance of ballistic constrictions in InAs/AlSb quantum wells’, *Appl. Phys. Lett.*, vol. 62, no. 12, pp. 1373–1375, Mar. 1993, doi: 10.1063/1.108683.

[49] K. G. Eyink et al., ‘Electrical and structural characterization of a single GaSbInAsGaSb quantum well grown on GaAs using interface misfit dislocations’, *J. Appl. Phys.*, vol. 104, no. 7, p. 074901, Oct. 2008, doi: 10.1063/1.2982277.

[50] M. J. Yang, C. H. Yang, B. R. Bennett, and B. V. Shanabrook, ‘Evidence of a Hybridization Gap in “Semimetallic” InAs/GaSb Systems’, *Phys. Rev. Lett.*, vol. 78, no. 24, pp. 4613–4616, Jun. 1997, doi: 10.1103/PhysRevLett.78.4613.

[51] L. Du, I. Knez, G. Sullivan, and R.-R. Du, ‘Robust Helical Edge Transport in Gated InAs/GaSb Bilayers’, *Phys. Rev. Lett.*, vol. 114, no. 9, p. 096802, Mar. 2015, doi: 10.1103/PhysRevLett.114.096802.

[52] K. Tomioka and T. Fukui, ‘Recent progress in integration of III–V nanowire transistors on Si substrate by selective-area growth’, *J. Phys D: Appl. Phys.*, vol. 47, no. 39, p. 394001, Sep. 2014, doi: 10.1088/0022-3727/47/39/394001.

[53] G. Koblmüller et al., ‘Self-induced growth of vertical free-standing InAs nanowires on Si(111) by molecular beam epitaxy’, *Nanotechnology*, vol. 21, no. 36, p. 365602, Aug. 2010, doi: 10.1088/0957-4484/21/36/365602.

[54] G. Grégoire et al., ‘Long catalyst-free InAs nanowires grown on silicon by HVPE’, *Crys-tEngComm*, vol. 23, no. 2, pp. 378–384, 2021, doi: 10.1039/D0CE01385D.

[55] D. Dalacu, A. Kam, D. G. Austing, and P. J. Poole, ‘Droplet Dynamics in Controlled InAs Nanowire Interconnections’, *Nano Lett.*, vol. 13, no. 6, pp. 2676–2681, Jun. 2013, doi:



10.1021/nl400820w.

[56] H. Schmid et al., ‘Template-assisted selective epitaxy of III–V nanoscale devices for coplanar heterogeneous integration with Si’, *Appl. Phys. Lett.*, vol. 106, no. 23, p. 233101, Jun. 2015, doi: 10.1063/1.4921962.

[57] M. F. Ritter et al., ‘Semiconductor Epitaxy in Superconducting Templates’, *Nano Lett.*, vol. 21, no. 23, pp. 9922–9929, Dec. 2021, doi: 10.1021/acs.nanolett.1c03133.

[58] J. Gooth et al., ‘Ballistic One-Dimensional InAs Nanowire Cross-Junction Interconnects’, *Nano Lett.*, vol. 17, no. 4, pp. 2596–2602, Apr. 2017, doi: 10.1021/acs.nanolett.7b00400.

[59] J. S. Lee et al., ‘Selective-area chemical beam epitaxy of in-plane InAs one-dimensional channels grown on InP(001), InP(111)<sub>B</sub>, and InP(011) surfaces’, *Phys. Rev. Mater.*, vol. 3, no. 8, p. 084606, Aug. 2019, doi: 10.1103/PhysRevMaterials.3.084606.

[60] M. Fahed, L. Desplanque, D. Troadec, G. Patriarche, and X. Wallart, ‘Threading dislocation free GaSb nanotemplates grown by selective molecular beam epitaxy on GaAs (001) for in-plane InAs nanowire integration’, *J. Cryst. Growth*, vol. 477, pp. 45–49, Nov. 2017, doi: 10.1016/j.jcrysgro.2016.12.029.

[61] F. Krizek et al., ‘Field effect enhancement in buffered quantum nanowire networks’, *Phys. Rev. Mater.*, vol. 2, no. 9, p. 093401, Sep. 2018, doi: 10.1103/PhysRevMaterials.2.093401.

[62] M. Friedl et al., ‘Template-Assisted Scalable Nanowire Networks’, *Nano Lett.*, vol. 18, no. 4, pp. 2666–2671, Apr. 2018, doi: 10.1021/acs.nanolett.8b00554.

[63] J. M. S. Orr et al., ‘Electronic transport in modulation-doped InSb quantum well heterostructures’, *Phys. Rev. B*, vol. 77, no. 16, p. 165334, Apr. 2008, doi: 10.1103/PhysRevB.77.165334.

[64] Z. Lei et al., ‘Quantum transport in high-quality shallow InSb quantum wells’, *Appl. Phys. Lett.*, vol. 115, no. 1, p. 012101, Jul. 2019, doi: 10.1063/1.5098294.

[65] C. T. Ke et al., ‘Ballistic superconductivity and tunable  $\pi$ -junctions in InSb quantum wells’, *Nat. Commun.*, vol. 10, no. 1, Art. no. 1, Aug. 2019, doi: 10.1038/s41467-019-11742-4.

[66] Z. Lei et al., ‘High-quality two-dimensional electron gas in undoped InSb quantum wells’, *Phys. Rev. Res.*, vol. 4, no. 1, p. 013039, Jan. 2022, doi: 10.1103/PhysRevResearch.4.013039.

- [67] S. V. Zaitsev-Zotov, Y. A. Kumzerov, Y. A. Firsov, and P. Monceau, ‘Luttinger-liquid-like transport in long InSb nanowires’, *J. Phys. Condens. Matter*, vol. 12, no. 20, p. L303, May 2000, doi: 10.1088/0953-8984/12/20/101.
- [68] C. Pendyala, S. Vaddiraju, J. H. Kim, J. Jacinski, Z. Chen, and M. K. Sunkara, ‘Self-nucleation and growth of group III-antimonide nanowires’, *Semicond. Sci. Technol.*, vol. 25, no. 2, p. 024014, Jan. 2010, doi: 10.1088/0268-1242/25/2/024014.
- [69] H. D. Park, S. M. Prokes, M. E. Twigg, Y. Ding, and Z. L. Wang, ‘Growth of high quality, epitaxial InSb nanowires’, *J. Cryst. Growth*, vol. 304, no. 2, pp. 399–401, Jun. 2007, doi: 10.1016/j.jcrysgro.2007.03.023.
- [70] P. Caroff et al., ‘High-Quality InAs/InSb Nanowire Heterostructures Grown by Metal–Organic Vapor-Phase Epitaxy’, *Small*, vol. 4, no. 7, pp. 878–882, 2008, doi: 10.1002/sml.200700892.
- [71] S. R. Plissard et al., ‘Formation and electronic properties of InSb nanocrosses’, *Nat. Nanotechnol.*, vol. 8, no. 11, pp. 859–864, Nov. 2013, doi: 10.1038/nnano.2013.198.
- [72] G. Badawy et al., ‘High Mobility Stemless InSb Nanowires’, *Nano Lett.*, vol. 19, no. 6, pp. 3575–3582, Jun. 2019, doi: 10.1021/acs.nanolett.9b00545.
- [73] L. Desplanque, A. Bucamp, D. Troadec, G. Patriarche, and X. Wallart, ‘In-plane InSb nanowires grown by selective area molecular beam epitaxy on semi-insulating substrate’, *Nanotechnology*, vol. 29, no. 30, p. 305705, May 2018, doi: 10.1088/1361-6528/aac321.
- [74] L. Desplanque, A. Bucamp, D. Troadec, G. Patriarche, and X. Wallart, ‘Selective area molecular beam epitaxy of InSb nanostructures on mismatched substrates’, *J. Cryst. Growth*, vol. 512, pp. 6–10, Apr. 2019, doi: 10.1016/j.jcrysgro.2019.02.012.

# 2

## Experimental techniques

### 1 Introduction

In this work, we aim at studying the growth conditions of InAs and InSb nanostructures with high crystalline quality as well as their transport properties, which, due to their reduced size, might strongly depend on the electronic states at their surfaces. Growing nanostructures and studying their properties in Ultra-High Vacuum (UHV) provide the best conditions to achieve this goal. Among the different growth techniques, Molecular beam epitaxy (MBE) is an ideal tool as it is known as the “layer by layer growth technique in UHV” and is thus quite appropriate to grow thin nanostructures. As to the transport measurements, it is convenient to work with a tool that allows an arbitrary arrangement of probes with separation between the probes smaller than the size of the nanostructures. Four-probe Scanning Tunnelling Microscopy (4P-STM) known also as Nanoprobe, gives this possibility under UHV conditions, as STM is a powerful technique for scanning the surfaces of nanostructures at the atomic or molecular level. When the four tips are brought into electrical contact with the nanostructures, the technique becomes appropriate to measure its intrinsic transport properties. The STM tips are operated under the control of a Scanning Electron Microscope (SEM) to enable the study

of transport in nanostructures with complex geometries. Finally, the electronic properties of the nanostructure surfaces are studied by means of Low Temperature (LT) -STM, where the sample surfaces are treated in the UHV preparation chamber equipped with a Raman system. This instrument provides information on the evolution of the surface chemistry during the treatment to save time as STM analyses performed at 77 K might be time-consuming. Other techniques were also used to obtain physical insights about the nanostructures morphology and their transport properties: SEM, TEM, Atomic Force Microscopy (AFM), X-ray Diffraction (XRD) and the Hall effect system.

In this chapter, the main growth and characterization techniques are presented.

## 2 Molecular Beam Epitaxy (MBE)

MBE is one of the most suitable techniques for high-crystalline-quality-nanostructure fabrication as the growth takes place in UHV conditions. This ensures a high purity growth environment: the probability of contamination is very low and the elementary atoms or molecules travel from the sources to the sample surface in collision-free conditions. Moreover, the growth rate with such a technique can be as low as 0.01ML/s. As the switching from one material to another can be done instantly, ultra-thin layers and abrupt interfaces can be achieved.

This growth method was invented in the late 1960s, to satisfy the increasing need of semiconductors with high crystalline quality. Its development for more than sixty years offers now materials essential for optoelectronics, spintronics and high speed or quantum electronic devices [1]. In terms of electron transport, MBE is the technique of choice for the production of two dimensional electron gas (2DEG) that exhibit electron mobility exceeding several millions  $\text{cm}^2/\text{V}\cdot\text{s}$  at cryogenic temperature in the GaAs/AlGaAs system [2]. Beyond this text book system where different coherent transport phenomena have been evidenced, MBE also provides solutions for the fabrication of 1D ballistic devices based on InAs or InSb nanowires [3]–[5], systems that may host Majorana bound states when the nanowires are coupled with a superconducting shell [6], [7].

## 2.1 The IEMN MBE System

The Riber Compact21 (C21™) MBE system used in this work is one of the three MBE reactors in the IEMN clean room. It is dedicated to III-V material growth (Figure 2.1(a)) whereas the other ones are dedicated to graphene/hBN epitaxy and Transition Metal Dichalcogenides growth. The III-V MBE system is coupled under UHV to the Electron Spectroscopy for Chemical Analysis (ESCA) chamber (Figure 2.1(b)). Thanks to cryogenic and ion pumps (blue box in Figure 2.1(a)), the residual pressure in the reactor in the standby mode is laying in the  $10^{-10}$  T range. The III-V MBE reactor is equipped with III-element evaporation cells (In, Ga and Al) as well as V-element valved crackers ( $\text{As}_4$ ,  $\text{Sb}_2$ ) and one high temperature gas injector (HTI) for  $\text{AsH}_3$  or  $\text{PH}_3$  cracking. The C21 system is equipped with a hydrogen plasma cell working with a RadioFrequency (RF) excitation coil. The inductive coupling of the RF excitation coil generates a plasma discharge that dissociates the molecular hydrogen. A 600W RF excitation at 13.56MHz is used to achieve atomic hydrogen from molecular flux. The atomic hydrogen used during selective epitaxial growth is proved to enhance the mask selectivity [8].

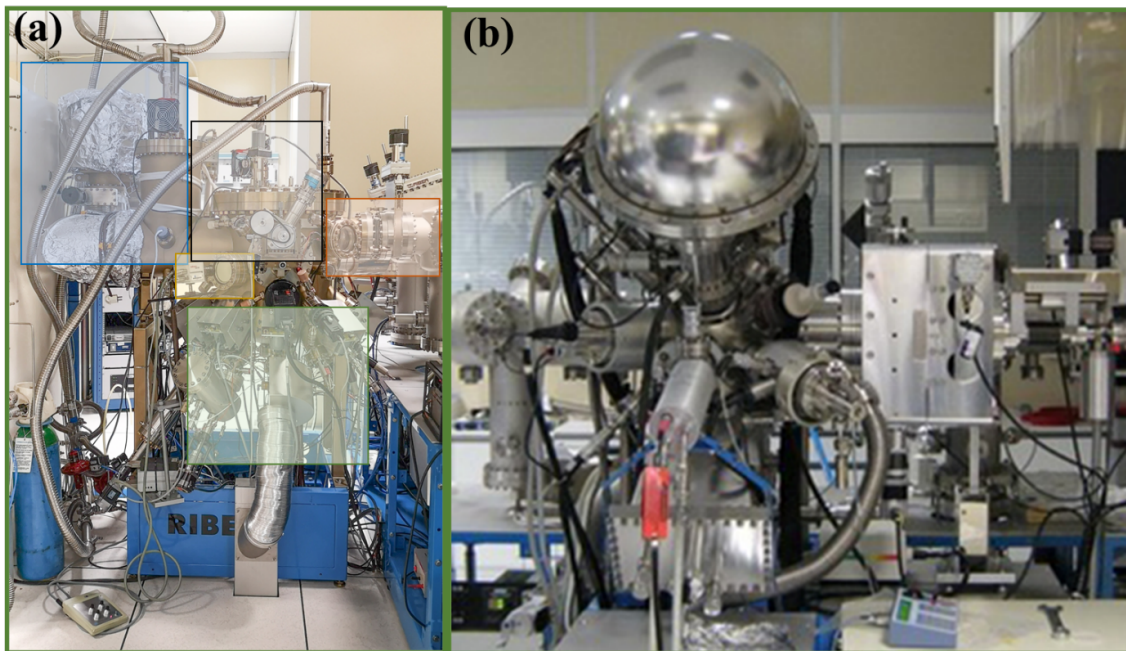


Figure 2.1 – Photographs of (a) III-V MBE Riber compact 21 reactor composed of : a transfer rod of samples from the intermediate chamber to the growth chamber (orange box) III-V growth chamber (black box), ion pump (blue box), RHEED screen with the camera (yellow box) and the valved cracker sources and shutters (green box), (b) Chamber for Electron Spectroscopy for Chemical Analysis (ESCA).

The III-V MBE system is composed of four vacuum chambers separated by gate valves: the introduction chamber for sample loading (load-lock), the outgassing chamber, an intermediate

chamber and the growth chamber.

### 2.1.1 Epitaxial growth

Molecular Beam Epitaxy is based on the three temperature law: the substrate surface temperature ( $T_s$ ) must be lower than the evaporation temperature of the III-element ( $T_{III}$ ) and larger than the evaporation temperature of the element V ( $T_V$ ) [9]. These conditions lead to a growth rate equal to the deposition rate of the III-element whereas V-element incorporates only in the presence of III-element, ensuring a stoichiometric composition. Based on these elementary components, III-V semiconductor thin layers are grown layer by layer on the surface of the wafer. One monolayer (ML) is relative to a complete layer of the compound III-V semiconductor in the direction normal to the substrate.

Effusion cells are used for the evaporation of group III elements (In, Ga and Al) with an atomic flux. The atomic flux of each component depends only on its evaporation temperature following an Arrhenius law [10]. The flux of each component is then controlled by its heating temperature.

The flux of group V elements (As, Sb) is produced with cells evaporating antimony and arsenic from solid state to  $As_4$  and  $Sb_4$  molecules. These molecules can be dissociated to As and  $As_2$  or Sb and  $Sb_2$  by passing through a high temperature cracking zone. The flux is then adjusted by tuning the opening of valves. In our experiments, the cracking zone of the arsenic cell is heated to 600°C, which is sufficient to avoid condensation of  $As_4$  molecules in the cracking zone but not enough to decompose them. For antimony, the 900°C temperature of the cracking zone ensures a decomposition of  $Sb_4$  molecules into  $Sb_2$  and Sb species. Moreover, arsenic  $As_2$  and phosphorus  $P_2$  fluxes can also be obtained by cracking respectively arsine  $AsH_3$  and phosphine  $PH_3$  using a High Temperature Injector (HTI).

The geometry of the growth chamber imposes that the evaporation cells are tilted with respect to the substrate surface. Therefore, the sample holder is rotated during the growth to ensure uniformity of the layer thickness and composition over a whole two-inch wafer.

The sample temperature is measured with different tools. The first one is the thermocouple that measures the sample holder temperature. Although, the thermocouple does not measure the real sample temperature, it allows the control of the sample heating by the radiation of a filament heater. The second tool is the pyrometer, that measures radiation coming from the sample. The displayed temperature during growth can be slightly affected by some parasitic

radiations coming from different cells. Finally, a KSA BandiT system allows the temperature measurement of the substrate by identifying the optical absorption threshold of the sample.

### 2.1.2 Growth control with Reflexion High Energy Electron Diffraction (RHEED)

The MBE system is equipped with a RHEED system (the RHEED screen can be seen in the yellow box in Figure 2.1 (a)). Theoretically, the RHEED diagram corresponds to the projection, on a plane screen, of the intersection image of the surface reciprocal lattice and the Ewald sphere of radius  $\frac{2\pi}{\lambda}$ , where  $\lambda$  is the electron De Broglie wavelength. Thanks to this technique, real time feedback on the surface reconstructions during growth is obtained. More than that, the RHEED is useful not only during sample growth or wafer deoxidization to detect surface reconstructions, surface roughness and crystalline state (amorphous, polycrystalline, monocrystalline) [11], but it is also used for element flux calibration. In order to calibrate indium growth rate for example, we use an InAs (100) wafer, on which oscillations of the specular beam intensity are monitored during the growth of InAs at a fixed In evaporation temperature (Figure 2.2). The period of these oscillations corresponds to the completion of one monolayer. Arsenic flux during the growth must be sufficiently high to ensure a layer-by-layer growth regime [12]. In order to calibrate the As flux, we set the In temperature to fix the growth rate and reduce the As flux to determine the critical flux below which the growth rate is reduced. At this point, stoichiometry is no more ensured meaning that effective As flux is just below the In one. To get a reliable measurement, this experiment must be performed at a temperature where As re-evaporation rate is quite low. With this RHEED oscillation method, the different III- and V-element fluxes can be calibrated. Similarly, a GaSb substrate is used to calibrate the Sb flux. In the following, the flux of the different elements are expressed in monolayer/s (ML/s), referenced to a (100) surfaces, as determined by this method.

The RHEED gun energy in this study is 20 kV.

The next part is dedicated to the presentation of the selective area growth procedure, where the deposition of III-V elements takes place in precise zones of the substrate allowing the direct epitaxial growth of one dimensional in-plane nanowires on a substrate.



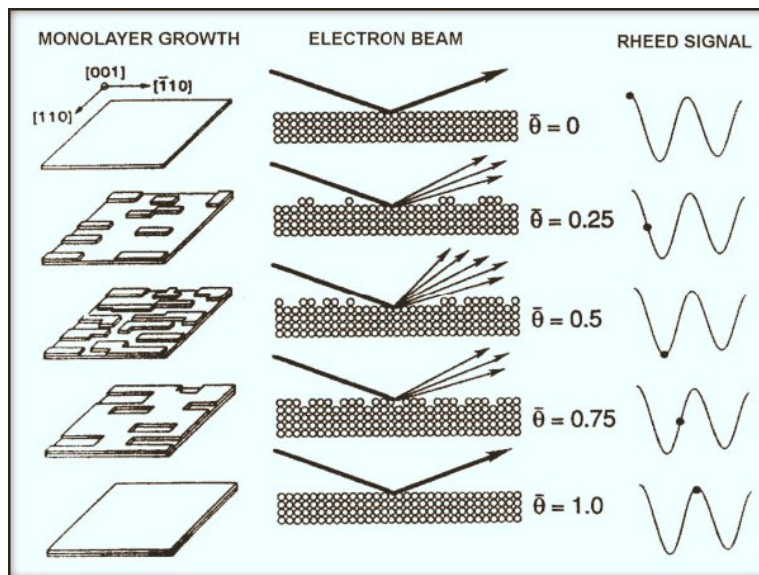


Figure 2.2 – The RHEED oscillations principle [12].

## 2.2 Definition of the mask

The sample preparation for selective area growth starts with the deposition of a dielectric film on the wafers. Most of the wafers used during this work consists of 2-inches InP wafers. The film is patterned and etched using lithography and RIE to form a mask in order to limit the lateral extent of the growth in the openings of the mask. These steps are illustrated in Figure 2.3. Later on, the samples are loaded into the MBE system where the epitaxial growth takes place.

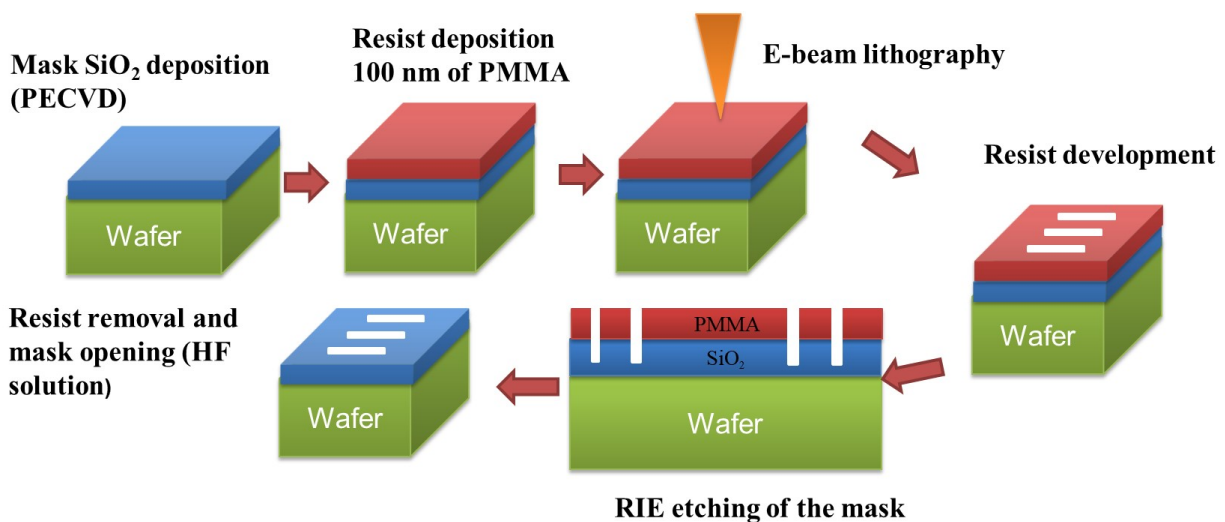


Figure 2.3 – Sketch of the different steps for the mask preparation that is used for selective area growth.

In more details, a 30 nm-thick  $\text{SiO}_2$  layer is deposited by Plasma Enhanced Chemical Vapor



Deposition (PECVD) at 300°C, using an OXFORD Plasmalab 80 plus system. Then, a 100 nm-thick PMMA 3% 495K photoresist is spin coated and heated at 180°C for 30 minutes in order to evaporate the solvent. The mask opening dimensions, geometries and positions are defined on the wafers by e-beam lithography. Figure 2.4 displays an example of a designed layout that was prepared for in-plane InAs and InSb nanowires selectively grown on InP (111) wafer. The layouts are prepared using the Layout Editor software [13]. These nanowires will be discussed respectively in chapter 3 and chapter 5.

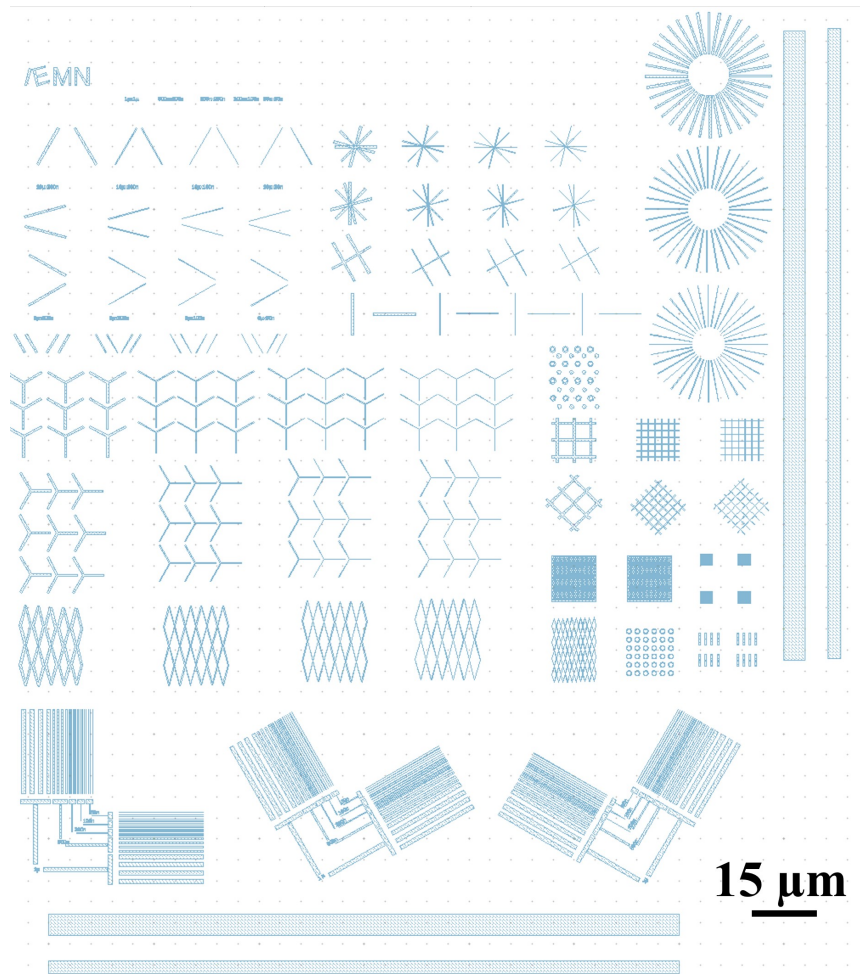


Figure 2.4 – Layout of the selectively grown nanostructures designed for the 4P measurements. More details about the layout are given in Figure A.6 in the Appendix 2

Figure 2.4 shows different patterns consisting of isolated 5  $\mu\text{m}$  or 10  $\mu\text{m}$ -long nanowires with multiple orientations. Five different widths were selected: 500 nm, 200 nm, 100 nm and 50 nm for each array of nanowires having a similar geometry. The 230  $\mu\text{m}$  x 200  $\mu\text{m}$  layout contains also more complex nanowire networks with more than one orientation and nanowire width. Figure A.6(b) presents a “sun-like” pattern where the nanowire orientation is sequentially tilted by 10°. This pattern will give information about the nanowire growth behaviour depending on the crystallographic orientations. Figure A.6(c) shows series of 20  $\mu\text{m}$ -long

rectangles with different widths: 1  $\mu\text{m}$ - (rectangles 1 to 4 from the left), 500 nm (5 to 8), 200 nm (9 to 12), 100 nm (13 to 16) and 50 nm (17 to 20). The first serie is parallel to the IEMN pattern in Figure A.6(a) and, thus, has the  $[0\bar{1}1]$  crystallographic orientation, whereas the second one is designed to be perpendicular. For a straightforward identification of the crystal direction, the IEMN pattern is always parallel to the wafer flats. The whole patterns are repeated every 3 mm on the sample. The exposure dose is 280  $\mu\text{C}/\text{cm}^2$ . After the writing process, the PMMA resist is developed in a methyl isobutyl ketone-Isopropanol MIBK/ IPA (30/60) solution for 90s.

As described in the sketch of Figure 2.3, the next step consists in etching the  $\text{SiO}_2$  film in the openings defined in the PPMA resist using Reactive Ion Etching (RIE) inside an OXFORD Plasmalab 80 system. Prior to the mask etching, a short  $\text{O}_2$  plasma is first used to clean the mask openings from residual resist. Then, the samples are exposed to a  $\text{CF}_4(20\text{sccm})/\text{CHF}_3(20\text{ sccm})/\text{Ar}(10\text{ sccm})$  plasma for 54s, which ensures a vertical etching of the  $\text{SiO}_2$  mask. The RF power is set at 100W and the chamber pressure during etching is around 50mTorr. Based on these conditions, the aperture depth is about 10 to 20 nm. The remaining resist that still covers the mask is, after that, removed by dipping the sample in an acetone solution at 50°C, followed by an ultrasonic bath for 5 min. After isopropyl alcohol cleaning, the sample is finally exposed to an  $\text{O}_2$  plasma for 30s to clean the whole  $\text{SiO}_2$  surface.

### 2.3 Control of the mask openings

Before loading the wafer into the MBE system, a wet etching step in diluted hydrofluoric acid (HF 1% solution) is necessary to complete the opening of the mask windows. However, as HF etching is an isotropic etchant, the  $\text{SiO}_2$  openings are etched in all directions during this step. This leads to an enlargement of the mask openings, which can depend on the wafer chemical composition. Optimizing the wet etching time of the mask is, therefore, essential to obtain in-plane nanowires with well-defined widths close to the nominal dimensions of the layout.

The dependency of the wet etching time to the wafer composition, thickness and conductivity is studied based on InSb(100) and InP wafers. On these wafers, a 30 nm-thick  $\text{SiO}_2$  mask is deposited and processed with the condition described above, except for wet etching time, which is finely tuned.

Figure 2.5(a) displays a SEM top view of the  $\text{SiO}_2$  mask opening obtained on a p-doped InSb (100) wafer after 30s HF etching. The mask opening of the cross pattern shows irregular edges

in both  $[1\bar{1}0]$  and  $[110]$  directions. While the nominal width of these apertures is 100 nm, this SEM image shows an opening width around 150 nm. Based on the image contrast, a brighter grey surface surrounds the mask apertures, indicating an etching of the InSb native oxide layer underneath, which extends to 350 nm. The accumulation of top and bottom etching of the  $\text{SiO}_2$  layer leads thus to the enlarged aperture and HF treatment needs to be shortened. Figure 2.5(b) is a SEM image of the mask aperture for a p-doped InSb (100) wafer after 20s of etching. The opening seems regular in the mask image contrary to the irregular etching behaviour seen in Figure 2.5(a). The aperture opening width is 115 nm close to 100 nm-wide nominal aperture. The InSb etching underneath persists but is limited to a width of 160 nm.

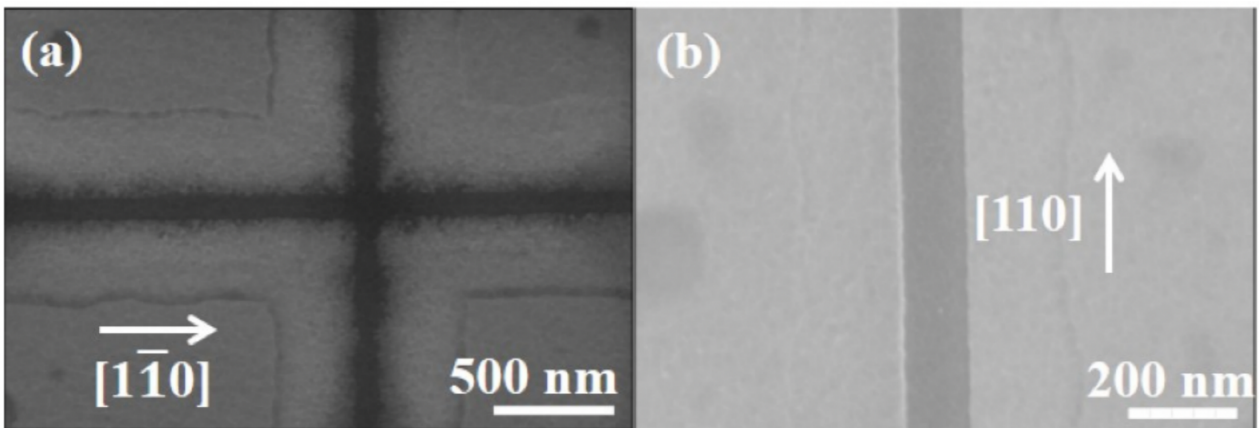


Figure 2.5 – Influence of a wet etching time on the mask aperture for (a) an InSb(100) wafer after 30s of etching, (b) an InSb(100) wafer after 20s of etching.

Figure 2.6(a) displays the mask opening of a cross pattern on a semi-insulating InP(111) wafer after 27s of wet etching. This image shows a regular mask profile at the edges. Based on the contrast, the mask seems well etched in the aperture. The real width of the apertures is around 75 nm in both directions, which is close to the 50 nm nominal width. 27s of wet HF etching is therefore enough for creating openings in  $\text{SiO}_2$  deposited on an InP(111) wafer and will be the selected etching time for the preparation of all the studied nanostructures presented in the chapter 3 and chapter 5. However, as shown in Figure 2.6(b), the apertures obtained after 30 s for a cross written in  $\text{SiO}_2$ , this time, deposited on a semi-insulating InP (100) wafer is not fully opened i.e the mask is not totally removed from these windows. 30s is not enough for the mask opening for a  $\text{SiO}_2$  layer on an InP(100) wafer. Therefore, as several parameters may impact the dry etching rate (conductivity and size of the wafer for instance, small variations in the  $\text{SiO}_2$  film thickness, etc.), the chemical etching duration has to be optimized for each process.

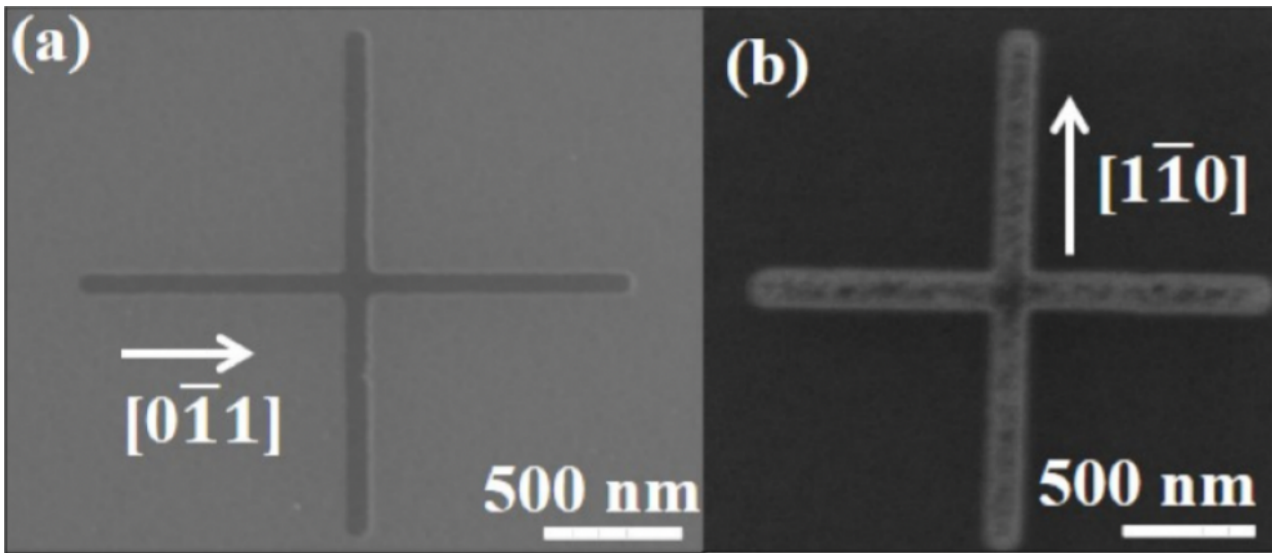


Figure 2.6 – Influence of a wet etching time of 30 s on the  $\text{SiO}_2$  mask aperture for two different wafer orientations: (a) an InP (111) wafer and (b) an InP (100) wafer. The nominal width of the mask aperture is 100 nm.

## 2.4 Selective Epitaxial growth

After the mask opening step, samples were loaded in the introduction chamber of the MBE system, then outgassed, generally at  $150^\circ\text{C}$ , for 1h. They were subsequently transferred to the III-V growth chamber. Thanks to the atomic hydrogen flux used during selective growth, the III and V elements form III-V compounds only in the mask openings and are re-evaporated outside, on the  $\text{SiO}_2$  protective layer[8].

As a selective growth example, a homoepitaxy of 50 nm-thick in-plane InSb nanowires is shown in Figure 2.7. In this case, the InSb (100) wafer was deoxidized under Sb flux with an atomic hydrogen flux exposure for 1 min while rising the substrate temperature to  $390^\circ\text{C}$ . Following previous works performed at IEMN on selective growth of InSb [14], an InSb layer with a nominal thickness of 50 nm was grown under atomic H flux with a growth rate of about 0.2ML/s, a Sb/Ga flux ratio of 10 (Sb flux is 2ML/s) and a growth temperature of  $390^\circ\text{C}$ .

Figure 2.7 displays SEM images of InSb nanostructures. The number of bright nanoparticles on the  $\text{SiO}_2$  mask is quite small and indicates a good selectivity. Moreover, these images show that, whatever the in-plane crystal orientations are, the nanowires are continuous along the different orientations. Their length extends up to 10  $\mu\text{m}$ . Figure 2.7(d) displays a honeycomb lattice. This SEM image shows that complex nanostructures can be built by the selective area growth (SAG) method with high quality.



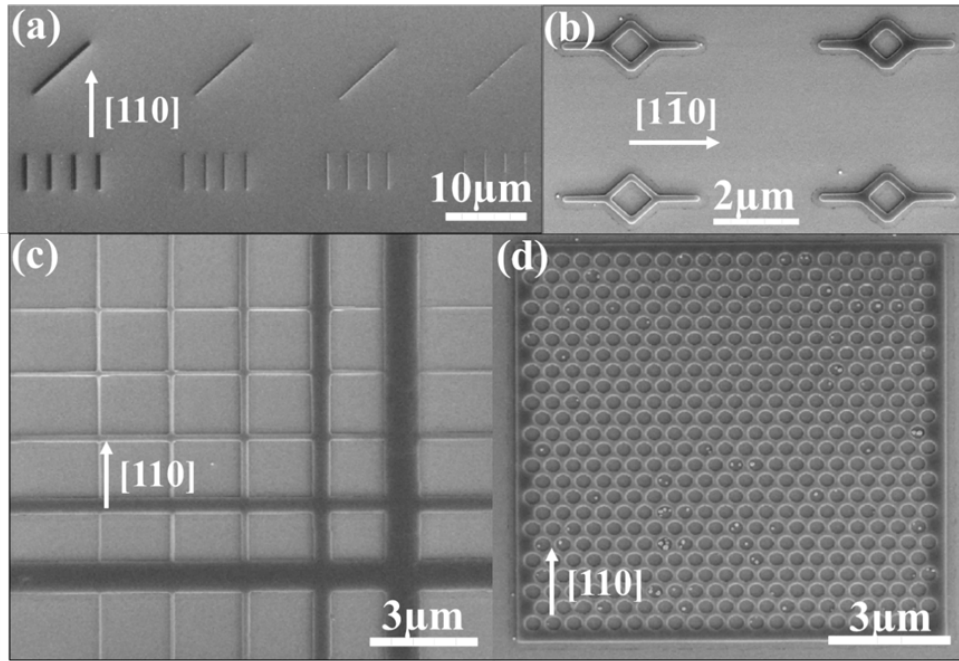


Figure 2.7 – SEM images of selectively grown InSb nanostructures on an InSb (100) substrate: (a) NWs (500nm, 200nm, 100nm and 50nm nominal widths (left to right)) with [110] and [100] orientations; (b) Aharonov-Bohm ring InSb nanostructures; (c) grid with 50nm, 100nm, 200nm and 500nm-wide NWs (left to right and top to bottom view); (d) honeycomb lattice.

## 2.5 Contact deposition for cryogenic measurements

For the macroscopic transport measurements, metallic contacts deposition on the nanowires is needed in order to allow wire bonding. This process concerns only the InAs/GaSb nanowires prepared for cryogenic measurements (See chapter 4, section 3.4), as transport in the other nanostructures will be investigated with the multiple probe STM only. Metallic patterns were prepared on the SiO<sub>2</sub> mask after the deposition of the SiO<sub>2</sub> layer and before the nanowire growth. They are used as alignment markers. 8μm x 8μm pads consisting of Ti (5 nm)/Pt (50 nm) bilayer are deposited for that. After the selective growth of the nanowires, metal pads composed of a Ti (100 nm)/Au (400 nm) bilayer are deposited as contacts to the nanowires. For this purpose, a standard lift-off process is performed. It starts with two different resist layers deposition on top of each other: a first layer of ARP-33% covered by a second layer of PMMA 950K 4%. After their uniform spreading on the surface by spin coating, the resists are annealed at 180°C for 3 min to become solidified. Then, the patterns, designed with layout editor, are written using the EBL technique with an exposure dose of 220 μC/cm<sup>2</sup>. The resists are subsequently developed in a (MIBK/IPA: 70 mL/70 mL) solution for 90s. The use of a double layer of resists gives an undercut profile that avoids the coating of the resist sidewalls when evaporating the metals to ensure a good lift-off procedure. After the metal deposition,

a lift-off process takes place for 2 hours in a SVC-14 solution at 70°C followed by 1 min of sonication for the remaining metal and resist removal.

### 3 Scanning Tunnelling Microscopy

Sixty years after the discovery of the wave-particle duality by Louis de Broglie in 1924, Gerd Binnig and Heinrich Rohrer built the first scanning microscope based on the tunnelling effect, called Scanning Tunnelling Microscope (STM). This invention was part of a project that they called the idea that “normally should never had worked” [15]. This impossible idea got them a Nobel prize in 1986 and induced a real revolution in the microscopy field as it pushed-up the microscope resolution to the atomic scale (Angstrom scale) as well as its capacity to investigate the electronic state of conductive materials surfaces.

The quantum mechanics, that is linked to the wave particle duality, is the essence of the STM principle. In classical mechanics, given two electrodes separated by a thin potential barrier, an electron with an energy lower than the potential barrier has a zero probability to cross it. However, this phenomenon is allowed in quantum mechanics, the electron having a non-zero probability to tunnel through the barrier. This phenomenon is called the tunnelling effect. Here, the electron is described as a wave function defined as an evanescent wave inside the barrier and as a progressive wave in each of the electrodes. In STM, the two electrodes consist of a metal tip and the surface of a conductive sample. They are separated by an insulator (vacuum) with a thickness  $d$  of a few angstroms, which corresponds to the (potential barrier) (Figure 2.8).

#### 3.1 Tunnelling current

Based on Figure 2.8, let us consider the variation of the potential as follows:

$$V(z) = \begin{cases} 0 & \text{for } z < 0 \text{ (region I)} \\ V_0 & \text{for } 0 < z < d \text{ (region II)} \\ 0 & \text{for } z > d \text{ (region III)} \end{cases} \quad (2.1)$$

An electron verifies the Schrödinger equation:

$$\left[ -\frac{\hbar^2}{2m} \frac{\partial^2}{\partial z^2} + V(z) \right] \psi(z) = E\psi(z) \quad (2.2)$$

where  $\hbar$  is the reduced Planck constant,  $m$  is the electron mass.

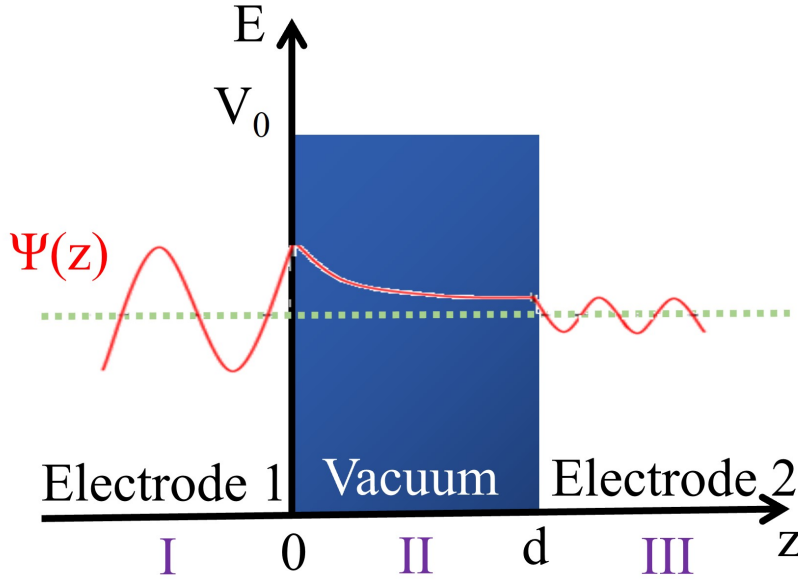


Figure 2.8 – Principle of the tunneling effect through a potential barrier (vacuum).

If we assume an electron with an energy  $E$  lower than the potential barrier height  $V_0$ , then the solutions of this equation in the three different regions I, II, III write as:

$$\psi(z) = \begin{cases} A_I e^{ikz} + B_I e^{-ikz} & \text{for } z < 0 \quad (\text{region I}) \\ A_{II} e^{pz} + B_{II} e^{-pz} & \text{for } 0 < z < d \quad (\text{region II}) \\ A_{III} e^{ikz} & \text{for } z > d \quad (\text{region III}) \end{cases} \quad (2.3)$$

Here,  $A_I$ ,  $A_{II}$ ,  $A_{III}$ ,  $B_I$  and  $B_{II}$  are constants.  $k$  equals to  $\sqrt{\frac{2mE}{\hbar^2}}$  and  $p$  is equal to  $\sqrt{\frac{2m}{\hbar^2}(V_0 - E)}$ .

Taking into account the boundary conditions for  $z = 0$  and  $z = d$ , we can deduce the transmission coefficient that is given by:

$$T(E) = \left. \frac{|A_{III}|}{|A_I|} \right|_{z=d} = \frac{1}{1 + \frac{1}{4E} \frac{V_0^2}{(V_0 - E)} \sinh^2 \left[ \sqrt{\frac{2m(V_0 - E)}{\hbar^2}} \cdot d \right]} \quad (2.4)$$

If we assume  $pd > 1$ ,  $T$  can be simplified to:

$$T \approx 16 \frac{E(V_0 - E)}{V_0^2} e^{-2pd} \quad (2.5)$$

The electron transmission from electrode 1 to electrode 2 depends exponentially on the distance  $d$ , with  $p$  being the vacuum decay constant, about  $10 \text{ nm}^{-1}$  for typical work functions.

The net tunnelling current depends on the total number of sample and tip surface electronic states that overlap within the energy range for which tunnelling can occur. Therefore, if a small and constant bias is applied across the electrodes, it shows an exponential variation with the separation between the tip and the sample. When a positive bias voltage is applied to the sample (or conversely, a negative voltage is applied to the tip), electrons in occupied states on the tip can elastically tunnel into the energy equivalent empty states of the sample. Similarly, a negative sample bias allows electrons occupying filled states on the surface to tunnel into empty states on the tip.

In the STM system, a metallic tip (in our case made up of tungsten W), acting as a probe electrode, is pushed down close to a semi-conductive surface by means of piezoelectric tubes. As explained above, it is necessary to apply a polarization voltage (sample bias) in order to obtain a tunnelling current for a sample-tip distance around 1 nm.

Measurements may take place in two different modes. The first one deals with the feedback off mode. Here, the sample-tip distance  $d$  is fixed, around several angstroms. The measured current variations as a function of the bias provides information on the density of electronic states. The second mode corresponds to the feedback on mode. In this case, the tunnelling current is maintained fixed and generally in the range of tens of picoamperes. While laterally scanning the surface of the sample, the tip accurately follows the topography of the surface. By recording the variation of the piezoelectric tubes along the vertical axis, the height variations  $\Delta z(x, y)$  of the sample can be plotted. This is the imaging mode most widely used. The displayed data in chapter 5 are acquired using this approach.



### 3.2 Tip preparation

In our case, tungsten tips are used for STM and also multiple probe transport measurements. They are obtained after a chemical etching of W wires inside a sodium hydroxide (NaOH) solution. The wire is surrounded by a circular cathode as illustrated in Figure 2.9(a). A DC voltage is applied to drive the electro-chemical reaction described as follows:

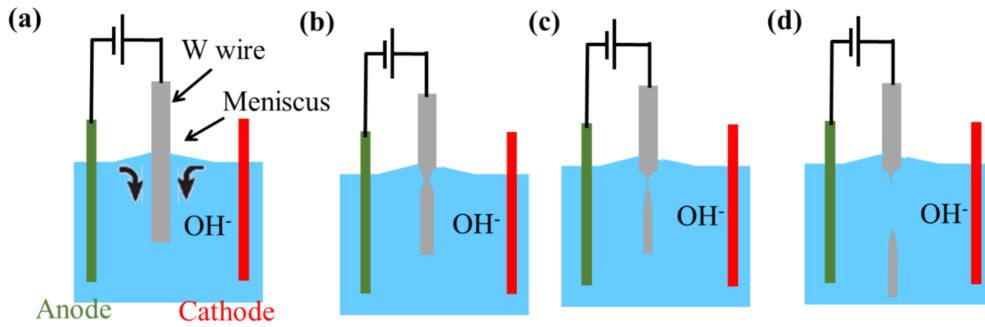
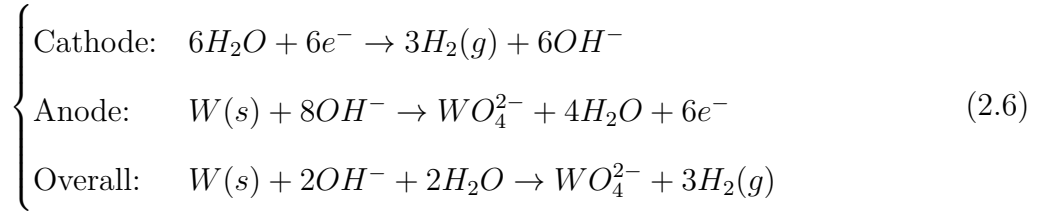


Figure 2.9 – Illustration of the tip etching method. (a) Formation of the meniscus. (b) Wire etching mostly in the meniscus region and the necking phenomenon. (c) The tip sharp apex starts to appear by continuous etching of the lower part. (f) The lower part breaks off producing a sharp tip.

Figure 2.9(b) and 2.9(c) show the etching of the W wire at the meniscus promoted by the capillary forces. As the etching rate at the top of the meniscus is higher than at the bottom of the wire, a necking shape is obtained. The reaction ends at the breakpoint observed in Figure 2.9(d) when the etched part of the wire becomes too thin and its lower part cannot be sustained by the tensile strength. This part falls in the solution and a sharp tip is obtained. A highly sharp tip is necessary to achieve atomic resolution when scanning. For contact measurements inside the 4P-STM system, that will be discussed later, tips with an apex curvature of some tens of nanometers (Figure 2.10) allow good contacts on 2D layers, 100 nm-wide and 200 nm-wide nanowires. After being introduced inside the STM system in an UHV environment, the tips are heated to remove any surface oxides that may have formed. This heating process not only cleans the tip but also ensures its stability for accurate measurements. This step is

controlled by the pressure variations inside the chamber. After the heating phase, the tips are "flashed" several times; this involves momentarily heating the tip to a high temperature and then allowing it to cool rapidly. Flashing serves to further clean the tip and remove any remaining contaminants, thereby ensuring that the tungsten tip is in optimal condition for high-resolution scanning.

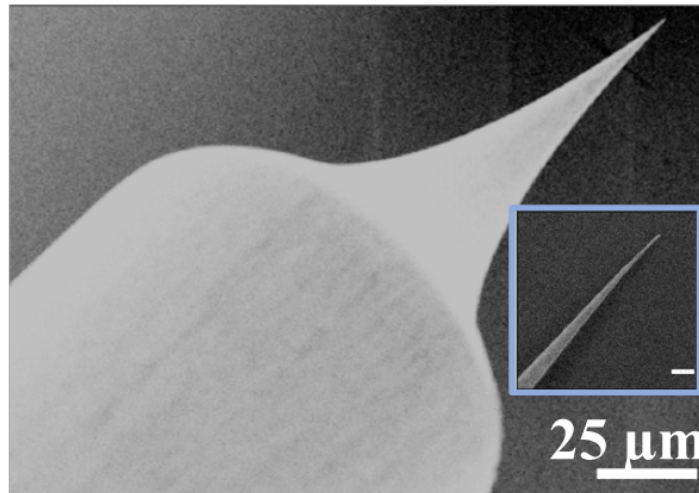


Figure 2.10 – SEM image of the tip apex, the inset shows a zoom of the apex. The scale in the inset image is 2μm.

### 3.3 Omicron LT-STM

The Low Temperature-Scanning Tunnelling Microscope LT-STM used in this work was developed by Omicron GmbH. It is located at the Institut Supérieur d'Electronique et du Numérique (ISEN-JUNIA).

Based on Figure 2.11, this LT-STM system is composed of three main chambers separated by gate valves. The load-lock chamber (Blue box in Figure 2.11) allows the samples and tips introduction to the system after being kept in a vacuum storage. This chamber is pumped with a turbomolecular pump to reach a pressure of about  $10^{-8}$  Torr. Samples are outgassed in this chamber at 120°C for few hours. Thanks to a transfer rod, samples and tips can be transferred to the preparation chamber delimited by the orange box in Figure 2.11. In this chamber, they are treated and stored. Pressure inside the preparation chamber is around  $10^{-10}$  Torr. The UHV is maintained thanks to an ionic pump and Titanium Sublimation Pumps (TSPs).

Generally, the sample surfaces are protected with a capping layer to preserve them from oxidation. The capping layer can be sublimated by heating the samples on the manipulator

of the preparation chamber. When samples are not capped, their surface is oxidized. The desorption of the oxide layer is achieved by means of simultaneous heating and atomic hydrogen eroding with an ion gun.

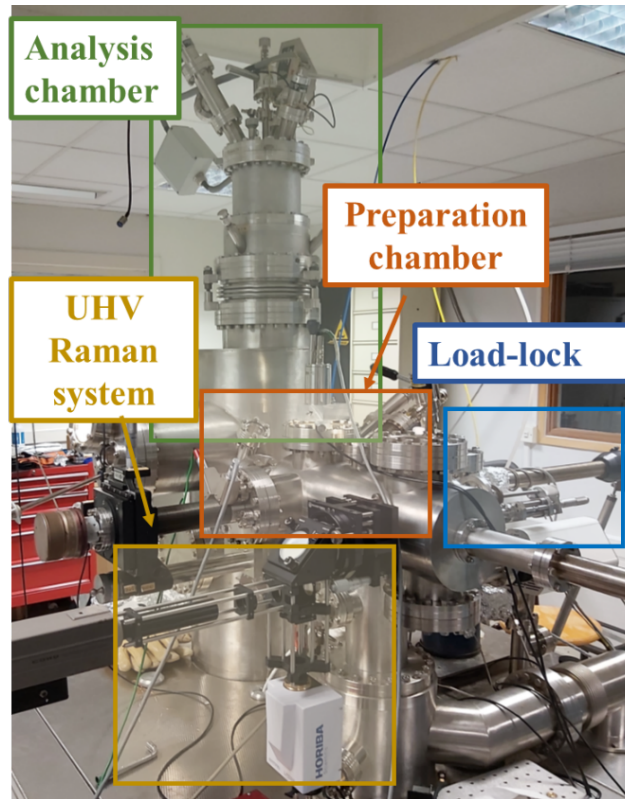


Figure 2.11 – Photograph of the LT-STM system.

In our case, InSb (100) and InSb (111) surfaces were deoxidized by annealing the samples respectively at 200°C and 300°C and sputtering their surfaces with atomic hydrogen from an ion gun with an acceleration voltage of 1.5 kV. The temperature was measured with a pyrometer and the deoxidation process was monitored with mass spectroscopy. This chamber is also equipped with an UHV Raman system (Yellow box in Figure 2.11). The laser beam of Raman spectroscopy emits at 532 nm. It is sent through an optical fiber to a superhead, fabricated by Horiba, and focused on the sample by an aspheric lens (AL108-B, Thorlabs). The UHV Raman systems is used to study the evolution of the sample surfaces when the oxide layer must be desorbed, as it will be presented later in chapter 5.

After that, the samples are introduced inside the analysis chamber defined by the green box in Figure 2.11. This chamber is maintained at  $10^{-11}$  Torr. It is equipped with a STM host in a cryogenic system consisting of an outer cryostat and an inner one. The outer one acts as a shield for the inner one. It is only filled with nitrogen when the inner cryostat can be filled either with nitrogen or helium depending on the desired temperature for cooling down the sample (77K or 5K respectively). Our samples were studied at 77K only. The piezoelectric

tube scanner is responsible for manipulating the tip-to-sample distance with atomic accuracy.

It holds the tip, which is connected to the preamplifier, one of the key element of the feedback loop controller facilitating real-time adjustments of the tip position based on measurement of the tunnelling current. For the coarse approach mechanism, a stepper motor is employed, capable of positioning the tip within a range of a few  $\mu\text{m}$  to the sample surface. This manual approach in the Z direction was monitored by means of a CCD camera. Once the tip is sufficiently close to the surface, the tunnelling approach is made to set the tip close enough to the surface by combining sequential displacements of both the piezoelectric tube and the coarse motor, thanks to the STM control system, a Nanonis controller designed by Specs GmbH.

## 3.4 Four-Probe-STM (4P-STM)

### 3.4.1 Technical description

The Nanoprobe system at IEMN was developed by Omicron (Figure 2.12). Similarly to the LT-STM system, it is composed of a load-lock chamber (grey box in Figure 2.12) in order to transfer the samples and tips into UHV. Both samples and tips can be stored inside the preparation chamber (blue box in Figure 2.12) and processed there. For example, the capped InAs (111) NWs studied in chapter 3 were annealed inside the preparation chamber at  $320^\circ\text{C}$  for 2h in order to sublimate the protective As cap before being transferred by means of a long transfer rod (yellow box in Figure 2.12) to the analysis chamber (orange box in Figure 2.12). Also, the W tips are deoxidized by direct current heating on the same manipulator. The multiple-probe STM is located in the analysis chamber. It is combined with a SEM (green box in Figure 2.12), that is pumped with its own ion pump, allowing to reach pressures in the high  $10^{-11}$  Torr in the whole analysis chamber. The STM is composed of a movable sample stage surrounded by four scanners that can freely move the tips on the sample surface. Three of them are piezoelectric tubes on top of which the tips are fixed at the end of long arms, limiting the vertical stability of the probes. The fourth one consists of piezoelectric stack with a more compact tip holder, allowing the acquisition of atomically-resolved STM images. For the navigation of the four independent STM probe tips, simultaneous SEM imaging is indispensable. This enables a large field of view for probe coarse positioning as well as fine positioning and rapid localisation of nanometer-sized structures. However, a high SEM resolution requires to mechanically couple the STM to the chamber, which inevitably

degrades the performances of the STM.

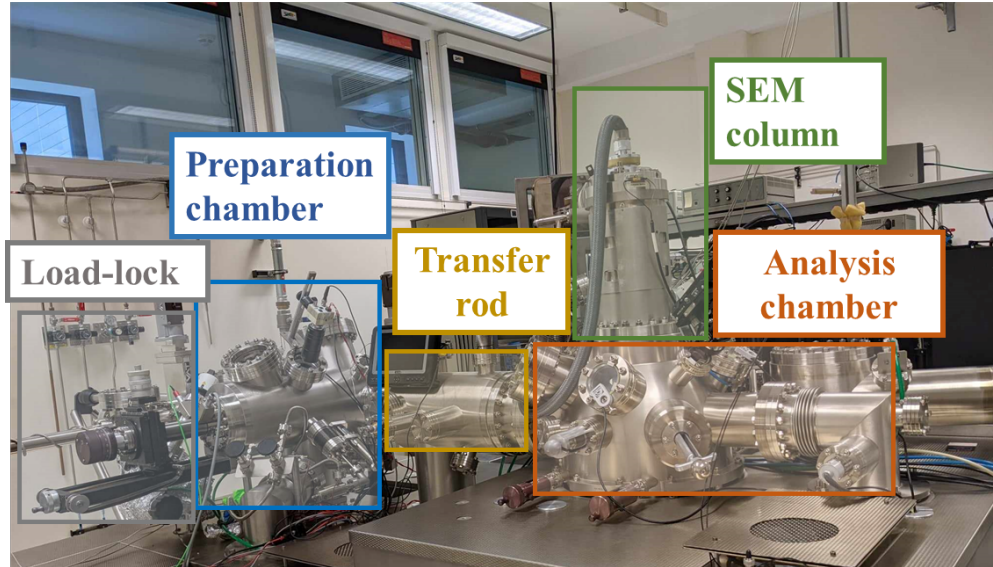


Figure 2.12 – Photograph of the 4P-STM system.

For the investigation of temperature-dependent behaviour of samples or devices, the Nanoprobe allows to work with sample temperatures up to 500 K by using an integrated solid-state heater and a Pt100 sensor for temperature measurement. Sample cooling down to 50 K was achieved with a LHe or LN<sub>2</sub> flow cryostat which is thermally connected by a copper braid. This fine braid also ensures mechanical de-coupling from vibrational noise. But as it is connected to the sample stage only, the tips are kept at room temperature, making the transport measurements tricky. For example, the thermalization of the tips to the sample temperature when in contact with a nanostructure may take a few hours. This may result in some contacting issues, such as a faster damage of the probes or noisy measurements. In this thesis, we cooled the stage with LN<sub>2</sub> to perform transport measurements at the minimum temperature of 115 K. Another difference with standard STM measurements resides in the use of substrates which are not necessarily conductive. For example, some of the investigated NWs were grown on semi-insulating InP and GaAs wafers. Thanks to the SEM, one tip can be electrically contacted to a NW to act as the electrical ground before the safe approach of the other tips. This configuration avoids a current flow through the substrate during the transport measurements.

### 3.4.2 Measurements of the resistance

To perform transport measurements, the probes were moved close to the sample with the coarse motors under the guidance of the SEM. The fine approach was performed using the

tunnelling approach of the STM control system. Once the tunnelling current was detected, the tip was further pushed down to the surface until a stable electrical contact was achieved. Figure 2.13 illustrates the four-probe arrangement inside the analysis chamber. The tip distance was controlled with piezoelectric motors operated by the Nanonis control system. Transport measurements take place with the electron beam off. Thanks to the use of switch boxes between the Omicron amplifiers and the microscope, the tips can be automatically disconnected from the Nanonis control system and connected to two Keithley source meters for 4P transport measurements. Prior to these measurements, 2P measurements between the different probes were usually performed to make the electrical contact valid and measure the contact resistances.

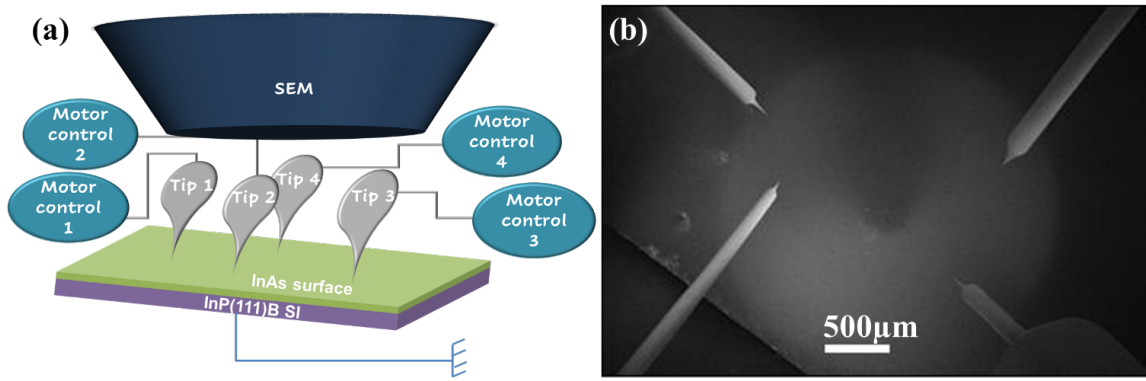


Figure 2.13 – (a) Representative scheme of the four-probe STM measurements inside the analysis chamber. (b) SEM image of the four probes closely approached to an InAs surface inside the analysis chamber of the four-probe STM.

## 2D thin films :

The principle of 4P-measurements consists in the injection and collection of a current with two probes and the measurement of the voltage across the two other probes, yielding the resistance of the layer by dividing the measured potential drop with the measured current. The advantage of the 4P-measurements is that the extracted resistance is independent of the contact resistances (Chapter 1). This can be achieved with an arbitrary arrangement of the tips on the sample as presented in Figure 2.14(a). The 4P-resistance of the 2-dimensional infinite sheet is then given by the following equation [16] :

$$R_{4P}(\vec{d}_1, \vec{d}_2, \vec{d}_3, \vec{d}_4) = -\frac{\rho_{2D}}{2\pi} \ln \left( \frac{|\vec{d}_3 - \vec{d}_4| \cdot |\vec{d}_2 - \vec{d}_1|}{|\vec{d}_3 - \vec{d}_1| \cdot |\vec{d}_2 - \vec{d}_4|} \right) \quad (2.7)$$

Where  $\rho_{2D}$  is the sample intrinsic sheet resistance.



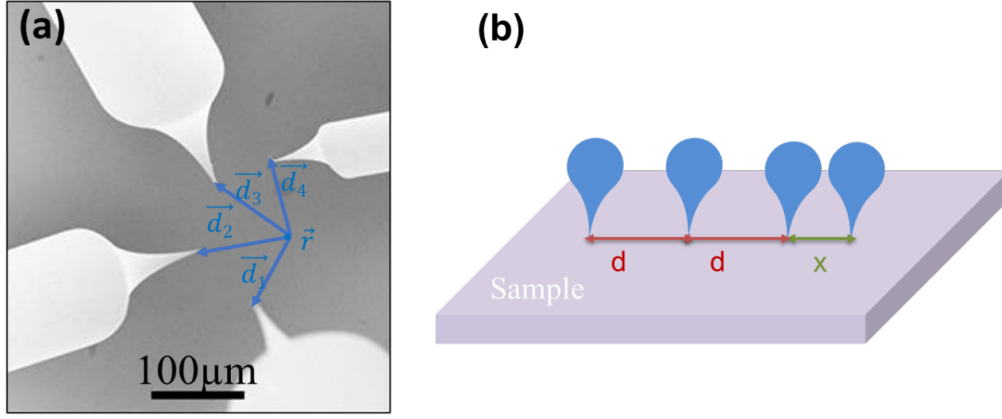


Figure 2.14 – (a) SEM image of four tips positioned in an arbitrary geometry on a sample. (b) 3D scheme illustrating four aligned non equidistant probes in contact with a sample.

In the case of four aligned but non-equidistant tips, where only one external tip is moved between the measurements, corresponding to the separation indexed  $x$  in Figure 2.14(b), while the separation  $d$  between the other tips is fixed, the 4P resistance becomes [16]:

$$R_{4P}(d, x) = \frac{\rho_{2D}}{2\pi} \left[ \ln\left(\frac{2x}{d}\right) - \ln\left(\frac{d}{x+d}\right) \right] \quad (2.8)$$

Finally, in case of four aligned and equidistant tips, where  $x = d$ , the 4P resistance of the 2-dimensional infinite sheet is given by [16], [17]:

$$R_{4P} = \frac{\ln(2)}{\pi} \cdot \rho_{2D} \quad (2.9)$$

Hence, with aligned equidistant-4-probe measurements, the resistance becomes theoretically independent of the interprobe distance  $d$  and such a method was used in this thesis to study the transport in a two-dimension electron gas of InAs thin films.

### Nanowires :

On NWs, the probes are always aligned. But, in contrast to thin films, only one inner tip is sequentially moved along the nanowire (Figure 2.15). As the probe in contact with the nanowire may create defects on its surface, we started all series of measurements with the largest possible separation between the inner probes. The 4P-resistance is then linearly dependent on the distance  $d$  [18] and is given by the following equation :

$$R_{4P} = \frac{\rho \cdot d}{S} \quad (2.10)$$

Where  $\rho$  is the nanowire resistivity and  $S$  is the nanowire transversal section.

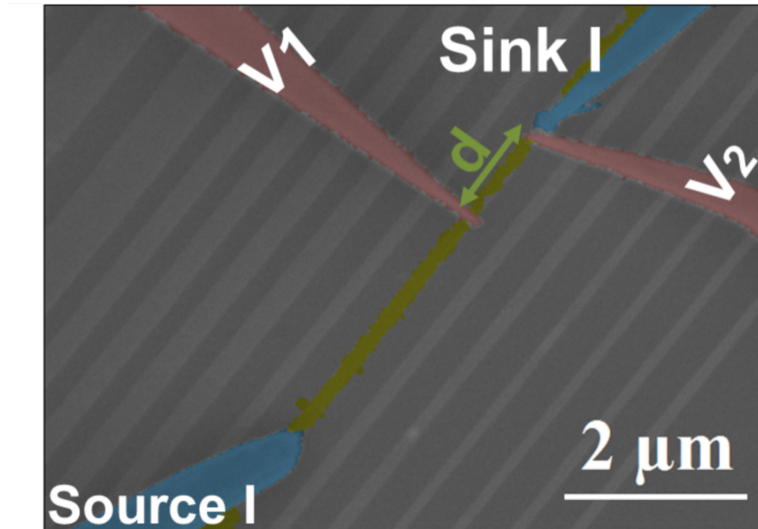


Figure 2.15 – (a) SEM image illustrating the 4P-STM measurements of an InAs nanowire. The current is injected by the source (blue) and the voltage is measured between the two inner probes (red tips). In this image the measured nanowire is coloured in yellow.  $d$  is considered as the varying distance between the two inner probes.

## 4 Atomic Force Microscopy AFM

Five years after the STM invention, Gerd binning, Calvin Quate and Christoph Gerber developed the Atomic Force Microscope AFM. This microscope gives the possibility to probe insulating wafers at the nanoscale [19]. The acquired data are collected by "feeling" or "touching" the surface with a mechanical probe. This nanoscale tip is attached to a small cantilever which acts as a spring. The tip interacts with the surface, causing a deflection of the cantilever, as shown in Figure 2.16(a). The bending of the cantilever is detected using a laser diode and a split photodetector. The force applied to the cantilever is adjusted using a feedback loop to keep the laser in the middle of the photodiode. While the tip scans the sample surface, it collects information on the topography. The two most known operating modes of the AFM are the contact mode and the tapping mode. In the contact mode, the tip is pressed into the surface and an electronic feedback loop monitors the tip-sample interaction force to keep the deflection constant throughout the scanning. The tapping mode, that is used during



this work, does not require a mechanical contact between the tip and the sample, strongly reducing the risk of damage. It is a resonant mode where the cantilever oscillates at high frequency near its resonance frequency. In this regime, the tip-sample interaction is driven by Van der Waals, electrostatic and capillary forces. It can be either attractive or repulsive. The registered topographic values are converted electronically to a pseudo 3D image which means that AFM give a pseudo-real images of samples topography. In air, the AFM has generally a vertical resolution of 0.1 nm and a lateral resolution around 10 nm due to the convolution effect [20].

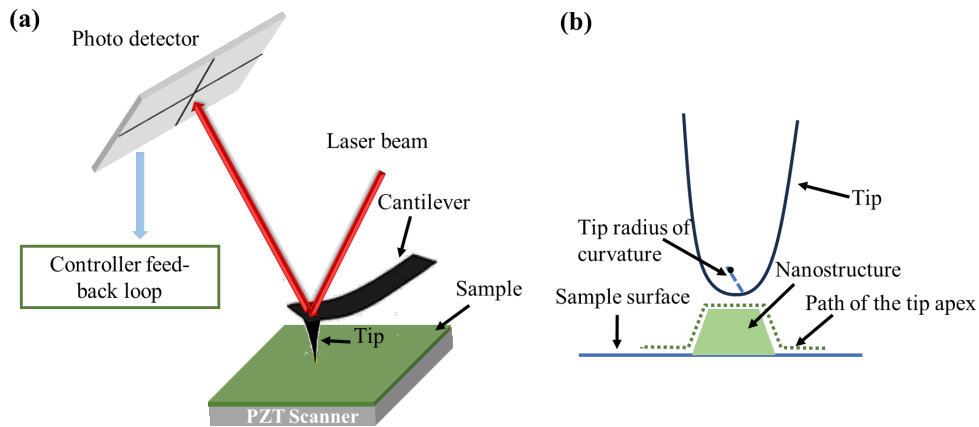


Figure 2.16 – Schematic representations of the (a) AFM scanning principle and (b) the convolution effect due to the finite size of the tip.

The AFM used in this work was the Veeco Dimension 3100. As the nanostructure dimensions are generally around some tens of nanometers, it was necessary to make sure that the tips were sharp enough to accurately measure the dimensions of the nanowires. In fact, images obtained by scanning a sample with an AFM tip are highly dependent on the AFM tip geometry and its radius of curvature, as shown in the Figure 2.16(b). AFM scans are an image of the convolution of the AFM tip and the surface. The smaller the surface features compared to the AFM tip dimensions, the less accurate the sample image on the computer screen is. In this case, the features may appear wider in AFM images and the hole may appear smaller. For all these reasons, NCHR-A silicon tips fabricated by Bruker with a radius curvature less than 10 nm (around 8 nm) were used during the experiments.

## 5 Hall effect measurements

Hall effect measurements are a direct application of the Hall effect discovered in 1879. The Hall resistance depends on the carrier mobility, concentration and the nature of the charge

carriers involved in the conduction:

$$R_{\square} = \frac{1}{n \cdot q \cdot \mu} \quad (2.11)$$

where  $R_{\square}$  is the sheet resistance,  $n$  is the charge density,  $q$  is the elementary electron charge, and  $\mu$  is the charge mobility. This technique allows the measurement of the sheet conductance in nano-films. In this work the Hall effect measurements in air were used for the transport study of the InAs nanostructures as a complementary tool to the 4P-STM. The experiments were performed with the HL5500 Hall setup located in the IEMN clean rooms. They required to build samples with appropriate geometries, corresponding to Hall-bars and van der Pauw microstructures (Figure 2.17(a)). After the epitaxial growth of 2D InAs-channel-heterostructures, a photoresist was deposited on the samples (AZ 1512). Then, the resist was exposed to the UV light through a chromium mask and subsequently developed in a MIF 726 solution. Then, the heterostructures were etched using a (HF/H<sub>2</sub>O<sub>2</sub>/H<sub>2</sub>O :1/1/200) solution. Finally, the remaining resist was removed in an acetone solution. Figure 2.17(a) shows examples of Hall bars and van der Pauw structures after the etching process. Figure 2.17(b) shows a 3D schematic representation of the etched samples. For ohmic contacts, In balls were deposited on the Mesa after being deoxidized in a HNO<sub>3</sub> solution for 1min and heated at 100°C for at least 30min. These indium balls were placed on the microstructures and heated to 200°C to allow In diffusion to the InAs channel (Figure 2.17(a)).

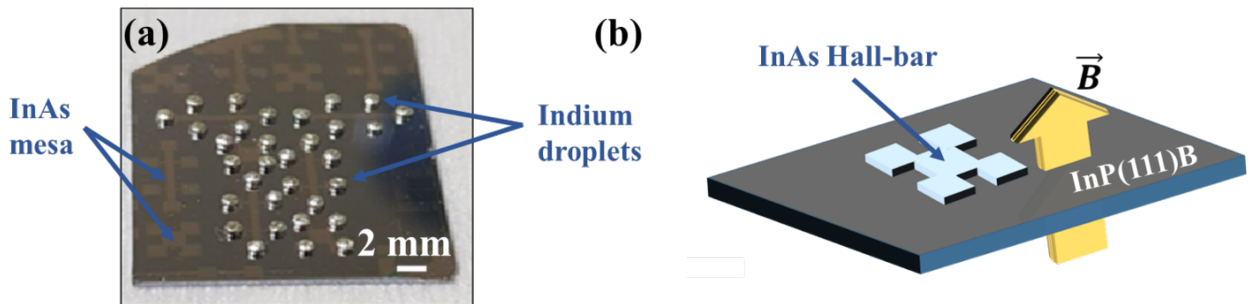


Figure 2.17 – (a) Etched sample with hall bars and van der Pauw microstructures. Indium balls (droplets) are deposited on the InAs mesa. (b) 3D scheme of samples B and C with InAs etched Hall bars.

During the Hall effect measurements a permanent magnetic field of 0.32 Tesla is applied to the sample. With these sub-millimetric sized structures, macroscopic probes can be well approached and positioned. The magnetic field is perpendicular to the plane of the electrical

lines running across the sample (Figure 2.17(b)). It generates a Lorentz force on the charge carriers that deflects them to one side of the Mesa. Measuring both the resistivity of the sample and the Hall voltage allow the determination of the Hall mobility and charge density inside the InAs layer. During this thesis, Hall bar InAs mesa were measured. The setup allows Hall effects measurements at RT and also at low temperatures. In our case, the transport properties of the samples took place at RT and also at 77K by cooling the sample in liquid nitrogen.

## 6 Complementary characterization techniques

During this work, a Gemini SEM developed by Zeiss was used to assess the quality of the etching process before growth and after growth to observe in-plane nanostructures. The high resolution SEM images allow to give insight into the growth mechanisms of the nanostructures. The applied focussed electron beam energy during measurement is 10kV and the in-lens imaging mode is used [21].

A X-ray diffraction (XRD) Panalytical system available at IEMN was also used to probe the structural quality of the 2D films. It permits the determination of the crystal lattice parameters and quantify the film relaxation in case of strained epitaxy.

Moreover, the TEM, STEM and EDX cross sectional analysis were used to investigate the structural and chemical composition of the nanostructures. For these studies extremely thin lamellas have to be prepared by ion milling of the nanostructures. This work has been done by David Troadec at IEMN. The TEM measurements were then performed by Gilles Patriarche in C2N. Information about the defects due to the lattice mismatch between the epitaxial layers and substrates and the shape of the core-shell nanostructures have been revealed by these studies.

Finally, the cryogenic magneto-transport measurements have been performed by Hermann Sellier at Néel Institute to probe the transport properties inside the in-plane InAs/GaSb nanowires grown on InP (Chapter 4).

## **7 Conclusion**

This chapter was dedicated to introducing the experimental techniques that will be pivotal in our upcoming analysis of nanostructures. Morphological characterizations, essential in understanding these transport properties, will be conducted using AFM, XRD, SEM, and TEM etc. For transport measurements, 4P-STM and Hall measurements will be used as complementary techniques, each offering unique insights. While Hall measurements will provide a macroscopic view of electrical properties in ambient conditions, 4P-STM will delve into their intrinsic transport properties within an UHV environment. This approach is expected to highlight the significance of nanowire passivation in differing environments.

Additionally, Raman spectroscopy, in conjunction with LT-STM, will be employed to study surface deoxidation processes. This ensemble of techniques, each with its specific strengths, is set to provide a comprehensive understanding of the nanostructures, laying the groundwork for the results and discussions in the following chapters.

## Bibliography

- [1] J. R. Arthur, ‘Molecular beam epitaxy’, *Surf. Sci.*, vol. 500, no. 1, pp. 189–217, Mar. 2002, doi: 10.1016/S0039-6028(01)01525-4.
- [2] V. Umansky, R. de-Picciotto, and M. Heiblum, ‘Extremely high-mobility two dimensional electron gas: Evaluation of scattering mechanisms’, *Appl. Phys. Lett.*, vol. 71, no. 5, pp. 683–685, Aug. 1997, doi: 10.1063/1.119829.
- [3] P. Aseev et al., ‘Ballistic InSb Nanowires and Networks via Metal-Sown Selective Area Growth’, *Nano Lett.*, vol. 19, no. 12, pp. 9102–9111, Dec. 2019, doi: 10.1021/acs.nanolett.9b04265.
- [4] S. Chuang, Q. Gao, R. Kapadia, A. C. Ford, J. Guo, and A. Javey, ‘Ballistic InAs Nanowire Transistors’, *Nano Lett.*, vol. 13, no. 2, pp. 555–558, Feb. 2013, doi: 10.1021/nl3040674.
- [5] J. Gooth et al., ‘Ballistic One-Dimensional InAs Nanowire Cross-Junction Interconnects’, *Nano Lett.*, vol. 17, no. 4, pp. 2596–2602, Apr. 2017, doi: 10.1021/acs.nanolett.7b00400.
- [6] Ö. Gül et al., ‘Ballistic Majorana nanowire devices’, *Nat. Nanotechnol.*, vol. 13, no. 3, pp. 192–197, Mar. 2018, doi: 10.1038/s41565-017-0032-8.
- [7] O. Kürtössy et al., ‘Parallel InAs nanowires for Cooper pair splitters with Coulomb repulsion’, *Npj Quantum Mater.*, vol. 7, no. 1, Art. no. 1, Sep. 2022, doi: 10.1038/s41535-022-00497-9.
- [8] M. Fahed, L. Desplanque, D. Troadec, G. Patriarche, and X. Wallart, ‘Selective area heteroepitaxy of GaSb on GaAs (001) for in-plane InAs nanowire achievement’, *Nanotechnology*, vol. 27, no. 50, p. 505301, Nov. 2016, doi: 10.1088/0957-4484/27/50/505301.
- [9] H. Freller and K. G. Günther, ‘Three-temperature method as an origin of molecular beam epitaxy’, *Thin Solid Films*, vol. 88, no. 4, pp. 291–307, Feb. 1982, doi: 10.1016/0040-6090(82)90169-9.
- [10] C. M. Yang and H. A. Atwater, ‘Selective solid phase crystallization for control of grain size and location in Ge thin films on silicon dioxide’, *Appl. Phys. Lett.*, vol. 68, no. 24, pp. 3392–3394, Jun. 1996, doi: 10.1063/1.116514.
- [11] W. Braun, ‘Monitoring surface roughness during film growth using modulated RHEED intensity oscillations’, *J. Cryst. Growth*, vol. 477, pp. 34–39, Nov. 2017, doi:

10.1016/j.jcrysgro.2016.12.082.

[12] ‘Reflection high energy electron diffraction’, Molecular Beam Epitaxy Research Group. [Online]. Available: <https://uwaterloo.ca/molecular-beam-epitaxy/facilities/epi-growth-and-monitoring/reflection-high-energy-electron-diffraction>

[13] ‘LayoutEditor the universal editor for GDSII, OpenAccess, OASIS... | LayoutEditor’. [Online]. Available: <https://layouteditor.com/>

[14] L. Desplanque, A. Bucamp, D. Troadec, G. Patriarche, and X. Wallart, ‘In-plane InSb nanowires grown by selective area molecular beam epitaxy on semi-insulating substrate’, *Nanotechnology*, vol. 29, no. 30, p. 305705, May 2018, doi: 10.1088/1361-6528/aac321.

[15] G. Binnig and H. Rohrer, ‘Scanning tunneling microscopy—from birth to adolescence’, *Rev. Mod. Phys.*, vol. 59, no. 3, pp. 615–625, Jul. 1987, doi: 10.1103/RevModPhys.59.615.

[16] B. Voigtländer et al., ‘Invited Review Article: Multi-tip scanning tunneling microscopy: Experimental techniques and data analysis’, *Rev. Sci. Instrum.*, vol. 89, no. 10, p. 101101, Oct. 2018, doi: 10.1063/1.5042346.

[17] I. Miccoli, F. Edler, H. Pfnür, and C. Tegenkamp, ‘The 100th anniversary of the four-point probe technique: the role of probe geometries in isotropic and anisotropic systems’, *J. Phys. Condens. Matter*, vol. 27, no. 22, p. 223201, May 2015, doi: 10.1088/0953-8984/27/22/223201.

[18] C. Durand et al., ‘Persistent enhancement of the carrier density in electron irradiated InAs nanowires’, *Nanotechnology*, vol. 24, no. 27, p. 275706, Jul. 2013, doi: 10.1088/0957-4484/24/27/275706.

[19] G. Binnig, C. F. Quate, and Ch. Gerber, ‘Atomic Force Microscope’, *Phys. Rev. Lett.*, vol. 56, no. 9, pp. 930–933, Mar. 1986, doi: 10.1103/PhysRevLett.56.930.

[20] ‘Fundamental Theory of Atomic Force Microscopy’. [Online]. Available: <https://nanoscience.gatech.edu/zlwang/research/afm.html>

[21] W. Zhou, R. Apkarian, Z. L. Wang, and D. Joy, ‘Fundamentals of Scanning Electron Microscopy (SEM)’, in *Scanning Microscopy for Nanotechnology: Techniques and Applications*, W. Zhou and Z. L. Wang, Eds., New York, NY: Springer, 2007, pp. 1–40. doi: 10.1007/978-0-387-39620-0\_1.

# 3

## Transport properties of oxidized and reconstructed InAs (111) nanostructures

### 1 Introduction

InAs exhibits very attractive transport properties for high speed low consumption electronic devices and quantum devices [1]–[3]. In order to take advantage of the high mobility usually encountered in this material, high-quality InAs thin films and 1D nanostructures are epitaxially grown on InP(111) wafers where the low surface energy promotes the growth of smooth InAs layers. The electric properties are then studied by in-situ 4-probe Scanning Tunnelling Microscopy (STM) that allows the intrinsic conduction measurements of nanostructures.

### 2 Optimizing growth conditions

In this section, the growth conditions of the InAs nanostructures are improved based on the study of the structural properties of the InAs layers.

## 2.1 Thin films

For each growth experiment in the MBE chamber, a maskless InP(111)<sub>B</sub> triangular wafer is mounted by indium bonding at the center of a two inches Si wafer. It is placed next to the patterned InP(111)<sub>B</sub> wafer described in the chapter 2. The growth of InAs on the InP(111)<sub>B</sub> surface is first characterized and the study of the film morphology will be used to further select optimized growth conditions for the NW growth.

### 2.1.1 Growth conditions

As the lattice mismatch between InAs and InP is about 3.3%, optimizing the growth conditions on the InAs nanostructures is the key point to avoid crystalline defects and dislocations that affect the transport properties inside the InAs film. Three samples are prepared to study the effect of the growth temperature and time on the InAs film morphology. The growth conditions of the samples are summarized in the following table.

Table 3.1 – Samples growth conditions

	<b>Sample A</b>	<b>Sample B</b>	<b>Sample C</b>
<i>Growth rate (ML/s)</i>	0.05	0.05	0.05
<i>As/In ratio</i>	120	120	120
<i>Temperature (°C)</i>	440	380	380
<i>Thickness (nm)</i>	10	10	30

Prior to the growth, the InP(111) wafers are introduced and outgassed in an ultrahigh vacuum chamber at 200°C for 1h and transferred to the III-V MBE growth chamber. Then, they are deoxidized under an As<sub>4</sub> flux combined with an atomic hydrogen flux for 30s at 470°C. The RHEED shows a (2×2) surface reconstruction at the InP (111) surface, which is predominantly terminated with As atoms [4]. Finally, the growth of the InAs film takes place and the InAs surface exhibits the same (2 × 2) surface reconstruction.

All samples are grown inside the MBE chamber with a 0.05 ML/s growth rate under an atomic hydrogen flux. The As/In ratio is set around 120. For the first sample that will be called sample A for better clarity, a 10 nm-thick InAs layer is epitaxially grown on the InP (111) surface at 440°C. The second sample, sample B, also consists of a 10 nm-thick InAs film but is grown at 380°C. The last sample, sample C, is grown with the same growth conditions as the sample B, but the thickness of the InAs layer is increased to 30 nm.



### 2.1.2 Morphology of the InAs surface

The surface morphology of the different samples is studied by SEM and AFM techniques, as illustrated in Figure 3.1. The SEM image of sample A, as seen in Figure 3.1(a), indicates that InAs initially nucleates by forming triangular islands that coalesce and merge. The presence of these islands is due to the lattice mismatch of InAs and InP. For a thickness of 10 nm, the islands cover about 50% of the InP surface. Their density is about  $0.06 \mu\text{m}^{-2}$ . An AFM image acquired at higher magnification (Figure 3.1(d)) shows that the grown InAs nanostructures consist of prisms with a triangular base and an average height of 20 nm. These islands are terminated at the top with triangular concentric terraces with a height of almost 5 nm. The total height is around 25 nm, hence, 10 nm higher than the intended nominal height.

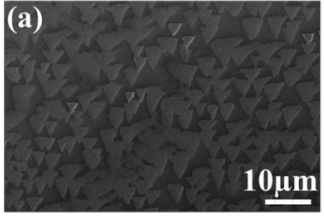
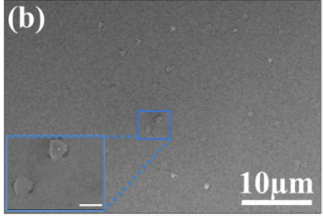
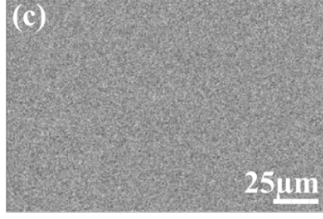
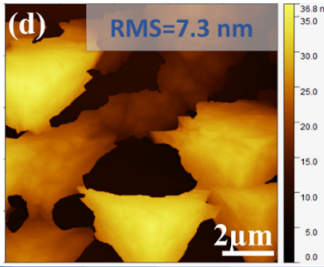
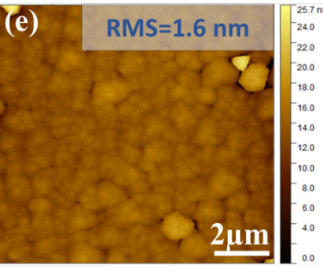
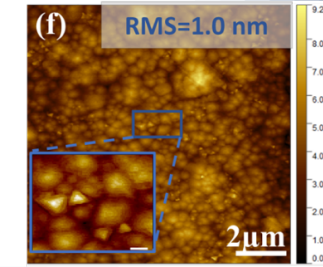
	Sample A	Sample B	Sample C
Temperature (°C)	440	380	380
Thickness (nm)	10	10	30
SEM images			
AFM images			

Figure 3.1 – SEM and AFM images of samples A (a,d). B (b,e) (the scale bar in the inset of (b) is  $1 \mu\text{m}$ -long) and C (c,f) respectively. The inset in (f) is a magnified view of the surface inside the blue rectangle in (f) where the scale bar is  $250 \text{ nm}$ -long.

Figure 3.1(b) displays the SEM image of sample B where the InAs thin film is smoother and seems to cover almost the whole InP surface. Some hillocks may appear as highlighted in the inset of Figure 3.1(b). Figure 3.1(e) is an AFM image scanned at a higher magnification. It shows that almost 99% of the surface is covered with granular coalescent structures. Moreover, the surface roughness measured in this  $10 \times 10 \mu\text{m}^2$  AFM image is around 1.6 nm which is 4.5 times lower than the surface roughness of the triangular islands of the sample A for the same image dimensions. Therefore, lowering the growth temperature from  $440^\circ\text{C}$  to  $380^\circ\text{C}$  leads to

a smoother growth: the InAs islands coalesce in the early growth stage causing a flattening of the InAs film on the InP(111)<sub>B</sub> surface. We believe that the growth temperature around 380°C is probably low enough to limit the In diffusion on the InP surface, preventing its accumulation in some areas of the surface compared to 440°C for sample A. In these conditions multiple InAs islands are grown all over the wafer surface and coalesce, whereas for sample A, larger InAs triangular islands are created because of the In diffusion.

The growth conditions of sample B are considered as relatively optimized growth conditions of a thin InAs layer on the InP(111)<sub>B</sub> wafer. In this vein, the third sample, sample C, is grown for a longer time aiming to a 30nm-thick film. The SEM image of sample C (Figure 3.1(c)) shows a full coverage of the InP surface, whereas the higher resolution AFM images (Figure 3.1(f) and the inset of the Figure 3.1(f)) show smaller granular and triangular structures than the ones seen in sample B. The surface roughness of the InAs surface of sample C, in the  $10 \times 10 \mu\text{m}^2$  AFM-image-dimension, is around 1.0 nm compared to 1.6 nm in sample B.

Figure 3.2(a) shows a higher resolution AFM image of sample A which confirms the concentric triangular form of the InAs terraces. These flat terraces cover few hundreds of nanometers of the surface. Figure 3.2(d) displays the acquired height profile along the blue line plotted in Figure 3.2(a). The average height of an InAs plane is around 3.5 Å, matching the theoretical monolayer thickness of an InAs (111) surface  $\frac{6.06}{\sqrt{3}} = 3.5$  Å. In the case of sample B, the islands are rather concentric, as shown in Figure 3.2(b). The height profile of Figure 3.2(e) shows some hundreds of nanometers-wide terraces separated, again, by an average step height of 3.5 Å. Concerning sample C (Figure 3.2(c)), the same magnification as in Figure 3.2(a) and 3.2(b) reveals circle-like InAs terraces, a shape similar to sample B, albeit wider. The extracted height profile from the blue line in the AFM image of sample C that is plotted in the Figure 3.2(f), presents an average InAs steps height also around 3.5 Å. Based on this AFM image, the unfilled surface separating the InAs terraces is not as deep as the holes separating the InAs islands in Figure 3.2(b), yielding a lower surface roughness.

In summary, a sample A grown at 440°C, shows non-coalescent InAs islands with a triangular shape. The islands cover only 50% of the InP surface. The surface roughness is 7.3 nm, much higher than the surface roughness of sample B where the InAs layer is grown at a lower temperature of 380°C and shows a surface roughness of 1.6 nm. Hence, the temperature is believed to be low enough to limit the indium adatom diffusion on the InP(111) surface, promoting the uniform growth of InAs. It leads to a surface coverage above 99% of the surface.

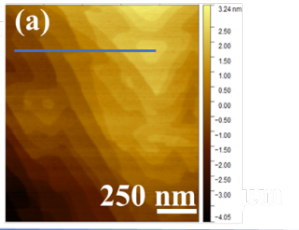
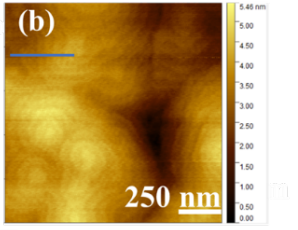
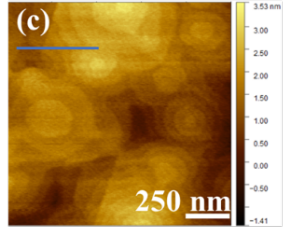
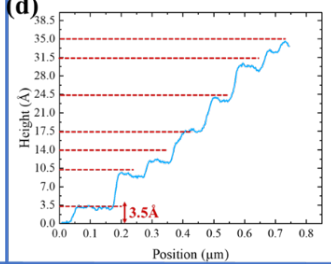
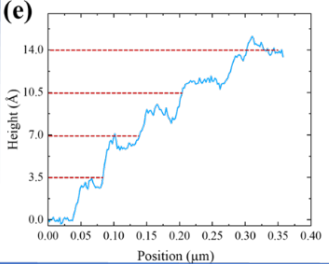
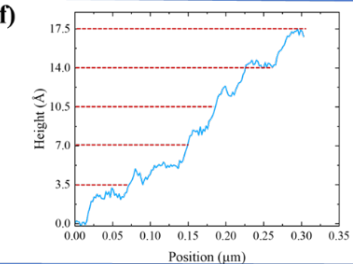
	Sample A	Sample B	Sample C
Surface coverage %	50	99	Full coverage
RMS (nm)	7.3	1.6	1.0
AFM images			
Profiles			

Figure 3.2 – AFM images and height profiles taken along the blue line plotted in the AFM images of samples A (a,d), B (b,e,) and C (c,f) respectively. Red dashed lines in (d), (e) and (f) correspond to the multiples of the theoretical InAs(111) monolayer step height ( $3.5\text{\AA}$ ).

Using the relatively optimized growth conditions of sample B, the third sample C is grown with a 30 nm-thick InAs layer instead of a 10nm-thick layer that further enhances the flatness of the surface. The roughness decreases to 1 nm. The InP surface is fully covered in this case. The circle-like InAs terraces seem more coalesced than those in the case of sample B. The surface defects of sample C like the triangular islands and granular defects presented in the inset of the Figure 3.1(f) have a smaller size than those found in sample B.

In the next part, the InAs film of the optimized samples, B and C, is studied using the XRD technique to further determine how it is strained with respect to the InP substrate.

### 2.1.3 InAs film relaxation

InAs is 3.3% mismatched with InP. Therefore, the growth of the InAs film may take place with several morphological defects like dislocations. The InAs film relaxation depends on the wafer orientation, the growth conditions of the InAs layer and on its thickness.

Figure 3.3 displays the XRD spectra measured on samples B and C. The large and narrow peak is attributed to the diffraction from the InP(111) substrate and the broad peak is attributed to the diffraction from the InAs film. A strain relaxation of about 50% for the 10 nm-thick InAs layer and of about 70% for the 30 nm-thick InAs layer can be deduced by fitting the

experimental spectra with a simulation.

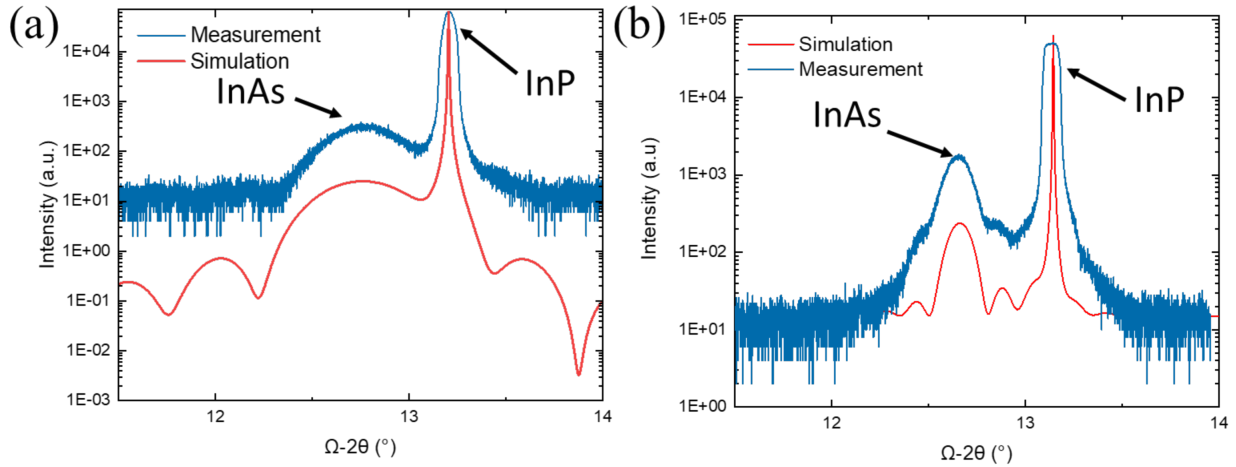


Figure 3.3 – (a) XRD data compared to the simulated spectrum assuming a 50% strain relaxation of the film for the 10 nm-thick epitaxial InAs layer on InP (111)<sub>B</sub>, (b) XRD data compared to the simulated spectrum assuming a 70% strain relaxation of the film for the 30 nm-thick epitaxial InAs layer on InP (111)<sub>B</sub>.

A longer growth time of the InAs film on the InP (111) surface leads to a smoothening due to the complete coalescence of the InAs islands. Sample C is more relaxed than sample B, in agreement with the accumulated strain as the layer thickness increases.

The structural properties of the InAs layers are summed-up in the following table.

Table 3.2 – Growth conditions and structural properties of the InAs layer relaxation for the different InAs thin films studied in this chapter.

	<b>Sample A</b>	<b>Sample B</b>	<b>Sample C</b>
<i>Growth rate (ML/s)</i>	0.05	0.05	0.05
<i>As/In ratio</i>	120	120	120
<i>Temperature (°C)</i>	440	380	380
<i>Thickness (nm)</i>	10	10	30
<i>Surface coverage (%)</i>	50	99	100
<i>RMS (nm)</i>	7.3	1.6	1.0
<i>Film relaxation (%)</i>	-	50	70

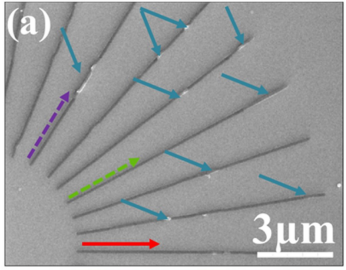
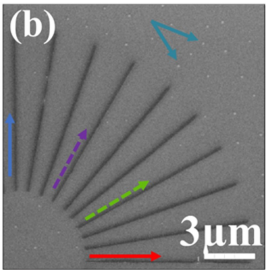
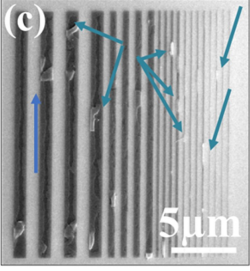
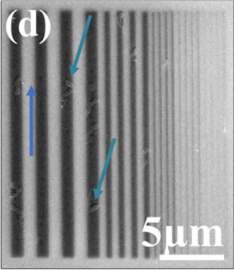
Based on the morphology of the InAs thin films studied in this section, sample C is believed to present the best quality.

## 2.2 InAs 111 nanowires

In this section, the three different epitaxial growth conditions described above will be applied to the selective area growth of InAs nanostructures on InP(111)<sub>B</sub>. Patterns are defined on the SiO<sub>2</sub> mask as described in chapter 2. For all three samples, the mask is identical. The InP wafers were respectively bonded on the same Si wafers as samples A, B and C described in the previous section. For this reason we will keep the nomenclature previously used where A<sub>SEL</sub>, B<sub>SEL</sub> and C<sub>SEL</sub> are selectively grown samples using the same conditions as A, B and C respectively.

We start with the description of the nanowire morphology for nanowires with different crystallographic orientations and widths of 50 nm, 100 nm, 200 nm, 500 nm and 1000 nm. At a first stage, the samples A<sub>SEL</sub> and B<sub>SEL</sub> are compared. As recalled in Figure 3.4, the growth conditions of both samples are a growth rate of 0.05 ML/s and an As/In ratio of 120. Because the growth takes place under an atomic hydrogen flux, the growth occurs only in the mask openings corresponding to the InP surface, and not on the SiO<sub>2</sub> mask, enabling a good selectivity [5].

Figures 3.4(a) and Figure 3.4(c) show SEM images of sample A<sub>SEL</sub> for nanowires grown with different crystallographic orientations and widths. The majority of the planar nanowires consist of isolated and non-coalesced islands within the openings, as pointed out by the blue-aqua arrows in these figures. These results are consistent with the InAs thin film growth behaviour of sample A that promotes an island growth mode. Due to the relatively high growth temperature, In adatoms diffuse and nucleate at several sites in the openings on the InP surface. Those islands are not seen in sample B<sub>SEL</sub> (Figures 3.4(b) and Figure 3.4(d)), as the mask openings seem to be homogeneously filled. Nevertheless, rare defects exist in some areas of the nanowires as pointed out by the blue-aqua arrows in Figure 3.4(d). As seen in this figure, these defects are present mainly on the largest nanowires. However, due to the lower growth temperature, we can notice, based on Figure 3.4(b), a few bright nuclei on the SiO<sub>2</sub> mask (pointed out by the blue-aqua arrows in Figure 3.4(b)) indicating that the growth selectivity, although still convenient, starts to degrade.

	Sample $A_{SEL}$	Sample $B_{SEL}$
<b>Growth rate (ML/s)</b>	0.05	0.05
<b>As/In ratio</b>	120	120
<b>Thickness (nm)</b>	10	10
<b>Temperature (°C)</b>	440	380
<b>NWs along different crystallographic orientations</b>		
<b>NWs with widths of 50 nm, 100 nm, 200 nm, 500 nm and 1000 nm (Right to left)</b>		




Figure 3.4 – SEM images of (a,b) InAs nanowires grown on InP(111)<sub>B</sub> wafers with a nominal width of 100nm for different crystallographic orientations on sample  $A_{SEL}$  and  $B_{SEL}$  respectively. The blue-aqua arrows underline numerous defects on the nanowires. (c,d)  $[2\bar{1}1]$ -oriented nanowires with 1000 nm, 500 nm, 200 nm, 100 nm and 50 nm nominal widths for the sample  $A_{SEL}$  and  $B_{SEL}$  respectively. The blue-aqua arrows underline defects on the nanowires.

As a conclusion, based on the comparison of the SEM images of both samples, decreasing the growth temperature from 440°C to 380°C limits the diffusion of In on the InP (111) surface and therefore promotes a better coverage of the InP surface in the mask openings. In this case, the mask selectivity decreases, but it is still convenient. The use of an atomic hydrogen flux during the growth extends the selectivity limit towards lower temperatures than the one described in [6], [7].

As for sample  $C_{SEL}$ , that is prepared with the same conditions as sample  $B_{SEL}$ , albeit to a longer growth time to obtain 30 nm-thick nanowires, the selectivity remains acceptable. A complete and homogeneous filling of the openings is achieved for 200 nm wide wires with different orientations (Figure 3.5(a)) and for the  $[2\bar{1}1]$ -oriented nanowires with different widths (Figure 3.5(b)). Figure 3.5(a) shows that the nanowires grown with the same conditions as the nanowires of sample  $B_{SEL}$  are almost defectless. Zooming at the extremity of the in-plane nanoribbons with a nominal width of 200nm enables the observation of the facets delimiting the nanostructure for different in-plane orientations. The nanowires grown along the main



crystallographic orientations are straight whereas in the case of some secondary orientations, the nanowires show a zigzag-edge. These directions do not match the natural lattice structure, leading to higher surface energy and less stable growth fronts.

The InAs nanowires grown along the  $\langle 11\bar{2} \rangle$  family of directions show vertical highly symmetric  $\{1\bar{1}0\}$  side walls [8] (see Figure 3.5(c)) whereas the NWs grown along the  $\langle 1\bar{1}0 \rangle$  directions family present asymmetric trapezoid cross-sections with a vertical  $\{11\bar{2}\}$  sidewall on one side and a slanted  $\{1\bar{1}0\}$  facet on the other side as presented in Figure 3.5(d) and explained by J.S.Lee et al. [9].

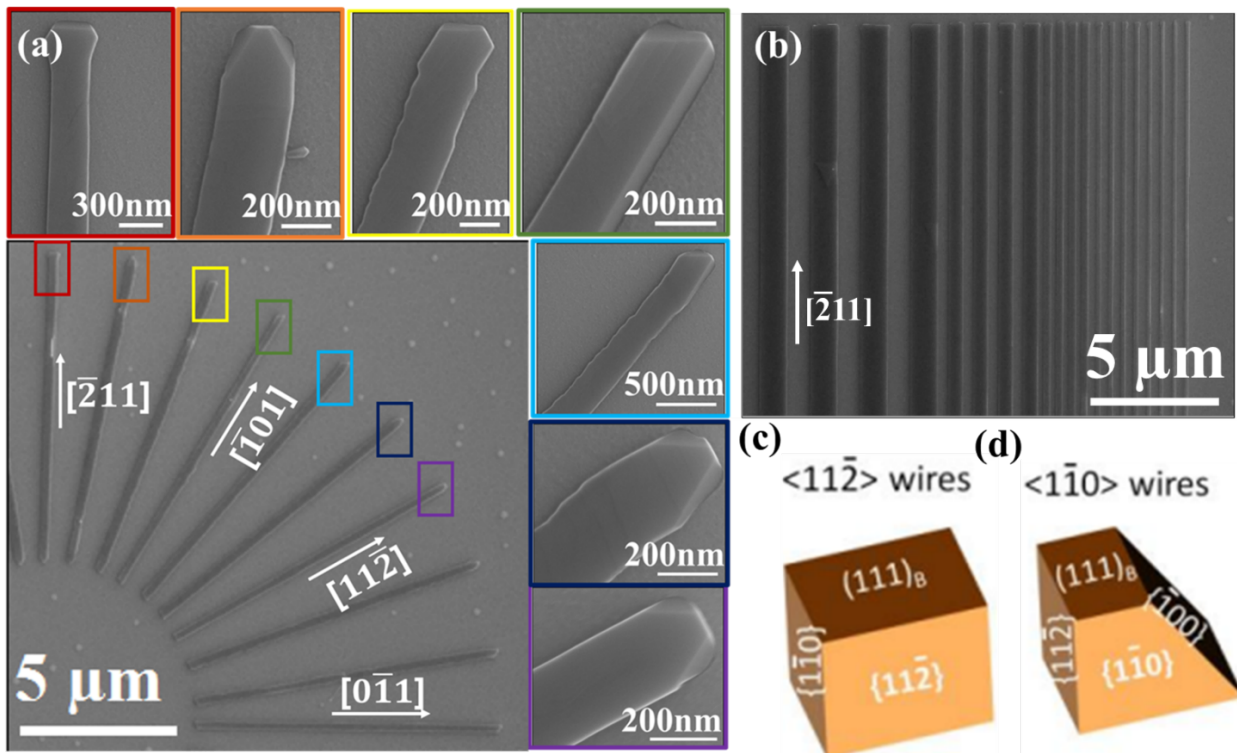


Figure 3.5 – (a) SEM images of 200 nm-wide InAs NWs with different in-plane orientations (rotation every  $10^\circ$  from  $[0\bar{1}1]$  to  $[2\bar{1}1]$ ) grown by SAE on  $\text{InP}(111)_B$  (sample  $C_{\text{SEL}}$ ). The different facets that are formed at the end of the NWs are highlighted in the different insets. (b) SEM images of 200 μm-long and  $[2\bar{1}1]$  oriented InAs NWs with different nominal widths (1000 nm down to 50 nm from left to right) (sample  $C_{\text{SEL}}$ ). (c) Schematic representation of the nanowire geometry along the  $\langle 2\bar{1}1 \rangle$  orientation.[5] (d) Schematic representation of the nanowire geometry along the  $\langle 1\bar{1}0 \rangle$  orientations [9].

The observation of such facets is also confirmed in Ref. [10]–[12]. For nanowires grown on (111) wafers, uniform faceting can only be achieved along two high-symmetry direction families:  $\langle 1\bar{1}0 \rangle$  and  $\langle 11\bar{2} \rangle$ . This phenomenon is driven by the imperative energy minimization of facet surfaces during the SAG process. The growth enhancement observed along the  $\langle 1\bar{1}0 \rangle$  and  $\langle 11\bar{2} \rangle$  orientations can be attributed to the localization of energy minima along these directions, according to the Wulff diagram pertinent to the  $\text{InAs}(111)_B$  facet.

M.E. Cachaza et al. prove that the relation between the growth mode of III-V semiconductors and the filling of the mask openings emerges as a complex equation governed by a set of factors, not only the crystallographic orientation, but also the mask geometry, which encompasses the pitch and width of the NW array, and its spatial positioning. Furthermore, the surface energy adds another layer of complexity, directing the morphology and the ensuing physical properties of the resultant structure [13].

The AFM image of the nanowires in sample  $C_{\text{SEL}}$  with a nominal height of 25 nm is visible in Figure 3.6. If we consider a residual  $\text{SiO}_2$  mask with a height of about 10 nm [5], the real height of the nanostructure is around 35 nm. For these series of nanowires grown along the  $[\bar{1}01]$  direction with a nominal mask width of 100 nm, the real width is 200 nm revealing a clear overgrowth of the InAs on top of the mask. This is observed in Ref. [6] for  $\langle 1\bar{1}0 \rangle$  directed nanowires.

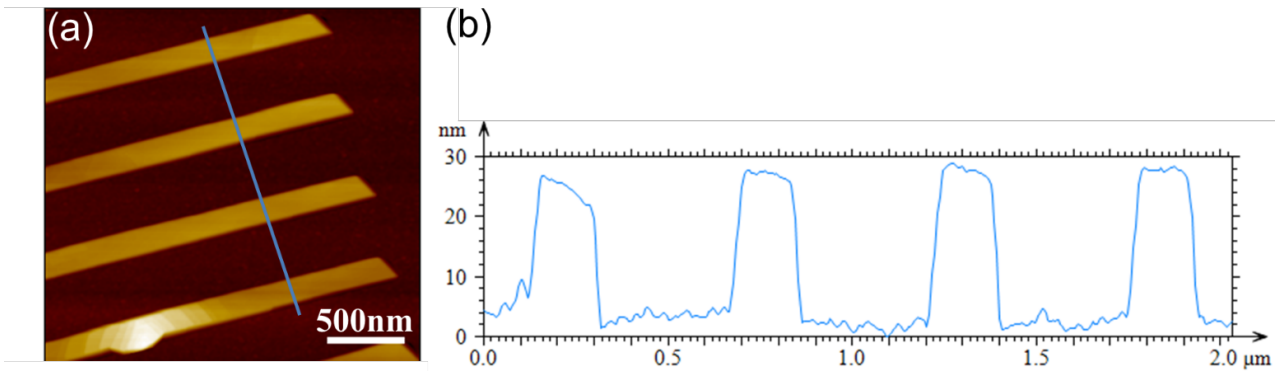


Figure 3.6 – (a) AFM image of a series of 200 nm-wide-nanowires along the  $[\bar{1}01]$  direction of the sample  $C_{\text{SEL}}$ . (b) Height profile of the NW series along the blue line plotted in (a).

Decreasing the growth temperature from 440°C to 380°C enhances the homogeneous filling of the openings despite the lower selectivity. The nanowires grown at 380°C with the longer duration show flat top facets, consistent with the highest structural quality obtained for the analog thin film. Therefore, sample  $C_{\text{SEL}}$  is chosen for carrying out the electrical measurements with in-situ multiprobe STM that will be presented in section 4.2.2.

### 3 Transport properties of InAs films with oxidized surfaces

In order to study the electronic properties of the InAs films with the best InAs crystalline quality (samples B and C), Hall effect measurements were performed. For this purpose, the



samples are etched in forms of Hall bars and Van der Pauw microstructures as explained in chapter 2.

Hall measurements are carried out for samples B and C at 300K. Transport in sample C is further studied at 77K. The values of the main parameters are summarized in Table 3.3.

Table 3.3 – Hall measurements of samples B and C at RT and at 77K.

Temperature (K)	Heterostructure	Sheet resistance ( $\Omega/\square$ )	Charges density ( $10^{12}\text{cm}^{-2}$ )	Mobility ( $\text{cm}^2/\text{Vs}$ )
77	30nm InAs (Sample C)	3300	-2.47	760
300	10nm InAs (Sample B)	38700	-1.10	148
	30nm InAs (Sample C)	2470	-2.42	1050

Sample B with an InAs thickness of 10 nm has a sheet resistance of  $38700 \Omega/\square$ . The charge density is  $-1.10 \times 10^{12} \text{ cm}^{-2}$  yielding a room temperature electron mobility of  $148 \text{ cm}^2/\text{V.s}$ . Sample C shows a sheet resistance of  $2470 \Omega/\square$  with a charge density of  $-2.42 \times 10^{12} \text{ cm}^{-2}$  and an electron mobility of  $1050 \text{ cm}^2/\text{V.s}$  at RT.

Therefore, a 16 times higher conductance is achieved in sample C compared with sample B.

The sheet resistance of a 2D surface is given by the following expression:

$$R_{\square} = \frac{1}{n \cdot q \cdot \mu} \quad (3.1)$$

Where  $R_{\square}$  is the sheet resistance,  $n$  is the surface charge density,  $q$  is the elementary electron charge and  $\mu$  is the charge mobility. The first reason that explains the lower sheet resistance of sample C is the larger thickness of the sample with respect to sample B. If we consider a homogeneous distribution of charges in the layer, one would indeed expect a 3 times lower sheet concentration for sample B than for sample C. Considering the measured Hall densities, the ratio is 2.2.

As the InAs layers are unintentionally doped, the charge carriers originate from:

- the intrinsic carrier concentration, which can be estimated in the  $10^{14} \text{ cm}^{-3}$  range at 300K [14]
- the bulk doping by background impurities
- the surface and interface state doping

The dependency of the sheet Hall density with the thickness reveals that a significant part of the sheet carrier concentration is coming from surface and interface states since this source

of doping is independent of the film thickness. For surface states, this is consistent with the surface Fermi level pinning in the conduction band reported for InAs [15].

This surface state doping also impacts the Hall mobility, as the electrons are concentrated near the surface and are thus more sensitive to surface roughness scattering. Consequently, the thinner sample B exhibits a much lower mobility than sample C.

At 77K, sample C has a sheet resistance of 3300  $\Omega/\square$  with a Hall density which is almost constant:  $-2.47 \times 10^{12} \text{ cm}^{-2}$  and an electron mobility of 760  $\text{cm}^2/\text{V.s}$ . Whereas the charge density for sample C does not much evolve, the electron mobility decreases. This is, probably, due to a reduced contribution of thermally activated bulk electrons to the transport properties compared to surface electrons with a low mobility [16].

In addition to surface defects issues, surface oxidation is believed to reduce the transport properties of the InAs thin films. The following section will, thus, be dedicated to the study of the InAs surface for both thin films and nanowires in UHV using in-situ four-probe-STM.

## **4 Transport properties of InAs (111) nanowires with cleaned facets**

### **4.1 Sample transfer protocol**

In order to investigate electron transport in non-oxidized InAs thin films and 1D nanostructures, samples C and  $C_{\text{SEL}}$  are studied by in-situ 4P-STM. Two issues have to be solved. The first one is the transfer of the sample from the MBE system to the 4P-STM system that requires an exposure of the nanostructures to the ambient atmosphere. The second issue is the  $\text{SiO}_2$  oxide layer that surrounds the nanostructures of the  $C_{\text{SEL}}$  sample and prevents any approach of the tips between the nanostructures, as no tunneling current can be detected. Although the use of a SEM limits the risk to position the tips away from a conductive nanostructure, there might be some uncertainty in the tip positioning for the narrowest nanostructures, especially when the tip is blunt or slightly tilted.

To overcome the first constraint, sample C is capped with an amorphous As layer just after the growth. During the process, the temperature of the manipulator is cooled down to  $5^\circ\text{C}$  and the sample is capped with As using an  $\text{As}_4$  flux for 5 min. In the case of sample  $C_{\text{SEL}}$ , the

sample is taken out of the MBE system and immersed in a HF 1% solution for 1min in order to totally remove the SiO<sub>2</sub> layer that surrounds the nanowires. Then the sample is loaded back inside the MBE system to get fully deoxidized at 400°C with an As flux combined with an atomic hydrogen flux. At the end of the oxide removal, the temperature of the manipulator is cooled down to 5°C and the sample is also capped with As using As<sub>4</sub> flux for 5 min. Previous works showed that an As cap layer can successfully protect the InAs nanostructures from oxidation and can be removed after heating the sample at 320°C for 2h without degrading the structural and electronic properties of the InAs nanowires [17]. These different steps are illustrated in Figure 3.7.

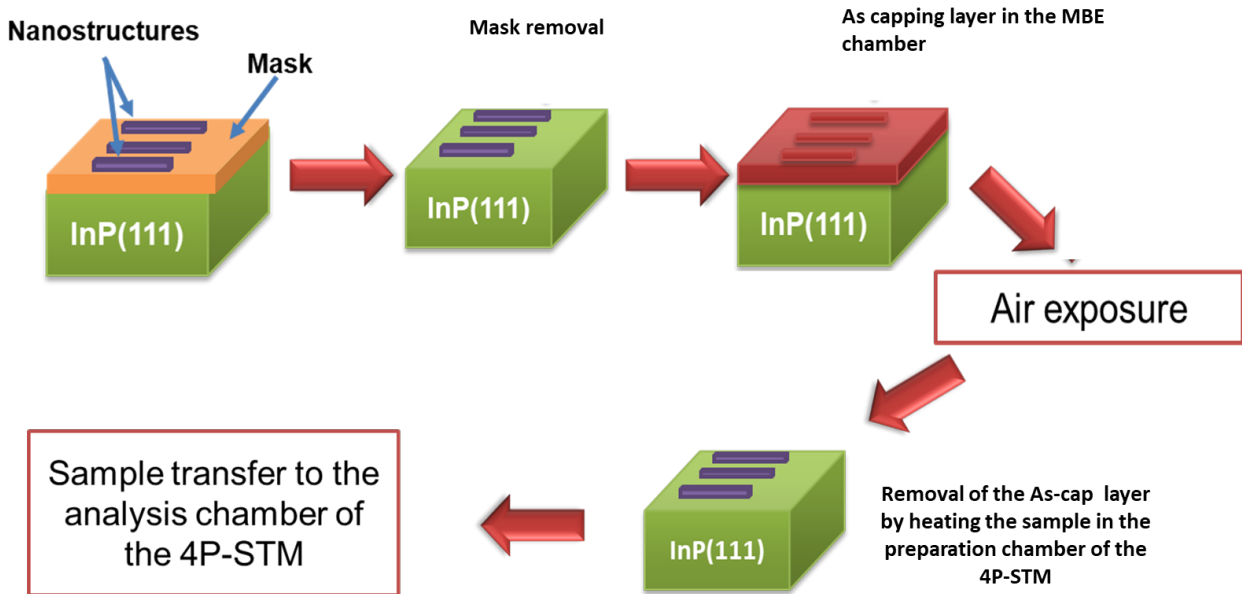


Figure 3.7 – Scheme illustrating the transfer process of sample  $C_{SEL}$  from the MBE system to the 4P-STM system.

Inside the 4P-STM system, samples are annealed at 120 °C in UHV for a few hours in the load lock in order to desorb water molecules. Once inside the preparation chamber, they are further annealed at 320°C for 2h to desorb the As protection layer. The uncapping process was monitored with a mass spectrometer and a pyrometer.

## 4.2 4P-STM measurements

For transport measurements with an arbitrary positioning of the probes, the samples are characterized with the four-probe STM system. As mentioned before, this instrument offers the possibility of contacting nanostructures with tungsten probes that can be moved freely and make direct electrical contacts. No metal deposition is therefore required in contrast with the Hall measurements. The fine approach of the four probes is performed using the tunnelling

approach of the STM control system. When the tunnelling current is detected, the tip is after that pushed down to the surface until a stable electrical contact is obtained.

#### 4.2.1 Resistivity of the reference 2D Electron Gas

In the case of sample C, a 4-aligned-probe configuration is used (Figure 3.8). As described in Chapter 2 (section 3.4.2) the current is injected and collected by the outer tips and the voltage is measured between the two inner probes.

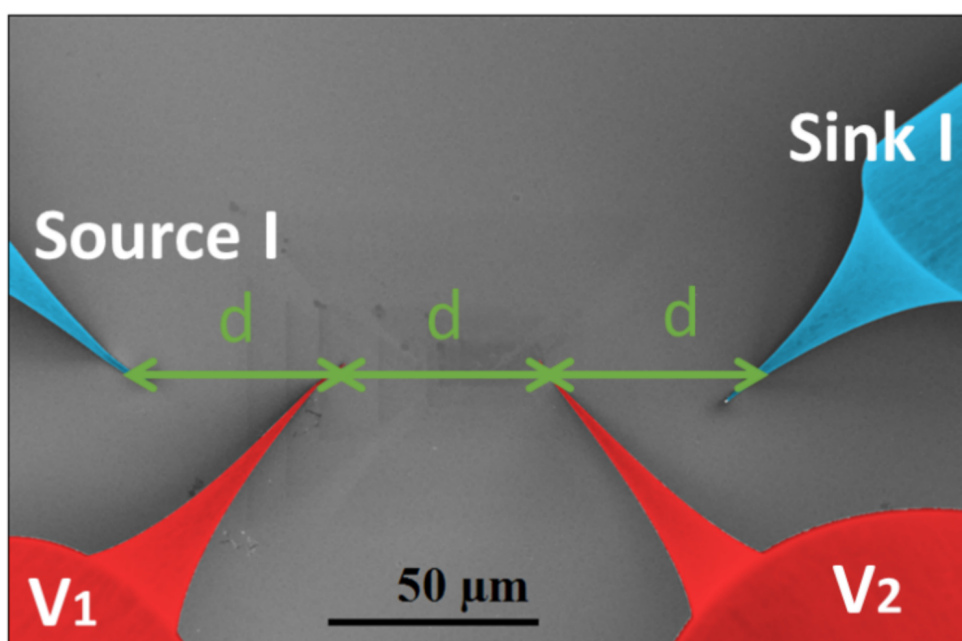


Figure 3.8 – False coloured SEM image illustrating the 4P-STM measurement with four aligned and equidistant probes. The blue outer probes are used to inject (source) and collect (sink) the current, whereas the red inner probes measured the potential drop  $V_1$ - $V_2$ .

The 4P resistance of the 2DEG is independent of the inter-probe distance  $d$  and it is given by equation 3.2 [18], [19]:

$$R_{4P} = \frac{\ln 2}{\pi} \cdot R_{\square} \quad (3.2)$$

Here  $R_{\square}$  corresponds to the 2DEG sheet resistance.

The four probe measurements are carried out at room temperature and also at 115 K using a liquid nitrogen flow enabling the cooling of the sample holder. The distance  $d$  is varied from 100  $\mu\text{m}$  down to few microns. For each measurement, the resistance value is extracted from a  $V(I)$  linear curve averaged from three to five 4P consecutive measurements with the Keithley source meters. Such an average is essential at low temperature where the  $V(I)$  curves

are more noisy than room temperature measurements due to the stronger instability of the electrical contacts caused by the difference of temperature between the cold sample and the tips maintained at room temperature.

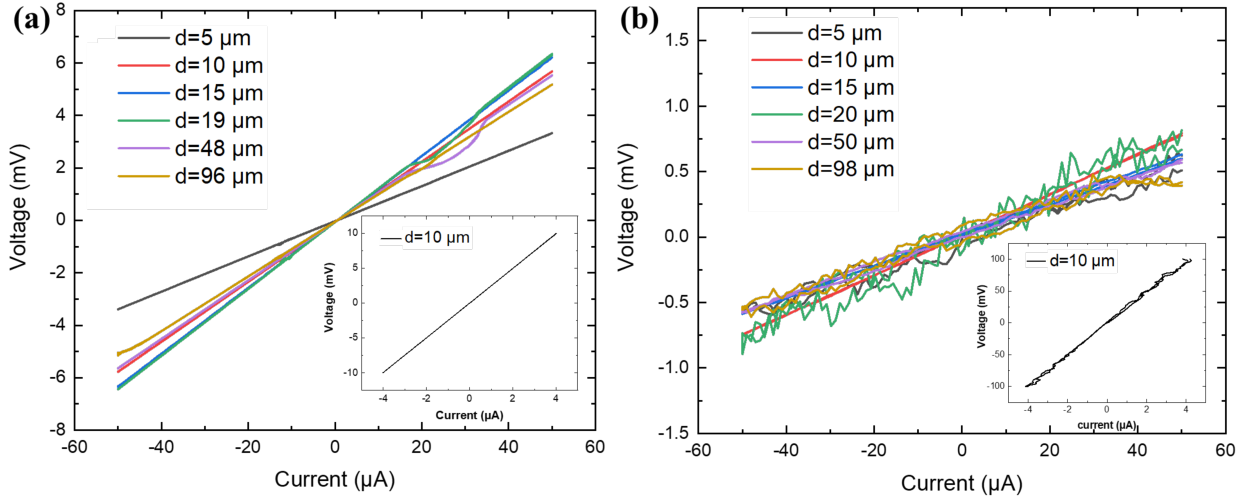


Figure 3.9 – (a) Curves of the 4P-STM measurements for the sample C at room temperature for different distances  $d$  between the two inner probes. Inset: 2P measurements performed at  $d = 9.6 \mu\text{m}$ . (b) Curves of the 115K 4P-STM measurements for sample C prepared on an  $\text{InP}(111)_\text{B}$  wafer for different distances  $d$  between the two inner probes. Inset: the 2P measurements performed at  $d=10\mu\text{m}$ .

For all measurements the applied current is swept from  $-50 \mu\text{A}$  to  $50 \mu\text{A}$ . Figure 3.9(a) shows the  $V(I)$  curves measured at room temperature for different distances  $d$  between probes arranged with a linear equidistant configuration. From these linear curves, we extract the resistance. The 4P-resistance variation against the distance  $d$  is given in the following table.

Table 3.4 – Four-probe-resistance against the distance  $d$  at 300K.

Distance $d(\mu\text{m})$	5	10	15	19	48	96
Resistance $R_{4P}(\Omega)$	65	114	126	127	109	104

The distance  $d$  varies from  $5\mu\text{m}$  to  $96 \mu\text{m}$ . The four-probes resistance  $R_{4P}$  seems almost constant and the mean value is  $115\Omega$ . This is consistent with the theoretical resistance behaviour given by equation 3.2. When the four-probe distance is below  $5\mu\text{m}$ , we observe a decrease of the resistance to about  $65\Omega$ . This decrease could be related to a lower density of crystal defects encountered by the electrons at this length scale. 4P-measurements with smaller inter-probe distances are needed to confirm this tendency. TEM cross-section analysis should also give more information about the crystal defect density in the film and confirms the correlation between transport properties and the quality of the InAs layer.

The two probes (2P)  $V(I)$  curve measured between the two inner probes for  $d=10\mu\text{m}$ , displayed in the inset of the Figure 3.9(a), shows a steeper slope. We sweep the voltage from  $-0.01\text{V}$  to  $0.01\text{V}$  and measure the corresponding current. The voltage is, however, plotted as a function of the current for better comparison with the 4P measurements. The measured current is almost about some microamperes that reveals resistance values around  $2.5\text{ k}\Omega$ .

We note that the resistance of the electrical contact is higher than the 4P resistance. The linear aspect of the 2P measurements reflects the ohmic contact between the tungsten tips and the InAs layer due to the conducting behaviour of this layer. As the Fermi level is pinned in the conduction band at the surface [16], an accumulation layer exists below the surface, allowing the formation of an ohmic contact.

Figure 3.9(b) displays the  $V(I)$  curves measured with the 4P-STM at  $115\text{K}$ . Despite a higher noise level, the  $V(I)$  curves are still linear. The four-probe-resistance variation against the distance  $d$  between the tips is summarized in Table 3.5.

Table 3.5 – Four-probe resistance against the distance  $d$  at  $115\text{K}$ .

<b>Distance <math>d(\mu\text{m})</math></b>	<b>5</b>	<b>10</b>	<b>15</b>	<b>20</b>	<b>50</b>	<b>98</b>
<b>Resistance <math>R_{4P}(\Omega)</math></b>	<b>115</b>	<b>153</b>	<b>120</b>	<b>155</b>	<b>135</b>	<b>116</b>

Here, the measured  $R_{4P}$  seems fluctuating between  $115\Omega$  and  $155\Omega$ , while the distance  $d$  between the inner tips is increased from  $5\mu\text{m}$  to  $98\mu\text{m}$ . We assume that the four-probe-resistance is almost constant around  $130\Omega$  at  $115\text{K}$ . This resistance is slightly higher than the average four-probe resistance measured at RT, which was  $115\Omega$ .

These low temperature measurements do not reveal a resistance drop at  $5\mu\text{m}$  as the one seen at RT. As the current is mainly due to electrons accumulated at the surface at low temperature, this may indicate a lower impact of threading defect scatterings on the mobility of surface electrons than that of bulk ones.

The inset curve of Figure 3.9(b) shows an example of the 2P  $V(I)$  curves measured at  $d=10\mu\text{m}$ . The 2P- resistance extracted from this linear curve is around  $25\text{ k}\Omega$ . Again, the contact resistance is higher than the sample resistance.

The graph in Figure 3.10 sums up the 4-probes measurement carried out at RT and at  $115\text{K}$  compared to the resistance values deduced from the Hall effect measurements at RT and  $77\text{K}$ .

For the 4-probes measurements, an uncertainty exists regarding the true distance as for blunt tips, the exact position where the probe is in contact with the surface is sometimes badly

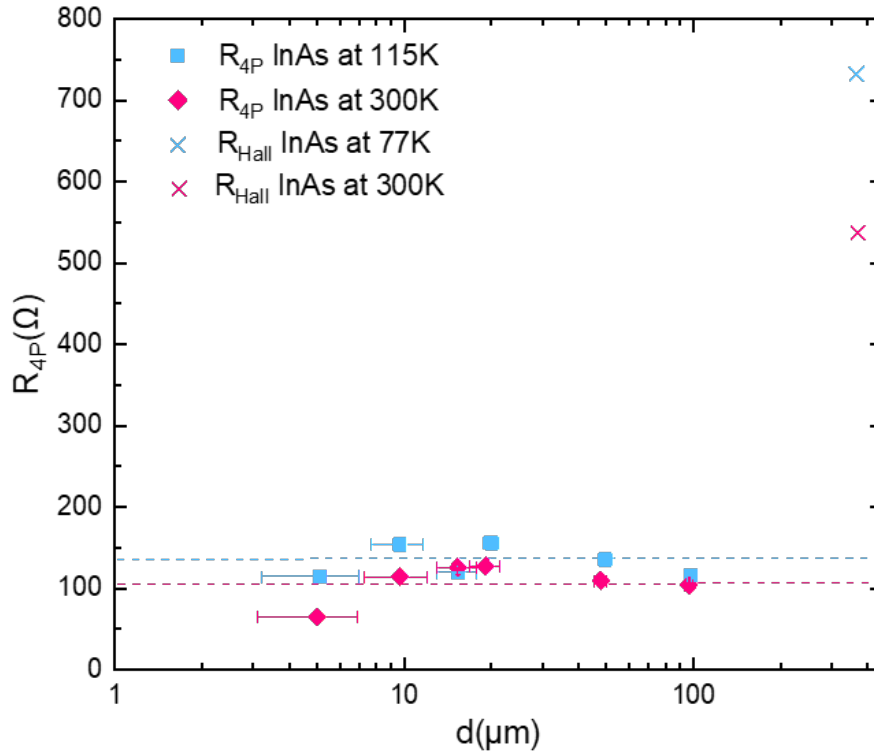


Figure 3.10 – Four-probe resistances of the InAs film grown on InP(111)<sub>B</sub> SI wafers (sample C) at RT and at 115K as a function of equidistant probe separations (square and rhombus) and Hall bars resistances measured at RT and at 77K (cross). The dashed horizontal lines correspond to the mean values of the 4P resistances.

defined based on the SEM observation of the tip only. Figure 3.11 is a simplified scheme using only two tips that illustrates the calculated distance based on the SEM images. Assuming  $R$  and  $R'$  as the radii of the curvature of the two tips, the distance is  $d \pm (R + R')$ . This uncertainty was quite large for some of the measurements and accounts for the large horizontal error bars seen in Figure 3.10. Despite this uncertainty, the resistance is almost constant when the tip separation varies, which is consistent with electronic transport in a homogeneous 2D layer. The average 4P-resistance is  $101 \Omega$  at RT and  $132 \Omega$  at 115K, yielding intrinsic sheet resistance of  $458 \Omega/\square$  at 300K and  $598 \Omega/\square$  at 115K, based on equation 3.2. These values are lower than the sheet resistances measured in air in the Hall bar configuration. We explain this change by different surface chemistry: the surface is oxidized in the Hall bars, whereas it consists of arsenic dangling bonds when analysed with 4-probe STM. Such a difference was also found for wurtzite InAs nanowires, although the nanowires with oxidized surface showed a smaller resistance than the nanowires exposing clean and well-ordered facets [17]. In this reference, because of the sidewalls, gold clusters having diffused from the seed Au particles acted as strong scatterers.

To conclude, the thin InAs film grown on InP(111) with the best crystalline quality exhibits a



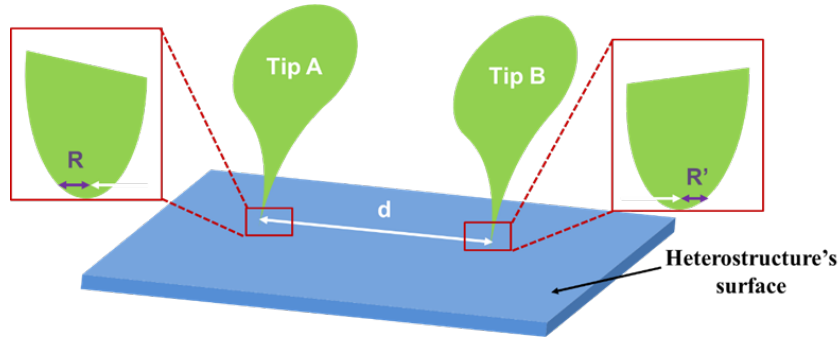


Figure 3.11 – Schematic of the distance  $d$  measured including the uncertainty induced by the radius of the STM tip based on the SEM images.

sheet resistance around  $2470 \Omega/\square$  at RT and  $3300 \Omega/\square$  at 77K when its surface is exposed to the air and oxidized. Its intrinsic sheet resistance is 5 times lower than the value measured in air conditions. The oxidization degrades the crystalline quality of the InAs layers and lowers the intrinsic conductivity at RT and nitrogen temperature. Moreover, the 4P-STM measurements confirm the decrease of the lower impact of bulk conductivity at low temperature.

If we fix the charge carrier density in the InAs film at RT to  $-2.42 \cdot 10^{12} \text{ cm}^{-2}$  as measured in the Hall bars, the intrinsic mobility of the charges is equal to  $5660 \text{ cm}^2/\text{V} \cdot \text{s}$ . This value is slightly higher to the Hall mobility of  $5400 \text{ cm}^2/\text{V} \cdot \text{s}$  measured by H. Schmidt et al. for InAs nanowires grown by the TASE technique [20]. If we consider that the charge carrier density at 115K does not change at 77K, as the measured electrons density is  $-2.47 \cdot 10^{12} \text{ cm}^{-2}$ , the electrons mobility at 115K would be  $4190 \text{ cm}^2/\text{V} \cdot \text{s}$ . The discussed data are resumed in the following table.

Table 3.6 – Mobilities, charges densities and sheet resistances of samples B and C at different temperatures.

Temperature (K)	Heterostructure	Sheet resistance ( $\Omega/\square$ )	Charges density ( $10^{12}\text{cm}^{-2}$ )	Mobility ( $\text{cm}^2/\text{Vs}$ )
77	30nm InAs (Sample C)	3300	-2.47	760
115	30nm InAs (Sample C)	598	-2.47	4190
300	10nm InAs (Sample B)	38700	-1.10	148
	30nm InAs (Sample C)	2470	-2.42	1050
	30nm InAs (Sample C)	458	-2.42	5660

#### 4.2.2 Sheet resistance of InAs nanowires

In case of the selectively area grown nanostructures, we restricted the study to nanowires grown along the two  $[\bar{2}11]$  and  $[0\bar{1}1]$  perpendicular directions. The nanowires have nominal thickness of 30 nm, a length of 20  $\mu\text{m}$  and nominal widths of 100 nm and 200 nm (giving almost 140 nm and 250 nm real widths respectively due to the HF opening of the windows).



The measurements principle is detailed in chapter 2 ( section 3.4.2). 4 Tips with diameters of about some tens of nanometers are contacted to the surface of the sample. For each measurement series, a current generator is used and can provide currents from  $-1 \mu\text{A}$  to  $1 \mu\text{A}$ . The voltage drop between the two inner probes is measured at each contact position of the moving tip, as shown in the graph of Figure 3.12(a). This graph sums up the  $V(I)$  linear curves extracted from the 4-probes measurements on a  $[0\bar{1}1]$  oriented nanowire grown in a 100 nm-wide opening where  $d$  is the distance between the two inner probes. The spectra are averaged from 5 consecutive  $V(I)$  measurements. Figure 3.12(b) shows 2P measurements illustrating averaged  $I(V)$  curves measured at different inner probe separations. The behaviour is not always ohmic and the resistance changes with the position of the inner tip. However, as long as all the tips are electrically connected to the nanowire, the four-probe resistance does not suffer from fluctuations in the contact resistances.

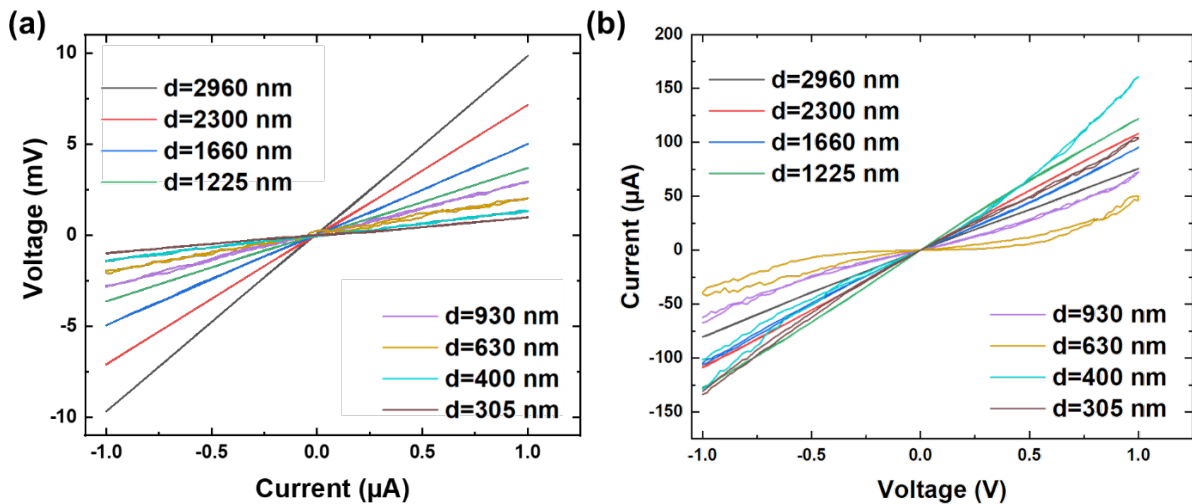


Figure 3.12 – (a) 4P averaged  $V(I)$  curves measured on a 100 nm-wide and  $[0\bar{1}1]$ -oriented nanowire (grown on an  $\text{InP}(111)_\text{B}$  SI wafer (sample  $\text{C}_{\text{SEL}}$ )) for different inter-probe distances  $d$ . (b) 2P averaged  $I(V)$  curves measured on the same nanowire for different inter-probe distances  $d$ .

Figure 3.13 sums up the 4P resistance against  $d$  measured for nanowires with widths of 100nm and 200 nm and oriented along the  $[\bar{2}11]$  and  $[0\bar{1}1]$  directions. The 4P resistance is linearly dependent to the spacing distance  $d$  between the two inner probes as found in [17], [19].

The four-probe resistance of the NWs is related to the resistivity of the InAs channel through the following equation:

$$R_{4P} = \frac{\rho \cdot d}{S} \quad (3.3)$$

Where  $\rho$  is the resistivity of the InAs channel,  $d$  refers to the distance between the inner probes, and  $S$  is the cross section of the wire. It is given by:

$$S = h \times W \quad (3.4)$$

Here  $h$  refers to the height of the wire and  $W$  is the width of the wire.

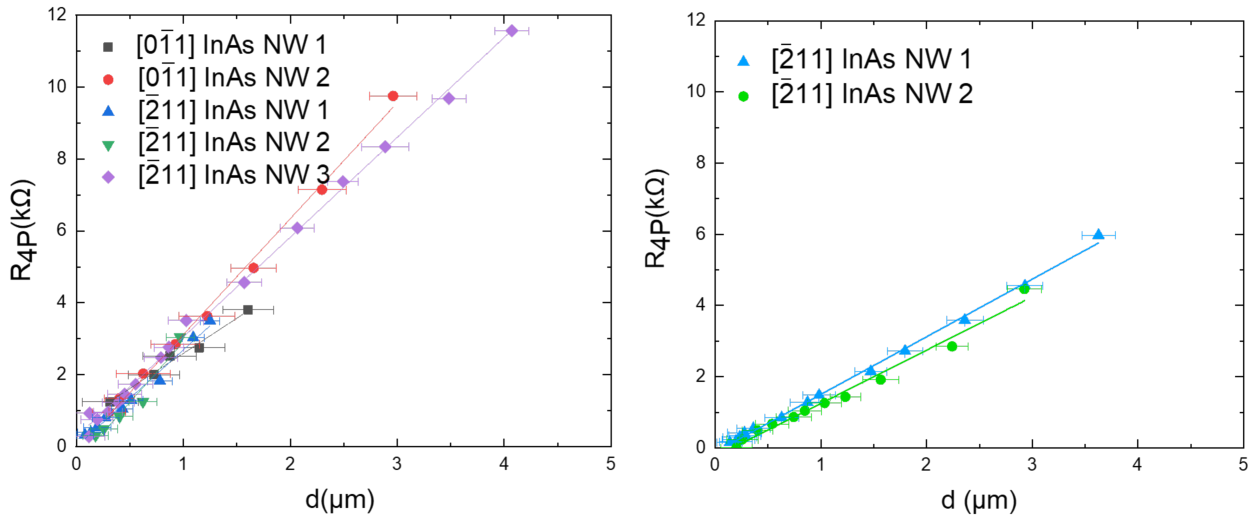


Figure 3.13 – 4-Probe resistance versus  $d$ . (Left) Measurement carried out on 100 nm-wide NWs grown on an InP(111)<sub>B</sub> SI wafer (sample C<sub>SEL</sub>). (Right) Measurements carried out on 200 nm-wide NWs. Lines correspond to best fits.

We know that transport predominantly occurs in the accumulation layer below the InAs surfaces of the nanowire due to the surface pinning of the Fermi level above the conduction band [16]. Therefore, we can convert the bulk resistivity into a sheet resistance. While the nanowires have different facets depending on their orientation, we assume that the conduction along the lateral facets is negligible with respect to the top facet as the nanowire growth was mainly with vertical side facets inside the openings for these two orientations.

The sheet resistance is then calculated based on the measured slopes of the linear fits of the  $R_{4P}$  resistance against the distance  $d$  between the inner probes and the measured widths of the nanowires.

Figure 3.14 summarizes the sheet resistance of the measured nanowires as well as the sheet resistance of the InAs thin film of sample C with both oxidized and non-oxidized surfaces. The nanowire sheet resistance is almost equivalent to the InAs thin film sheet resistance. It proves

that the width of the nanowires at 100 nm is large enough, implying an amount of surface scattering equivalent to the one involved in the thin film. Also, we do not see any significant variation of the resistance for both nanowire orientations. This observation is consistent with the predominant contribution of the top facet to the conduction of the wires.

When compared with free-standing InAs nanowires, which have a wurtzite structure, the sheet resistance of our zinc blende SAG is lower than the sheet resistance inside free-standing oxidized InAs nanowires epitaxially grown in previous works by C. Durand et al. [17]. As the mean diameter of these nanowires was about 70 nm, we estimate a nanowire width equal to a semicircle perimeter (about 220 nm). As their resistance per unit length  $R_{4P}/d$  was 6.3 k $\Omega/\mu\text{m}$ , the estimated sheet resistance was about 1386 $\Omega/\text{sq}$ . This value is higher than the mean sheet resistance measured for the SAG nanowires, around 400  $\Omega/\text{sq}$ , whatever their orientation is. The NW sheet resistance is also lower than the InAs nanowires grown by the TASE technique along the [110] orientation by H. Schmid et al. [20] and the InAs nanowires grown by VLS technique by M. Scheffler et al. [21]. But conductance measurements of these nanowires took place in air with oxidized nanowires. In fact, the oxidation of the InAs surface seem to damage dramatically the layer (almost 4 times) as the electrons transport takes place mostly at the InAs surface. Thus, it is affected by the interfacial states caused by the InAs native oxide. This confirms the efficiency of the As cap layer in the passivation of the InAs surfaces clearly yielding enhanced conductance.

## 5 Conclusion

Due to the important lattice mismatch between InAs and InP, InAs nanostructures on InP wafers may present morphological and surface defects that certainly affect the transport properties inside the InAs. This chapter was dedicated to the study of the growth conditions, to obtain high quality thin films and 1D InAs nanostructures grown on InP(111)<sub>B</sub> semi-insulating wafers.

We have found that lowering the growth temperature of the InAs thin film and 1D nanowires promotes a better coverage and a relatively faster coalescence of the InAs islands with a nominal thickness of about 10 nm. Moreover with 3 times thicker nanostructures, a better relaxed InAs film and a continuous growth in the openings have been obtained, yielding InAs nanostructures with less surface and morphological defects based on the XRD, AFM and SEM study. We consequently measured relatively higher mobilities and conductance in this sample.

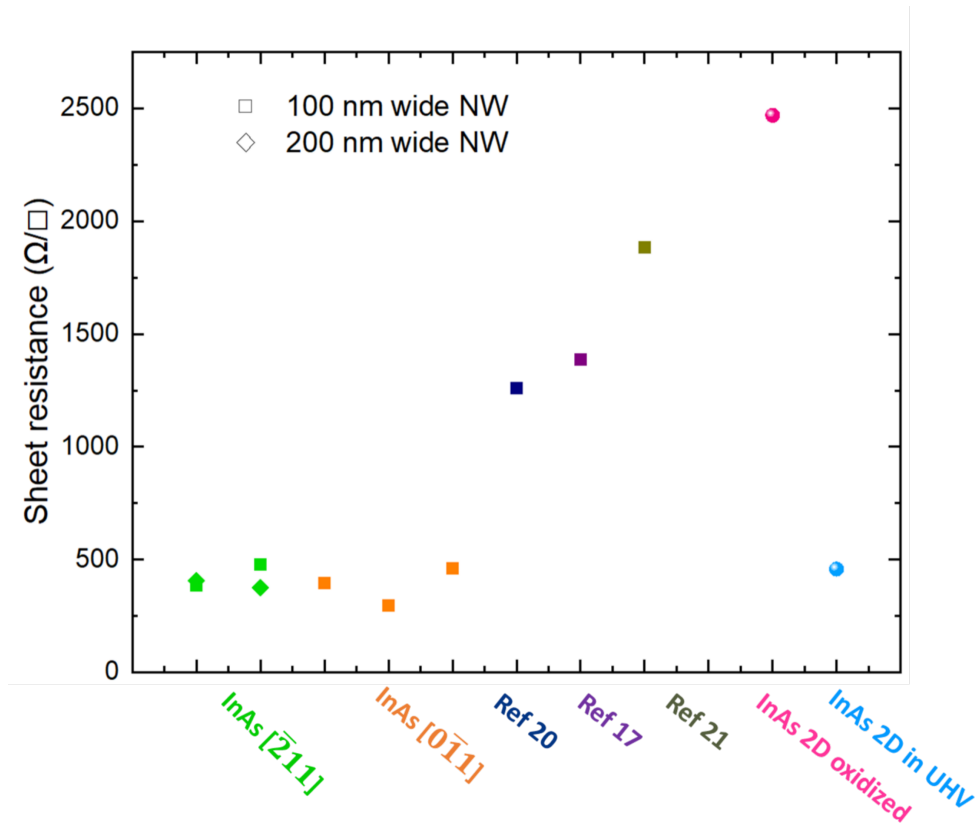


Figure 3.14 – Summary of the sheet resistances measured in InAs NWs of sample  $C_{SEL}$  and from literature benchmarked with the sheet resistance of the sample C (oxidized and non-oxidized).

The conduction inside the InAs layer decreases at low temperature for both oxidized and non-oxidized samples. This is probably due to the suppression of the bulk charge carriers at low temperature leading to a transport dominated by surface electrons.

The 1D nanostructures selectively grown along both main crystal orientations, the  $[\bar{2}11]$  and  $[0\bar{1}1]$  directions, show vertical InAs side facets whereas the nanowires grown along other intermediary directions with a rotation variation of  $10^\circ$  show trapezoid sections and present a zigzag facet shape. The sheet resistance of the 1D InAs nanostructures is similar to the sheet resistance of the InAs thin film and mostly independent of the nanostructure width at least for the  $[\bar{2}11]$  oriented nanowires with 100 nm and 200 nm nominal widths. This suggests that the transport inside the nanowires occurs mostly on the top facet on the nanowires.

The oxidation of the InAs surface reduces about 5 times the conduction inside the InAs thin film. It also degrades the conductivity of the 1D InAs nanostructures, supporting the use of a protective layer, such as an As cap layer to achieve the highest conductance.

## Bibliography

- [1] E. Y. Chang, C. I. Kuo, and H. T. Hsu, ‘InAs Quantum Well Transistors for High-Speed Low Power Applications’, *ECS Trans.*, vol. 13, no. 3, p. 75, May 2008, doi: 10.1149/1.2913082.
- [2] S. Heedt et al., ‘Signatures of interaction-induced helical gaps in nanowire quantum point contacts’, *Nat. Phys.*, vol. 13, no. 6, pp. 563–567, Jun. 2017, doi: 10.1038/nphys4070.
- [3] F. Krizek et al., ‘Field effect enhancement in buffered quantum nanowire networks’, *Phys. Rev. Mater.*, vol. 2, no. 9, p. 093401, Sep. 2018, doi: 10.1103/PhysRevMaterials.2.093401.
- [4] J. Dadras, J. H. Park, and C. Ratsch, ‘Effects of dopants on electronic surface states in InAs’, *Phys. Rev. B*, vol. 99, no. 24, p. 245406, Jun. 2019, doi: 10.1103/PhysRevB.99.245406.
- [5] M. Fahed, L. Desplanque, D. Troadec, G. Patriarche, and X. Wallart, ‘Selective area heteroepitaxy of GaSb on GaAs (001) for in-plane InAs nanowire achievement’, *Nanotechnology*, vol. 27, no. 50, p. 505301, Nov. 2016, doi: 10.1088/0957-4484/27/50/505301.
- [6] P. Aseev et al., ‘Selectivity Map for Molecular Beam Epitaxy of Advanced III–V Quantum Nanowire Networks’, *Nano Lett.*, vol. 19, no. 1, pp. 218–227, Jan. 2019, doi: 10.1021/acs.nanolett.8b03733.
- [7] V. G. Dubrovskii, ‘Criterion for Selective Area Growth of III-V Nanowires’, *Nanomaterials*, vol. 12, no. 20, Art. no. 20, Jan. 2022, doi: 10.3390/nano12203698.
- [8] F. Krizek et al., ‘Scalable quantum nanowire networks grown by molecular beam epitaxy’.
- [9] J. S. Lee et al., ‘Selective-area chemical beam epitaxy of in-plane InAs one-dimensional channels grown on InP(001), InP(111)<sub>B</sub>, and InP(011) surfaces’, *Phys. Rev. Mater.*, vol. 3, no. 8, p. 084606, Aug. 2019, doi: 10.1103/PhysRevMaterials.3.084606.
- [10] N. Moll, A. Kley, E. Pehlke, and M. Scheffler, ‘GaAs equilibrium crystal shape from first principles’, *Phys. Rev. B*, vol. 54, no. 12, pp. 8844–8855, Sep. 1996, doi: 10.1103/PhysRevB.54.8844.
- [11] P. Krogstrup et al., ‘Advances in the theory of III–V nanowire growth dynamics’, *J. Phys. Appl. Phys.*, vol. 46, no. 31, p. 313001, Aug. 2013, doi: 10.1088/0022-3727/46/31/313001.
- [12] M. Henini, ‘Molecular beam epitaxy from research to mass-production — Part 1’, III-Vs

Rev., vol. 9, no. 3, pp. 32–34, Jun. 1996, doi: 10.1016/S0961-1290(96)80125-6.

[13] M. E. Cachaza et al., ‘Selective area growth rates of III-V nanowires’, *Phys. Rev. Mater.*, vol. 5, no. 9, p. 094601, Sep. 2021, doi: 10.1103/PhysRevMaterials.5.094601.

[14] ‘Band structure and carrier concentration of Indium Arsenide (InAs)’: <http://www.ioffe.ru/SVA/NSM/Semicond/InAs/bandstr.html>.

[15] L. Ö. Olsson, C. B. M. Andersson, M. C. Håkansson, J. Kanski, L. Ilver, and U. O. Karlsson, ‘Charge Accumulation at InAs Surfaces’, *Phys. Rev. Lett.*, vol. 76, no. 19, pp. 3626–3629, May 1996, doi: 10.1103/PhysRevLett.76.3626.

[16] P. A. Alekseev et al., ‘Unified mechanism of the surface Fermi level pinning in III-As nanowires’, *Nanotechnology*, vol. 29, no. 31, p. 314003, Aug. 2018, doi: 10.1088/1361-6528/aac480.

[17] C. Durand et al., ‘Persistent enhancement of the carrier density in electron irradiated InAs nanowires’, *Nanotechnology*, vol. 24, no. 27, p. 275706, Jul. 2013, doi: 10.1088/0957-4484/24/27/275706.

[18] B. Voigtländer et al., ‘Invited Review Article: Multi-tip scanning tunneling microscopy: Experimental techniques and data analysis’, *Rev. Sci. Instrum.*, vol. 89, no. 10, p. 101101, Oct. 2018, doi: 10.1063/1.5042346.

[19] I. Miccoli, F. Edler, H. Pfnür, and C. Tegenkamp, ‘The 100th anniversary of the four-point probe technique: the role of probe geometries in isotropic and anisotropic systems’, *J. Phys. Condens. Matter*, vol. 27, no. 22, p. 223201, May 2015, doi: 10.1088/0953-8984/27/22/223201.

[20] H. Schmid et al., ‘Template-assisted selective epitaxy of III–V nanoscale devices for coplanar heterogeneous integration with Si’, *Appl. Phys. Lett.*, vol. 106, no. 23, p. 233101, Jun. 2015, doi: 10.1063/1.4921962.

[21] M. Scheffler, S. Nadj-Perge, L. P. Kouwenhoven, M. T. Borgström, and E. P. A. M. Bakkers, ‘Diameter-dependent conductance of InAs nanowires’, *J. Appl. Phys.*, vol. 106, no. 12, p. 124303, Dec. 2009, doi: 10.1063/1.3270259.

# 4

## In-plane InAs/GaSb nanostructures grown on III-V (001) substrates

### 1 Introduction

In the previous chapter, we have demonstrated the importance of the surface passivation of InAs nanowires to preserve their transport properties. Arsenic capping has been demonstrated efficient for the transfer from the MBE system to the STM set-up, but this solution is not compatible with the fabrication of nanodevices and a more robust protective solution has to be found. On the other hand, the large lattice mismatch between InAs and GaAs or InP semi-insulating substrates induces a plastic relaxation of InAs associated with the formation of dislocations that can affect the electron transport properties (even if the dislocations may be confined in the interface plane with the substrate for nanostructures). As GaSb is nearly lattice matched with InAs and exhibits a positive conduction band offset with InAs, it may provide a solution both for surface passivation and mismatch accommodation with the GaAs substrate. Such a solution is investigated in this chapter.

First, InAs/GaSb 2D heterostructures are grown on GaAs (100) and characterized with transport measurements to validate the concept and benchmark our results with InAs/AlGaSb heterostructures [1]–[4]. Then, the growth of InAs/GaSb core-shell in-plane nanostructures on InP (001) is reported. Their transport properties are studied with intrinsic conductance measurements by 4P-STM before the fabrication of elementary nano-devices and their characterization with cryogenic magneto-transport measurements at the Neel Institute.

## 2 InAs/AlGaSb 2-Dimensional-Electron-Gas (2DEG)

### 2.1 Presentation

As already discussed in chapter 1, InAs exhibits a low electron effective mass that can provide a large electron mobility at room temperature. However, it is highly mismatched to GaAs and InP wafers. A good trade-off between lattice mismatch, conduction band-offset and air stability of the barrier can be obtained using a ternary  $\text{Al}_{0.8}\text{Ga}_{0.2}\text{Sb}$  alloy. But, previous experiments performed at IEMN have shown that the MBE-selective-growth of aluminium based compounds is very complicated to achieve. This is explained by the fact that aluminium presents a strong chemical affinity with the atoms of the  $\text{SiO}_2$  mask consequently, Al based III-V semiconductors result in a high probability of nucleation on the mask. The InAs/GaSb system is thus considered as an alternative. However, it is essential to assess its transport property as a 2DEG, for the subsequent use of the heterostructure in in-plane core-shell nanostructures based on SAG. For a better understanding of the charges confinement inside the InAs/GaSb system, simulations have been carried out using the Nextnano software for both quantum wells [5].

The simulation of Figure 4.1(a) confirms the type II band line-up at the AlGaSb-InAs interfaces and the resulting confinement of electrons in the InAs channel. The advantage of the  $\text{Al}_{0.8}\text{Ga}_{0.2}\text{Sb}$  barriers resides in the large conduction band offset with respect to the InAs channel allowing good electron confinement. With a surface Fermi level assumed near the middle of the band gap of GaSb, the sheet electron density integrated over the thickness of the channel is in the  $10^{12} \text{ cm}^{-2}$  range at room temperature. As presented in Figure 4.1(b), the InAs/GaSb stack is characterized by a broken gap band line-up. Most of the states in the InAs conduction band lie clearly below the highest energy states of the GaSb valence band. This heterostructure shows also, a significant density of holes concentrated near the bottom



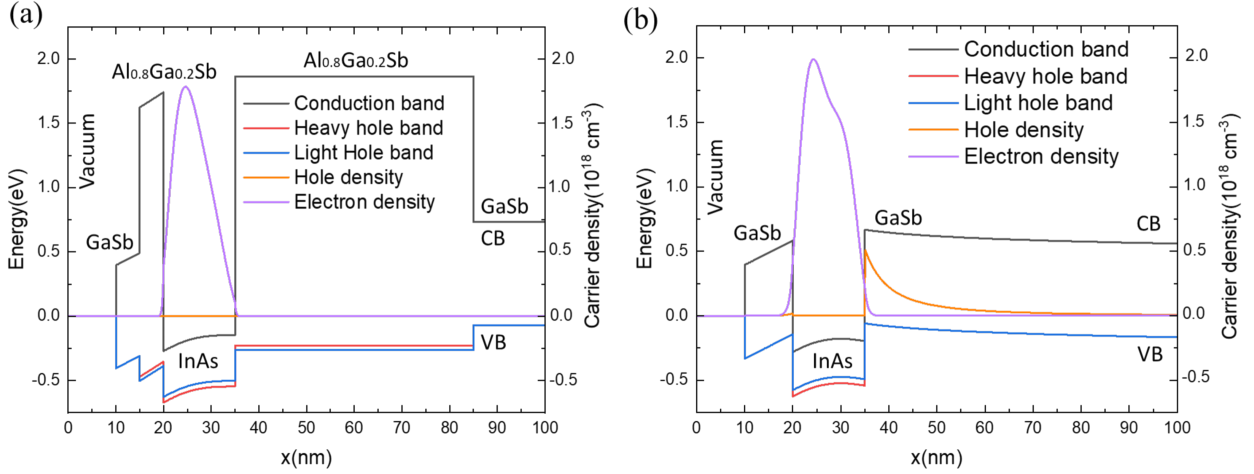


Figure 4.1 – (a) Band diagram and charge carrier distribution simulated with Nextnano simulation for the InAs/Al<sub>0.8</sub>Ga<sub>0.2</sub>Sb quantum well. (b) Band diagram and charge carrier distribution simulated with Nextnano simulation of the InAs/GaSb quantum well.

InAs-GaSb interface.

As the electron is predominantly confined in the quantum well, the InAs/Al<sub>0.8</sub>Ga<sub>0.2</sub>Sb and InAs/GaSb systems offers good prospects to build efficient n-type channels. The next section is dedicated to the growth and the transport characterization of the InAs/Al<sub>0.8</sub>Ga<sub>0.2</sub>Sb [4] and InAs/GaSb quantum wells, avoiding the use of aluminium compounds.

## 2.2 Growth conditions

The growth is performed by Molecular Beam epitaxy on semi-insulating GaAs (100) wafers. Prior to the growth, substrates are outgassed at 200°C for 1 hour under ultra-high vacuum before being transferred to the MBE chamber. In order to remove the native oxide layer from the surface, wafers are annealed at 580°C under As<sub>4</sub> flux with 1 min atomic Hydrogen flux exposure while raising-up the temperature. The deoxidization of the surface leads to a sharp RHEED pattern indicating a (2 × 4) As-terminated surface reconstruction [6]. A 100 nm thick GaAs buffer layer is then added to smooth the surface at 580°C with a growth rate of 1ML/s and an As/Ga ratio of 2.[7].

The structures of the two samples are depicted in Figure 4.2.

On top of the GaAs buffer, a 1.2 nm-thick AlSb layer is grown at 480°C as it has been proven in previous works in our group that this interlayer thickness gives a better interface structure with the GaSb buffer [8], [9]. A 1 μm thick GaSb buffer layer is subsequently deposited at

510°C with a growth rate of 0.7 ML/s and a Sb/Ga ratio of 3.5, in order to mitigate the defects and dislocations resulting from the large lattice mismatch between the GaSb film and GaAs [7].

The first sample consists of a 15 nm-thick InAs channel grown on a 50 nm thick  $\text{Al}_{0.8}\text{Ga}_{0.2}\text{Sb}$  bottom barrier and covered with a top 5 nm thick  $\text{Al}_{0.8}\text{Ga}_{0.2}\text{Sb}$  top barrier. This barrier is protected from oxidation with a 5 nm thick GaSb cap. This structure is grown at 500°C with a growth rate of 0.7 ML/s the AlGaSb layers, 0.5 ML/s for the GaSb layers and 0.5 ML/s for the InAs channel. The Sb and As fluxes were fixed at 2.5ML/s and 2ML/s respectively.

For the second sample, the  $\text{Al}_{0.8}\text{Ga}_{0.2}\text{Sb}$  barriers are replaced by pure GaSb (Figure 4.2(b)) and the growth is performed with the same conditions than for sample A.

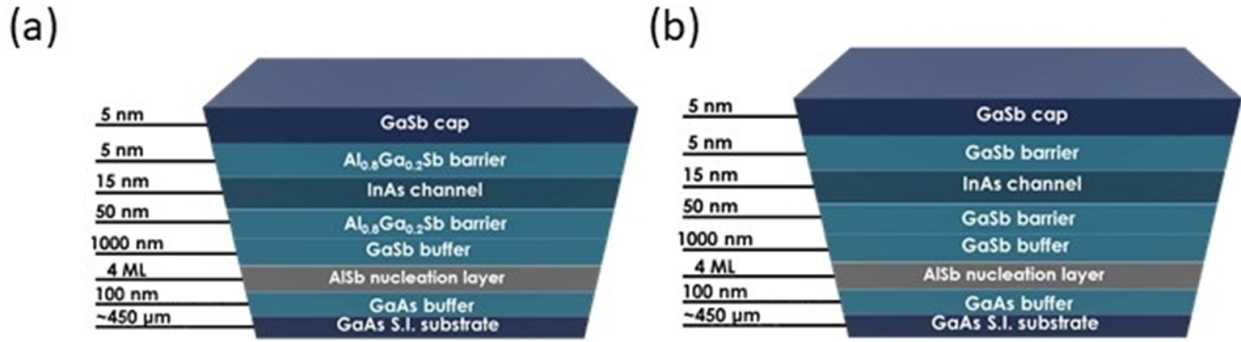


Figure 4.2 – Structures the InAs/ $\text{Al}_{0.8}\text{Ga}_{0.2}\text{Sb}$  (a) and InAs/GaSb. (b) epilayers grown on semi-insulating GaAs (100) SI.

Figure 4.3 displays the XRD spectrum of the  $\text{Al}_{0.8}\text{Ga}_{0.2}\text{Sb}/\text{InAs}$  sample. A quite good agreement between the experimental and the simulated peaks can be obtained considering a full relaxation of the 1  $\mu\text{m}$ -thick GaSb layer and the AlGaSb layers and the InAs layer being fully strained with respect to GaSb.

## 2.3 Hall effect measurements

Hall effect measurements are performed on these two samples after the definition of Hall bars mesa using optical lithography and chemical etching, as described in chapter 2. Room temperature and 77K results are summarized in Table 4.1.

At room temperature, the sample with the  $\text{Al}_{0.8}\text{Ga}_{0.2}\text{Sb}$  barriers exhibits a high electron mobility of 33500  $\text{cm}^2/\text{V} \cdot \text{s}$ . This is consistent with the best results previously achieved at IEMN for Si-doped AlSb/InAs heterostructures grown on InP substrates ( $\mu = 34300 \text{ cm}^2/\text{V} \cdot \text{s}$  at RT [1]). The measured Hall density is consistent with the electron density estimated with

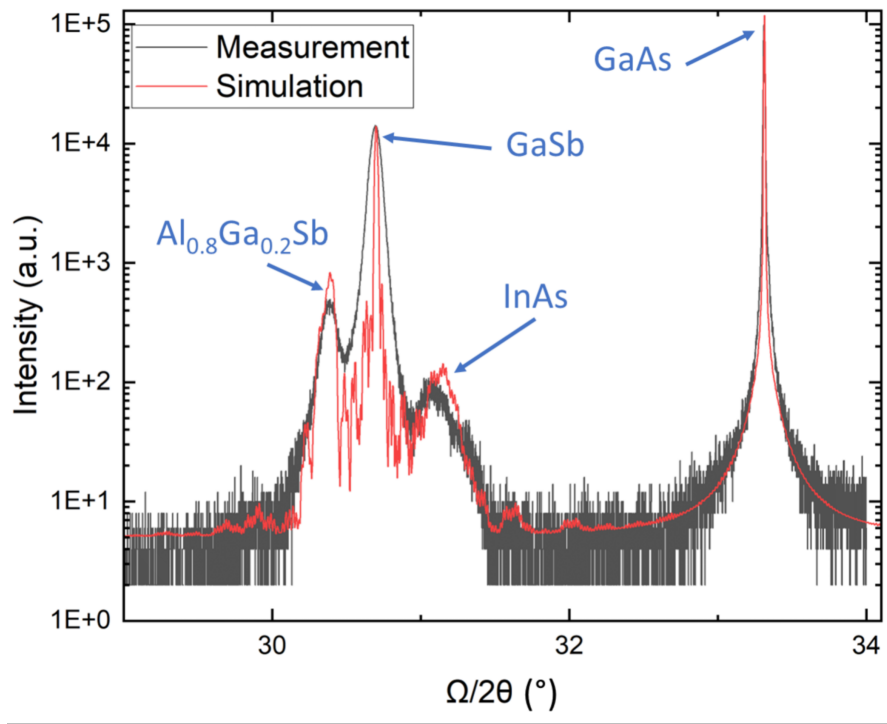


Figure 4.3 – XRD spectrum of the InAs/Al<sub>0.8</sub>Ga<sub>0.2</sub>Sb sample compared to the simulated spectrum assuming a full relaxation of the GaSb layer and fully strained InAs and AlGaSb layers with respect to GaSb.

Table 4.1 – Hall data measured on Al<sub>0.8</sub>Ga<sub>0.2</sub>Sb/InAs and GaSb/InAs heterostructures at RT and 77K.

Temperature (K)	Heterostructure	Sheet resistance ( $\Omega/\square$ )	Charges density ( $10^{12}\text{cm}^{-2}$ )	Mobility ( $\text{cm}^2/\text{Vs}$ )
77	Al <sub>0.8</sub> Ga <sub>0.2</sub> Sb/InAs	16	-1.26	301000
	GaSb/InAs	42	-1.00	150000
300	Al <sub>0.8</sub> Ga <sub>0.2</sub> Sb/InAs	117	-1.60	33500
	GaSb/InAs	114	-2.10	26000

Nextnano simulations.

At 77 K, we observe an improvement of the Hall mobility mainly due to the reduction of phonon scattering effects [8]–[10]. The measured value (above 300000  $\text{cm}^2/\text{V} \cdot \text{s}$ ) overpasses the best results achieved in the lab for Si-doped AlSb/InAs heterostructures grown on InP substrates ( $\mu = 223000 \text{ cm}^2/\text{V} \cdot \text{s}$  at 77 K [1]) probably because of the absence of Si dopants in the barrier and thus limited Coulomb interactions with this remote ionized impurities. The mobility is also similar to the 12 K mobility measured by H. R. Blank et al. for an InAs/AlGaSb quantum well grown on GaAs [11].

In the sample with GaSb barriers, the associated Hall density is larger than for InAs/AlGaSb QW and evolves from  $2.1 \times 10^{12} \text{ cm}^{-2}$  at 300 K to a lower value of  $1 \times 10^{12} \text{ cm}^{-2}$  at 77 K. This phenomenon may be related to the broken gap nature of the band offset between InAs

and GaSb that provides, as can be seen in the simulation of Figure 4.1(b), a significant concentration of holes at room temperature in the GaSb bottom barrier near the interface with the InAs quantum well. Their contribution to the Hall transport measurements may explain the lower Hall mobility in this sample.

The lower conduction band offset with bottom and top barriers for this sample also induces a larger extension of the electron wave functions in the barriers and thus a lower electron mobility. The Hall mobilities ( $26\,000\text{ cm}^2\text{V}^{-1}\text{s}^{-1}$  at RT and  $150\,000\text{ cm}^2\text{V}^{-1}\text{s}^{-1}$  at 77 K) are lower than the Hall mobilities of the sample with AlGaSb barriers, both at room temperature and 77 K.

The sheet resistance for InAs/Al<sub>0.8</sub>Ga<sub>0.2</sub>Sb and InAs/GaSb structures at room temperature are quite similar with about  $117\ \Omega/\square$  and  $114\ \Omega/\square$  respectively. However, at 77 K, the InAs/AlGaSb quantum wells exhibits a clearly lower sheet resistance ( $16\ \Omega/\square$ ) than for the InAs/GaSb one ( $42\ \Omega/\square$ ). At room temperature, the slightly lower electron mobility in InAs/GaSb QW is counterbalanced with its larger charge density. At low temperature, this is no longer the case and the larger mobility for InAs/AlGaSb QW results in a lower sheet resistance.

In the next section, the transport properties of the InAs channel are studied with four-probe STM. As mentioned before, this instrument offers the possibility of contacting nanostructures at arbitrary positions as the tungsten probes can be moved freely and make direct electrical contacts. No metal deposition is therefore required to perform measurements.

## 2.4 In-situ 4P STM Transport measurements

Both samples are introduced in the 4P-STM chamber in UHV (around  $10^{-11}$  Torr). Inside the analysis chamber of this instrument, four already prepared tungsten probes with apex diameters of a few tens of nanometers are moved down closer to the sample surface with the coarse approach. As large Hall bars mesa have been processed on the samples for the Hall measurements, the four probes are placed on the top of one of the mesa (Figure 4.4). Probes are then moved down closer to the sample using the tunnelling approach of the STM control system. After the detection of the tunnelling current, the tips are further pushed down until stable electrical contacts are achieved.

The principle of the measurements is similar to what has been performed on the InAs thin

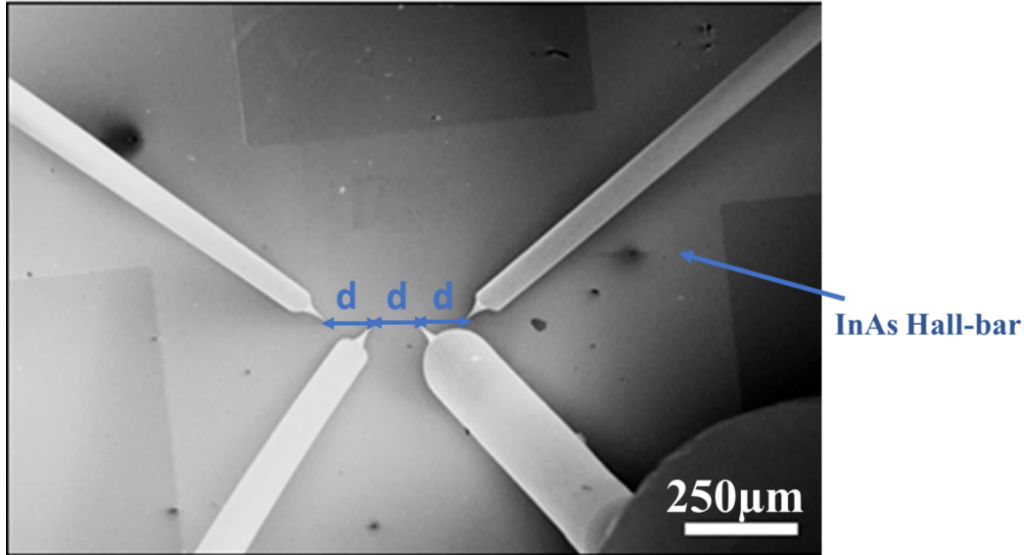


Figure 4.4 – SEM image of the four probes contacting the heterostructure surface inside the UHV analysis chamber of the four probe-STM.

films in chapter 3. It consists in injecting the current in the structure with the outer probes and measuring the voltage induced by the resistance of the layer with the inner probes. Thus, we are insensitive to the contact resistances and can measure the resistance of the layer varying the distance  $d$  between the two inner probes. We use the 4-aligned-equidistant-probe-configuration for the measurement as shown in the SEM image of Figure 4.4. According to the model presented by I. Miccoli et al. [12], the resistance for a 2DEG should be independent of the inter-probe distance  $d$  for this configuration. The 2D sheet resistance is given by equation 3.2.

#### a. InAs/AlGaSb 2DEG

The distance  $d$  between probes is varied from about  $5 \mu\text{m}$  to  $100 \mu\text{m}$ . For each measurement, the four probe resistance value is extracted from a  $V(I)$  linear curve averaged from several 4P consecutive measurements with Keithley Source-Meters. As shown in Figure 4.4 for  $d=15 \mu\text{m}$ , the applied current is varied from  $-150 \mu\text{A}$  to  $150 \mu\text{A}$ , while the voltage is measured between the two inner probes. The inset of Figure 4.5, displaying the  $I(V)$  curve measured between the two inner probes for the same distance, reveals the Schottky character of the tip/sample contacts and the importance of the 4-probe-configuration to evaluate the intrinsic resistance of the layer, independently from the contact resistance. This resistance arises from both the native oxide layer on the GaSb top layer and the AlGaSb barrier.

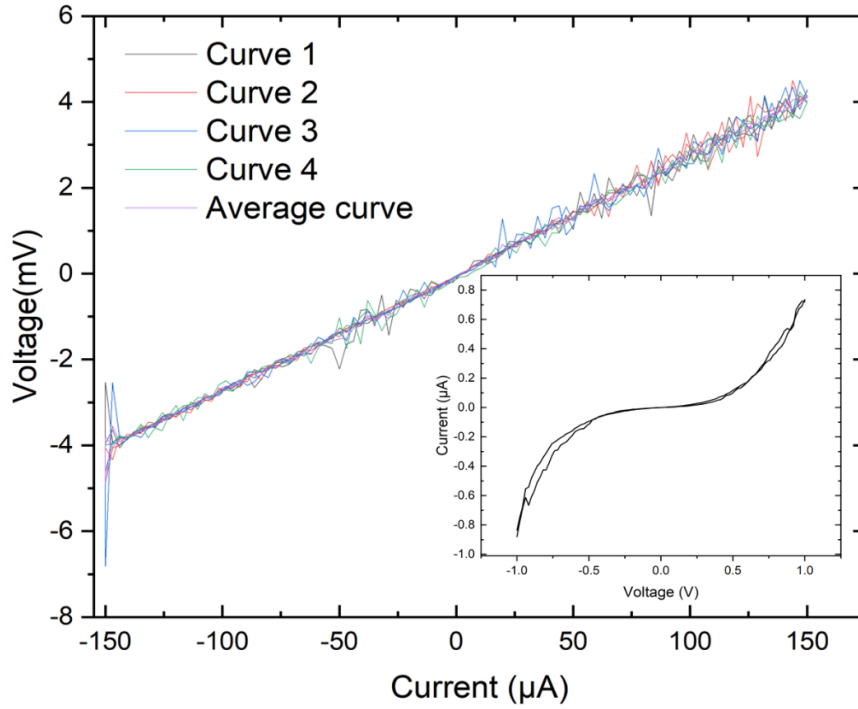


Figure 4.5 – Multiple and reproducible 4P measurement at  $d=15\mu\text{m}$ , (inset) 2P measurement for the same distance  $d=15\mu\text{m}$ .

The Table 4.2 summarizes the 4P resistances deduced from the different  $V(I)$  data measured on the InAs/Al<sub>0.8</sub>Ga<sub>0.2</sub>Sb heterostructure for  $d$  varying between 5  $\mu\text{m}$  and 100  $\mu\text{m}$ .

Table 4.2 – Four-probe-resistance with respect to the inter-probe distance  $d$  measured at 300K on the InAs/Al<sub>0.8</sub>Ga<sub>0.2</sub>Sb heterostructure.

Distance $d(\mu\text{m})$	5	10	50	100
Resistance $R_{4P}(\Omega)$	33	27	27	25

The mean four-probe resistance is 28  $\Omega$  with a small deviation of  $\pm 4 \Omega$  for more than a decade of distance range. This is consistent with the independence of the resistance with  $d$ , as described by equation 2.9. This value is about 4 times lower than the 4P-resistance measured on the oxide free InAs thin film directly grown on InP(111)<sub>B</sub> substrate studied in the previous chapter, whereas the thickness of the InAs layer is half. This confirms the positive impact of the buffer layer on the crystal quality of the InAs channel (threading dislocations and roughness). It also shows the reduction of surface scattering events when the channel is protected with a top barrier.

4P-STM measurements are also performed with the same configuration at 115K using a nitrogen flux that cools down the sample. But as the probes are at room temperature before the contact, it takes time to get them thermalized to the sample temperature. This makes the

tips unstable on the surface and the contact more complicated to achieve.

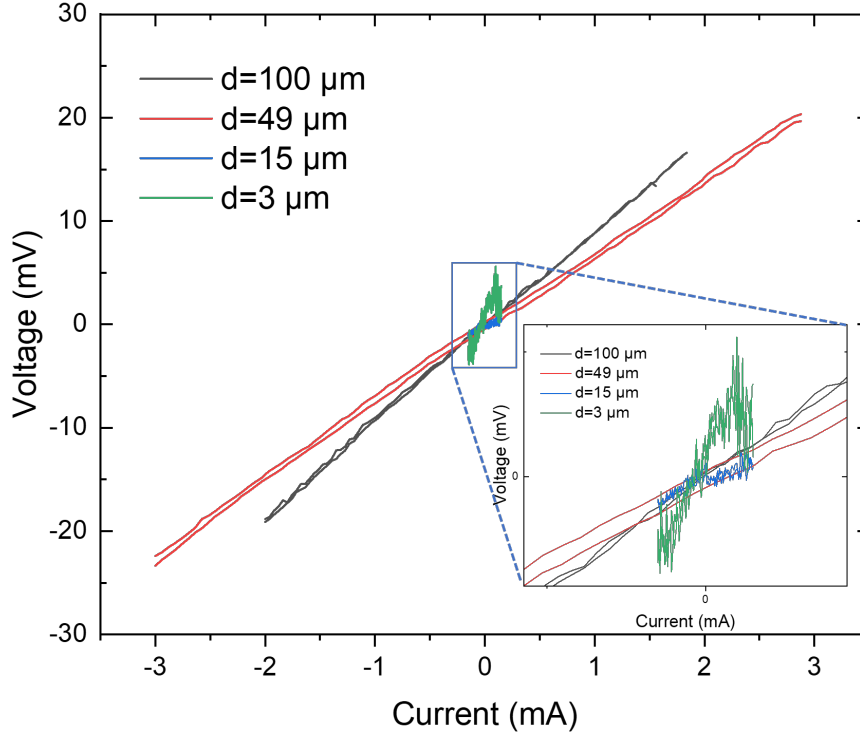


Figure 4.6 – Curves of the 4P-STM measurements for the InAs/Al<sub>0.8</sub>Ga<sub>0.2</sub>Sb quantum well at 115K for different distances  $d$  between the two inner probes.

Figure 4.6 displays the curves extracted from 4P measurements on the InAs/Al<sub>0.8</sub>Ga<sub>0.2</sub>Sb quantum well at 115K for different distances  $d$ . The red and black curves are relative to 4P measurements where the inter-probe distances  $d$  are 49  $\mu\text{m}$  and 100  $\mu\text{m}$  respectively. For these measurements the applied current is between -3 mA to 3 mA and -2 mA to 2 mA respectively. The voltage is linearly dependent on the applied current and 4P resistances can be extracted. For measurements when the distance  $d$  is about 15  $\mu\text{m}$  and 3  $\mu\text{m}$  the applied current is from -150  $\mu\text{A}$  to 150  $\mu\text{A}$ . The green and blue curves are relative to 4P measurements where the inter-probe distances  $d$  are 3  $\mu\text{m}$  and 15  $\mu\text{m}$  respectively. The curves are much noisier than the red and black curves as can be seen in the inset of the Figure 4.6. They are obtained by integrating the dc signal over one or more power line cycles (Number of Power Line Cycle NPLC), during the measurements with the Keithley tool, from 1s to 10s. This helps rejecting the noise for some of these low temperature measurements. For all these measurements at different distances we extracted the resistance values from the  $V(I)$  curves.

The mean value of the 4P-resistances extracted from the  $V(I)$  curves (Table 4.3) is 11  $\Omega$  with a deviation of  $\pm 4 \Omega$  for  $d$  varying from 3  $\mu\text{m}$  to 100  $\mu\text{m}$ . The average  $R_{4P}$  is thus two times lower than the  $R_{4P}$  value of the 2DEG at 300K.

## b. InAs/GaSb 2DEG



Table 4.3 – Four-probe-resistance against the distance  $d$  at 115K of the InAs/Al<sub>0.8</sub>Ga<sub>0.2</sub>Sb sample.

<b>Distance <math>d(\mu\text{m})</math></b>	<b>3</b>	<b>15</b>	<b>50</b>	<b>100</b>
<b>Resistance <math>R_{4P}(\Omega)</math></b>	<b>12</b>	<b>15</b>	<b>7</b>	<b>10</b>

Table 4.4 – 4P resistance against the distance  $d$  at 300K of the InAs/GaSb sample

<b>Distance <math>d(\mu\text{m})</math></b>	<b>0.7</b>	<b>2.5</b>	<b>5</b>	<b>10</b>	<b>50</b>	<b>100</b>
<b>Resistance <math>R_{4P}(\Omega)</math></b>	<b>34</b>	<b>31</b>	<b>33</b>	<b>20</b>	<b>25</b>	<b>28</b>

The Table 4.4 illustrates the 4P-resistance of the InAs/GaSb quantum well at 300K. For this sample, the mean four probe resistance is  $28.5 \Omega$  with a deviation of  $\pm 7 \Omega$  for a distance  $d$  varying by a factor of 140, from  $700 \text{ nm}$  to  $100 \mu\text{m}$ . This is, also, consistent with the theoretical resistance behaviour illustrated by the equation 2.9. The average 4P-resistance is similar to the one measured for the InAs/Al<sub>0.8</sub>Ga<sub>0.2</sub>Sb heterostructure. Due to the instability of the tips at low temperature, 4P measurements have not been performed for this sample.

## 2.5 Comparison between both techniques

Figure 4.7 summarizes the 4P measurements carried out at RT and at 115K compared to the sheet resistance values deduced from the Hall measurements at RT and 77K. A quite good agreement between both measurements is obtained indicating that the sheet resistance of the two samples at sub-millimetric range (Hall bar dimensions) does not much evolve down to the range of a few microns.

We recall that a 30 nm-thick InAs 2D layer directly grown on an InP(111) wafer, studied in chapter 3, exhibited a 4P resistance around  $101 \Omega$  at RT and  $132 \Omega$  at 115K in best cases, when non oxidized. These resistance values are higher than those obtained in the (Al)GaSb heterostructures in ambient air and UHV conditions. This highlights the interest of the (Al)GaSb buffer and cap layers for protecting the InAs film from oxidation and misfit dislocations as well as providing a quite good electron confinement inside the channel.



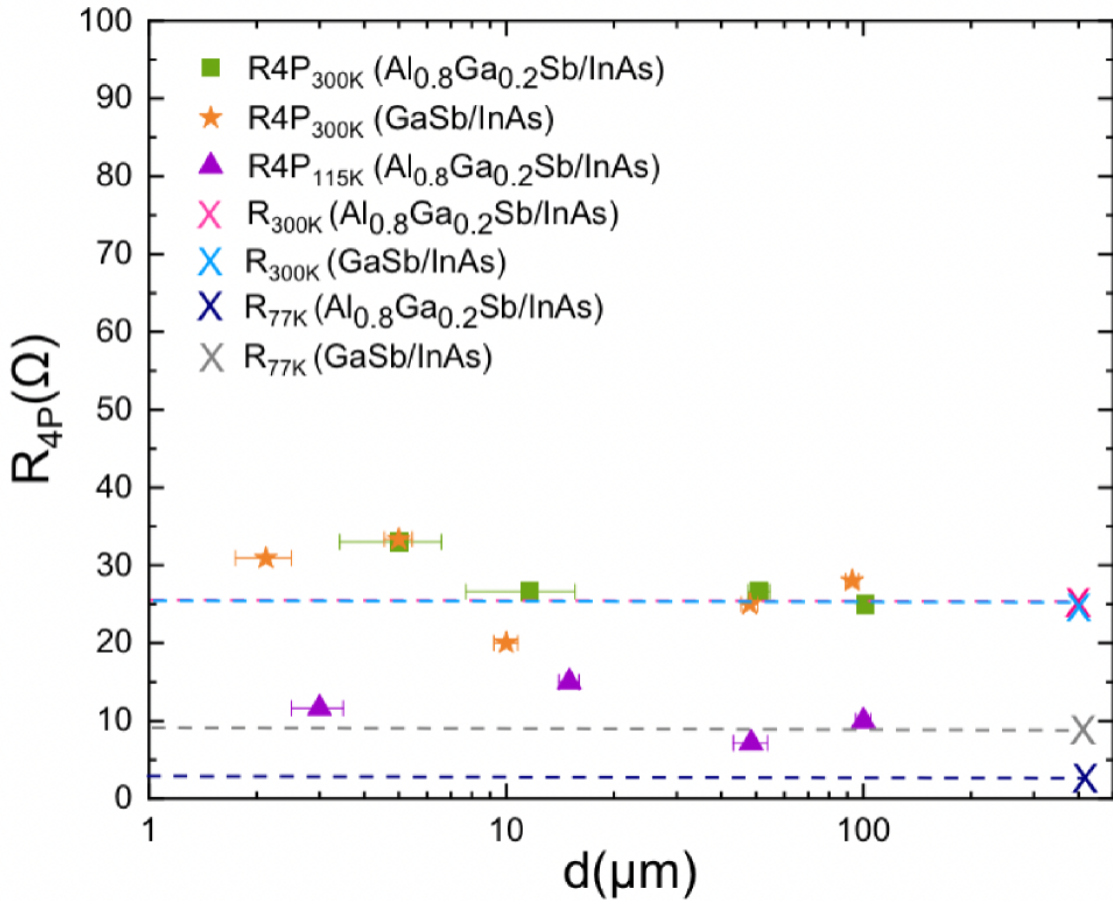


Figure 4.7 – Variation of the four-point probe resistance as a function of equidistant probe separation and equivalent four-probe resistances deduced from Hall measurements (crosses). Horizontal dash lines are projections of the Hall values over the full range of distances to guide the eye.

Moreover, the good matching between Hall resistances and the 4P ones for the InAs QWs validates the use of the 4P-STM set-up as an efficient and non-destructive tool to estimate the intrinsic conductance of in-plane nanostructures. In the next part, this set-up will be used to study the transport properties of in-plane InAs/GaSb core-shell nanowires grown by selective area MBE.

### 3 InAs/GaSb in-plane nanowires

#### 3.1 Growth conditions

In the case of selective growth, the sample preparation starts with a dielectric mask deposition on the wafer. This mask is used to control the position and the dimensions of the planar nanostructures on the wafer (See chapter 2). After the mask fabrication, the samples are

introduced in the MBE system for the growth.

Two different samples are grown on InP (001) substrates with the same conditions but using two different masks. Figure 4.8 presents the layout designed to grow one field of nanowires dedicated to four-probe measurements. The field area is about  $190 \mu\text{m} \times 170 \mu\text{m}$ . This is sufficiently large to be detected in the 4P-STM system thanks to the combined scanning electron microscope. A matrix of a few fields spaced with 3 mm between each other is patterned on a sample. Simple nanowires of different widths (50 nm, 100 nm, 200 nm and 500 nm) and lengths ( $5 \mu\text{m}$  and  $10 \mu\text{m}$ ) are fabricated, with orientations both in the  $[110]$ ,  $[0\bar{1}1]$  and  $[100]$  in-plane crystallographic directions. More complex structures like nanowires networks and rings are also designed.

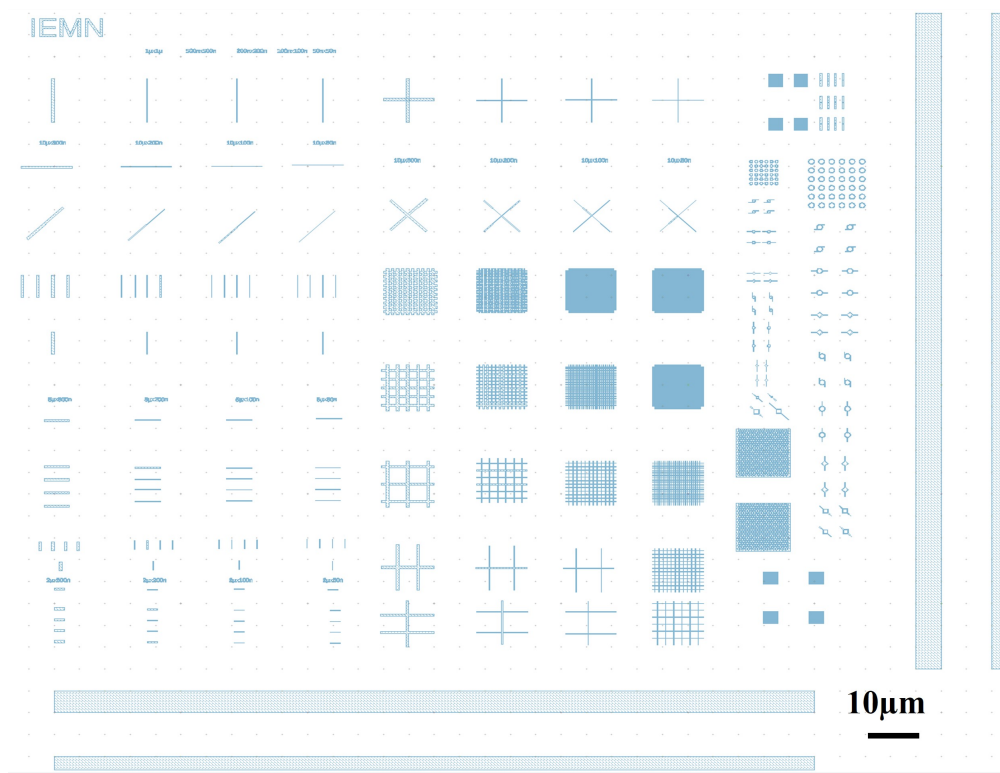


Figure 4.8 – Layout for the selectively grown nanostructures designed for the 4P-measurements. More details about the layout are given in Figure A.7 of the Appendix 2

The second mask is designed to perform electrical measurements at cryogenic temperatures and under magnetic field at Neel Institute. For this kind of measurements, metallic contacts must be deposited on the nanowires and markers have to be designed prior to the dielectric mask opening to enable the alignment of the lithographic level of metal contacts with the selective area grown nanostructures. The layout of the mask with these different devices is shown in Figure 4.9.

The markers for e-beam alignment consist of  $8 \times 8 \mu\text{m}^2$  Ti(5 nm)/Pt(50 nm) squares deposited

on the SiO<sub>2</sub> layer by e-beam lithography, metal evaporation and lift-off.

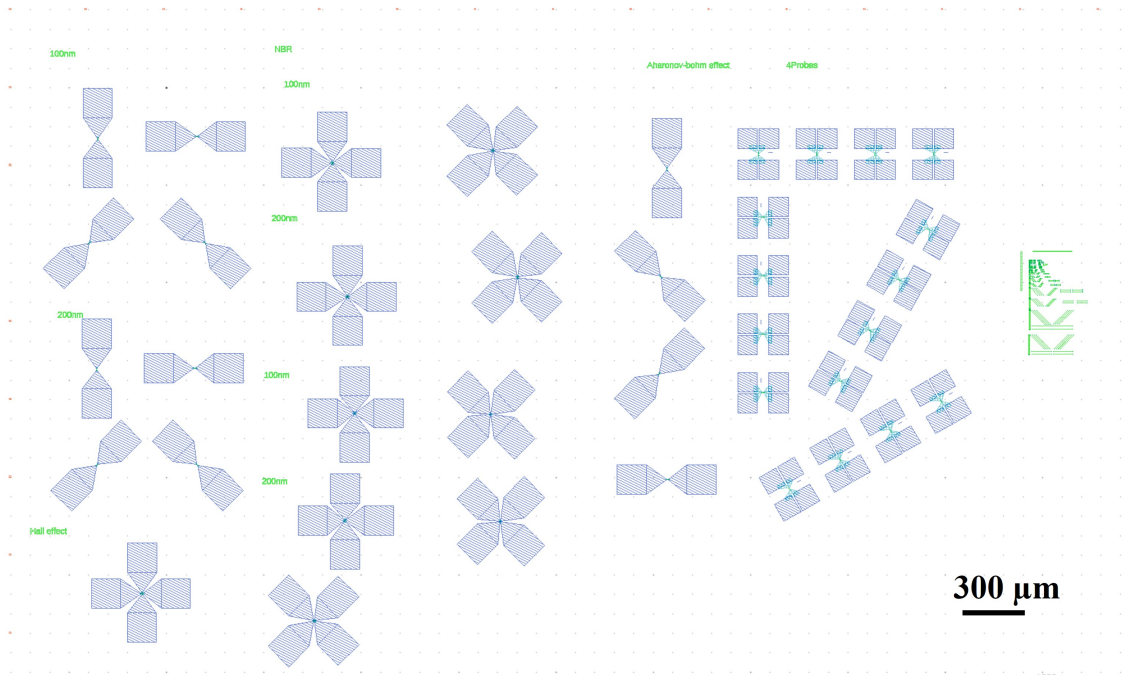


Figure 4.9 – Layout of the selectively grown nanostructures for cryogenic measurements. More details about the layout are given in Figure A.8 of the Appendix 2

After the dielectric mask opening using the method previously described in chapter 3, the samples are bonded on Si wafers with bare InP(001) wafers for RHEED and temperature control matters. Then, the samples are outgassed in the ultra-high-vacuum preparation chamber at 180°C for 1h and transferred to the III-V MBE growth chamber. Before the growth, the InP (001) wafers are deoxidized under Arsenic ( $As_4$ ) flux with an atomic Hydrogen flux exposure for 1 min while rising up the substrate temperature to 470°C.

Previous works have studied the selective growth and the integration of InAs with a GaSb buffer on GaAs (001) [13]. In our case, the growth is performed on InP (001) wafers. A GaSb buffer with a nominal thickness of 100 nm is grown under atomic H flux with a growth rate of about 0.1 ML/s and a Sb/Ga flux ratio of 2.5. After this step, the RHEED exhibits a  $(1 \times 3)$  pattern characteristics of a Sb-rich GaSb surface. 1 ML of In is deposited after the interruption of the Ga and Sb flux and before the exposure of the surface to As, in order to promote the formation of In-Sb bonds at the interface between GaSb and InAs. The idea is to balance the strain and delay the relaxation of the tensile strained InAs layer on GaSb. The channel consists of a 10 nm-thick-InAs layer with a 0.2 ML/s growth rate and an As/In flux ratio of about 5. At this stage, the RHEED exhibits a  $(2 \times 4)$  surface reconstruction. Finally, a 10 nm-thick GaSb shell is deposited with the same growth condition as the buffer layer. These growth conditions were optimized, during previous works at IEMN, to provide best

results in terms of selectivity and nanostructure continuity inside the mask openings, despite the high lattice mismatch between GaSb and InP. Indeed, M. Fahed et al. demonstrated that a relatively low temperature combined to an atomic hydrogen flux and a low Sb/Ga flux ratio during the GaSb growth ensure a good selectivity with respect to the SiO<sub>2</sub> mask, while continuous NWs can be achieved along the [1 $\bar{1}$ 0] and [110] crystallographic orientations. We note that a larger Sb/Ga flux ratio leads to the nucleation of small islands along the stripes as it favours the formation of (111)<sub>B</sub> facets [13].

A scheme of the grown structure is represented in the Figure 4.10.

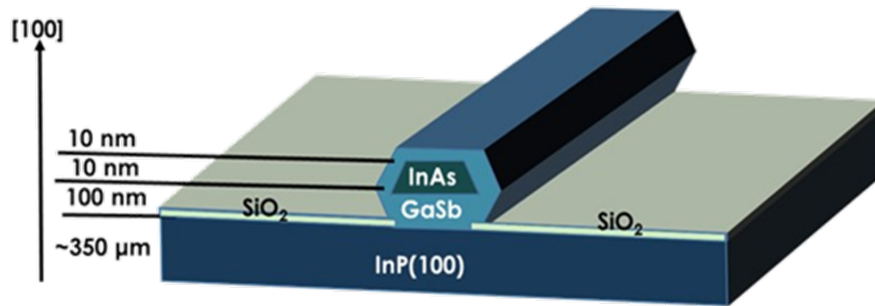


Figure 4.10 – Cross-section scheme representing the InAs/GaSb core-shell nanostructures grown on InP (001).

Figure 4.11(a) displays a SEM overview of the nanostructures after growth. Some nanostructures are highlighted in the magnified views of Figures 4.11(b) to 4.11(g): crossing NW array (b), Hall bars (c), [110], [1 $\bar{1}$ 0] or [100] oriented single NWs (d to f) and nano-rings (g). The small density of nuclei on the SiO<sub>2</sub> mask indicates a quite good selectivity. These figures show that the nanowires are continuous, up to 4 μm, along the different orientations.

Zoomed SEM images in the inset of Figures 4.11(d) and 4.11(f) clearly show the formation of well-defined facets delimiting the nanostructure shape. They are a first clue of the good crystallographic quality of the material. Transmission Electron Microscopy (TEM) and Energy Dispersive X-ray (EDX) analysis are then performed to investigate more deeply their structural characteristics. STEM lamellas are prepared by David Troadec at IEMN whereas TEM is done by Gilles Patriarche at C2N.

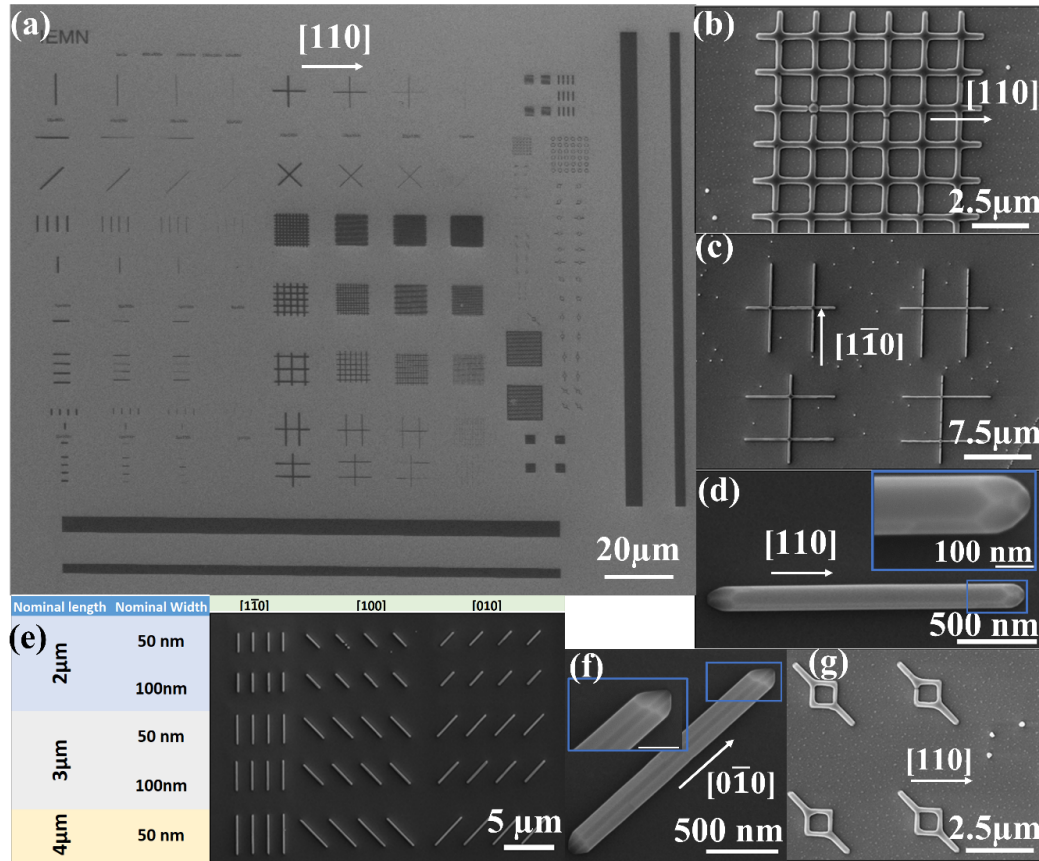


Figure 4.11 – SEM images of the InAs/GaSb selectively grown nanostructures on InP (100) SI wafers: (a) Overview of a nanostructure field. (b,c) Images of complex networks and hall bar nanoribbons. (d,e,f) Images of simple nanowires with 100 nm and 200 nm nominal widths along different crystallographic orientations, with zooms of the side facets in the insets. (g) Ring nanostructures.

### 3.2 Morphological study

Figure 4.12 displays the cross sectional High-Angle-Annular-Dark-Field (HAADF)-STEM and EDX analysis of a single InAs/GaSb NW for two different crystallographic orientations [110] and [100] and two stripes with nominal widths of 100 nm and 200 nm.

A first view of the different cross section images of the 100 nm-wide and the 200 nm-wide [110] nanowires (Figures 4.12(a-j)) confirms the formation of (111) side facets for the GaSb buffer layer with an angle of  $54^\circ$  with the substrate. For the nanostructures grown inside 100 nm wide openings, the nanostructures exhibit a hexagonal prism shape delimited by a top (001) surface, two upper  $(111)_B$  side facets and two lower  $(111)_A$  facets joining the interface with the substrate. This is consistent with the observation made by Fahed et al. [13]. The EDX images enable the identification of InAs and GaSb areas within the nanostructure cross-section. They show that the InAs channel grows on top of the (001) and  $(111)_B$  facets of the GaSb buffer. It



is fully covered with the GaSb cap layer. The embedded InAs channel is about 15 nm-thick, what is slightly larger than the nominal 10 nm thickness.

For the [100]-oriented nanowires (Figures 4.12(k) to 4.12(t)), the nanostructures look more like a flat cylinder with reduced (111) facets and vertical (010) ones appearing on the side walls. The shape of the InAs layer is also slightly different as it grows mainly on the top (001) surface of GaSb but also a little bit on the (010) vertical side walls. Almost no InAs growth can be detected on the (111) facets of GaSb.

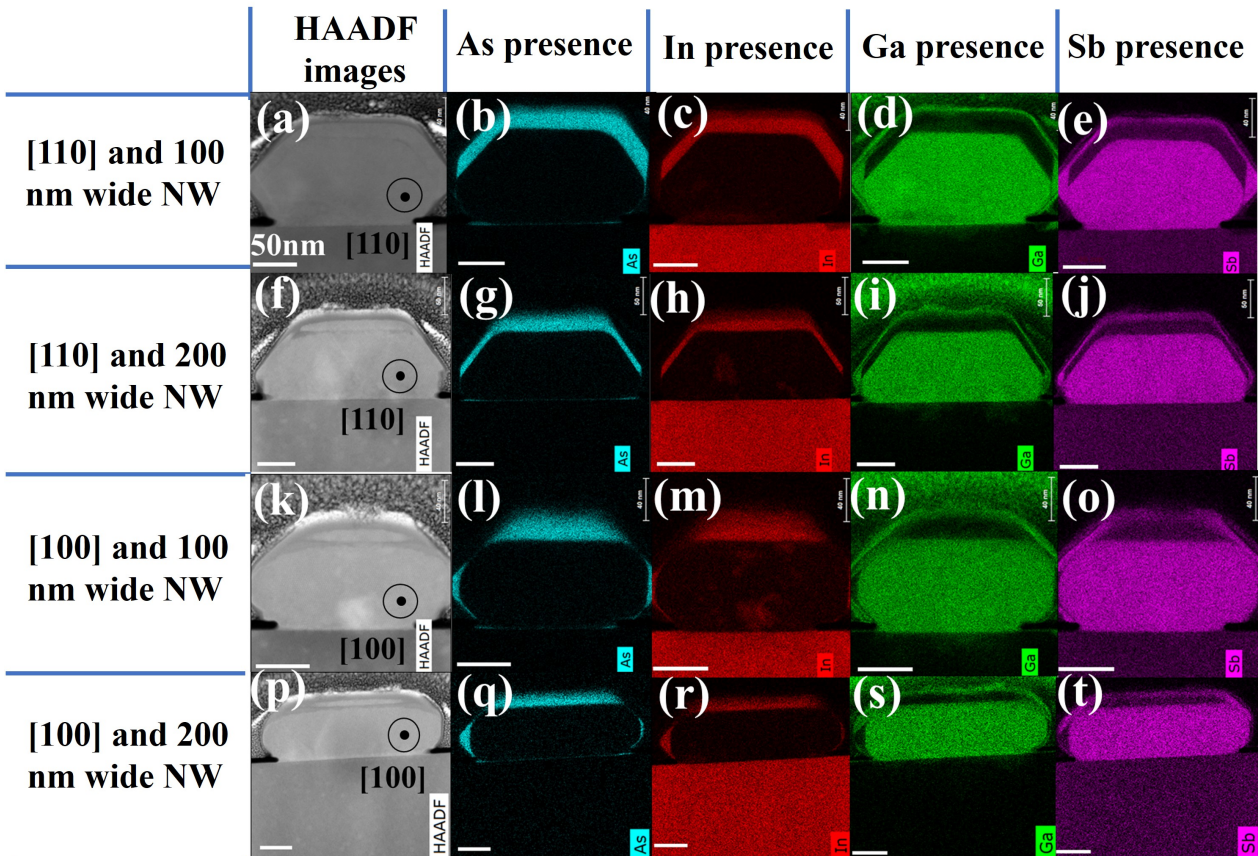


Figure 4.12 – HAADF and associated EDX micrographs of nanowires grown by SAG inside [110]-oriented openings with a nominal width of 100 nm (a-e) and 200 nm (f-j) and [100]-oriented openings with a nominal width of 100 nm (k-o) and 200 nm (p-t). The scale bar represents 50 nm.

Figure 4.13 displays cross-section TEM bright field micrographs of the nanowires presented in Figure 4.12. Threading dislocations that can be observed in the GaSb buffer are pointed out with red arrows. For both orientations, some dislocations originating from the GaSb/InP mismatched interface clearly thread up to the (001) InAs/GaSb interface. A threading dislocation is also visible for the [110]-oriented 100 nm wide nanowire (Figure 4.13(a)). However, the aspect ratio between buffer thickness and mask opening impedes the defect to reach the (001) interface between InAs and GaSb. Instead, it joins the (111) interface. On the [100]-oriented

NW, no threading defect can be clearly observed (Figure 4.13(c)).

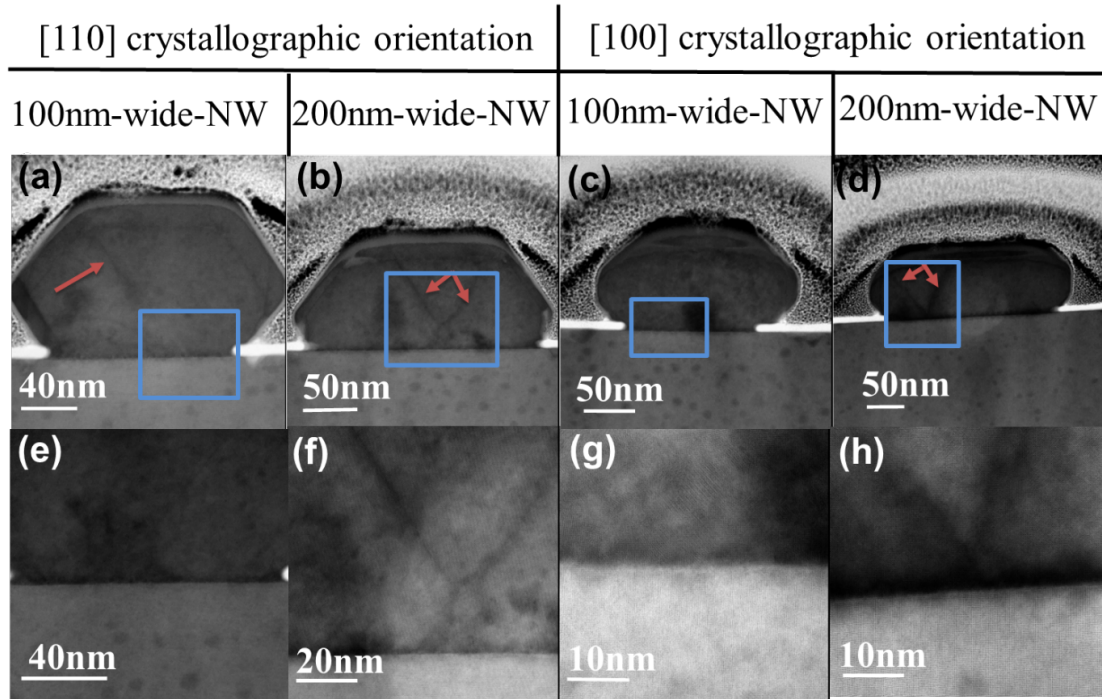


Figure 4.13 – TEM bright field micrographs of in-plane [110] or [100]-oriented InAs/GaSb NWs grown inside (a and e) a 200 nm-wide mask aperture or (b and f) a 100 nm-wide mask aperture, (c and g) a 100 nm-wide mask aperture, (d and h) a 200 nm-wide mask aperture. (e), (f), (g) and (h) are magnified views of the InP-GaSb interface inside the blue rectangles indicated in images (a), (b), (c) and (d) respectively.

In conclusion, for the narrowest nanowires, the GaSb buffer layer and shell seem to protect efficiently the InAs channel from scattering phenomena originating from mismatch accommodation with the InP substrates and from surface states. One may thus expect enhanced electronic transport properties for this “core-shell” nanostructures with respect to the one presented in chapter 3.

### 3.3 Transport measurements

In order to study the electrical properties of these nanowires, and especially their sheet resistance, four-probe STM measurements are carried out at room temperature on the sample designed with the first mask.

Compared to measurements carried out for the 2D-heterostructures, the principle of these measurements is that we move only one of the four probes positioned on the NW surface to measure the evolution of the electrical characteristics for varying distances from the injecting current probe (Figure 4.14). One advantage of this configuration is that, with only one tip that moves on the top of the nanowires we reduce the probability of degradation of the

nanostructures with the tips. At each position on the wire, a resistance value is deduced from the linear  $V(I)$  curves (Figure 4.14).

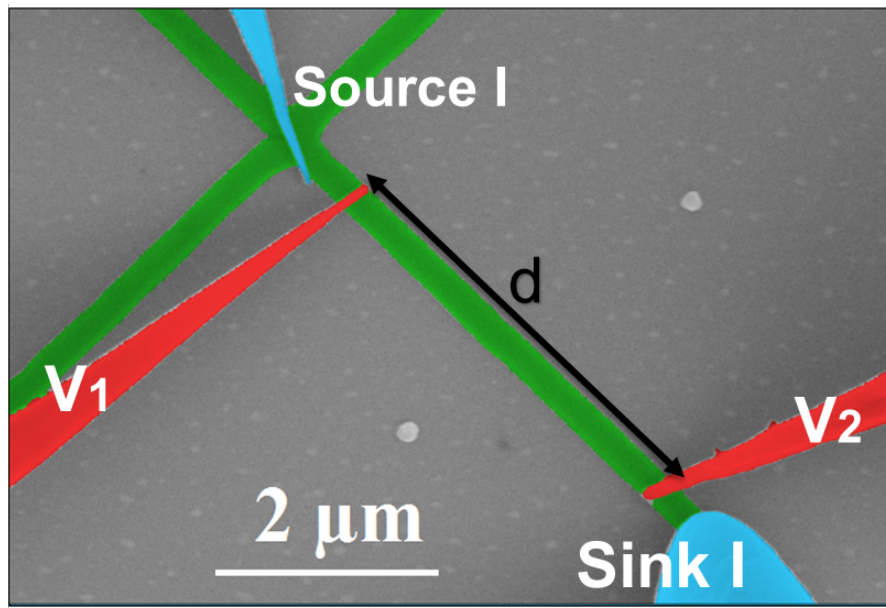


Figure 4.14 – Colorized SEM image presenting a 4P measurement performed on one branch of a cross-bar NW (in green). The current is injected and collected by external probes (blue) and the voltage is measured by the internal probes (red) separated by the distance  $d$ .

Measurements are performed on nanowires with nominal widths of 100 nm and 200 nm and grown along the [110] and [010] crystallographic orientations.

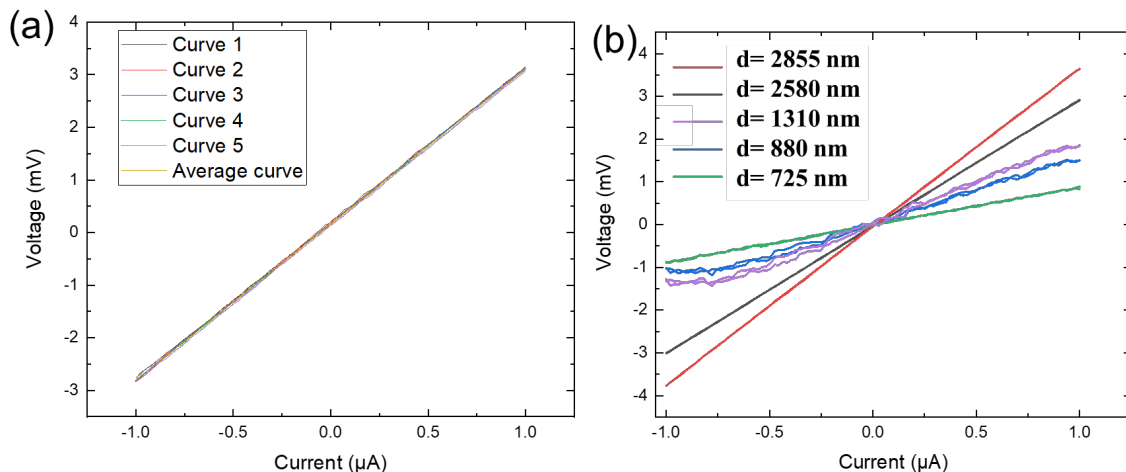


Figure 4.15 – (a) Multiple 4P measurement at  $d=2580$  nm for a 100 nm wide nanowire with the [110] orientation grown on an InP (100) SI wafer. (b) 4P averaged  $V(I)$  curves measured with different inner probe separations on the same nanostructure.

Unlike the in-plane 30 nm-thick InAs NWs directly grown on InP(111), that are studied in chapter 3, the  $\text{SiO}_2$  mask is not etched here prior to the STM measurement, as the GaSb



layer would also be etched with the HF solution used for SiO<sub>2</sub> etching [14]. Hence, the tunnelling approach of the probes on the NW surface is more complicated in this case as the insulating properties of the SiO<sub>2</sub> layer surrounding the nanostructures impedes the detection of the tunnelling current when the probe is in contact with the oxide layer. This can cause severe damages to the probe. For this reason, the four tips are manually approached and then contacted on the top of the nanostructures. In spite of these cautions, tips have been bent during the approach or some nanowires damaged during the measurements as shown in Figure 4.16.

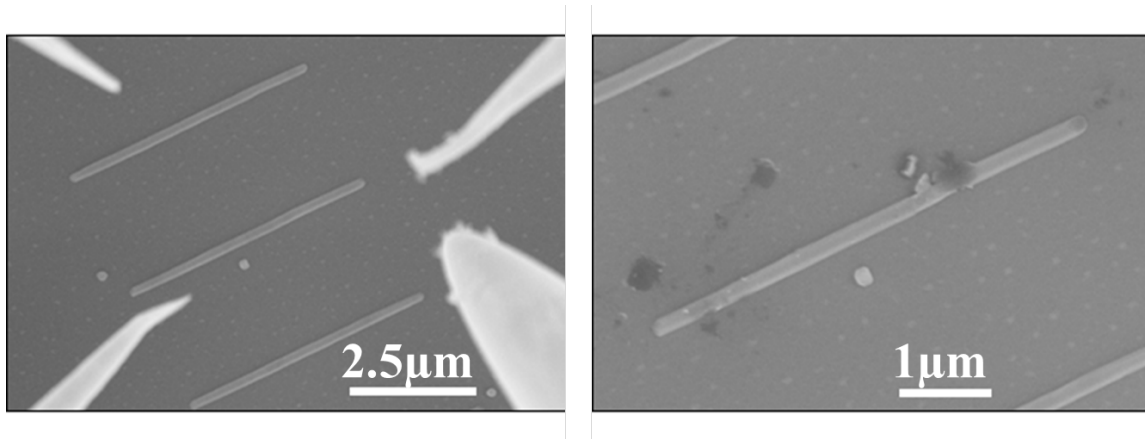


Figure 4.16 – (Left) SEM image showing the tip deterioration during the probe approach on one nanowire and (Right) SEM image presenting the nanowire after measurements.

The two graphs of Figure 4.17 show the evolution of the four-probe resistance with respect to the distance  $d$  between the two inner probes for all the measured InAs/GaSb nanowires. All these graphs exhibit a linear variation of the 4P-resistance with the distance as expected [9]. The resistance seems also quite independent to the NW direction. The uncertainty bars shown in these graphs take into account the tip diameters as explained in chapter 3.

In order to estimate the sheet resistance of the InAs channel, we use the equation linking the four probe resistance  $R_{4P}$  to the sheet resistance of the InAs channel  $R_{sheet}$ :

$$R_{sheet} = \frac{R_{4P}}{d} \cdot W \quad (4.1)$$

where  $d$  is the NW length and  $W$  the width of the InAs channel.

Based on the EDX images of Figure 4.12, the width of the InAs channel inside NWs oriented along [110] is evaluated by the addition of the width of the InAs layer on the (100) top facet of the GaSb buffer and the width of the InAs wings laying on the (111) GaSb side facets. For

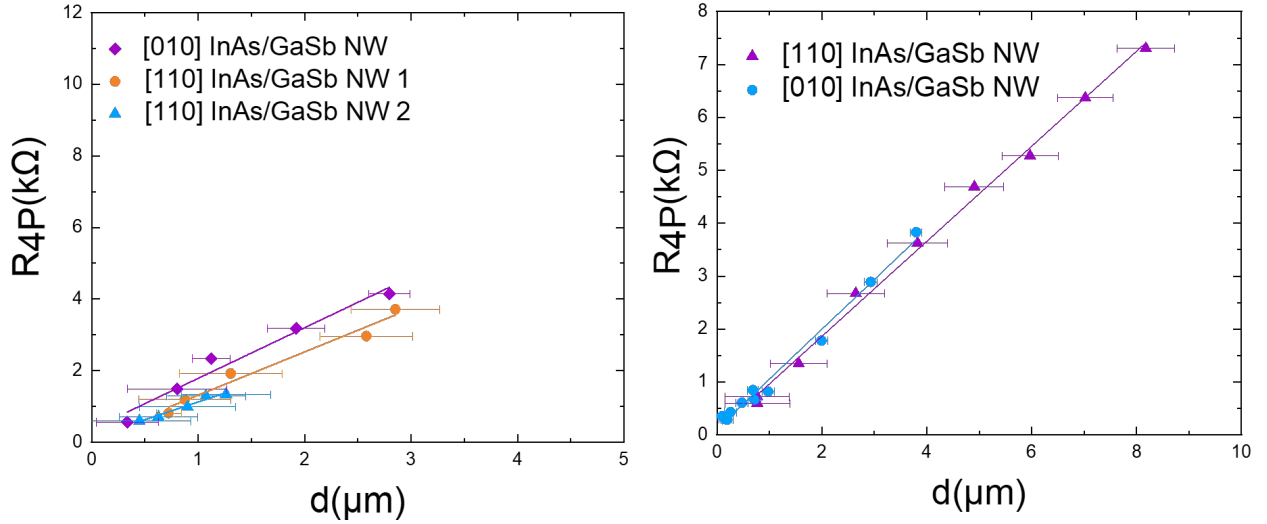


Figure 4.17 – 4P-resistance versus distance  $d$  for 100 nm wide NWs (left) or 200 nm-wide NWs (Right). Lines correspond to the best linear fit. NWs grown on an InP(100) SI wafer

NWs oriented along the [010] direction, we consider only the width of the InAs channel laying on top of the (100) top facet. We also assume that the [100]-oriented nanowires studied by STEM and TEM measurements are equivalent to [010]-oriented ones.

In Table 4.5, the widths and sheet resistances of the InAs channel measured on InAs/GaSb core-shell nanowires are listed and compared to the measurements carried out on 30 nm-thick InAs nanowires directly grown on InP(111), as detailed in the previous chapter.

Table 4.5 – Summary of the sheet resistances of all the measured nanowires.

Nominal width (nm)	Nanowire	$R_{4P}/d$ ( $\Omega/\text{nm}$ )	Real width (nm)	sheet resistance ( $\Omega/\square$ )
200	InAs/GaSb [010]	0.94	238	224
	InAs/GaSb [110]	0.89	306	273
	InAs111 $\bar{2}11$	1.62	250	405
	InAs111 $[211]_2$	1.50	250	374
100	InAs/GaSb [010]	1.40	161	225
	InAs/GaSb [110]	1.20	158	190
	InAs/GaSb [110]	0.89	158	141
	InAs $\bar{2}11$	2.86	143	384
	InAs $[211]_2$	3.34	143	479
	InAs $[211]_3$	2.77	143	397
	InAs $[0\bar{1}1]$	1.95	143	280
InAs $[0\bar{1}1]_2$	3.22	143	462	

The sheet resistance for 200 nm-wide InAs/GaSb nanowires is about  $250\Omega/\square$  as an average value of the two studied crystallographic orientations. A slight decrease of the sheet resistance can be noticed for the 100 nm-wide NWs. This could be related to the lower density of threading dislocations reaching, through the buffer, the top InAs channel, as observed with TEM

analysis. Even if some variations are measured between two different [110]-oriented NWs, it seems that the sheet resistance is slightly better along this direction.

The average sheet resistances of the different nanowires are plotted in Figure 4.18 and compared with the sheet resistance of the InAs/GaSb 2DEG. If we compare with the sheet resistance measured on 30 nm-thick-InAs NWs grown on InP(111) (sheet resistance above  $300\Omega/\square$ ), the improvement achieved with the InAs/GaSb core-shell configuration is evident with estimated values close to the 2DEG configuration.

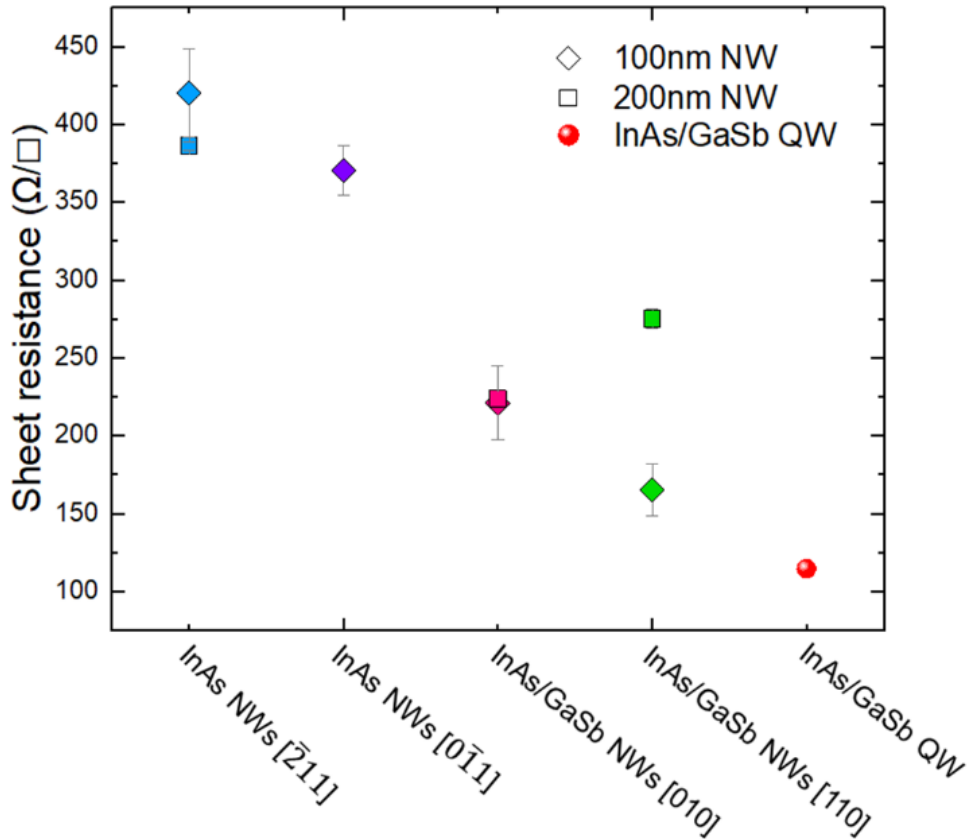


Figure 4.18 – Sheet resistance estimated from four-probe resistance measurements on all the measured NWs benchmarked with the sheet resistance of InAs/GaSb 2DEG. InAs NWs are grown on InP (111)<sub>B</sub> SI wafer, InAs/GaSb NWs are grown on an InP (100) SI wafer and InAs/GaSb QW grown on a GaAs (100) SI wafer.

### Comparison with the state of the art:

Comparing our sheet resistance with the best values published for InAs NWs in the literature is not simple because different parameters have to be taken into account (channel thickness, NW width or diameter, gate command...). For this reason, we rather compare the resistivity of the InAs channel. Assuming a real channel thickness of about 25 nm, deduced from the TEM cross-section micrographs of our nanowires (10 nm thicker than the 15 nm-nominal-channel-thickness), the resistivity of the InAs channel is  $0.5\text{ m}\Omega \cdot \text{cm}$  for 200-nm-wide nanowires and

0.45 m $\Omega$ ·cm for 100-nm-wide nanowires. This is higher than the value deduced for 2DEG with a 15 nm thick InAs channel (0.17 m $\Omega$ ·cm). However, this resistivity is more than 4 times lower than the resistivity reported by Heike Riel et al. for a 25 nm height InAs channel grown by template assisted MOCVD [15] and Y. Mols et al. for 100 nm-wide InAs fins selectively grown on Si substrates [16]. A fair comparison would however require gated or magneto-transport measurements to estimate separately the role of charge density and electron mobility in the resistivity and to assess the crystal quality.

Based on the sheet carrier density of the InAs/GaSb quantum well measured by Hall effect, we could assume a sheet electron density of  $2.1 \times 10^{12}$  cm $^{-2}$ . In this case, the electron mobility inside the 100 nm wide InAs/GaSb core-shell NWs would be of about 20000 cm $^2$ /V·s at room temperature. This estimation is about 11 times larger than the RT Hall mobility measured on InAs NWs grown by TASE [15].

Assuming such a mobility, we can estimate an electron mean free path larger than  $1\mu\text{m}$  at room temperature according to equation 4.2 [17].

$$l_e = \frac{\hbar\sqrt{2\pi n_s}}{q} \cdot \mu \quad (4.2)$$

where  $l_e$  is the electrons mean free path inside the channel,  $\mu$  refers to the charge mobility,  $h$  refers to Planck's constant,  $n_s$  corresponds to the sheet charges density and  $q$  to the elementary charge.

This value is about 6 times larger than the 150 nm mean free path reported by S.Chuang et al. in an InAs nanowire with a radius of 34 nm [18].

In order to confirm these estimations, magneto-transport measurements at cryogenic temperatures in the Neel institute are performed with dedicated devices. Their fabrication is detailed in the following part.

### 3.4 Device fabrication for magneto-transport measurements

For the cryogenic measurements, as these kind of measurements cannot be performed in 4P-STM setup, metal deposition is necessary in order to contact the nanowires.

Based on the lift-off process presented in the Chapter 2, small area pads consisting of a Ti/Pt

(5 nm /50 nm) metal bilayer is first deposited on some part of the NWs. Larger (150 x 150  $\mu\text{m}^2$ ) and thicker (100 nm Ti/400 nm Au) metal pads are then evaporated to enable the wire bonding for cryogenic measurements. Different devices are studied: single NWs with two contacts, single NWs with 4 contacts, NW crosses with 4 contacts (Figure 4.19(a)) and ring structures for Aharonov-Bohm phase-coherent transport investigation (Figure 4.19(b)). The inset of the Figure 4.19(b) shows some discontinuities in the Ti/Pt layer at the NW edges.

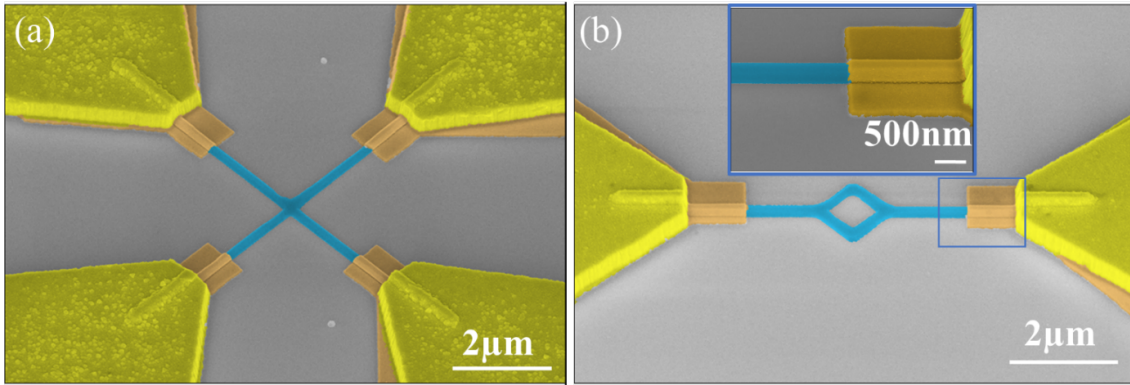


Figure 4.19 – False coloured tilted SEM images of InAs/GaSb based devices. The blue coloured patterns are the InAs/GaSb NWs, the orange coloured layers correspond to the (Ti/Pt) layers and the yellow coloured structures refer to the (Ti/Au) thick contacts. (a) NWs junctions-based devices, (b) Aharonov-Bohm (rings) nanostructure-based devices. The inset in (b) is a zoomed SEM image on the part of the nanostructure where the (Ti/Pt) contacts are deposited.

Cryogenic measurements are carried out by Hermann Sellier at the Néel Institute. The measurements are performed at 0.3K. Figure 4.20 displays a 4P-magneto resistance variations with respect to the perpendicular magnetic field in a Hall configuration ( $R = \frac{\text{transverse voltage}}{\text{longitudinal current}}$ ) for a device fabricated from two perpendicular NWs in the [100] and [010] crystallographic orientations (Figure 4.19(a)). The 4P Hall magneto-resistance is linearly varying with the magnetic field with a slope of about 750  $\Omega/\text{T}$ . As the sheet resistance deduced from 2P-measurements of the NW is about 170  $\Omega/\square$ , the estimated electron density and mobility are about  $8.3 \times 10^{11} \text{ cm}^{-2}$  and 44000  $\text{cm}^2/(\text{V} \cdot \text{s})$ .

Figure 4.21 displays the magneto-resistance measurements performed at 0.3K on a single NW with four contacts. The small variations of the resistance with the magnetic field are attributed to Universal Conductance Fluctuations (UCF) indicating that coherent interference phenomena occur within the NW.

Concerning the mean value of the magneto-resistance, it differs by a factor of about 3 between single 2P-NW and 4P-NW. The sheet resistance and mobility deduced from the magneto-resistance for a 12  $\mu\text{m}$  long NW in the 2P configuration (Figure 4.21(a)) are respectively 240  $\Omega/\square$  and 31000  $\text{cm}^2/(\text{V} \cdot \text{s})$  with a symmetric  $R_{2P}(B)$  curve. We consider that 2P

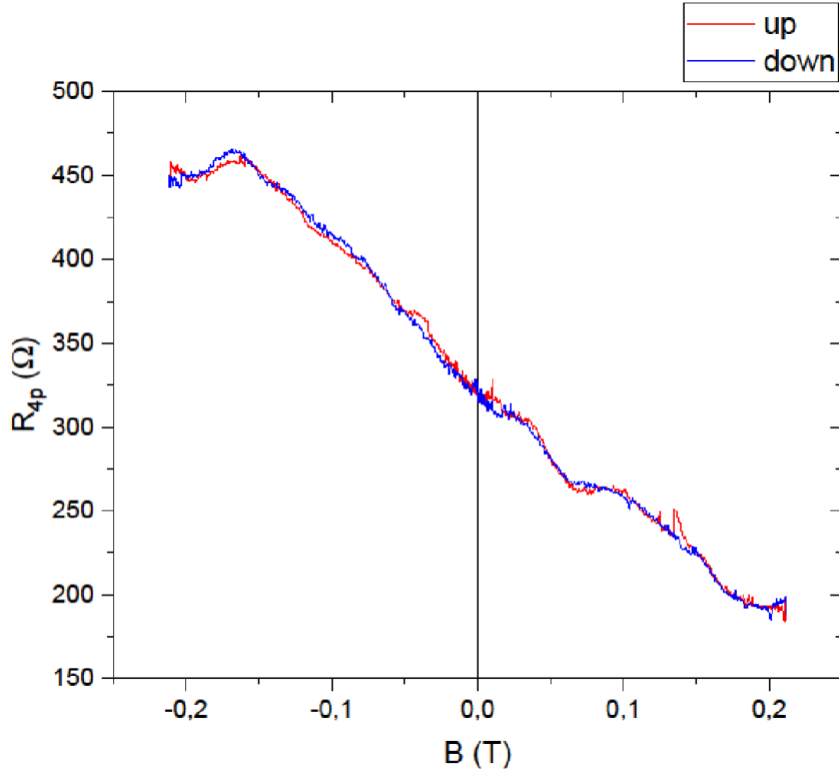


Figure 4.20 – Magneto-resistance variations depending to the applied magnetic field of InAs/GaSb junction of two perpendicular 100 nm-wide and 4.25  $\mu\text{m}$  long NWs grown along the [100] and [010] orientations.

measurements are not relevant for quantitative analysis due to the large contact resistance. With a 4P configuration on the same NW, the magneto-resistance of a 2  $\mu\text{m}$  long segment reveals a sheet resistance of 67  $\Omega/\square$  associated to an electron mobility of 110000  $\text{cm}^2/(\text{V} \cdot \text{s})$ . These values are estimated considering the mean distance between the 1  $\mu\text{m}$  long inner metal contacts. If we consider instead, the length of the NW between the metal contacts (about 1  $\mu\text{m}$ ), the sheet resistance is double and thus the resulting electron mobility is half (55000  $\text{cm}^2/(\text{V} \cdot \text{s})$ ).

Eventually, from the correlation field of the oscillating  $R_{4P}(B)$  (correlation field = typical distance between features), a phase coherence length larger than 400 nm can be deduced but temperature dependent measurements have to be carried out for a more accurate determination.

To our knowledge, these values are larger than all reported electron mobility inside InAs NWs. The 44000  $\text{cm}^2/(\text{V} \cdot \text{s})$  value measured on the crossing NWs is 5 times higher than the reported electron mobility inside 440 nm-wide and  $\langle 110 \rangle$ -oriented-InAs NWs demonstrated by Cui et al. (about 8000  $\text{cm}^2/(\text{V} \cdot \text{s})$ ) [19], confirming the crucial impact of surface passivation.

Negative-bend-resistance measurements (discussed in chapter 1, section 1.3) carried out on crossing NWs have also been observed up to 10K but further experiments are needed to confirm this observation and clearly demonstrate ballistic effects. In the same vain, Aharonov-Bohm oscillations could not be observed on ring nano-structures probably because of the two large number of conductance channels in the nanostructure. For such kind of measurements, a back or top gate is highly desirable to tune the charge density and thus the number of conducting channels in the nanostructure.

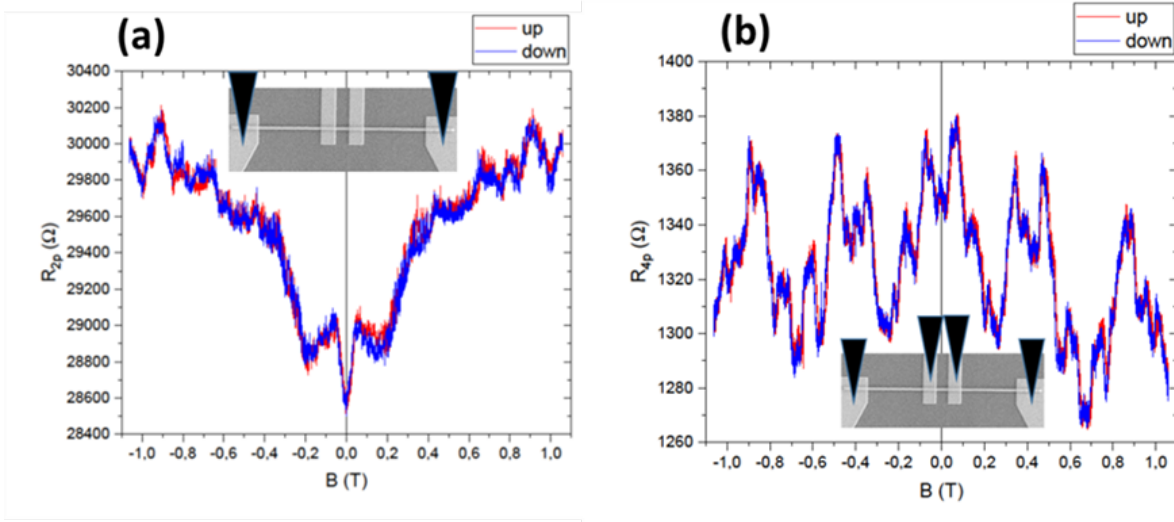


Figure 4.21 – Magneto-transport measurements performed at 0.3K on single NW with 12  $\mu\text{m}$  2P (a) or 2  $\mu\text{m}$  4P (b) configuration.

## 4 Conclusion

The InAs/ $\text{Al}_{0.8}\text{Ga}_{0.2}\text{Sb}$  and InAs/GaSb quantum wells grown on GaAs (001) are highly conductive with consistent 4P-STM and Hall effect resistances both about 28  $\Omega$  at 300K. The Hall mobility inside the former heterostructure is slightly larger than the one inside the InAs/GaSb quantum well. This is explained by the stronger electron confinement caused by the higher conduction band offset with AlGaSb barriers than with GaSb ones.

The mobility at liquid nitrogen temperature increases up to state of the art values for AlGaSb/InAs QW and, although slightly degraded for the GaSb/InAs QW, it is clearly better than the one measured inside the 30 nm-thick-InAs channel directly grown on the InP(111) wafer in the chapter 3. For the GaSb/InAs QW, the transport properties are compatible with mesoscopic transport experiments. The 1D InAs/GaSb core shell nanowires grown by SAG exhibit also a low sheet resistance close to the InAs/GaSb QW at room temperature,



particularly for [110] oriented nanostructures with shrunk mask opening width, and consistently with the STEM study that shows a lower threading defect density in this case. We also notice an improved conductivity for in-plane InAs/GaSb core-shell NWs with respect to the 30 nm-thick in-plane InAs NWs directly grown on InP(111) discussed in the previous chapter.

Even if ballistic phenomena inside the in-plane nanostructures couldn't be clearly evidenced for now, the electron mobility that could be estimated from 4P-STM measurements (up to  $20000 \text{ cm}^2/(\text{V} \cdot \text{s})$  at 300 K) and cryogenic magneto-transport experiments (larger than  $55000 \text{ cm}^2/(\text{V} \cdot \text{s})$  at 0.3 K) bears the comparison with state of the art values for comparable InAs NW.

## Bibliography

- [1] L. Desplanque, D. Vignaud, and X. Wallart, ‘High mobility metamorphic AlSb/InAs heterostructures grown on InP substrates’, *J. Cryst. Growth*, vol. 301–302, pp. 194–198, Apr. 2007, doi: 10.1016/j.jcrysgro.2006.11.229.
- [2] G. Moschetti et al., ‘Anisotropic transport properties in InAs/AlSb heterostructures’, *Appl. Phys. Lett.*, vol. 97, no. 24, p. 243510, Dec. 2010, doi: 10.1063/1.3527971.
- [3] Y. Wang et al., ‘Antimony-Mediated Control of Misfit Dislocations and Strain at the Highly Lattice Mismatched GaSb/GaAs Interface’, *ACS Appl. Mater. Interfaces*, vol. 5, no. 19, pp. 9760–9764, Oct. 2013, doi: 10.1021/am4028907.
- [4] A. Westlund et al., ‘Nanochannel diodes based on InAs/Al<sub>80</sub>Ga<sub>20</sub>Sb heterostructures: Fabrication and zero-bias detector properties’, *J. Vac. Sci. Technol. B*, vol. 33, no. 2, p. 021207, Mar. 2015, doi: 10.1116/1.4914314.
- [5] ‘nextnano - Software for semiconductor nanodevices’. Accessed: Sep. 25, 2023. [Online]. Available: <https://www.nextnano.de/>
- [6] L. Desplanque et al., ‘AlSb nucleation induced anisotropic electron mobility in AlSb/InAs heterostructures on GaAs’, *Appl. Phys. Lett.*, vol. 100, no. 26, p. 262103, Jun. 2012, doi: 10.1063/1.4730958.
- [7] Y. Wang, P. Ruterana, L. Desplanque, S. El Kazzi, and X. Wallart, ‘Strain relief at the GaSb/GaAs interface versus substrate surface treatment and AlSb interlayers thickness’, *J. Appl. Phys.*, vol. 109, no. 2, p. 023509, Jan. 2011, doi: 10.1063/1.3532053.
- [8] V. Gopal, V. Souw, E.-H. Chen, E. P. Kvam, M. McElfresh, and J. M. Woodall, ‘Temperature-dependent transport properties of InAs films grown on lattice-mismatched GaP’, *J. Appl. Phys.*, vol. 87, no. 3, pp. 1350–1355, Feb. 2000, doi: 10.1063/1.372062.
- [9] N. Gupta et al., ‘Temperature-dependent electron mobility in InAs nanowires’, *Nanotechnology*, vol. 24, no. 22, p. 225202, Apr. 2013, doi: 10.1088/0957-4484/24/22/225202.
- [10] X. Zianni, C. D. Simserides, and G. P. Triberis, ‘Electron scattering by optical phonons in Al<sub>x</sub>Ga<sub>1-x</sub>As/GaAs/Al<sub>x</sub>Ga<sub>1-x</sub>As quantum wells’, *Phys. Rev. B*, vol. 55, no. 24, pp. 16324–16330, Jun. 1997, doi: 10.1103/PhysRevB.55.16324.
- [11] H.-R. Blank, M. Thomas, K. C. Wong, and H. Kroemer, ‘Influence of the buffer layers

on the morphology and the transport properties in InAs/(Al,Ga)Sb quantum wells grown by molecular beam epitaxy’, *Appl. Phys. Lett.*, vol. 69, no. 14, pp. 2080–2082, Sep. 1996, doi: 10.1063/1.116886.

[12] I. Miccoli, F. Edler, H. Pfnür, and C. Tegenkamp, ‘The 100th anniversary of the four-point probe technique: the role of probe geometries in isotropic and anisotropic systems’, *J. Phys. Condens. Matter*, vol. 27, no. 22, p. 223201, May 2015, doi: 10.1088/0953-8984/27/22/223201.

[13] M. Fahed, L. Desplanque, D. Troadec, G. Patriarche, and X. Wallart, ‘Selective area heteroepitaxy of GaSb on GaAs (001) for in-plane InAs nanowire achievement’, *Nanotechnology*, vol. 27, no. 50, p. 505301, Nov. 2016, doi: 10.1088/0957-4484/27/50/505301.

[14] E. M. Costa, B. A. Dedavid, and A. Müller, ‘Investigations of structural defects by etching of GaSb grown by the liquid-encapsulated Czochralski technique’, *Mater. Sci. Eng. B*, vol. 44, no. 1, pp. 208–212, Feb. 1997, doi: 10.1016/S0921-5107(96)01747-3.

[15] J. Gooth et al., ‘Ballistic One-Dimensional InAs Nanowire Cross-Junction Interconnects’, *Nano Lett.*, vol. 17, no. 4, pp. 2596–2602, Apr. 2017, doi: 10.1021/acs.nanolett.7b00400.

[16] Y. Mols et al., ‘Structural analysis and resistivity measurements of InAs and GaSb fins on 300 mm Si for vertical (T)FET’, *J. Appl. Phys.*, vol. 125, no. 24, p. 245107, Jun. 2019, doi: 10.1063/1.5096015.

[17] Ch. A. Lehner et al., ‘Limiting scattering processes in high-mobility InSb quantum wells grown on GaSb buffer systems’, *Phys. Rev. Mater.*, vol. 2, no. 5, p. 054601, May 2018, doi: 10.1103/PhysRevMaterials.2.054601.

[18] S. Chuang, Q. Gao, R. Kapadia, A. C. Ford, J. Guo, and A. Javey, ‘Ballistic InAs Nanowire Transistors’, *Nano Lett.*, vol. 13, no. 2, pp. 555–558, Feb. 2013, doi: 10.1021/nl3040674.

[19] Z. Cui, R. Perumal, T. Ishikura, K. Konishi, K. Yoh, and J. Motohisa, ‘Characterizing the electron transport properties of a single  $\langle 110 \rangle$  InAs nanowire’, *Appl. Phys. Express*, vol. 7, no. 8, p. 085001, Jul. 2014, doi: 10.7567/APEX.7.085001.

# 5

## MBE growth and characterization of InSb nanostructures

### 1 Introduction

As shown in chapter 1, InSb is a very interesting III-V semiconductor for spintronics [1] and quantum computer conception [2][3]. For these applications, in-plane InSb nanowire networks with very good surface properties are highly desired. The existing scalable bottom-up methods to produce such arrays consist mainly of selective area atomic hydrogen assisted MBE-SAG on AlGaSb (100) [4], MOCVD SAG [3] or metal-sown MBE on InP(111) substrate [5]. In this chapter, atomic hydrogen assisted MBE-SAG of InSb on InP wafers is investigated. After optimizing the nucleation conditions, InSb nanostructures are fabricated and their morphology and surface properties are analysed using SEM, AFM and low temperature STM. A process for the deoxidization of the InSb surface after the transfer from MBE to STM is proposed.

## 2 InSb growth optimization on InP wafers

The lattice mismatch between InSb and InP is 10.4%. Optimizing the growth conditions is crucial for the fabrication of high crystal quality in-plane InSb nanostructures. In this part, we focus on the growth of InSb on InP(100) and InP(111) wafers.

### 2.1 Nucleation of InSb on un-masked InP(100)

#### a. Growth conditions

In order to study the nucleation of InSb on InP, a nominal thickness of InSb of only 10 nm is deposited on InP. Different sets of samples are grown to study the impact of the growth rate, the growth temperature and the Sb/In flux ratio on the nucleation.

First, InP (100) wafers are loaded and outgassed in ultrahigh vacuum at 200°C for 1h and then transferred to the MBE growth chamber. After that, they are deoxidized under an As<sub>4</sub> flux combined with an atomic hydrogen flux for 30s and progressively increasing the substrate temperature from 300°C to 470°C. The growth conditions of the different samples are summarized in Table 5.1. All samples are grown with conditions compatible with selective area growth (low growth rate and atomic hydrogen flux). For the first set (samples V1<sub>100</sub>, V2<sub>100</sub> and V3<sub>100</sub>), the growth rate is varied from 0.05 to 0.2 ML/s whereas constant growth temperature of 390°C and Sb flux of 2ML/s are used. For the second set of samples (samples T1<sub>100</sub> and T2<sub>100</sub>), two different temperatures are studied (390°C and 405°C) while constant growth rate of 0.05 ML/s and Sb flux of 6 ML/s are used.

Table 5.1 – Growth conditions of V1<sub>100</sub>, V2<sub>100</sub>, V3<sub>100</sub>, T1<sub>100</sub> and T2<sub>100</sub> samples.

	<b>V(In)<sub>100</sub></b>	<b>V(In)<sub>200</sub></b>	<b>V(In)<sub>300</sub></b>	<b>T<sub>100</sub></b>	<b>T<sub>200</sub></b>
<i>Growth rate (ML/s)</i>	0.05	0.1	0.2	0.05	0.05
<i>Sb flux (ML/s)</i>	2	2	2	6	6
<i>Sb/In</i>	40	20	10	120	120
<i>Temperature (°C)</i>	390	390	390	390	405
<i>Thickness (nm)</i>	10	10	10	10	10

#### b. Impact of the growth rate

For all samples grown on InP(100) substrates, the RHEED rapidly turns to a spotty patterns indicating a three dimensional growth and the formation of faceted islands. This is confirmed by the SEM images of the three samples obtained with different growth rates in Figure 5.1.

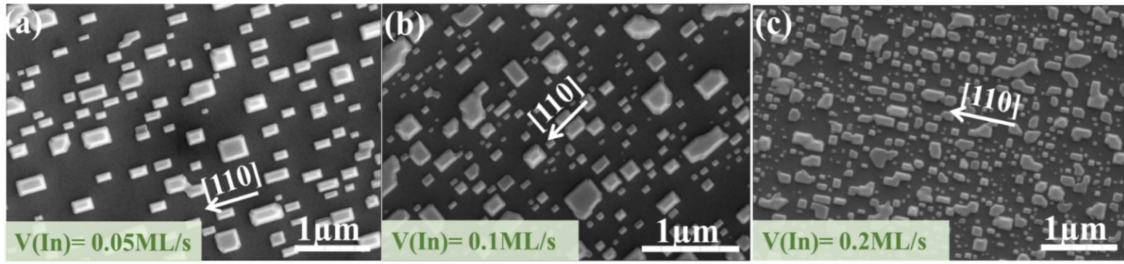


Figure 5.1 – SEM images of the samples (a) V1<sub>100</sub>, (b) V2<sub>100</sub>, and (c) V3<sub>100</sub>. InSb islands grown on InP(100) wafers

The bright-grey islands correspond to the InSb nanostructures and the dark background to the uncovered InP surface. In all images, InSb nanostructures exhibit an elongated shape along the [110] direction. As expected, a higher growth rate leads to an increase of the island density as the diffusion length of In adatoms is reduced. At the highest growth rate of 0.2 ML/s (sample V3<sub>[100]</sub>), we observe badly-defined rectangular islands surrounded by a large density of smaller nuclei. At the intermediate growth rate (sample V2<sub>[100]</sub>), the density of the smallest islands and nuclei is reduced and becomes quasi-null for the lowest growth rate (sample V1<sub>[100]</sub>). This change occurs along with an evolution of the island shape, which turns progressively to a very regular rectangle oriented along the [110] direction for very low growth rate. This same nucleation behaviour was reported by S. El Kazzi et al. for the growth of GaSb nanostructures along the [110] orientation on GaP (100) [6]. According to these authors, the anisotropy of the growth is explained by the larger incorporation of Ga on {111}A edge facets for high Sb fluxes.

### c. Impact of the growth temperature

Figures 5.2(a) and 5.2(b) display AFM images of the surface for the two samples T1<sub>100</sub> and T2<sub>100</sub> respectively. Both AFM images exhibit InSb islands elongated in the [110] crystallographic orientation, consistent with the ones seen in Figure 5.2(a). Figures 5.2(c) and 5.2(d) are height profiles obtained across InSb islands outlined in Figures 5.2(a) and 5.2(b) respectively. The blue line corresponds to the height profile along the [110] direction whereas the green line is relative to the  $[\bar{1}\bar{1}0]$  orientation. The height profiles show that the InSb islands grown at higher temperature have a thickness of about 100 nm, whereas the nanostructures grown at 390°C are about 85 nm-thick. For both samples, the side angles of the profiles are between 45° and 60°.

Taking into account the convolution with the AFM tip and the orientation of the scan with respect to the nanostructure orientation, this may indicate the creation of (111) side facets

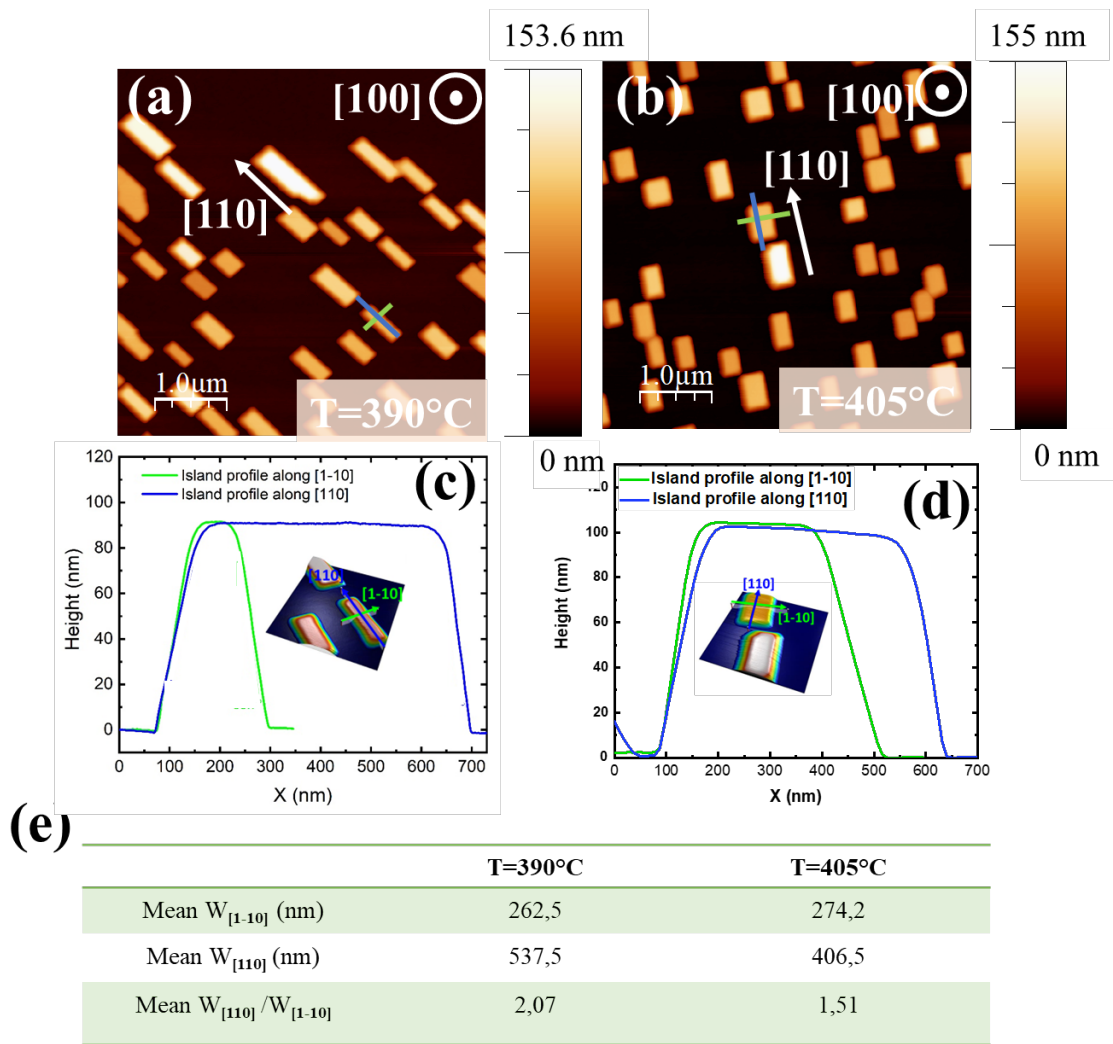


Figure 5.2 – AFM image of the InSb nanostructures after the deposition of a nominal thickness of 10 nm on the InP (100) substrate at (a) 390°C (sample T1<sub>100</sub>) and (b) 405°C (sample T2<sub>100</sub>). Scale bar is 1 μm. (c) Height profile of an InSb island of sample T1<sub>100</sub> along the  $[1\bar{1}0]$  (green line) and the  $[110]$  (blue line) directions. (d) Height profile of an InSb island of sample T2<sub>100</sub> along the  $[1\bar{1}0]$  (green line) and the  $[110]$  (blue line) directions. (e) The Table summarizes the mean width along both crystal directions for the islands observed on samples T1<sub>100</sub> and T2<sub>100</sub>.

which form a 54° angle with the substrate. Such an observation agrees with the side facets obtained for GaSb islands grown on GaP [6]: Sb-terminated  $(111)_B$  facets form in the  $[1\bar{1}0]$  direction while In-terminated  $(111)_A$  facets form in the  $[110]$  direction. The mean island dimensions, summarized in Figure 5.2(e), indicate that the lower growth temperature promotes the elongation of the islands in the  $[110]$  direction and thus the formation of  $(111)_B$  facets.

As in the case of GaSb grown on GaP [9], the anisotropy of InSb islands under large Sb flux can be attributed to the excessive Sb flux that saturates the incorporation sites for indium on the  $(111)_B$  facets. This promotes their diffusion and incorporation to the  $(111)_A$  facets and thus the elongation of the islands. When the temperature increases from 390°C to 405°C, Sb



re-evaporation is enhanced and this effect is softened.

The impact of the Sb flux on the island elongation is confirmed if we compare sample V1<sub>100</sub> and T1<sub>100</sub> which are grown at the same growth rates and temperatures but with different Sb flux.

#### d. Conclusion

On InP(100) substrate, the use of growth conditions compatible with SAG leads to the formation of small area trapezoidal islands 10 times thicker than the nominal deposited thickness. Interestingly, combining a low growth rate with a very large Sb flux promotes the formation of (111)<sub>B</sub> facets, which suggest a minimization of their surface energy under large Sb flux. In the next section, we will thus investigate the growth on InP(111)<sub>B</sub> substrate to take benefit from the low surface energy of InSb (111)<sub>B</sub> to promote 2D growth.

## 2.2 Growth of InSb on un-masked InP(111)<sub>B</sub>

The same deoxidization process and set of growth parameters as the ones selected for the growth performed on InP(100) are used on InP(111)<sub>B</sub> (samples V1<sub>111</sub>, V2<sub>111</sub> and V3<sub>111</sub>). An additional set of samples (samples A, B and C) with low growth rate of 0.05 ML/s, a very large Sb flux of 6 ML/s and a temperature of 390°C is prepared with different thickness of 10, 30 and 100 nm. These growth conditions are summarized in Table 3.

Table 5.2 – Growth conditions of samples V1<sub>111</sub>, V2<sub>111</sub>, V3<sub>111</sub>, sample A, sample B and sample C.

	V1 <sub>111</sub>	V2 <sub>111</sub>	V3 <sub>111</sub>	Sample A	Sample B	Sample C
<i>Growth rate (ML/s)</i>	0.05	0.1	0.2	0.05	0.05	0.05
<i>Sb flux (ML/s)</i>	2	2	2	6	6	6
<i>Temperature (°C)</i>	390	390	390	390	390	390
<i>Thickness (nm)</i>	10	10	10	10	30	100

Figure 5.3(a) is a graph illustrating the evolution of the coverage of the InP(111)<sub>B</sub> surface with InSb at different growth rates for the same amount of deposited material. Based on the comparison of Figure 5.3(b-d), it shows that decreasing the growth rate from 2 ML/s to 0.05ML/s enhances the surface coverage. At 0.05ML/s, the InSb film covers more than 75% of the InP substrate (Figure 5.3(b)). This is much more important than what have been achieved on InP(100). This is primarily due to the much larger island size that are formed

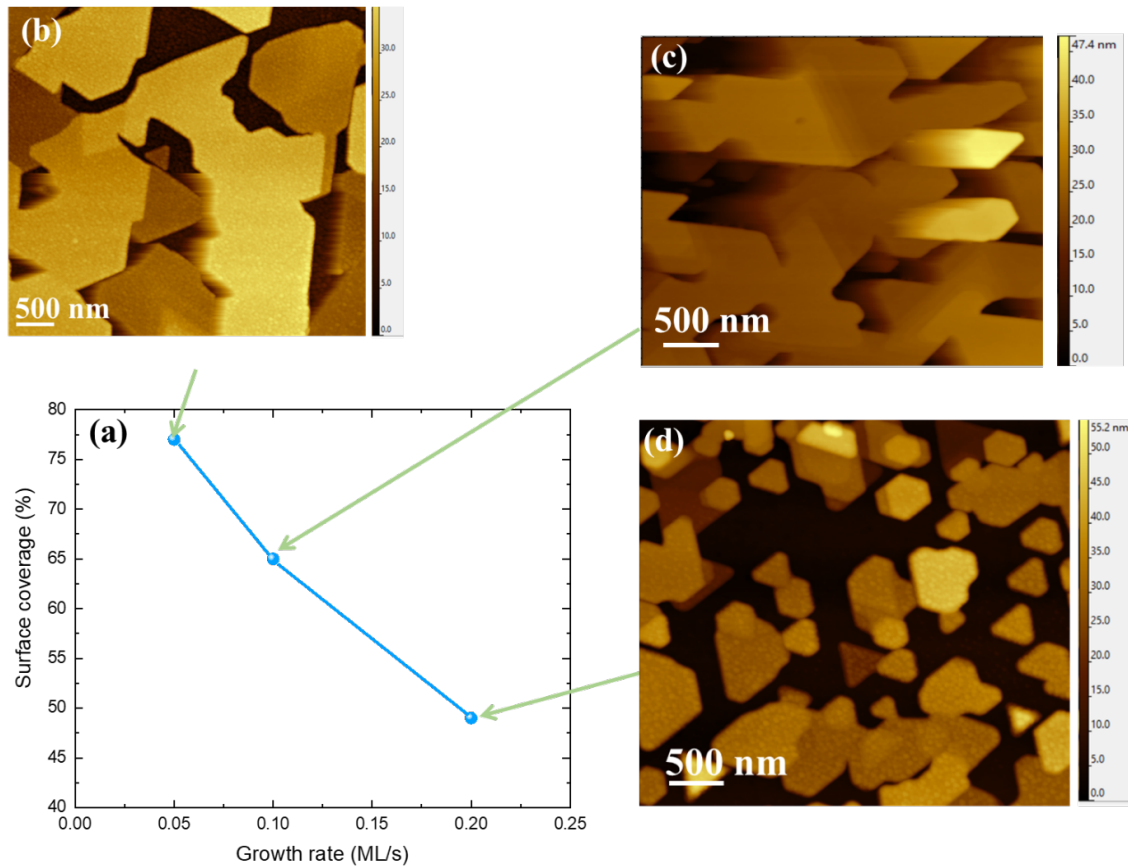


Figure 5.3 – (a) variation of the InP (111)<sub>B</sub> surface covered by InSb at different growth rates for the deposition of a nominal thickness of 10 nm at 390°C and corresponding AFM images of the surface for growth rates of (b) 0.05 ML/s, (c) 0.1 ML/s and (d) 0.2 ML/s.

on InP(111)<sub>B</sub> than on InP(100). It is consistent with the low surface energy of InSb(111)<sub>B</sub> deduced from the previous results. Figures 5.4(a) and 5.4(b) are respectively SEM and 3D-AFM micrographs of the 10 nm-thick sample grown at the lowest growth rate of 0.05 ML/s with a large Sb/In flux ratio of 120 (sample A). Under these conditions, a quasi-2D growth mode is achieved with a surface coverage of about 90%. Once again, the enhanced surface coverage confirms the low surface energy of InSb(111)<sub>B</sub>. It also suggests a low interface energy between highly mismatched InSb layer and InP substrate. A small density of triangular hillocks on the surface can be noticed on the surface. One of them is highlighted in the inset of Figure 5.4(a). These triangular pyramids are probably related to the formation of mirror twin defects at the mismatch InSb/InP interface. The resulting 180° rotation of the crystal leads to the observation of InSb islands delimited by a (111)<sub>A</sub> top surface and (111)<sub>B</sub> side facets. As the large Sb flux promotes the (111)<sub>B</sub> facets, (111)<sub>A</sub> top surface progressively disappears at the benefit of (111)<sub>B</sub> side facets, explaining the shape of the pyramidal islands.

Figure 5.4(c) displays the XRD analysis of sample A. A good fit between experimental and simulated spectra is achieved considering a 95% relaxation of the InSb film.

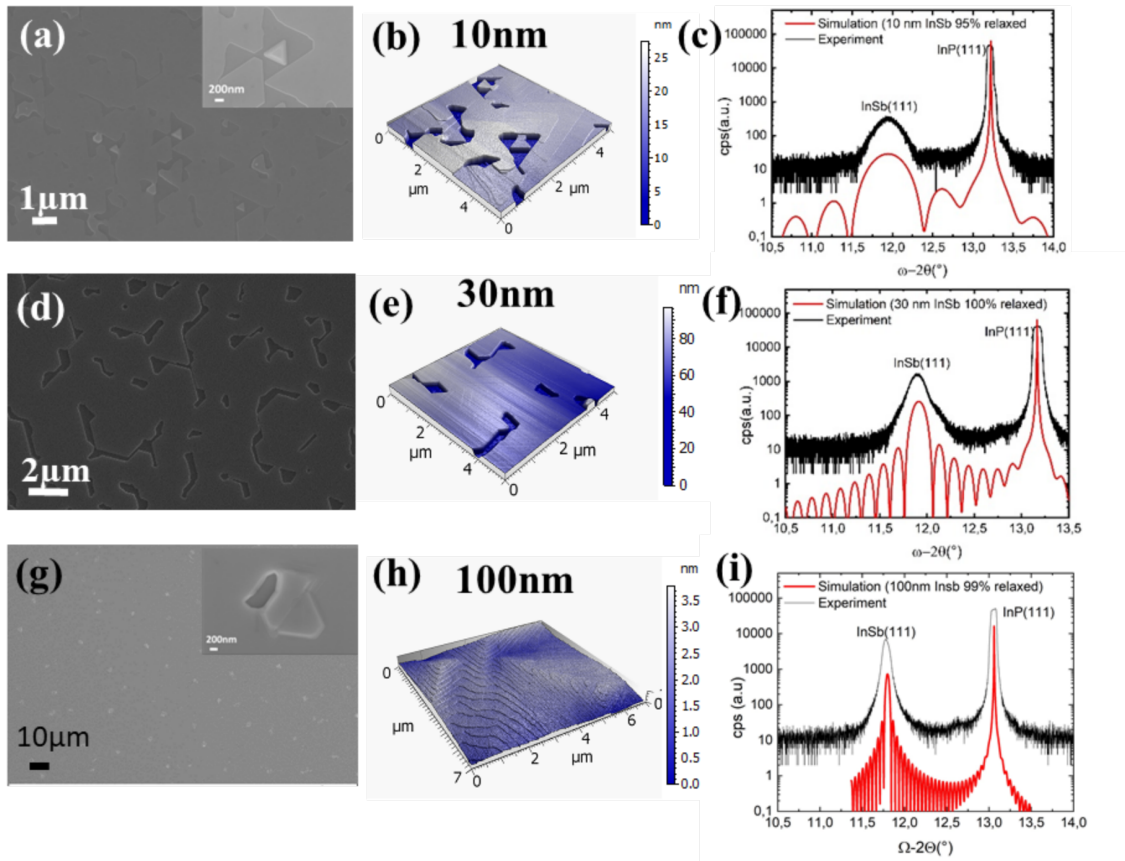


Figure 5.4 – SEM (a, d and g) micrographs, AFM images (b, e and h) and XRD spectra (c, f and i) of InSb layers on InP(111)<sub>B</sub> with a nominal deposited thickness of 10 nm (sample A), 30 nm (sample B) and 100 nm (sample C) respectively. Inset of (a) and (g) display a magnified view of a hillock observed on the surface. Scale bars are 200 nm long.

Figures 5.4(d) and 5.4(e) present SEM and AFM images of sample B. Both Figures show that after 30 nm deposition, the surface coverage is about 93%. Figure 5.4(f) presents the experimental XRD spectra of this sample compared with a simulation assuming a full relaxation of the InSb film.

Figure 5.4(g) and 5.4(h) are the SEM and AFM images of sample C. After the deposition of 100 nm, the InP surface seems almost fully covered albeit the presence of a few defects, one of which being highlighted in the inset of Figure 5.4(g). The density of these defects, probably related to the initial formation of twin defects, is around  $2.6 \times 10^5 \text{ cm}^{-2}$ . In a large area between defects, a smooth surface is obtained, as revealed by the large terraces observed in Figure 5.4(h). For this sample, Figure 5.4(i) presents a good fit between experimental and simulated XRD spectra for a 99% relaxation of the InSb film.

Figure 5.5(a) is an AFM analysis of sample B. The InSb film exhibits some holes on the surface. These holes have a depth around 50 nm that reveals an InSb layer which is 20 nm thicker than the nominal thickness, as shown in Figure 5.5(c). This greater thickness than initially intended

can be attributed to the fact that the surface coverage is not total. Furthermore, there is a potential uncertainty in the Indium deposition rate, estimated at 0.05 ML/s, which could also contribute to the observed discrepancy in layer thickness. Figure 5.5(a), also, reveals a 12 nm RMS roughness due to the presence of holes in the InSb film. The magnified view of flat areas shown in Figure 5.5(b) reveals terraces extending over several hundred nanometers. The height profile measured along the black segment in Figure 5.5(b) reveals a first step height of about  $7.5\text{\AA}$  (Figure 5.5(d)). This value is twice the value of InSb(111) monolayers ( $\frac{6.48\text{\AA}}{\sqrt{3}} = 3.74\text{\AA}$ ). The apparent height steps is then relative to a one double-step terrace and two single-step terraces. We note that single-step terraces are visible, as shown in the right-top area of Figure 5.5(b).

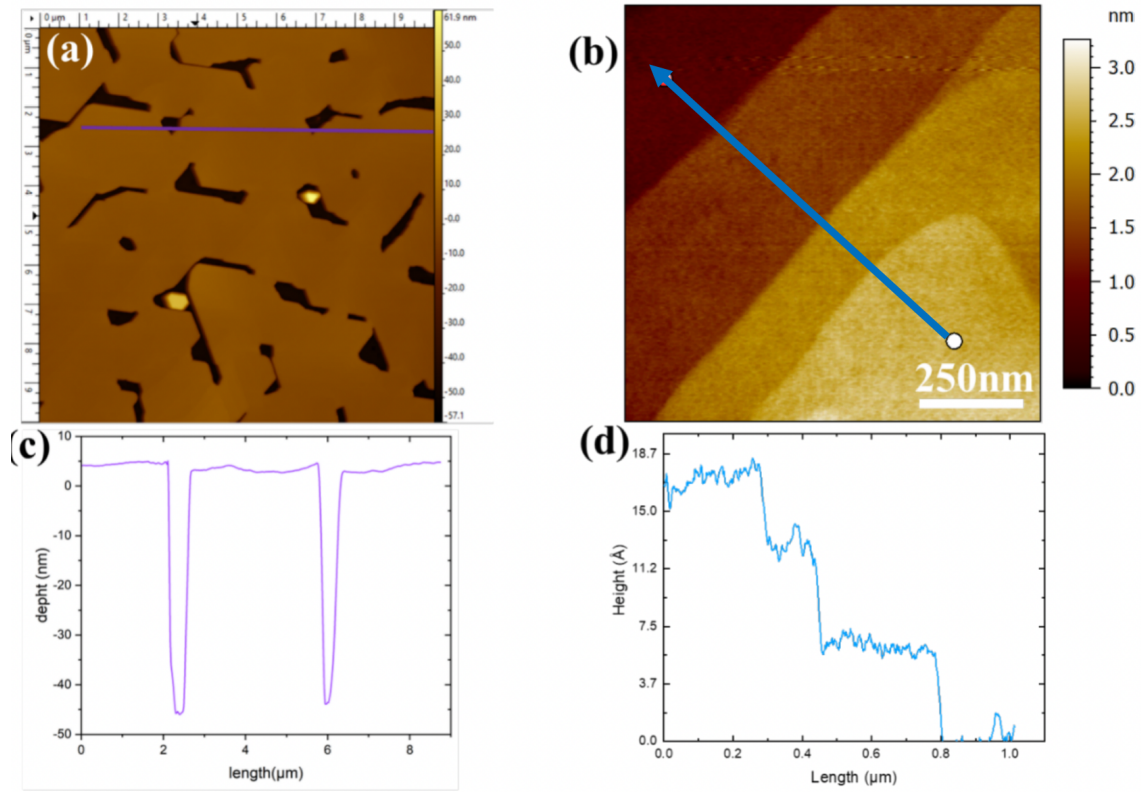


Figure 5.5 – (a) AFM image of the sample B. (b) Depth profile of the hole along the purple line in (a), (c) Higher resolution AFM image than in (a) showing InSb terraces. (d) Height profile along the black line in (c).

As a conclusion, with a low growth rate and a high Sb/In flux ratio, InSb deposited on  $\text{InP}(111)_B$  exhibits a growth mode with large 2D relaxed islands that rapidly coalesce to achieve an almost full coverage of the InP surface at a nominal thickness of 100 nm. Despite the large lattice mismatch, the InSb film is rapidly accommodated to InP as demonstrated by the quasi-full relaxation measured with XRD. Interestingly, it already starts at the beginning of the growth. This suggests the formation of an efficient misfit dislocation network accommodating the mismatch at the interface with InP. TEM should be performed to confirm the existence

of this dislocation network on thin films.

Although a very low surface roughness can be measured on several  $\mu\text{m}^2$  areas, a low density of small defects probably originating from the initial formation of hillocks during the nucleation are still observed after 100 nm growth. With selective growth limited to micrometre scale areas, one would expect to get rid of these defects and achieve high quality InSb in-plane nanostructures directly grown on InP.

## 2.3 Selective area growth of InSb on InP(111)<sub>B</sub>

### 2.3.1 Nucleation of InSb inside nanoscale openings

In this section, the deoxidization and growth conditions used for the nucleation study on InP(111)<sub>B</sub> (Table 5.3, 10 nm-thick series) are applied on InP(111)<sub>B</sub> substrates patterned with a SiO<sub>2</sub> mask as described in chapter 2. The nominal widths of the openings in the SiO<sub>2</sub> layer are about 50 nm, 100 nm, 200 nm, 500 nm and 1  $\mu\text{m}$ . The nanowire length is about a few micrometres and different in-plane orientations are studied.

The denomination of the different samples and their growth conditions are indicated in Table 5.3.

Table 5.3 – Growth conditions for 10 nm-thick selective area grown InSb on InP(111)<sub>B</sub> samples.

	<b>SAG 1</b>	<b>SAG 2</b>	<b>SAG 3</b>	<b>SAG 4</b>
<i>Growth rate (ML/s)</i>	0.2	0.1	0.05	0.05
<i>Sb flux (ML/s)</i>	2	2	2	6
<i>Temperature (°C)</i>	390	390	390	390
<i>Thickness (nm)</i>	10	10	10	10

Figure 5.6 displays SEM images of the different samples, focusing on a set of nanowires oriented along the  $[\bar{2}11]$  crystallographic direction. The nominal width of the mask openings varies between 1  $\mu\text{m}$  (left) and 50 nm (right).

First, all the images show no nucleation outside the mask openings confirming a very good selectivity with respect to the SiO<sub>2</sub> areas.

Regarding the morphology of the InSb growth inside the openings, a clear evolution between the different samples can be seen in Figure 5.6. For sample SAG1 (Figure 5.6(a)), all the



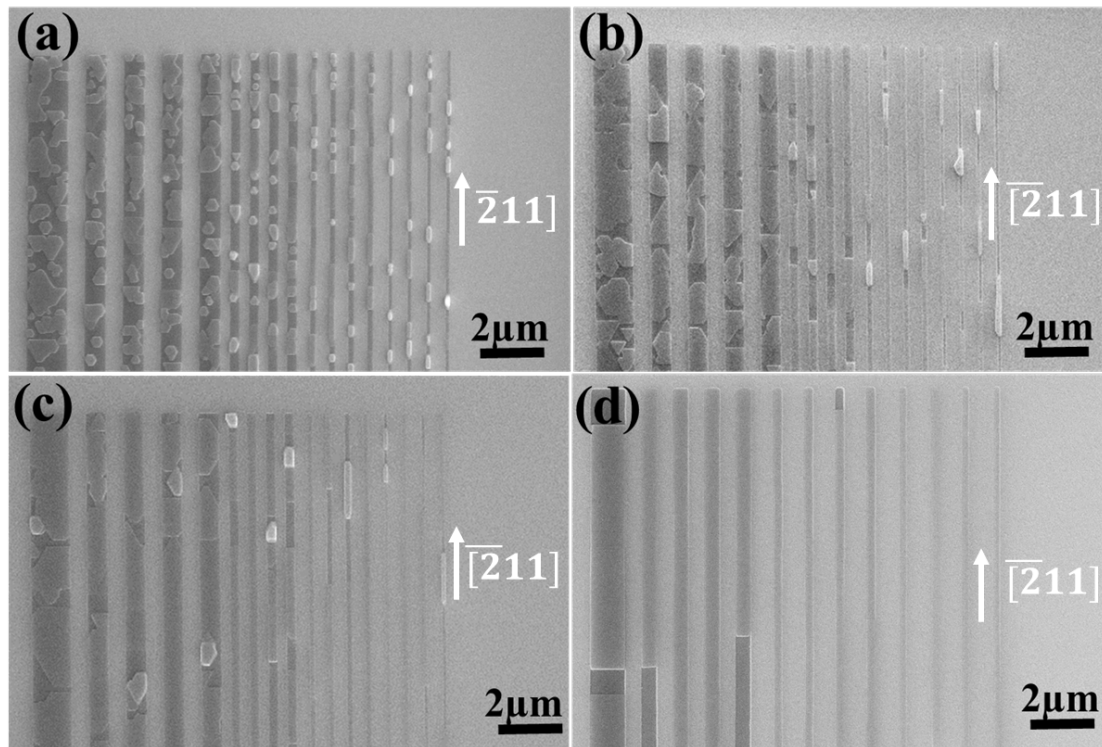


Figure 5.6 – SEM images of the InSb deposition with a nominal thickness of 10 nm by atomic H-assisted MBE into SiO<sub>2</sub> openings forming an array of 20 μm-long parallel nanowires oriented along  $[\bar{2}11]$  with different widths from 1 μm (first opening from left), 500 nm (openings 2 to 5), 200 nm (openings 6 to 9), 100 nm (openings 10 to 13) and 50 nm (last four openings to the right). (a) sample SAG1, (b) sample SAG2, (c) sample SAG3 and (d) sample SAG4. InSb NWs grown on InP (111)<sub>B</sub> wafers

mask openings contain small sized isolated islands without any well-defined shape. As the growth rate is decreased to 0.1 ML/s (Figure 5.6(b)), InSb islands are more spread inside the wide openings whereas their shape follows the mask for narrow apertures, except some thicker islands that seem to spread out of the mask. For the lowest growth rate (Figure 5.6(c)), the mask openings are almost completely filled. Inside the narrow openings, several μm-long nanowires can be achieved although a few segments appear thicker and extend laterally over the mask.

For the same growth rate but with the largest Sb flux (Figure 5.6(d)), homogenous and continuous nanowires over more than 10 μm are formed inside the narrow openings whereas 500 nm and 1 μm wide apertures contain very large rectangular islands.

InSb growth inside the mask openings is thus improved when reducing the growth rate and increasing Sb flux. This is consistent with the results presented for un-masked InP substrates in the previous section where 2D InSb growth is optimized for very large Sb/In flux ratio. After a nominal deposition of 10 nm, InSb has almost completely filled narrow apertures.

### 2.3.2 Selective growth of in-plane InSb nanowires

For sample SAG5, the same growth conditions than for sample SAG4 are used but the nominal deposited thickness is 30 nm. Different nanostructures grown in this sample are presented in Figure 5.7.

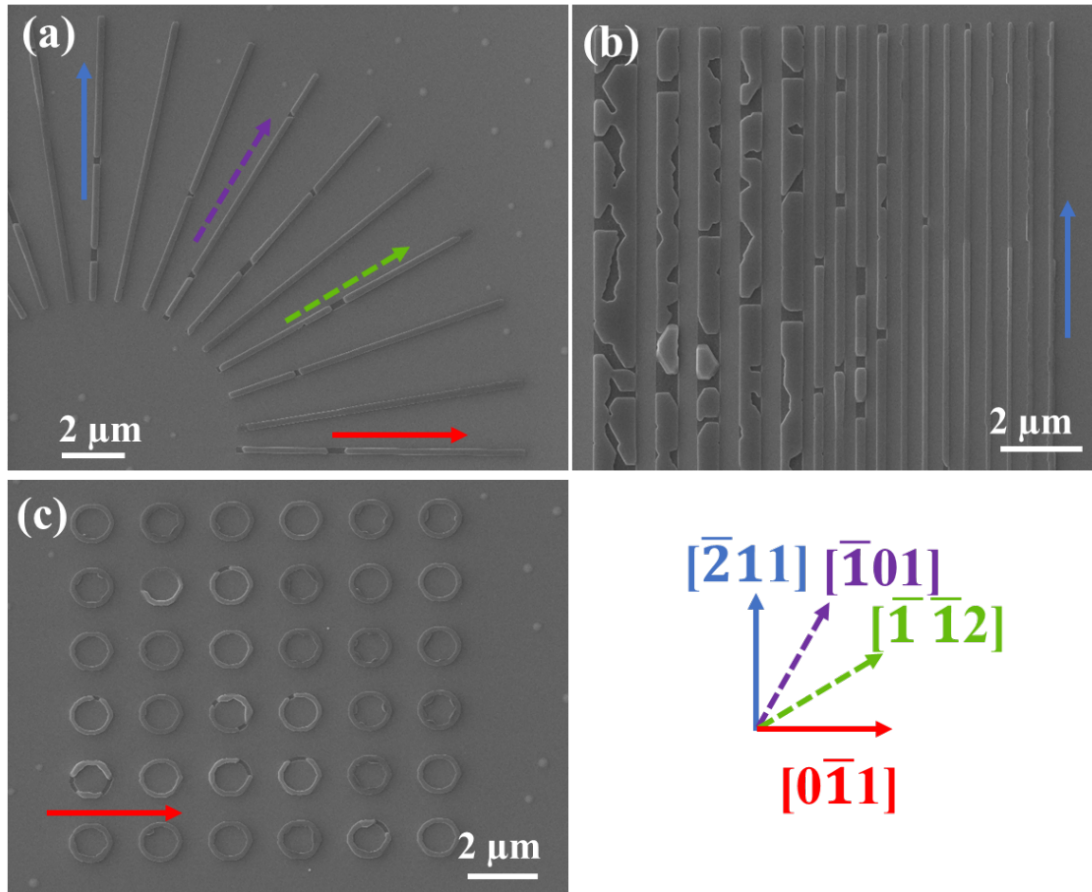


Figure 5.7 – SEM images of different patterns of the sample SAG5 (30 nm-thick InSb NWs grown on an InP (111)<sub>B</sub> wafer at 390°C with a growth rate of 0.05ML/s and a flux ratio of 120). (a) 200 nm-wide InSb NWs in different in-plane orientations (rotation every 10° from  $[0\bar{1}1]$  to  $[\bar{2}11]$ ) of SAG5. (b) SEM images of 20 μm-long and  $[\bar{2}11]$  oriented InSb NWs with different nominal widths (1000 nm down to 50 nm from left to right). (c) Rings with 1 μm inner diameters. Pattern opening is 100 nm.

The SEM images in Figure 5.7 show a very small number of InSb nuclei on the SiO<sub>2</sub> mask, ensuring a good selectivity. Figure 5.7(a) proves that whatever the opening orientations are, continuous nanowires over several micron distance can be achieved along the different directions despite some local discontinuities. Their length is up to 10 μm. Figure 5.7(b) shows that for NWs grown along the  $[\bar{2}11]$  orientation, larger apertures than 200 nm are not fully filled showing incompletely coalesced islands. Figure 5.7(c) displays a ring pattern. A few rings show some height discontinuities, but in overall the rings present a good quality using these growth conditions.



Figure 5.8 presents AFM images at the extremities of 20  $\mu\text{m}$ -long in-plane InSb nanowires oriented along the  $[\bar{2}11]$  or  $[0\bar{1}1]$  crystallographic directions on sample SAG5. Apertures of 50 nm and 100 nm nominal widths are investigated here. The height profiles of the different nanowires presented in Figures 5.8(a) to 5.8(d) show that the height of all the nanowires is about 20 nm. If we take into account the  $\text{SiO}_2$  mask thickness of about 10 nm, this means that the thickness of the InSb nanostructures is about 30 nm, matching the nominal intended thickness. Whatever the crystallographic directions, the nanowires grown inside openings with a width of 50 nm are wider than the initial width, reaching 150 nm. Similarly, the nanostructures grown inside the 100 nm-wide openings have a width of about 200 nm. This difference can be attributed to three effects:

- The HF treatment performed at the end of the mask etching enlarges the width of the aperture with respect to the nominal one.
- A lateral growth of the InSb nanostructures outside the mask openings.
- An artefact due to a tip convolution during the AFM measurements.

Considering the difference between the nominal widths and the measured one, we can estimate that these three elements contribute to an enlargement of about 100 nm for the measured width.

The profiles of Figure 5.8(e) suggest that the nanowires are delimited by vertical side facets. This is consistent with the results obtained for selectively grown InAs nanowires on InP(111) wafers in chapter 3 and reference [7]. For both directions, we can also notice a very flat top NW facet. The nanowires along the  $[\bar{2}11]$  and  $[1\bar{1}0]$  directions display highly symmetrical  $\{1\bar{1}0\}$  and  $\{11\bar{2}\}$  vertical sidewalls.

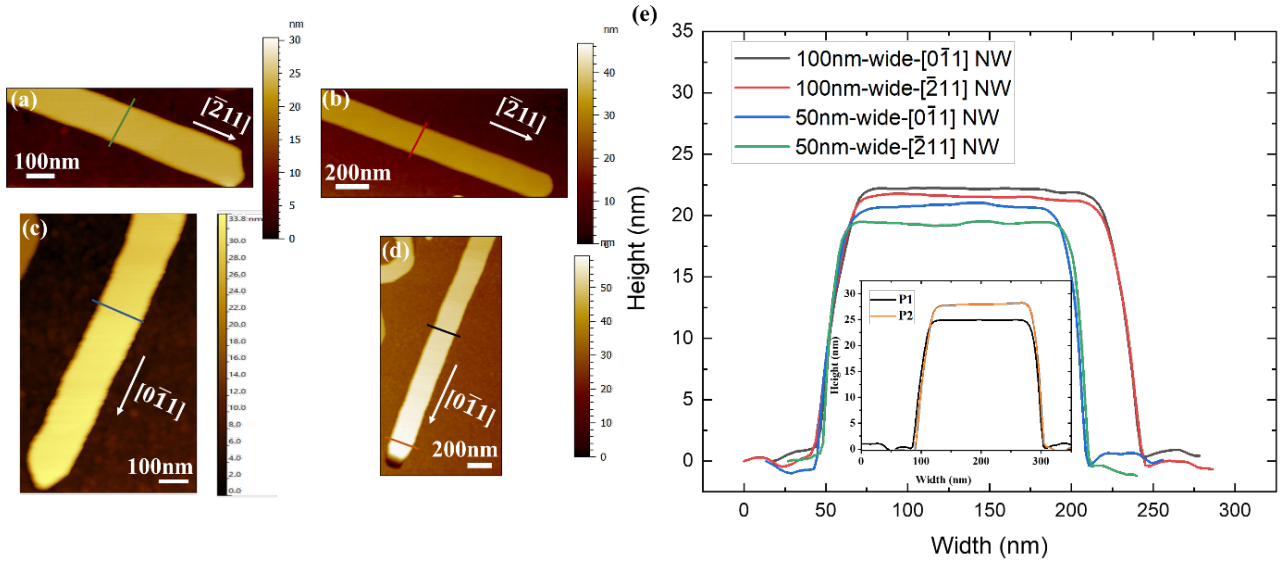


Figure 5.8 – AFM images of 30 nm-thick InSb nanowires grown by SAG on InP(111)<sub>B</sub> with a growth rate of 0.05 ML/s and a Sb/In flux ratio of 120 (sample SAG5). Nominal aperture widths are 50 nm (a and c) and 100 nm (b and d) for in-plane orientation along the  $[\bar{2}11]$  direction (a and b) or the  $[0\bar{1}1]$  direction (c and d). (e) Height profiles along the green, red, blue and black lines in (a), (b), (c) and (d) respectively. The inset shows a height profile along the two (black and orange) lines in (d).

Figure 5.9(a) displays the HAADF-STEM cross section micrograph of a nanowire grown on sample SAG5. The TEM lamella has been prepared by D.Troadeac at IEMN after the selection of one nanowire with a nominal width of 100 nm and oriented along  $[01\bar{1}]$ . The TEM analysis has been performed at CEA Leti by Pierre-Henry Jouneau and Nicolas Chaize.

Interestingly, no threading defects are observed in the InSb material. InSb exhibits a flat (111) top facet. At the SiO<sub>2</sub> interface, side facets are curved following the profile of the mask. Once outside the mask window, some lateral growth is observed in the right side of the nanowire and the side facet looks more like a vertical facet as observed in the AFM profile of the previous figure. Figure 5.9(f) is a zoomed STEM image of the side interface between the mask and the InSb nanostructure. This dark-grey part of the nanowire in this figure reveals an amorphous InSb layer at the SiO<sub>2</sub> interface with a thickness around 3.4 nm. This amorphous layer can be due to the roughness of the sides of the mask. Figure 5.9(g) reveals a sharp interface between InP and InSb. A numerical filtered image of the red dashed square in this figure (Figure 5.9(h)) highlights a periodic array of 60° misfit dislocations at the InP-InSb interface. According to Figure 5.9(h) these dislocations are spaced with an average distance of 3.24 nm that coincides with the theoretical distance value that is given by  $d = \frac{a_{\text{InP}(111)}}{|f|\sqrt{3}}$  and equals 3.26 nm [8], where  $f$  is that lattice mismatch (between InSb and InP in this case) presented in

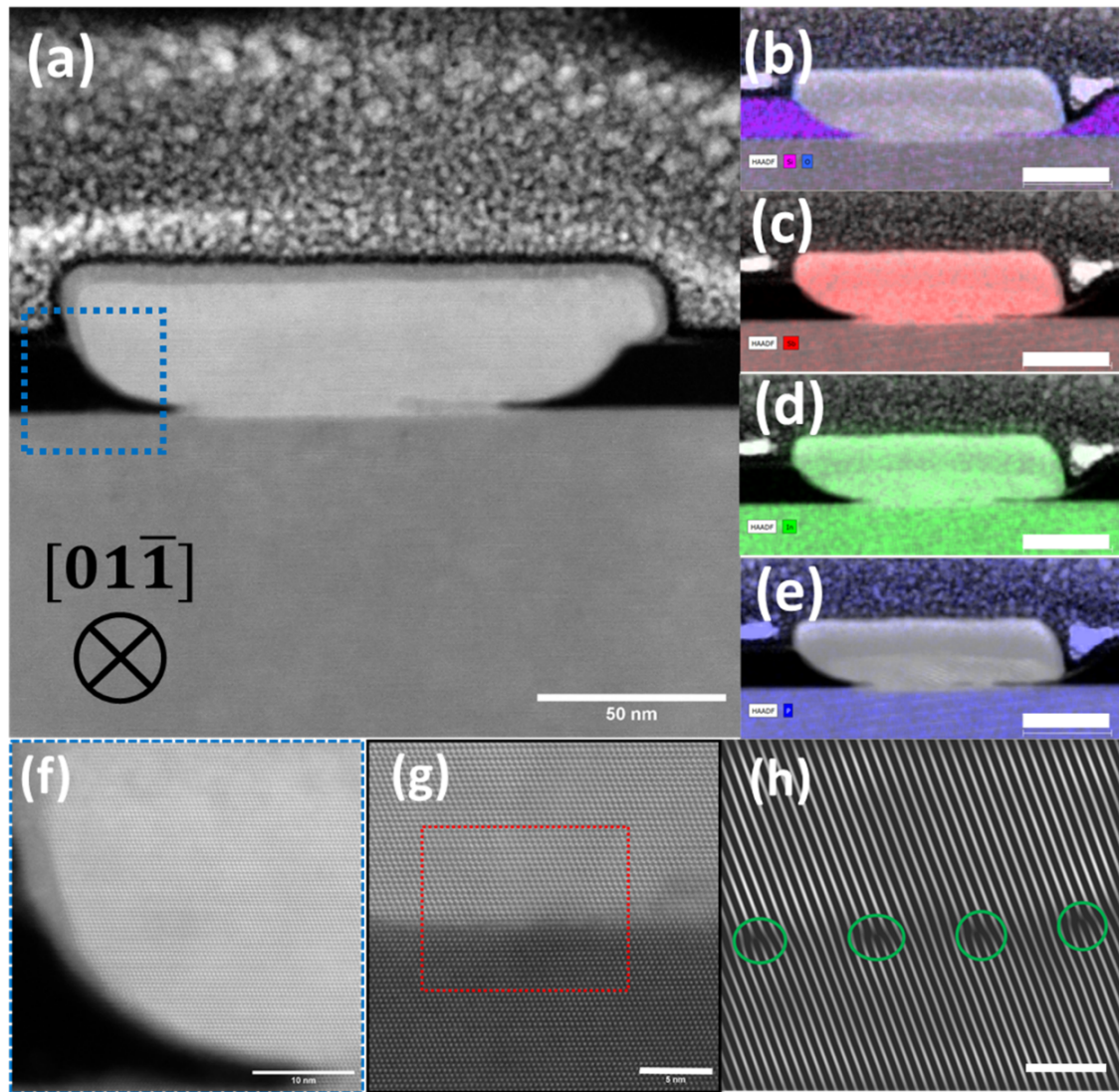


Figure 5.9 – (a) HAADF-STEM cross section of a  $[01\bar{1}]$ -oriented InSb NW belonging to sample SAG5 (30 nm-thick InSb NWs grown on an InP  $(111)_B$  wafer at  $390^\circ\text{C}$  with a growth rate of  $0.05\text{ML/s}$  and a flux ratio of 120). Scale bar is 50 nm. Elemental mapping of the cross-section highlighting (b) Si (pink) and O (light blue), (c) Sb (red), (d) In (green) and (e) P (blue). Scale bar is 40 nm. (f) Magnified view of the area delimited by a blue dashed square in (a). Scale bar is 10 nm. (g) High-resolution image of the InSb/InP interface. Scale bar is 5 nm. (h) Numerical filtered image of the red dashed square area in (g) highlighting the interface misfit dislocations (green circles), scale bar is 3 nm.

chapter 1. The dark grey zone on top of the nanowire (Figure 5.9(a)) reveals an amorphous layer that we attribute to the preparation of the thin slice with the focus ion beam. Indeed, the Pt mask is not thick enough to protect the NW surface from the Ga ion beam.

EDX images of Figures 5.9(b) to 5.9(e) confirm the In and Sb composition of the InSb nanostructure.

As a conclusion, we have shown that high quality InSb nanostructures directly grown on the highly mismatched InP $(111)_B$  surface can be obtained by combining a low growth rate and a

high Sb flux. The nanowires grown inside sub-200 nm apertures are smooth and continuous over several  $\mu\text{m}$ s. The cross section HAADF-STEM analysis shows no threading defects inside the InSb nanowires and a strain relaxation by the formation of regularly spaced misfit dislocations at the InP-InSb interface.

### 3 Atomic structures of the InSb (100) and (111)<sub>B</sub> surfaces resulting from deoxidation

Similar to the transport properties of the InAs nanowires characterized in UHV with the Nanoprobe setup, we aim at investigating the transport properties of the InSb nanowires in UHV. As shown in the previous chapter, this environment allows to study the intrinsic properties of the nanowires with clean and reconstructed facets, before any treatments resulting from the subsequent fabrication of electrical contacts. As the UHV STM and Nanoprobe tools are not connected to the MBE system, the samples have to be exposed to air for their transfer between the different systems. Therefore, the nanowires could get easily oxidized during this transfer and a reproducible method must be designed to study InSb nanowires with clean and well-ordered facets. To establish such a method, we focus on the study of the InSb (100) and (111)<sub>B</sub> surfaces, instead of nanowires, because finding an array of nanowires and positioning the STM tip on a single nanowire within a reasonable time is not straightforward.

As a supplement to traditional deoxidation methods, InSb nanostructures are capped using arsenic (As), antimony (Sb), and selenium (Se) inside the MBE chamber, followed by uncapping procedures in the LT-STM system. For arsenic-capped samples, a minimum evaporation temperature of 320°C is mandatory. Noting that antimony within the InSb layer evaporates at a temperature of 230°C [9], this solution is hard to implement. Moreover, we found that As intermix with Sb in the crystal surface planes. The antimony-capped alternative presented challenges, because the oxidation of the capping layer prevents its sublimation, as verified from Raman spectroscopy with persistent antimony layers left on the surface. Selenium-capped samples, as corroborated by XPS analyses conducted by Xavier Wallart, resulted in elemental intermixing, evidenced by the formation of In-Se and In-Sb-Se bonds. Cumulatively, these capping experiments posed considerable complications, as no capping layer could be entirely withdrawn. The following section delves into the deoxidation of InSb surfaces via atomic hydrogen flux.

### 3.1 The InSb (100) surface reconstruction after deoxidation

As the study of the oxide desorption is quite demanding in STM to find the appropriate conditions that yield a clean and well-ordered surface, a more direct and non-invasive tool is combined with the STM characterization: Raman spectroscopy in UHV. Because of the significant analysis depth of Raman spectroscopy, this technique is usually not suitable for the study of the semiconductor surfaces. In order to increase its surface sensitivity, an InSb heterostructure is prepared. It consisted of an InSb/Al<sub>0.3</sub>In<sub>0.7</sub>Sb quantum well grown on an InSb (100) wafer.

#### 3.1.1 Growth of the InSb heterostructure

The growth of an InSb/Al<sub>0.3</sub>In<sub>0.7</sub>Sb quantum well is performed by MBE on n-type doped InSb (100) wafers ( $10^{18}$  cm<sup>-3</sup> Te doping). Prior to the growth, the substrate is outgassed at 150°C for 1h under ultra-high vacuum before being transferred to the MBE chamber. The MBE growth is carried out after the wafer deoxidation under a Sb flux and atomic hydrogen (for 10s) while heated progressively until 400°C. The heterostructure included a 20nm-thick InSb buffer layer epitaxially grown on the InSb wafer. This buffer is covered by a 10 nm-thick Al<sub>0.3</sub>In<sub>0.7</sub>Sb barrier. Finally, a 30 nm-thick InSb top layer is added. The growth of all the layers in the heterostructure is carried out at 390°C. The InSb buffer layer growth is achieved with a growth rate of 0.20 ML/s and a Sb/In ratio of 10. For the 10 nm-thick Al<sub>0.3</sub>In<sub>0.7</sub>Sb alloy, the growth rate is 0.29 ML/s and the V/III ratio is 7. Finally, the InSb cap layer is grown with the same conditions as the ones used for the InSb buffer layer. The RHEED shows a (2 × 3) surface reconstruction while depositing the Al<sub>0.3</sub>In<sub>0.7</sub>Sb layer, which turns into a (2 × 4) reconstruction for the InSb surface. The following table displays the growth conditions of the different layers in the heterostructure.

Table 5.4 – Growth conditions of the InSb/Al<sub>0.3</sub>In<sub>0.7</sub>Sb quantum well

	Growth rate (ML/s)	V/III ratio	Temperature (°C)	Thickness (nm)
InSb top layer	0.20	10	390	30
Al <sub>0.3</sub> In <sub>0.7</sub> Sb barrier	0.29	7	390	10
InSb buffer layer	0.20	10	390	20



### 3.1.2 Monitoring the oxide desorption

As illustrated in Figure 5.10(a), during the sample transfer to the LT-STM, the sample is oxidized as it is exposed to ambient air. Inside the preparation chamber of the LT-STM system, the deoxidation process is achieved with an ion gun fed by a molecular hydrogen flux. We selected an annealing temperature of 200°C and eroded the sample for 50 min with 1.5 keV H<sup>+</sup> ions.

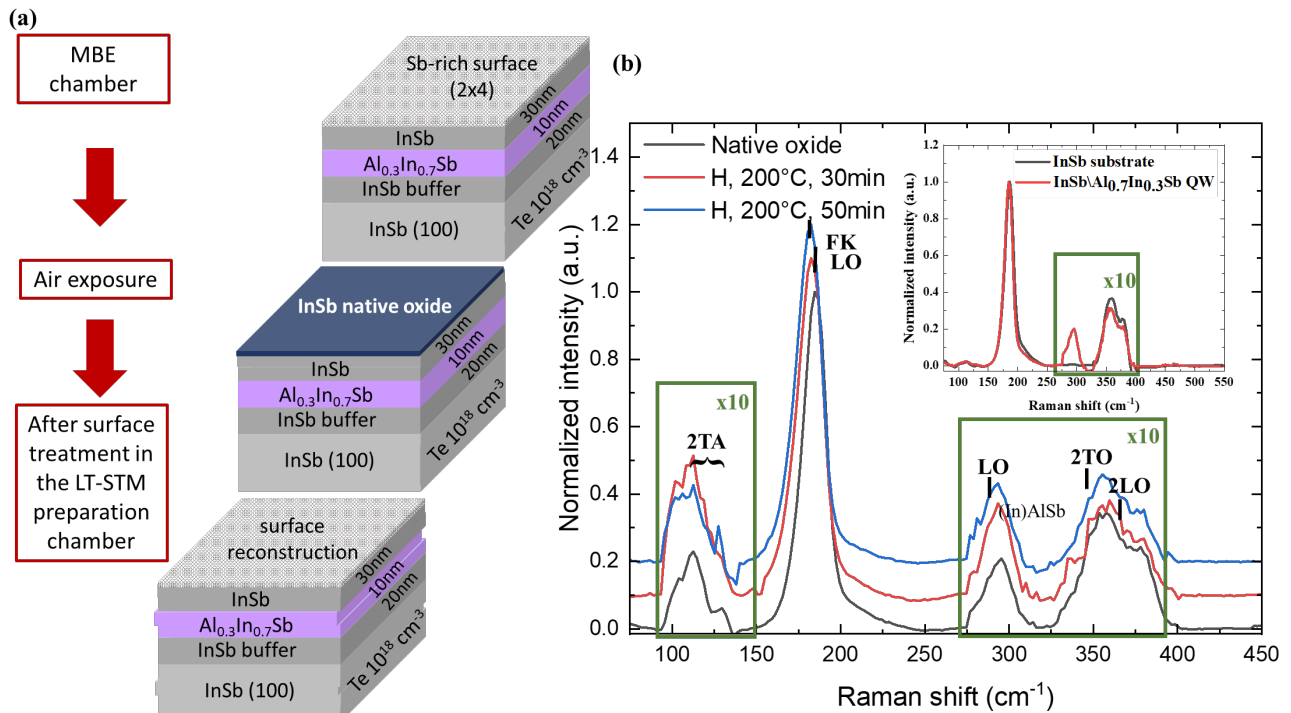


Figure 5.10 – (a) Scheme illustrating the transfer process of the InSb/Al<sub>0.3</sub>In<sub>0.7</sub>Sb QW from the MBE system to the LT-STM system. (b) UHV-Raman spectra of the heterostructure before and upon simultaneous annealing and hydrogen sputtering of the sample. The transverse acoustic, transverse and longitudinal optical, the Fuchs-Kliwler surface phonon modes are labelled TA, TO, LO, FK respectively. The spectra are vertically shifted for convenience. The inset illustrates the Raman spectrum of the heterostructure compared to an InSb (100) substrate spectrum.

Figure 5.10(b) compares three Raman spectra of the heterostructure measured at different stages of the oxygen removal from the InSb (100) surface: before the deoxidation of the surface (black spectrum), after 30 min of ion sputtering with the sample maintained at 200°C (red spectrum) and after 50 min of deoxidation with the same conditions (blue spectrum). The Raman excitation used a wavelength of 532 nm.

In order to identify the different peaks of the heterostructure, the Raman spectrum measured before deoxidation was compared to the Raman spectrum of an InSb (100) substrate, as

presented in the inset of Figure 5.10(b). Both spectra show similar peaks, except the peak at  $298\text{ cm}^{-1}$  that is seen for the sample with the InSb/Al<sub>0.3</sub>In<sub>0.7</sub>Sb quantum well only. Therefore, this peak is identified as the phonon modes of the InAlSb barrier. This is consistent with Ref. [10] where the peak is attributed to the (In)AlSb-like LO phonons [11], [12]. As the deoxidation process changes the InSb surface only, this peak related to a buried structure is not affected by the sputtering process. It is, therefore, taken as a reference. The intense peak observed at  $190\text{ cm}^{-1}$  in all spectra is attributed to the LO phonon line of bulk InSb. It could also include a small contribution of the TO phonon line at  $180\text{ cm}^{-1}$  as the incident laser beam is not totally aligned to the surface normal. The smaller peaks appearing at  $117\text{ cm}^{-1}$ ,  $362\text{ cm}^{-1}$ , and  $381\text{ cm}^{-1}$  are respectively attributed to the 2TA, 2TO and 2LO phonon modes [14], [14]. As shown in Figure 5.10(b), the desorption of the oxide layer by hydrogen provokes a small shift of the main peak. After 50 min of hydrogen sputtering, it is centred at  $186\text{ cm}^{-1}$ . Based on Ref. [15], we attribute this new position to the stronger contribution of the surface, as this wave number is consistent with the loss peak measured by High Resolution Energy Electron Loss Spectroscopy (HREELS) on the  $c(2 \times 8)$  reconstructed In-rich InSb (001) surface. A Fuchs-Kliewer surface phonon mode of InSb would then be favoured [17].

### 3.1.3 STM study of the surface structure

Figure 5.11(a) is a STM image of the InSb surface after 50 min of hydrogen eroding at  $200^\circ\text{C}$ . It shows a clean surface with terraces where periodic rows are observed. The height profile corresponding to the blue segment in Figure 5.11(a) shows a step of  $3.6\text{ \AA} \pm 0.5\text{ \AA}$  between two terraces [Figure 5.11(c)]. It matches with the theoretical step height of  $\frac{6.47}{2} = 3.24\text{ \AA}$  for the InSb (100) crystal. Periodic rows extend along the [110] direction, as illustrated in the magnified STM image of Figure 5.11(b). A FFT image deduced from an enlarged part of Figure 5.11(b) and its inverse image presented in Figure 5.11(d) and 5.11(f) show a periodicity of two along the [110] direction [18]. Along the other direction, no sharp spot is visible, indicating that the periodicity is probably partial, although we can see regular rows on the STM image. However, the dark row can be filled every two rows, consistent with a previous work [18], as it will be discussed later. According to the FFT image the periodicity in this layer is around  $1.8\text{ nm}$  that matches with the In row periodicity of the  $c(8 \times 2)$  reconstruction in the InSb crystal, equal to  $1.83\text{ nm}$  [18]. The diamond cell in Figure 5.11(e) shows a  $c(8 \times 2)$  unit cell. These STM results support the  $c(8 \times 2)$  surface reconstruction measured with UHV Raman spectroscopy after deoxidation.



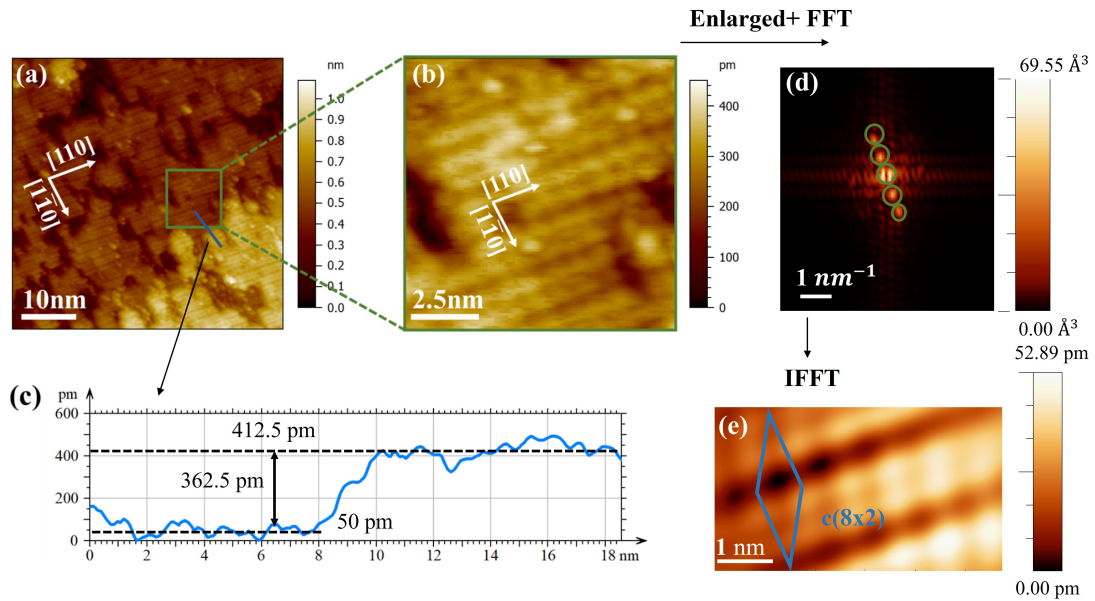


Figure 5.11 – (a) STM image of the InSb (100) surface obtained at 77K. Feedback parameters  $V_s = -0.75\text{V}$  and  $I_t = 110\text{ pA}$ . (b) Magnified view corresponding to the green square shown in (a). (c) Height profile along the blue segment in (a), black dashed lines correspond to mean value of the fluctuations of the blue profile at each terrace level (d) FFT image of an enlarged part of (b), green circles correspond to bright points. (f) Inverted FFT image of (d).

This atomic reconstruction seems similar to the results published by G.Goryl et al. [18], which dealt with an InSb (100) surface deoxidized with a 700 eV  $\text{Ar}^+$  ion-beam and annealed at 700K for several hours. Indeed, G. Goryl et al. [18] confirmed with X-ray diffraction and FM-AFM measurements at RT that the obtained surface shows a  $c(8 \times 2)$  atomic reconstruction which seems to be a common reconstruction for element-III-rich InSb, GaAs and InAs (100) surfaces. This atomic surface reconstruction was strongly debated. Kumpf et al. [19] proposed the  $\zeta(4 \times 2)$  model. Lee et al. performed DFT calculations that evinced this model, arguing that the most stable and favourable reconstruction was the  $c(8 \times 2)$  [20]. In general Sb rich surfaces present  $(1 \times 1)$ ,  $c(4 \times 4)$  and asymmetric  $(1 \times 3)$  surface reconstructions that are less ordered than the  $c(8 \times 2)$  reconstruction [21].

G-Goryl et al. demonstrated that the  $c(8 \times 2)$  surface reconstruction can be only stable for sample temperatures above 180K [22]. The RT  $c(8 \times 2)$  symmetry would be lowered from  $c2mm$  to  $p2$  [22] and the structure would not be similar to the  $\zeta(4 \times 2)$  model any more. According to this reference, additional features appear at low temperatures. Added to that, some structural irregularities aligned in chains running in the  $\frac{1}{2} [110]$  direction, have been revealed in the same work. Figure 5.12(a) is a STM image of  $c(8 \times 2)$  reconstruction of the InSb/ $\text{In}_{0.7}\text{Al}_{0.3}\text{Sb}$  quantum well. Green arrows point at the irregular features observed in the InSb surface. These irregular shapes correspond to the protruding defects and defects with

long or short form present in every two dark rows, respectively shown in Figures 5.12(b-f) [22]. They are usually attributed to In atoms. Their packing caused disorder, which is partly at the origin of the lack of long-range periodic structure in the FFT images along the  $[\bar{1}10]$  direction.

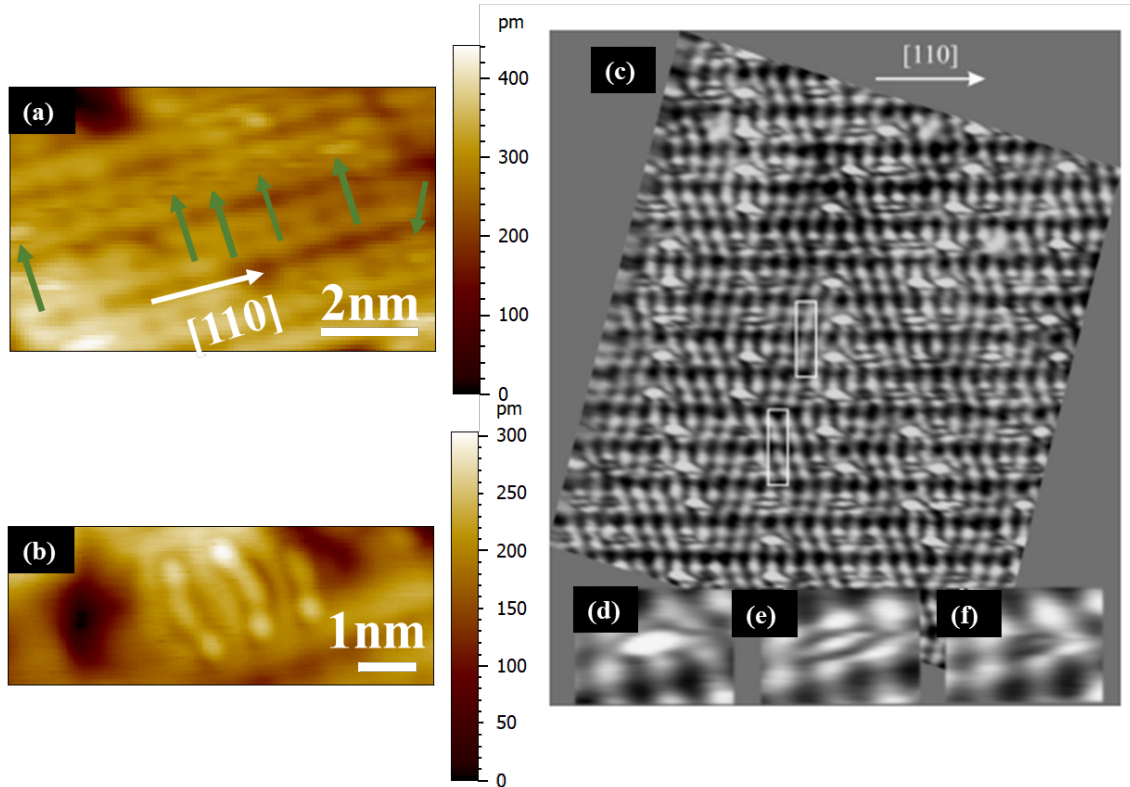


Figure 5.12 – (a) STM image of the InSb/In<sub>0.7</sub>Al<sub>0.3</sub>Sb quantum well (sample bias= -0.7V, tunnelling current 110pA). (b) enlarged flower-like pattern of the InSb/In<sub>0.7</sub>Al<sub>0.3</sub>Sb quantum well (sample bias= -0.7V, tunnelling current 110pA). (c) STM image of the  $c(8 \times 2)$  InSb(100) surface acquired at 77 K ( $25 \times 25 \text{ nm}^2$ , sample bias: 0.5 V, tunnelling current: 50 pA). White rectangles indicate  $c(8 \times 2)$  unit cells for two differently tilted domains. The frame is drift corrected and rotated to align the  $[110]$  direction horizontally in order to show the structure angles clearly. (d) Enlarged “protruding defect”. (e) “Elongated long” form. (f) “Elongated short” form [22]. All STM images are measured at 77K.

## 3.2 Reconstruction of the InSb $(111)_B$ surface

### 3.2.1 Monitoring the oxygen desorption

In order to study the surface of an InSb(111) layer, the sample B, which was described above and consisted of a 30 nm-thick InSb film grown on an InP(111) wafer, is considered. At the end of the MBE growth, the RHEED indicates a  $(2 \times 2)$  Sb-rich reconstruction. The sample is then exposed to ambient air while being transferred to the LT-STM system. It is, therefore,

deoxidized in the STM system, using the same method as before. However, due to the lower surface free energy of the InSb {111} surface with respect to the InSb {100} surface (600 instead of 1100 ergs/cm<sup>2</sup> [23]), a higher annealing temperature of 300°C was selected. The sputtering was also lengthened to reach 1 hour.

Figure 5.13 compares two Raman spectra of the InSb surface obtained before and after hydrogen eroding. In both spectra a main peak, observed at 180 cm<sup>-1</sup>, corresponds to the TO phonon mode. The small shoulder observed on the right side of this peak is relative to the LO phonon mode. A smaller peak is visible at 305 cm<sup>-1</sup>. We attribute it to the TO phonon of the InP(111) substrate [24]. It appears because of the deeper penetration of the excitation wavelength than the thickness of the InSb layer. Small peaks are seen between 350 cm<sup>-1</sup> and 382 cm<sup>-1</sup> and are assigned to 2TO and 2LO phonon modes.

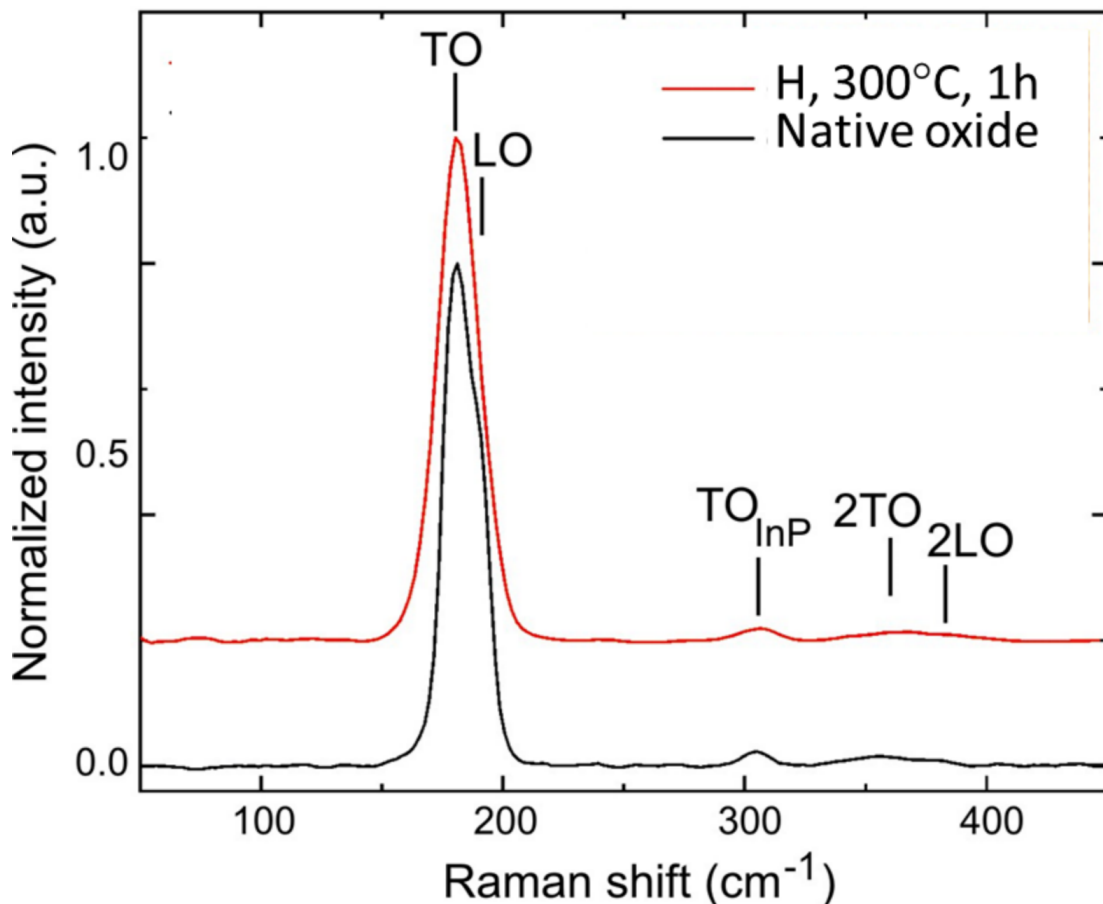


Figure 5.13 – UHV-Raman spectra of the InSb/InP(111)<sub>B</sub> heterostructure before and after 1h of simultaneous annealing and hydrogen sputtering.

Both spectra look similar. Except a slight broadening of the main peak, that we attribute to the use of different optical gratings, Raman spectroscopy does not detect any significant shift of this peak in comparison with the oxide desorption of the InSb (100) surface. For the InSb (111) surface, the TO mode contributes much more to the signal. We believe that this mode

is less sensitive to a structural modification of the surface, or the surface reconstruction does not involve the formation of phonon modes that strongly differ from the bulk structure. As a result, the removal of the oxygen surface cannot be monitored with Raman spectroscopy.

### 3.2.2 STM study of the surface structure

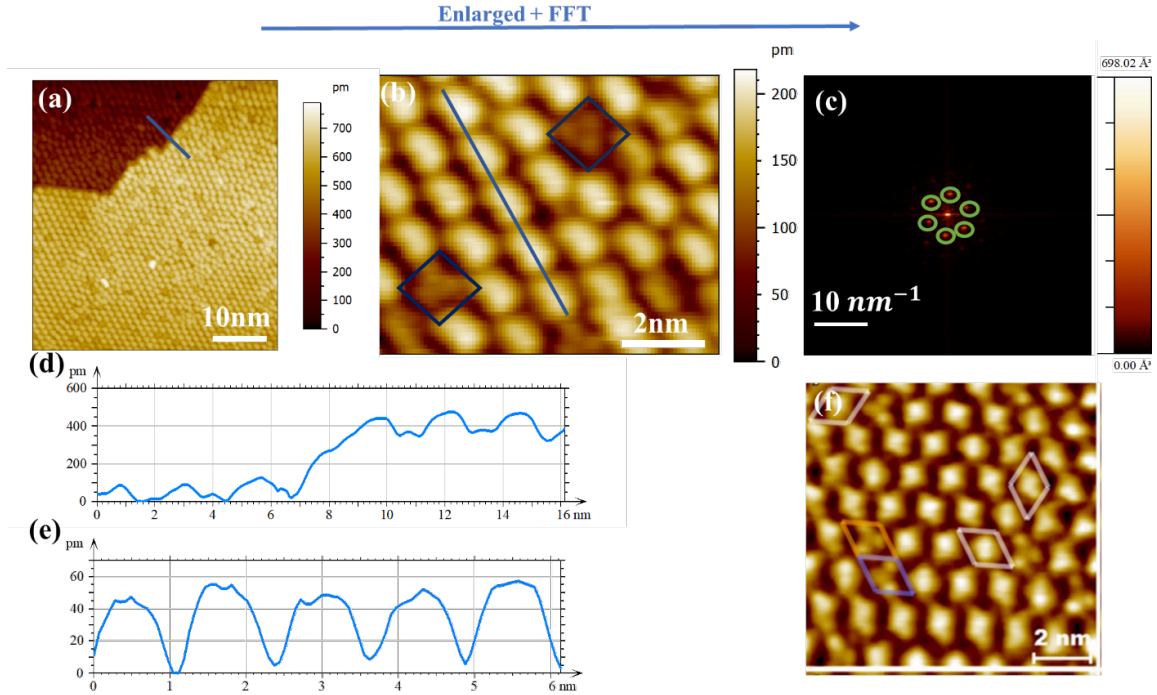


Figure 5.14 – (a) STM image of the InSb (111)<sub>B</sub> surface measured at 77K. Feedback parameters:  $V_s = -1.8\text{V}$  and  $I_t = 150\text{ pA}$ . (b) Atomically-resolved STM image showing two different types of defects surrounded by a blue diamond. (c) FFT image of an enlarged part of (a), green circles correspond to bright points. (d) and (e) Height profiles along the blue segments in (a) and (b) respectively. (f) Comparison with the literature [25] for an occupied-state STM image measured at room temperature, where the atomic structure corresponds to a  $(3 \times 3)$  reconstruction.

Figure 5.14(a) shows a STM image of the sample surface after hydrogen eroding for 1h at  $300^\circ\text{C}$ . A well-ordered crystalline structure is seen on both terraces. The height profile along the blue segment across the two adjacent terraces yields a step height of  $3.7 \pm 0.1 \text{ \AA}$ . This value corresponds to the theoretical monolayer thickness of an InSb (111) surface that is  $\frac{6.48}{\sqrt{3}} = 3.74 \text{ \AA}$ . Figure 5.14(c) is a FFT image calculated from the STM image in Figure 5.14(a). It suggests a  $(3 \times 3)$  atomic reconstruction for this surface, consistent with Ref. [25]. It corresponds to an In-rich InSb (111) surface with the module of both lattice vectors equal to 2.27 nm. This reconstruction differs from the  $(2 \times 2)$  structure observed at the end of the growth. As the  $(2 \times 2)$  reconstruction corresponds to a Sb-rich structure, the removal of the oxide layer, which involved an annealing at  $300^\circ\text{C}$ , causes the desorption of Sb atoms, yielding

an In-rich surface in the STM system.

We note that the atomically-resolved features in Figure 5.14(b) have an elongated shape instead of the diamonds seen at room temperature in the STM image observed by [25] as illustrated in Figure 5.14(f). This discrepancy could be caused by a tip artefact as elongated shapes are also observed in the STM image of Ref. [26]. However, another explanation could rely in the different temperatures used to image the surface, 77 K in our study versus 300 K in Ref. [27]. These features have been attributed to the contribution of hexamer rings to the STM contrast. The hexamers consist of two pairs of bonded In adatoms separated by Sb adatoms [26] [27]. In this  $\text{In}_4\text{Sb}_2$  elliptic ring, the adatoms vibrate at room temperature, making the ring more symmetric. By studying the surface at low temperature, the vibrations become frozen, giving rise to an elongated contrast, signature of the  $\text{In}_4\text{Sb}_2$  clusters. Conversely, a few features, highlighted in Figure 5.14(b), show a different symmetry with fainter contrast. Based on Ref.[26] , we attribute them to hexamer ring with alternating Sb and In adatoms, the so-called beta  $\text{In}_3\text{Sb}_3$  ring.

## 4 Conclusion

This chapter focused on planar InSb nanostructures directly grown on InP wafers. The growth conditions were optimized to overcome structural growth defects which are known to arise due to the high lattice mismatch between InSb and InP.

In fact, for InSb 2D growth on InP(100) wafers, 3D rectangular-based islands are formed on the surface. Optimizing the growth conditions of the InSb film by increasing the growth rate enhances the island density. But, it is still complicated to form InSb 2D film on InP (100) wafers whatever the growth conditions are.

In the case of the growth on InP(111) wafers, due to the lower surface energy, 2D films are formed in this case. Increasing the Sb/In ratio to 120 by lowering the growth rate and increasing the Sb flux has been found to enhance the continuity of the InSb films and 1D nanowires selectively grown inside  $\text{SiO}_2$  mask openings.

In case of a 30 nm-thick InSb films, prepared with a 0.05ML/s growth rate and a 120 Sb/In ratio at 390°C, it is fully relaxed on InP. The film covered 93% of the surface even though holes deeper than 30 nm are still present. The holes disappear for a 100 nm-thick film. However, when InSb nanowires are selectively grown with the same conditions a thickness of 30nm-

thick is enough to produce high quality nanowires due their reduced width.  $[\bar{2}11]$ ,  $[0\bar{1}1]$  and  $[01\bar{1}]$  oriented nanowires show vertical side facets with some lateral growth on the  $\text{SiO}_2$  mask. Despite some misfit defects present at the InP-InSb interface, the HAADF-STEM images confirmed the good quality of the InSb nanocrystal.

The reconstruction of the (100) and (111) surfaces were further investigated with scanning tunnelling microscopy. A full desorption of the oxide is obtained at a minimum temperature of  $200^\circ\text{C}$  under hydrogen eroding for about 1 hour. For the InSb (100) surface, the STM revealed an In-rich  $c(8 \times 2)$  reconstructed InSb surface. As to the InSb (111) surface, an In-rich InSb surface with the  $(3 \times 3)$  reconstruction was obtained. Both results show that the desorption of the oxide using hydrogen eroding and annealing leads to a loss of the Sb adatoms, preventing the recovery of the Sb-rich reconstructions occurring at the end of the growth.

## Bibliography

- [1] Z. Yang et al., ‘Spin Transport in Ferromagnet-InSb Nanowire Quantum Devices’, *Nano Lett.*, vol. 20, no. 5, pp. 3232–3239, May 2020, doi: 10.1021/acs.nanolett.9b05331.
- [2] M. De La Mata et al., ‘Twin-Induced InSb Nanosails: A Convenient High Mobility Quantum System’, *Nano Lett.*, vol. 16, no. 2, pp. 825–833, Feb. 2016, doi: 10.1021/acs.nanolett.5b05125.
- [3] R. L. M. Op Het Veld et al., ‘In-plane selective area InSb–Al nanowire quantum networks’, *Commun. Phys.*, vol. 3, no. 1, p. 59, Mar. 2020, doi: 10.1038/s42005-020-0324-4.
- [4] L. Desplanque, A. Bucamp, D. Troadec, G. Patriarche, and X. Wallart, ‘In-plane InSb nanowires grown by selective area molecular beam epitaxy on semi-insulating substrate’, *Nanotechnology*, vol. 29, no. 30, p. 305705, May 2018, doi: 10.1088/1361-6528/aac321.
- [5] P. Aseev et al., ‘Ballistic InSb Nanowires and Networks via Metal-Sown Selective Area Growth’, *Nano Lett.*, vol. 19, no. 12, pp. 9102–9111, Dec. 2019, doi: 10.1021/acs.nanolett.9b04265.
- [6] S. El Kazzi, L. Desplanque, X. Wallart, Y. Wang, and P. Ruterana, ‘Interplay between Sb flux and growth temperature during the formation of GaSb islands on GaP’, *J. Appl. Phys.*, vol. 111, no. 12, p. 123506, Jun. 2012, doi: 10.1063/1.4729548.
- [7] J. S. Lee et al., ‘Selective-area chemical beam epitaxy of in-plane InAs one-dimensional channels grown on InP(001), InP(111)<sub>B</sub>, and InP(011) surfaces’, *Phys. Rev. Mater.*, vol. 3, no. 8, p. 084606, Aug. 2019, doi: 10.1103/PhysRevMaterials.3.084606.
- [8] D. Hull and D. J. Bacon, ‘Chapter 5 - Dislocations in Face-centered Cubic Metals’, in *Introduction to Dislocations (Fifth Edition)*, D. Hull and D. J. Bacon, Eds., Oxford: Butterworth-Heinemann, 2011, pp. 85–107. doi: 10.1016/B978-0-08-096672-4.00005-0.
- [9] O. E. Tereshchenko, ‘Structure and composition of chemically prepared and vacuum annealed InSb(001) surfaces’, *Appl. Surf. Sci.*, vol. 252, no. 21, pp. 7684–7690, Aug. 2006, doi: 10.1016/j.apsusc.2006.03.068.
- [10] Y. Zhang et al., ‘Molecular beam epitaxial growth of AlSb/InAsSb heterostructures’, *Appl. Surf. Sci.*, vol. 313, pp. 479–483, Sep. 2014, doi: 10.1016/j.apsusc.2014.06.009.
- [11] E. D. Palik, *Handbook of Optical Constants of Solids*, vol. 3. Academic Press, 1998.



- [12] V. P. Gnezdilov, D. J. Lockwood, and J. B. Webb, ‘Resonant Raman scattering in an InSb/In<sub>1-x</sub>Al<sub>x</sub>Sb strained-layer superlattice and in In<sub>1-x</sub>Al<sub>x</sub>Sb epilayers on InSb’, *Phys. Rev. B Condens. Matter*, vol. 48, no. 15, pp. 11234–11239, Oct. 1993, doi: 10.1103/physrevb.48.11234.
- [13] W. Kiefer, W. Richter, and M. Cardona, ‘Second-order Raman scattering in InSb’, *Phys. Rev. B*, vol. 12, no. 6, pp. 2346–2354, Sep. 1975, doi: 10.1103/PhysRevB.12.2346.
- [14] C. Seok et al., ‘Raman Spectroscopy of the Damages Induced by Ar-Ion Beam Etching of InSb(100) Surface’, *ECS Solid State Lett.*, vol. 3, no. 3, pp. P27–P29, Dec. 2013, doi: 10.1149/2.009402ssl.
- [15] S. D. Evans, L. L. Cao, R. G. Egdell, R. Droopad, S. D. Parker, and R. A. Stradling, ‘Protective overlayer techniques for preparation of InSb(001) surfaces’, *Surf. Sci.*, vol. 226, no. 1, pp. 169–179, Feb. 1990, doi: 10.1016/0039-6028(90)90163-3.
- [16] R. Fuchs and K. L. Kliewer, ‘Optical Modes of Vibration in an Ionic Crystal Slab’, *Phys. Rev.*, vol. 140, no. 6A, pp. A2076–A2088, Dec. 1965, doi: 10.1103/PhysRev.140.A2076.
- [17] S. Kaku, K. L. Hiwatari, and J. Yoshino, ‘Scanning tunneling microscopy of strained--Sn(001) surface grown on InSb(001) substrate’, *Appl. Surf. Sci.*, vol. 571, p. 151347, Jan. 2022, doi: 10.1016/j.apsusc.2021.151347.
- [18] G. Goryl et al., ‘Structure of the indium-rich InSb(001) surface’, *Phys. Rev. B*, vol. 82, no. 16, p. 165311, Oct. 2010, doi: 10.1103/PhysRevB.82.165311.
- [19] C. Kumpf et al., ‘Subsurface Dimerization in III-V Semiconductor (001) Surfaces’, *Phys. Rev. Lett.*, vol. 86, no. 16, pp. 3586–3589, Apr. 2001, doi: 10.1103/PhysRevLett.86.3586.
- [20] S.-H. Lee, W. Moritz, and M. Scheffler, ‘GaAs(001) Surface under Conditions of Low As Pressure: Evidence for a Novel Surface Geometry’, *Phys. Rev. Lett.*, vol. 85, no. 18, pp. 3890–3893, Oct. 2000, doi: 10.1103/PhysRevLett.85.3890.
- [21] C. F. McConville et al., ‘Surface reconstructions of InSb(100) observed by scanning tunneling microscopy’, *Phys. Rev. B*, vol. 50, no. 20, pp. 14965–14976, Nov. 1994, doi: 10.1103/PhysRevB.50.14965.
- [22] G. Goryl, O. Boelling, S. Godlewski, J. J. Kolodziej, B. Such, and M. Szymonski, ‘Low temperature InSb(001) surface structure studied by scanning tunneling microscopy’, *Surf. Sci.*, vol. 601, no. 17, pp. 3605–3610, Sep. 2007, doi: 10.1016/j.susc.2007.07.002.

- [23] J. W. Cahn and R. E. Hanneman, '(111) Surface tensions of III–V compounds and their relationship to spontaneous bending of thin crystals', *Surf. Sci.*, vol. 1, no. 4, pp. 387–398, Oct. 1964, doi: 10.1016/0039-6028(64)90006-8.
- [24] J. H. Park, M. Pozuelo, B. P. D. Setiawan, and C.-H. Chung, 'Self-Catalyzed Growth and Characterization of In(As)P Nanowires on InP(111)<sub>B</sub> Using Metal-Organic Chemical Vapor Deposition', *Nanoscale Res. Lett.*, vol. 11, no. 1, p. 208, Dec. 2016, doi: 10.1186/s11671-016-1427-4.
- [25] J. Mäkelä et al., 'Crystalline and oxide phases revealed and formed on InSb(111)<sub>B</sub>', *Sci. Rep.*, vol. 8, no. 1, Art. no. 1, Sep. 2018, doi: 10.1038/s41598-018-32723-5.
- [26] J. Wever et al., 'A new type of reconstruction on the InSb(111) surface determined by grazing incidence X-ray diffraction', *Surf. Sci.*, vol. 321, no. 3, pp. L225–L232, Dec. 1994, doi: 10.1016/0039-6028(94)90179-1.
- [27] W. Kiefer, W. Richter, and M. Cardona, 'Second-order Raman scattering in InSb', *Phys. Rev. B*, vol. 12, no. 6, pp. 2346–2354, Sep. 1975, doi: 10.1103/PhysRevB.12.2346.

# Conclusion

This thesis is dedicated to the epitaxial growth and characterization of InAs and InSb in-plane nanostructures grown by selective area molecular beam epitaxy, with a specific focus on overcoming the lattice mismatch challenge when both materials are grown on standard GaAs and InP substrates. The journey started by laying a theoretical foundation that offered a broad overview of the material science behind these nanostructures, their crystallographic structures and their electronic properties. One of the critical milestones in this research was the optimization of growth conditions for both InAs and InSb nanostructures. Our study revealed that even slight adjustments to the growth temperature and V to III element flux ratios could have a profound impact on the material quality. For example, the modified growth conditions for InAs resulted in better island coverage and coalescence, enhancing the electronic transport properties. Likewise, careful tuning of the Sb/In flux ratio during the growth of InSb films and nanowires led to improved film continuity, a challenge that was compounded by the inherent lattice mismatch between the materials and their substrates.

This research also emphasized the role of buffer layers. The incorporation of pseudo-morphic buffer layers emerged as a pivotal factor in mitigating charge scatterings caused by lattice mismatch accommodation. This finding aligns well with the objective of enhancing the quality of the InAs and InSb layers, further amplifying their suitability for next-generation electronic applications.

Transport properties stand at the core of any applications that these materials might have in advanced quantum devices. Hence, an entire segment of this thesis was devoted to understanding how variations in structural quality could influence these properties. Multiple characterization techniques, including low-temperature scanning tunnelling microscopy (LT-STM) and four-probe scanning tunnelling microscopy (4P-STM), were employed. A noteworthy advantage of employing 4P-STM is its ability to make contact-free measurements, eliminating the need to deposit metallic contacts on the nanowires. The technique uses tips that can

move freely on the surface, making contacts with a nanometric precision. Furthermore, the measurements are conducted in ultra-high vacuum (UHV) conditions. This combination of high-precision contact and controlled environment allows for the measurement of the intrinsic properties of our nanostructures with high reliability and fidelity. The collected data provided not just validation for the improvements seen in mobility and conductance, but they also stood as a testament to the effectiveness of the chosen growth optimization strategies. Notably, we demonstrated the protective role of the GaSb shell in guarding the InAs core from oxidation—a critical feature for maintaining the structural and electrical integrity of the nanowires. This protection manifests in exceptionally high conductance and electron mobilities, outpacing comparable literature values. For instance, we measured electron mobilities as high as  $44000 \text{ cm}^2/(\text{V} \cdot \text{s})$  at 1.5 K for InAs/GaSb nanowires. Remarkably, although still lower, these nanowires showed conductance values more closely aligned with those measured in 2D electron gases (2DEGs), underscoring their utility in high-performance applications. Additionally, our quantitative research on InAs (111) nanostructures revealed the impact of oxidation on transport properties.

Looking forward, the results from this thesis offer promising avenues for further research and technological applications. The mobility values obtained from both 4P-STM and cryogenic magneto-transport measurements within the InAs nanostructures are sufficiently promising to warrant subsequent investigations into ballistic transport within these nanostructures. The development of InAs/GaSb nanowire-based devices with top or back gates would be a significant next step. Such a configuration would enable the direct observation and manipulation of the ballistic regime in these nanowires. By fine-tuning the gate voltages, we may gain further insights into ballistic transport phenomena, which could, in turn, open the door to quantum devices. In this realm of ballistic transport studies for InAs and InSb, an innovative strategy, could also, involve the integration of superconductive shells. This approach opens up the potential for developing selectively grown, in-plane hybrid heterostructures, combining the unique properties of these semiconductors with superconductivity. Such hybrid structures are anticipated to play a pivotal role in advancing quantum device technology. Moreover, the deoxidation study of the InSb surface inside the LT-STM system allows the study of the transport properties of these nanostructures inside the 4P-STM system with no need to an additional passivation process. This method ensures a more accurate representation of the intrinsic characteristics of InSb nanostructures. Additionally, within the scope of the 'Inspiring' ANR project involving IEMN, CEA-LETI and NEEL, the possibility of passivating InSb

surfaces with a CdTe layer is being explored. This passivation aims to preserve the inherent properties of InSb, thereby enhancing its suitability for advanced semiconductor applications. This approach not only underscores the versatility of InAs and InSb nanostructures in quantum research but also signifies a leap towards preserving and manipulating their intrinsic properties for groundbreaking applications in nanotechnology and quantum computing.

# Appendix 1 : Fundamentals of ballistic versus diffusive transport

When carriers are in motion, they might be scattered by phonons or by the imperfections of the crystal (roughness, dislocations, impurities etc.). In this context, the mean free path corresponds to the average distance travelled by electrons between two collisions and the relaxation time refers to the average time taken between two successive collisions. The mean free path and the relaxation time are related by the following equation:

$$l = v_F \tau \quad (\text{eq A.1})$$

Here,  $l$  designs the mean free path,  $v_F$  is the velocity of the electrons at the Fermi level and  $\tau$  is the relaxation time.

When an electric field is applied across the material, the electrons are accelerated. But as they become scattered, they adopt a finite average velocity, the drift velocity, which is proportional to the electric field. The factor of proportionality, the so-called mobility, is related to the relaxation time by  $\mu = \frac{q\tau}{m^*}$ , where  $q$  is the carrier charge and  $m^*$  is the effective mass of the electrons. This relationship explains why materials with high electron mobilities or low effective mass are attractive for ballistic transport.

The transport regimes in a material depends on the ratio between the average mean free path and the dimensions of the conductor. For a two-dimensional system, if we call  $L$  the material length and  $W$  the material width, then:

- When  $(L, W) \gg l$ , the transport is diffusive (see Figure A.1), which is the most common mode of transport in bulk materials. In this case, carriers exhibit a drift motion in the direction of the applied voltage.

- If  $l \gg (L, W)$ , the transport is ballistic (see Figure A.1). Here, electrons flow through the device without collisions.
- A third case exists when  $L \approx l > W$ , the transport is called quasi-ballistic. This conduction regime lies between the ballistic and diffusive regimes. Carriers have a low probability of undergoing collisions.

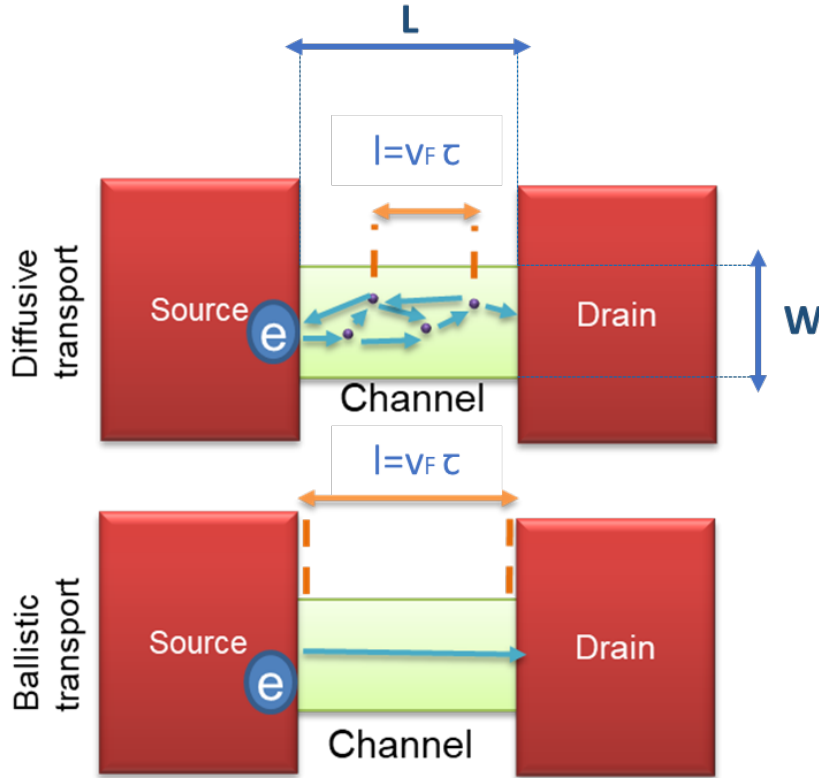


Figure A.1 – Diffusive and ballistic transport in a channel.

The diffusive regime is well described by the Drude model [1]. In the presence of an electric field  $E$ , the conductance  $G$  depends on the conductivity and the dimensions of the conductor, the carrier concentration and to their mobility. It is given by equation A.2:

$$G = qn\mu \cdot \frac{W}{L} \quad (\text{eq A.2})$$

Where  $q$  is the carrier charge,  $n$  is the carrier density and  $\mu$  is the mobility. The material conductance depends consequently on the mobility and thus on the carrier effective mass. The lower the carrier effective mass in a material is, the higher the conductance is.

Under certain conditions, the phase coherence of carriers is preserved over sufficiently large distances, allowing quantum interference to take place. This type of transport is, consequently, called "coherent" electron transport. In the case of this type of transport, the conductance



is described by the Landauer-Büttiker formalism [2], [3]. The model consists of a ballistic conductor with a length  $L$  that is connected on both sides by two metal contacts (electrodes) with two different Fermi levels  $E_{F1}$  and  $E_{F2}$ , as presented in the Figure A.2.

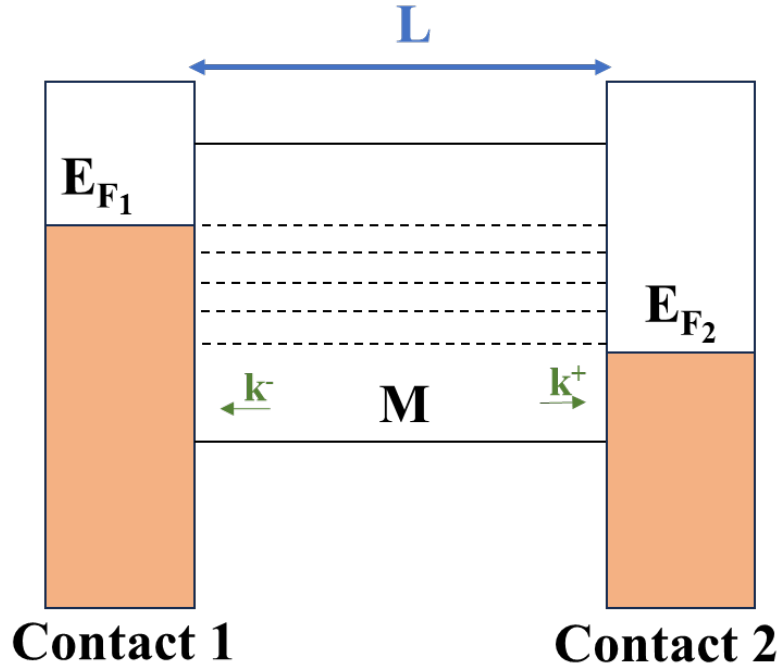


Figure A.2 – Simplified scheme of a ballistic conductor with a length  $L$  connected to two electrodes 1 and 2 with Fermi energies  $E_{F1}$  and  $E_{F2}$  respectively.  $M$  is the number of channels in which electrons propagate between the electrodes.

The confinement of electronic states in the direction perpendicular to the current flow leads to the existence of several energy sub-bands  $E_s$ . The sub-bands are also called channel  $M(E)$  (Figure A.2). Carriers occupy all states with energies below the Fermi energy,  $E_F$ . Carriers traveling from the left contact to the right contact occupy the  $k^+$  states, while carriers moving in the opposite direction occupy the  $k^-$  states. In the absence of a bias between the contacts, the Fermi energies in both contacts being at the same position, the symmetry of the dispersion relation ensures that the current generated by the carriers in the  $k^+$  compensates the generated current by the carriers in the  $k^-$  states, resulting in the absence of current. The presence of a bias  $V_{\text{bias}}$  between the electrodes leads to a shift of one Fermi energy with respect to the other one. Hence, a current flows and can be calculated using the Landauer expression as follows [3].

$$\begin{aligned}
 I &= \frac{q}{L} \sum_{s,k} \frac{1}{\hbar} \frac{\partial E_s(k)}{\partial k} [f(E_s - E_{F1}) - f(E_s - E_{F2})] \\
 &= \frac{2q}{2\pi} \sum_s \int dk \frac{1}{\hbar} \frac{\partial E_s(k)}{\partial k} [f(E_s - E_{F1}) - f(E_s - E_{F2})] \quad (\text{eq A.3}) \\
 &= \frac{2q}{h} \int dE [f(E_s - E_{F1}) - f(E_s - E_{F2})] M(E)
 \end{aligned}$$

(the transition from a discrete summation to a continuous integration elegantly reflects the dense and continuous nature of energy states within the ballistic transport regime.)

$$I \approx \frac{2q^2}{h} M \frac{E_{F1} - E_{F2}}{q}$$

Here,  $\hbar$  is the reduced Planck constant.  $s$  refers to the transverse subbands, including spin degeneracy.  $\frac{\partial E_s}{\partial k}$  is the group velocity of the carriers and  $[f(E_s - E_{F1}) - f(E_s - E_{F2})]$  gives the difference in occupation probabilities for electrons at the source and drain. The transition from Expression 1 to Expression 2 is essentially the replacement of the discrete summation over  $k$ -states with an integral. This is done using the density of states in  $k$ -space for a one-dimensional system, which is given by  $\frac{L}{2\pi}$  per unit length for each  $k$ -state. The factor of 2 comes from the spin degeneracy, assuming that each  $k$ -state is doubly degenerate due to spin.

As  $I = G \cdot V_{\text{bias}}$  and  $V_{\text{bias}} = \frac{E_{F1} - E_{F2}}{q}$ , the material conductance is then given by the equation A.4:

$$G \approx \frac{2q^2}{h} M = G_0 M \quad \text{with } G_0 = \frac{2q^2}{h} \quad (\text{eq A.4})$$

Equation A.4 highlights a quantized conductance for ballistic transport regime. The ballistic conductance is then proportional to the number of the channels (sub-bands) of the material that are between the Fermi levels ( $E_{F1}$  and  $E_{F2}$ ) of the electrodes separated by an energy  $qV_{\text{bias}}$ .

A beautiful example of a quantized conductance was experimentally demonstrated by S. Frank et al. using arc-produced multiwalled carbon nanotubes (MWCNT)[4]. The experimental scheme is presented in Figure A.3(a) where a CNT fiber is brought down to be contacted to a metal in the liquid phase at room temperature (mercury, cerrolow, gallium). With this setup, the authors observed a conductance per single carbon nanotube that equals  $G_0$  independently of the NT length or widths. This value is half the expected theoretical value for CNTs as a metallic WNT is known to have two bands crossing the Fermi level [5], [6]. This value increases

in discrete steps being proportional to  $G_0$  when additional NTs of the MWCNT get in contact with the metal liquid (Figure A.3(b)).

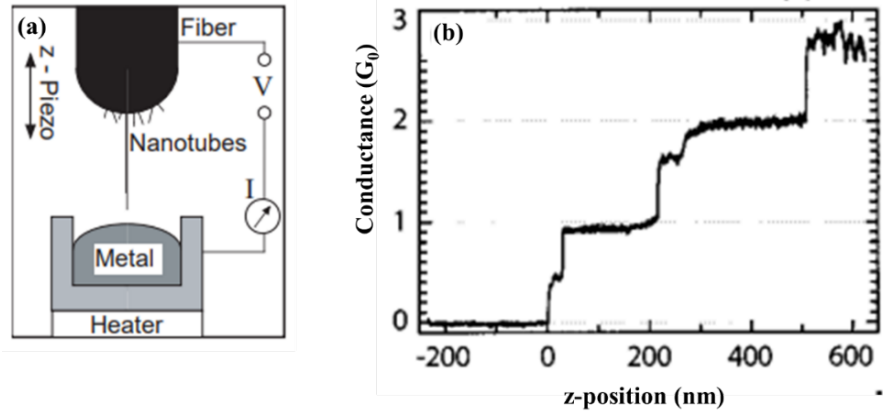


Figure A.3 – (a) Schematic diagram of the experimental setup. The nanotube contact is lowered under SPM control to a liquid metal surface. After contact is established, the current  $I$  is measured as the fiber is moved into the liquid metal, so that the conductance can be determined as a function of the position of the nanotube contact. (b) Conductance as a function of the dipping length into the liquid mercury contact. The quantized conductance of  $G_0$  corresponds to a single nanotube making contact to mercury. The other quantized conductance values correspond to two and three nanotubes making contact to the metal. [Adapted from [4]].

Ballistic transport was also observed in InAs/AlSb quantum wells grown on GaAs (100) wafers by MBE. When constrictions are built in two-dimensional electron gas (2DEG), quantized conductance steps can be seen at low temperature [7], [85]. S. J. Koester et al. benefited from large band offset between InAs and AlSb, that generated high confined electron density and mobility in the 2DEG. The high transport quality of the InAs/AlSb 2DEG allowed ballistic transport observation up to the  $\mu$  scale. For 1D systems, J. Gooth et al. observed ballistic transport inside InAs nanowires, as conductance plateaus are measured at integer multiples of  $G_0$ , as seen in Figure A.4 [8]. Remarkably, the hallmark of this 1D sub-bands survives when cross-junctions are fabricated along the nanowires. In principle, such a cross-junction causes the scattering of free charge carriers, which is detrimental to the transmission of 1D modes, hence destroying ballistic effects. However, the quantized conductance plateaus versus the gate voltage were observed for several number of junctions (Figure A.4(b)) at 4K, albeit to a reduced intensity. The transport across multiple NW junctions is therefore not dominated by the number of junctions along the nanowire, which can be considered transparent, but rather by the mean free path of charge carriers. Figure A.4(c) displays the measured  $G^{-1}$  dependency to the wires length. For all wires, a clear transition exists around 800 nm. Below this threshold, the resistance of the nanowire is constant, signature of ballisticity; above the threshold, the resistance increases linearly with the nanowire length, corresponding to a diffusive regime.

Consequently, the length for which the resistance variations change of slope represents the electrons mean free path.

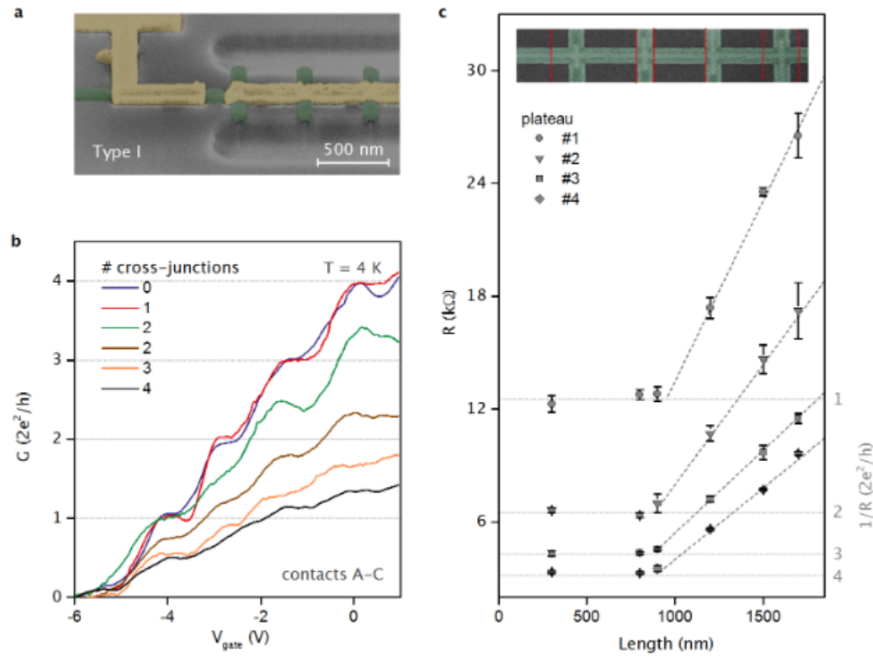


Figure A.4 – The 1D quantum transport across multiple NW junctions. (a) False-colored SEM image of a device with 0 cross-junctions. (b) Conductance versus  $V_{\text{gate}}$  curves for various numbers of cross-junctions in the transport channel ( $l = 300$  nm, blue;  $l = 800$  nm, red;  $l = 900$  nm, green;  $l = 1200$  nm, brown;  $l = 1500$  nm, orange;  $l = 1700$  nm, black). On all curves, the same average contact resistance of  $6.7$  k $\Omega$  has been subtracted. (c) Experimental plateau resistance (symbols) as a function of channel length  $l$ . The values are obtained by averaging the data in (b) over the full width at half-maximum of the minima of the transconductance. The error reflects the standard deviation. The red dotted lines in the SEM inset mark the position of the right contact relative to the position of the left contact that corresponds  $L = 0$  at the bottom axis. [8].

The variation of the resistance  $R$  is expressed as a function of the wire length  $L$  as follows:

$$R = G_0^{-1} \left( 1 + \frac{L}{l} \right) = R_{\text{Ballistic}} \left( 1 + \frac{L}{l} \right) \quad (\text{eq A.5})$$

When the wire length is inferior to the mean free path  $L < l$ , its resistance is equal to  $R_{\text{Ballistic}}$ . When  $L \gg l$ , the resistance increase linearly with  $L$ . This behavior is also experimentally confirmed by S. Chuang et al. [9] who studied the transport characteristics of 31 nm-diameter InAs nanowire based Field Effect Transistors (FETs).

When a four probe configuration is used, with two outer electrodes that drives the current and to inner electrodes that measure the potential drop, the ballistic resistance  $R_{\text{ballistic}}$  should drop to zero if the inner electrodes are non-invasive. 4P measurements were carried out by R. de Picciotto et al. A 1D GaAs/AlGaSb system created from the depletion of a GaAs/AlGaAs

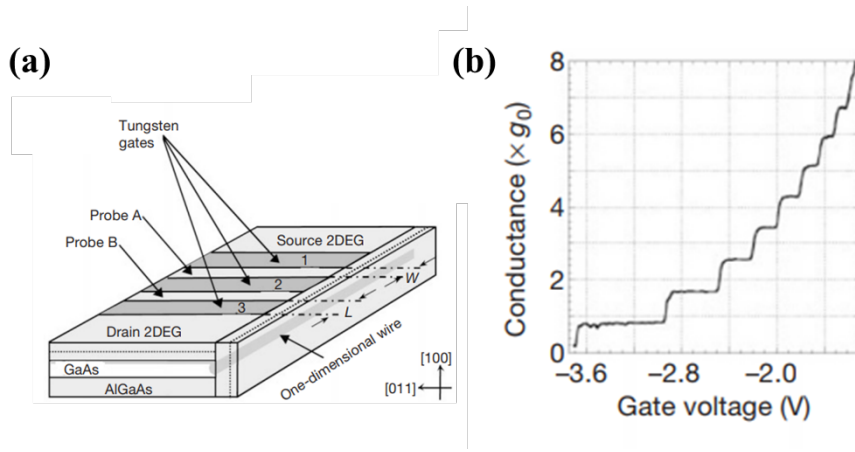


Figure A.5 – (a) Geometry of the cleaved-edge overgrowth (CEO) device. The fabrication starts with a high-quality 2DEG created by epitaxial growth of a unilaterally doped GaAs quantum well onto a [001] GaAs substrate [10]. (b) A representative result of a two-terminal conductance measurement of a CEO wire at 300 mK.

2DEG by means of top gate electrodes (Figure A.5(a)) [10]. Electrons density and mobility of the 2DEG were  $2.5 \times 10^{11} \text{ cm}^{-2}$  and  $4.0 \times 10^6 \text{ cm}^2/(\text{V} \cdot \text{s})$  respectively. The system is presented in Figure A.5(b). The 2P measurements proved the ballistic regime in the whole wire, with the occurrence of conductance plateaus as the gate voltage is negatively swept. When four probes were used, the resistance dropped to zero, demonstrating a ballistic regime in the quantum and minimal invasiveness of the inner contacts.

## **Bibliography**

- [1] J. B. Sousa, J. O. Ventura, and A. Pereira, *Transport Phenomena in Micro- and Nanoscale Functional Materials and Devices*. Elsevier, 2021.
- [2] R. Landauer, ‘Spatial variation of currents and fields due to localized scatterers in metallic conduction’, *IBM J. Res. Dev.*, vol. 32, no. 3, pp. 306–316, May 1988, doi: 10.1147/rd.323.0306.
- [3] S. Datta, *Electronic Transport in Mesoscopic Systems*. Cambridge University Press, 1997.
- [4] S. Frank, P. Poncharal, Z. L. Wang, and W. A. de Heer, ‘Carbon Nanotube Quantum Resistors’, *Science*, vol. 280, no. 5370, pp. 1744–1746, Jun. 1998, doi: 10.1126/science.280.5370.1744.
- [5] W. Tian and S. Datta, ‘Aharonov-Bohm-type effect in graphene tubules: A Landauer approach’, *Phys. Rev. B*, vol. 49, no. 7, pp. 5097–5100, Feb. 1994, doi: 10.1103/PhysRevB.49.5097.
- [6] L. Chico, L. X. Benedict, S. G. Louie, and M. L. Cohen, ‘Quantum conductance of carbon nanotubes with defects’, *Phys. Rev. B*, vol. 54, no. 4, pp. 2600–2606, Jul. 1996, doi: 10.1103/PhysRevB.54.2600.
- [7] S. J. Koester, C. R. Bolognesi, M. J. Rooks, E. L. Hu, and H. Kroemer, ‘Quantized conductance of ballistic constrictions in InAs/AlSb quantum wells’, *Appl. Phys. Lett.*, vol. 62, no. 12, pp. 1373–1375, Mar. 1993, doi: 10.1063/1.108683.
- [8] J. Gooth et al., ‘Ballistic One-Dimensional InAs Nanowire Cross-Junction Interconnects’, *Nano Lett.*, vol. 17, no. 4, pp. 2596–2602, Apr. 2017, doi: 10.1021/acs.nanolett.7b00400.
- [9] S. Chuang, Q. Gao, R. Kapadia, A. C. Ford, J. Guo, and A. Javey, ‘Ballistic InAs Nanowire Transistors’, *Nano Lett.*, vol. 13, no. 2, pp. 555–558, Feb. 2013, doi: 10.1021/nl3040674.
- [10] R. de Picciotto, H. L. Stormer, L. N. Pfeiffer, K. W. Baldwin, and K. W. West, ‘Four-terminal resistance of a ballistic quantum wire’, *Nature*, vol. 411, no. 6833, Art. no. 6833, May 2001, doi: 10.1038/35075009.

# Appendix 2 : Masks layouts



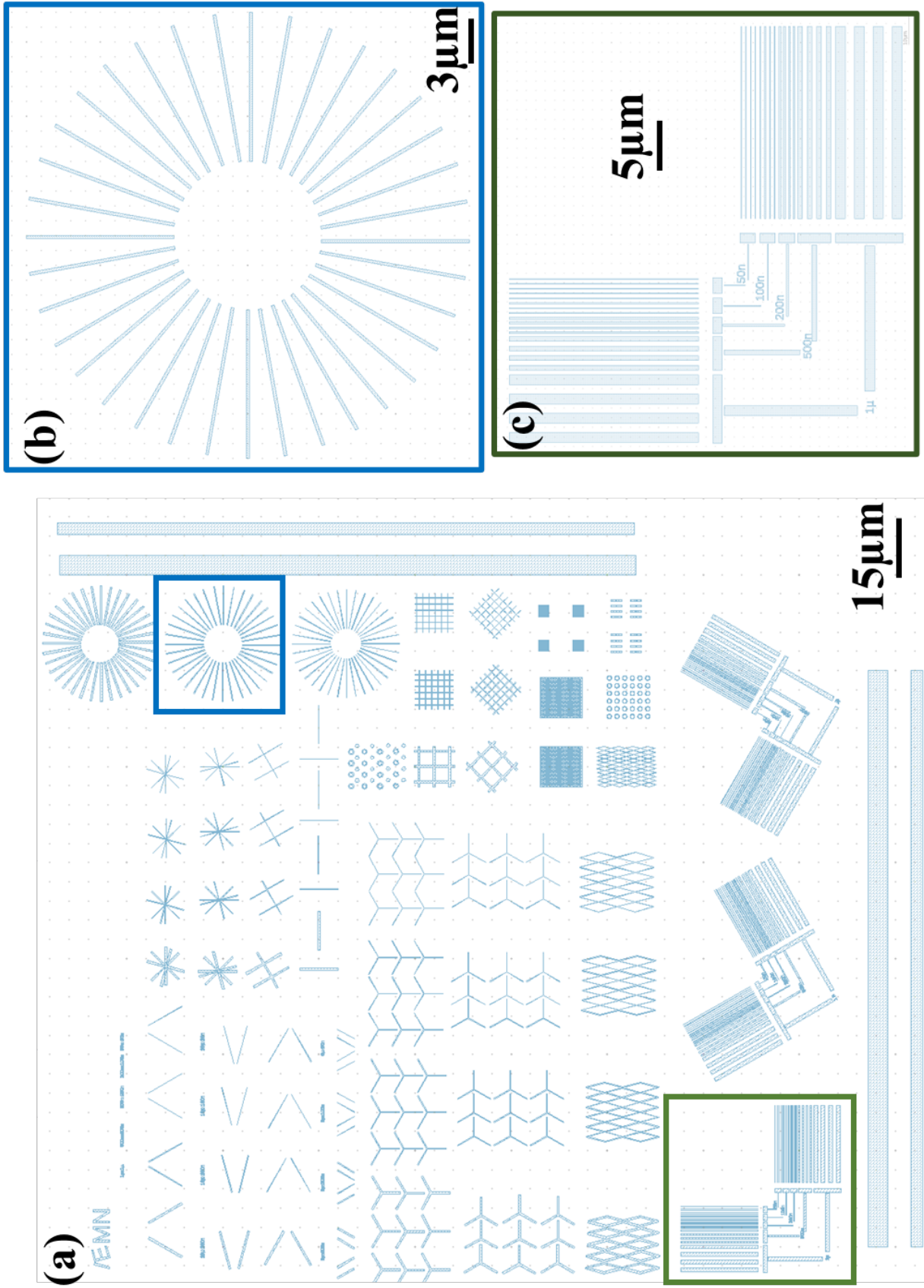


Figure A.6 – (a) Layout of the selective epitaxy designed to grow nanostructures on (111)-oriented substrates for the 4P measurements (Same as Figure 2.4) (b) Sun-like pattern with 100 nm-wide and 10 µm-long rectangles tilted by 10°. (c) 20 m-long rectangles with different widths



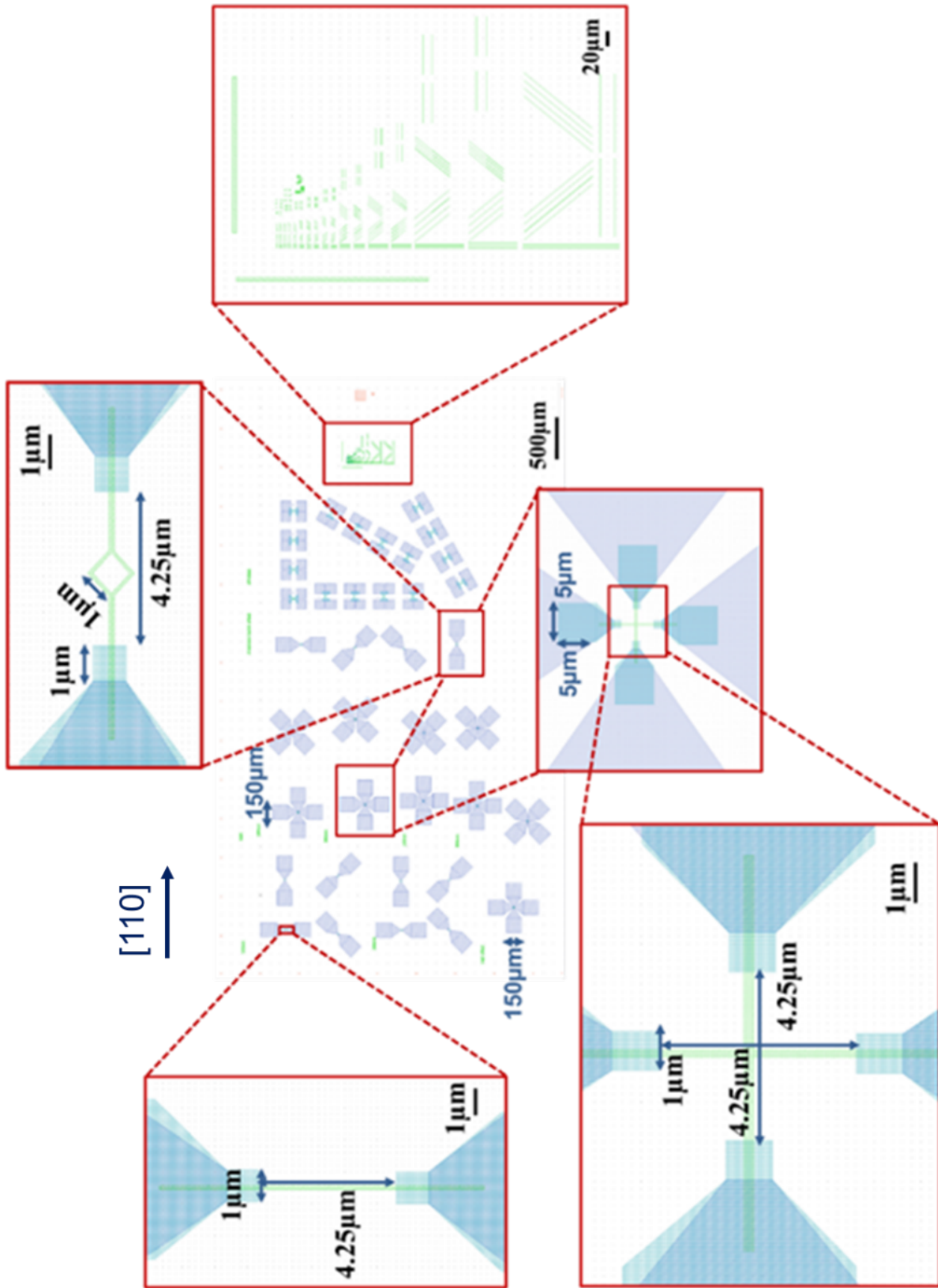


Figure A.8 – Layout of the selectively grown nanostructures designed for the cryogenic measurements

# List of Publications and Communications

## List of Communications

- Wijden Khelifi, Maxime Berthe, Christophe Coinon, Bruno Grandidier, Ludovic Desplanque. *Characterization of electron transport inside InAs/GaSb quantum nanostructures using four probe scanning tunnelling microscopy*. 2ème édition des Rencontres Jeunes C’Nano Nord-Ouest, RJNO 2022, C’Nano Nord-Ouest, May 2022, En ligne, France. [hal-03663746](#)
- Wijden Khelifi, Maxime Berthe, Christophe Coinon, Bruno Grandidier, Ludovic Desplanque. *Characterization of electron transport inside InAs/GaSb quantum nanostructures using four probe scanning tunnelling microscopy*. 23eme forum des microscopies à sondes locales, Mar 2022, Saint-Valery-sur-Somme, France. [hal-03613245](#)
- Wijden Khelifi, Christophe Coinon, Maxime Berthe, David Troadec, Gilles Patriarche, Bruno Grandidier, Ludovic Desplanque. *High Mobility InAs/GaSb Quantum Well and in-Plane Core-Shell Nanostructures Grown on Highly Mismatched Substrates*, ICMBE, Sep 2022, Scheffield, United Kingdom. [hal-04334320](#)
- Wijden Khelifi, Pierre Capiod, Christophe Coinon, Maxime Berthe, X. Wallart, et al. *InSb thin films and selective area MBE grown nanostructures on InP(111)B substrate*. International Conference on Molecular Beam Epitaxy (ICMBE) 2022, Sep 2022, Sheffield - UK, France [hal-04332162](#)

## List of Publications

- W. Khelifi et al., *Improving the intrinsic conductance of selective area grown in-plane InAs nanowires with a GaSb shell*, Nanotechnology, vol. 34, no. 26, p. 265704, Apr. 2023, [doi:](#)

[10.1088/1361-6528/acc810](https://doi.org/10.1088/1361-6528/acc810).

- W. Khelifi et al., *Ultrahigh vacuum Raman spectroscopy for the preparation of III–V semiconductor surfaces*, *Rev. Sci. Instrum.*, vol. 94, no. 12, p. 123702, Dec. 2023, doi: [10.1063/5.0152031](https://doi.org/10.1063/5.0152031).